

Data-Driven Predictive Models: Computational Bias in Characterization of Spent Nuclear Fuel

Présentée le 31 janvier 2022

Faculté des sciences de base
Laboratoire de physique des réacteurs et de comportement des systèmes
Programme doctoral en énergie

pour l'obtention du grade de Docteur ès Sciences

par

Ahmed Salaheldin Ahmed SHAMA

Acceptée sur proposition du jury

Dr S.-R. Cherkaoui, président du jury
Prof. A. Pautz, Dr D. Rochman, directeurs de thèse
Dr G. Ilas, rapporteuse
Dr P. Schillebeeckx, rapporteur
Prof. A. Manera, rapporteuse

This thesis is dedicated to those who think nuclear power is part of the solution and the future.

Interviews and speeches of Richard Feynman have inspired me, motivated me to change my career, and to start an interesting journey that allowed me to achieve this thesis. The following is a quote from a BBC TV interview (1981):

"One way that's kind of a fun analogy to try to get some idea of what we're doing here to try to understand nature is to imagine that the gods are playing some great game like chess. Let's say a chess game. And you don't know the rules of the game, but you're allowed to look at the board from time to time, in a little corner, perhaps. And from these observations, you try to figure out what the rules are of the game, what [are] the rules of the pieces moving.

You might discover after a bit, for example, that when there's only one bishop around on the board, that the bishop maintains its color. Later on, you might discover the law for the bishop is that it moves on a diagonal, which would explain the law that you understood before, that it maintains its color. And that would be analogous we discover one law and later find a deeper understanding of it.

Ah, then things can happen--everything's going good, you've got all the laws, it looks very good--and then all of a sudden some strange phenomenon occurs in some corner, so you begin to investigate that, to look for it. It's castling--something you didn't expect.

We're always, by the way, in a fundamental physics, always trying to investigate those things in which we don't understand the conclusions. We're not trying to all the time check our conclusions; after we've checked them enough, they're okay. The thing that doesn't fit is the thing that's most interesting--the part that doesn't go according to what you'd expect.

Also, we can have revolutions in physics. After you've noticed that the bishops maintain their color and that they go along on the diagonals and so on, for such a long time, and everybody knows that that's true; then you suddenly discover one day in some chess game that the bishop doesn't maintain its color, it changes its color. Only later do you discover the new possibility that the bishop is captured and that a pawn went all the way down to the queen's end to produce a new bishop. That could happen, but you didn't know it.

And so it's very analogous to the way our laws are. They sometimes look positive, they keep on working, and all of a sudden, some little gimmick shows that they're wrong--and then we have to investigate the conditions under which this bishop changed color... happened... and so on... And gradually we learn the new rule that explains it more deeply.

Unlike the chess game, though... In the case of the chess game, the rules become more complicated as you go along, but in the physics when you discover new things, it becomes more simple. It appears on the whole to be more complicated because we learn about a greater experience; that is, we learn about more particles and new things, and so the laws look complicated again. But if you realize that all of the time, what's kind of wonderful is that as we expand our experience into wilder and wilder regions of experience, every once in a while, we have these integration in which everything is pulled together in a unification, which it turns out to be simpler than it looked before."

— Richard Feynman

Acknowledgements

I would like to acknowledge and thank those who helped me in so many ways, personally and academically, reaching the goals presented in this thesis.

Sincere thanks are to Prof. Andreas Pautz and Dr. Ben Volmert for enabling this research project, their trust in finalizing it as planned, and later on providing supervision and support. Also, sincere thanks are to Dr. Susanne Pudollek for continual supervisions and guidance during my stay in Nagra, also the support for the tasks I have been assigned to.

I sincerely thank my scientific advisors Dr. Stefano Caruso and Dr. Dimitri Rochman for their contribution to this thesis. I am in debt to them, providing guidance and patiently coaching me a great deal of scientific research expertise and methods.

Thanks are to Dr S.-R. Cherkaoui, Dr. Germina Ilas, Dr. Peter Schillebeeckx, and Prof. Dr. Annalisa Manera for their valuable review of the thesis and agreeing to be on the jury of the defense.

Special thanks are to the LRT team in PSI, Hakim Ferroukhi and Dr. Alexander Vasiliev who supported my work with their team and providing valuable suggestions.

Additionally, I am grateful to the proof-readers in Nagra Angela and Linda for reviewing the thesis and research papers.

I am thankful to my friends and office-mates in Nagra Valentyn and Stathis, and in PSI Marianna, Petra, and Aaron, and my EPFL friends and colleagues Lessa and Daniel for constructive discussions, sharing ideas, the after-work drinks, and the weekend BBQs as well.

Also, heartfelt thanks for the personal support are to my family: my mother, brother, sisters, and Christelle. Being with me in the ups and downs enabled this work.

Baden, Switzerland
November 20, 2021

A. Shama

Abstract

Characteristics of the spent nuclear fuel (SNF) are typically calculated, requiring validation *a priori*. The validation process relies on the difference between calculations and measurements, namely the bias. Usually, predicting the bias based on benchmarks is essential, which motivated the present research, focusing on SNF decay heat and Cs-137, U-235, and Pu-239 concentrations.

The validation benchmarks are from open-literature, *i.e.*, SNF design and irradiation specifications, as well as the measurements of their characteristics. For the decay heat, they correspond to 262 measurements, conducted at the Clab and the GE-Morris facilities. For the radionuclide concentrations, they are 285 post-irradiation-examination samples, obtained from the SFCOMPO database. The calculations rely on the SCALE code system, namely the Polaris code and the SCALE-based nuclear data.

Uncertainties of nuclear data and SNF design and operational history are propagated to the calculated quantities, for two purposes: (1) to assess if the biases are statistically significant, given the calculated uncertainties, and (2) to obtain correlation matrices between the benchmarks. Statistical analyses, resampling and z-tests, are applied on the validation and uncertainty analyses data. They indicate that the biases in several of the analyzed characteristics are significant with respect to uncertainties in the calculated values. For the decay heat case, the biases are considered not significant considering both the calculated and experimental uncertainties. It is also shown that it is crucial to include the correlations between the benchmarks into the hypothesis testing.

Then, a novel approach is followed, by applying machine learning (ML) methods to predict the bias of calculated SNF characteristics. The predictive performance is analyzed by comparing the ML-based bias predictions and the validation-based biases. The analyzed ML models predict the bias using highly similar benchmarks or neighbors of the benchmarks, namely *Random Forests* (RF) and *Weighted k-Nearest Neighbors* (KNN). Also, the linear model is analyzed.

This research shows that the bias of the decay heat and Pu-239 concentration can be predicted with a reasonable accuracy, relying on specific features of validation benchmarks, or their correlations. The predicted biases bear statistically significant similarities to the observed ones from the validation procedure, using both the RF and the KNN models. The variances in the original validation data are significantly reduced. The models predict the bias using the spectral index for the decay heat and the hydrogen-to-fissile atom ratio for the Pu-239 concentration. Also, the correlation matrices show that they are informative in predicting the bias of both characteristics. In the case of the U-235 and Cs-137 concentrations, biases could not be satisfactorily predicted. Additionally, the linear models have shown unsatisfactory performance.

KEYWORDS:

SNF, validation, bias, predictive models, neighborhood schemes, correlation matrix, SCALE, Polaris

ZUSAMMENFASSUNG

Die Eigenschaften abgebrannter Brennelemente (BE) werden in der Regel berechnet und müssen *a priori* validiert werden. Der Validierungsprozess stützt sich auf die Differenz zwischen Berechnungen und Messungen, d.h. den Bias. Üblicherweise ist es unerlässlich, den Bias anhand von Benchmarks vorherzusagen. Dies ist der Hintergrund dieser Forschungsarbeit, deren Fokus auf der Nachzerfallswärme abgebrannter BE und der Konzentrationen von Cs-137, U-235 und Pu-239 liegt.

Die Validierungs-Benchmarks stammen aus der freien Literatur, d.h. aus BE-Auslegungs- und Bestrahlungs-Spezifikationen sowie aus Messungen von BE-Eigenschaften. Im Fall der Nachzerfallswärme beruhen sie auf 262 Messungen, die im Clab-Zwischenlager (SKB, Schweden) bzw. in der Morris-Anlage von General Electric (USA) durchgeführt wurden. Für die Radionuklidkonzentrationen basieren sie auf 285 Proben aus Nachbestrahlungsuntersuchungen, die aus der SFCOMPO-Datenbank stammen. Die Berechnungen stützen sich auf das SCALE-Codesystem, d.h. im Besonderen auf den Polaris-Code und entsprechende SCALE-basierte nukleare Daten.

Unsicherheiten bei den nuklearen Daten und bei der Auslegung und betrieblichen Herkunft der abgebrannten BE werden aus zwei Gründen in die Berechnungsergebnisse propagiert: (1) zur Prüfung, ob die Bias hinsichtlich der errechneten Unsicherheiten statistisch bedeutend sind, und (2) um Korrelationsmatrizen zwischen den Benchmarks zu erhalten. Statistische Analysen, *Resampling* und *z-Tests*, werden auf die Daten der Validierungs- und Unsicherheitsanalysen angewandt. Sie deuten darauf hin, dass die Bias bei mehreren der analysierten Eigenschaften in Bezug auf die Unsicherheiten bei den errechneten Werten bedeutend sind. Im Fall der Nachzerfallswärme werden die Bias jedoch durch die zusätzliche Berücksichtigung der experimentellen Unsicherheit als nicht signifikant eingeschätzt. Es hat sich auch gezeigt, dass es unerlässlich ist, die Korrelationen zwischen den Benchmarks in die Hypothesenprüfung einzubeziehen.

Anschliessend wird ein neuer Ansatz für die Vorhersage des Bias der Eigenschaften abgebrannter BE angewendet, der auf Machine-Learning-Methoden (ML) beruht. Die Vorhersageleistung wird durch einen Vergleich der ML-basierten Bias-Vorhersagen mit den validierungsbasierten Bias analysiert. Die analysierten ML-Modelle sagen mithilfe von sehr ähnlichen Benchmarks oder benachbarten Benchmarks, d.h. Random Forests (RF) und *Weighted k-Nearest Neighbors* (KNN), den Bias vorher. Zusätzlich wird das lineare Modell untersucht.

Diese Forschungsarbeit zeigt, dass der Bias der Nachzerfallswärmeleistung und der Pu-239-Konzentration anhand spezifischer Merkmale der Validierungs-Benchmarks oder ihrer Korrelationen verhältnismässig zuverlässig vorhergesagt werden kann. Die vorhergesagten Bias weisen

mithilfe der RF- und KNN-Modelle statistisch bedeutende Ähnlichkeiten zu denen auf, die im Rahmen des Validierungsverfahrens beobachtet wurden. Die Abweichungen in den ursprünglichen Validierungsdaten werden erheblich reduziert. Die Modelle sagen den Bias mithilfe des Spektralindex für die Nachzerfallswärme und mithilfe des Atomzahlverhältnisses zwischen Wasserstoff und spaltbaren Isotopen für die Pu-239-Konzentration vorher. Die Korrelationsmatrizen erweisen sich bezüglich der Vorhersage des Bias beider Eigenschaften als informativ. Im Fall der Konzentrationen von U-235 und Cs-137 konnten die Bias nicht zufriedenstellend vorhergesagt werden. Die linearen Modelle zeigten ebenso eine unbefriedigende Leistung.

SCHLÜSSELWÖRTER:

Abgebrannte Brennelemente, Validierung, Bias, Vorhersagemodelle, Nachbarschaftsbasierte Methoden, Korrelationsmatrix, SCALE, Polaris

Contents

Acknowledgements	V
Abstract	VII
ZUSAMMENFASSUNG	IX
Contents	XI
List of Figures.....	XV
List of Tables.....	XXIII
List of Abbreviations	XXV
List of Vocabulary	XXIX
Chapter 1 Introduction.....	1
1.1 Worldwide status of spent nuclear fuel	1
1.2 Status of radioactive waste in Switzerland.....	2
1.3 International projects addressing SNF characterization.....	3
1.4 Motivation of the current research project.....	4
1.5 Relevant SNF characteristics.....	5
1.6 Needs of validation	6
1.7 Needs of explaining and predicting the bias	8
1.8 Predictive modelling paradigm.....	9
1.9 The research questions and hypotheses	10
1.10 Potential applications	11
1.11 Structure of the Thesis.....	12
Chapter 2 Validation Benchmarks	13
2.1 Decay heat benchmarks.....	13
2.1.1. Measurements at the GE-Morris facility.....	14
2.1.2. Measurements at the Clab facility.....	14
2.1.3. Fuel assembly designs and irradiation data	15
2.1.4. Decay heat experimental uncertainties	16
2.2 Post-irradiation-examination benchmarks	18

2.2.1. Characteristics of the PIE Benchmarks	18
2.2.2. Burnup values for the PIE samples	20
2.2.3. Measurements of the radionuclide concentrations	20
2.2.4. Excluded SFCOMPO benchmarks	22
Chapter 3 Modelling and Simulations Codes	25
3.1. Validation tools	25
3.1.1. Polaris code	25
3.1.2. ORIGEN code	26
3.2. Uncertainty propagation.....	26
3.3. Machine learning	26
3.4. Computational requirements	27
Chapter 4 Validation and Uncertainty Propagation Schemes.....	29
4.1. Implementation of Polaris on the decay heat benchmarks.....	29
4.2. Implementation of Polaris on the PIE benchmarks	30
4.3. Implementation of Sampler for uncertainty analyses	33
4.4. Validation and uncertainty measures	35
Chapter 5 Hypothesis Testing on the Bias	37
5.1 Non-parametric tests	37
5.2 Parametric z-test.....	38
Chapter 6 Machine Learning Schemes	41
6.1 Description of the chapter	41
6.2 Application of predictive modelling of the bias	41
6.3 Prediction vs. inference	42
6.4 Predictive performance evaluation	45
6.5 Model validation	45
6.6 The law of parsimony: one-standard-error rule	46
6.7 Machine learning models.....	47
6.8 Resampling methods	52
6.9 Model selection	53
6.10 Predicting the bias from validation benchmarks	57
6.10.1. Predicting the bias based on integral parameters of the benchmarks	57
6.10.2. Predicting the bias based on the correlation between benchmarks	58
6.11 Detection and removal of outliers	61

6.12	Final models of the bias predictive procedures.....	65
6.13	Features extraction.....	66
Chapter 7	Validation Results	69
7.1	SNF decay heat	69
7.2	U-235 concentration.....	73
7.3	Pu-239 concentration	74
7.4	Cs-137 concentration.....	75
7.5	Comparison with literature.....	82
Chapter 8	Uncertainty Analyses	83
8.1	Calculated uncertainties and fractional variances.....	83
8.2	Uncertainties from nuclear data and fractional variances of XS, FY and DD.....	87
8.3	Relevant design and operational parameters	90
8.4	Assumptions of burnup uncertainties	93
8.5	Correlations between benchmarks.....	94
9.4.1.	<i>Decay heat correlations</i>	<i>95</i>
9.4.2.	<i>Correlations of the Cs-137, U-235, and Pu-239 concentrations.....</i>	<i>95</i>
Chapter 9	Significance of the Bias Based on the Validation Data	99
9.1	Significance of the bias based on simultaneous testing	102
Chapter 10	Significance of the Bias Based on the Validation and Uncertainty Data	107
10.1	Significance testing of the bias using calculated uncertainties	107
10.2	Significance testing of the bias using calculated and experimental uncertainties.....	110
10.3	Correlations between the decay heat measurements	111
10.4	Weights of the decay heat benchmarks	112
Chapter 11	Predicting the Bias of SNF Characteristics	113
11.1	Features extraction.....	113
11.1.1.	<i>Design matrix based on correlations between the benchmarks</i>	<i>113</i>
11.1.2.	<i>Design matrix based on integral features of the benchmarks</i>	<i>113</i>
11.2	Predictions of the ML models.....	116
11.2.1.	<i>Linear models based on integral parameters of the benchmarks.....</i>	<i>116</i>
11.2.2.	<i>Linear models based on correlations between the benchmarks</i>	<i>117</i>
11.2.3.	<i>Predictive performance of the decay heat bias.....</i>	<i>120</i>
11.2.4.	<i>Predictive performance of the U-235 concentration bias</i>	<i>124</i>
11.2.5.	<i>Predictive performance of the Pu-239 concentration bias.....</i>	<i>126</i>
11.2.6.	<i>Predictive performance of the Cs-137 concentration bias</i>	<i>128</i>

11.2.7. Predictive performance along with outliers detection and removal	130
11.2.8. Final models.....	133
Chapter 12 Conclusions	137
12.1 Applicability domain	140
12.2 Potential applications	140
12.3 Future work.....	141
Bibliography	143
Appendix I. Modelling the Rebuilt SFAs of Clab Benchmarks	153
Appendix II. Specifications of the PIE Benchmarks and Modelling Assumptions	157
II.1 PWR cases	158
II.1.1 Calvert Cliffs-1 (CC-1).....	158
II.1.2 Genkai-1 (GK-1)	160
II.1.3 Mihama-3 (M-3)	162
II.1.4 Neckarwestheim-2 (N-2)	164
II.1.5 Obrigheim-1 (OG-1)	166
II.1.6 Ohi-1 and Ohi-2 (O1 and O2).....	169
II.1.7 Takahama-3 (T3).....	171
II.1.8 Three Mile Island-1 (TMI-1).....	173
II.1.9 Trino Vercellese-1 (TV1)	175
II.1.10 Turkey Point-3 (TP-3).....	179
II.1.11 Yankee-1 (Y-1).....	181
II.2 BWR cases	186
II.2.1 Cooper-1 (C-1)	186
II.2.2 Dodewaard-1 (D-1)	188
II.2.3 Fukushima Daini-1 (FD1)	191
II.2.4 Fukushima Daini-2 (FD2)	194
II.2.5 Garigliano-1 (G1)	199
II.2.6 Gundremmingen-1 (GN1).....	202
II.2.7 Japan Power Demonstrations Reactor-1 (JPDR-1)	205
Appendix III. Polaris Input Files	209
IV.1. Polaris input for PIE sample DM3, SFA Y012, reactor Dodewaard-1	211
IV.2. Polaris input for PIE sample GG, SFA BT03, reactor Calvert Cliffs-1	215
Appendix IV. Permutation Tests on the Decay Heat Data	219
Appendix V. ORIGEN Calculations of the Decay Heat.....	223
Curriculum Vitae.....	225

List of Figures

Figure 1. Tons of HM contained in SNF in year 2020 (top), and the prospected amount in year 2050 (bottom) (figure from Reference [4]).	2
Figure 2. Selected Polaris models of BWR SFAs (top 3 rows) and PWR SFAs (bottom row). The BWR models are asymmetric, while the majority of the PWRs have quarter symmetry. The models are (from left to right, top to bottom): GE7, GE8, GE9, SVEA-64, SVEA-100, W14x14, W15x15, and W17x17. Fuel rods are shown in different colors to reflect differences in densities, enrichments, and gadolinium content.	16
Figure 3. Uncertainties in the decay heat measurements [12,27]. Uncertainties are reported at upper and lower values, marked at the ends of each line along with values of both the measured decay heat and the corresponding uncertainty. Uncertainties are interpreted as 2σ , and intermediate values are linearly interpolated between the listed upper and lower values.	17
Figure 4. Characteristics of the considered PIE samples. Left: the axial height of the sample (z) with respect to the active length of the fuel rod (H) vs. the coolant density. Right: the sample enrichment vs. the sample given burnup. Additionally, BWR MOX samples are marked with “X”.	19
Figure 5. Correction factors applied on the burnup of the PIE samples. The dashed blue lines are the 2.5% and 97.5% percentiles (i.e., an interval that contains 95% of the observations).	20
Figure 6. Experimental uncertainties (2σ) for the PIE samples, based on SFCOMPO [11].	22
Figure 7. Measured U-235, Pu-239, and Cs-137 concentrations vs. the sample given burnup. The plotted bars are experimental uncertainties (2σ).	22
Figure 8: A subjective view of the placement of various ML model types between interpretability and predictive performance.	44
Figure 9: Trade-off between the bias and variance of a machine learning model. Simpler models have higher bias, which indicates under-fitting. Complex models have higher variance, which indicates over-fitting. Both are model defects increasing the total error of the model.	44
Figure 10: Application of the OSE rule. The optimal model contains 12 variables. A simpler model is chosen following the OSE rule, containing lower number of variables (4 variables).	47
Figure 11: Linear model in CSA using the correlation between benchmarks (figure from Reference [83]). A target application is fully correlated with benchmarks at unit correlation.	49
Figure 12: KNN model using Gaussian weights. The red points are used for predictions at x_0 , and the yellow area is the scale of the weights assigned to these points (figure from Reference [82]). The blue line is the underlying model generating the data, and the green line is the KNN model prediction.	50
Figure 13: A tree build on a 2D predictor space (left). Making predictions of the response using the tree proceeds by averaging the response of the observations located in the same terminal node (R_1, R_2, \dots, R_5). The terminal nodes are intervals on the predictor space (right) (figure from Reference [75]).	51
Figure 14: Illustration of common sampling techniques on a dataset of size 10. The splits of the holdout, bootstrapping and the 5-fold cross-validation are random.	55
Figure 15: Illustration of a nested cross-validation. A 5-fold cross-validation (inner loop) is nested within a LOOCV (outer loop). The inner loop performs model selection and training, and the outer loop is for performance assessment of the model selection and training procedure. Testing results are not random, being LOOCV, and the selection and training results depend on the random splitting of the data.	56

Figure 16. Flowchart of performance assessment of features and model selection procedure applied for learning from integral benchmark parameters. The size of the design matrix is $N \times P$, where N is the number of benchmarks and P is the number of predictors (i.e., features). Also, B is the bias, x and X are subset and all benchmark features, h and H are subset and all model hyperparameters, and j is a single benchmark. The algorithm starts at the design matrix (in orange color) and output the paired prediction/observation data (in green color).....	58
Figure 17. Decomposition of the correlation matrix of size $N \times N$ into N individual correlation vectors (for training and testing), along with submatrices of size $N - 1 \times N - 1$ for validation. The correlation and bias data are combined to result in the design matrices.	59
Figure 18. Similar to Figure 17, implementing matrix decomposition for validation, training, and testing. Unlike the approach described in Figure 17, the validation relies on data resampling (e.g., using LOOCV) on the correlation vector – along with the bias vector, optimizing model parameters for their performance on the validation section of the correlation vector.....	60
Figure 19. Flowchart of the performance assessment of the model selection procedure applied for learning from the correlation between the benchmarks. N is the number of benchmarks, B and ρ are their biases and correlations, M and S are the correlation matrix (all data) and a subset correlation matrix, h and H are subset and the entire model's hyperparameters, J is a correlation vector, and j is a single benchmark. The algorithm starts at the correlation matrix and the bias vector (in orange color) and output the paired prediction/observation data (in green color).....	61
Figure 20. Flowchart of outliers detection and removal based on the design matrix of the integral benchmark parameters. The algorithm starts at the design matrix having $N \times P$ size (in orange color) and output the reduced design matrix having the $N - o \times P$ size (in green color).	63
Figure 21. Flowchart of outliers detection and removal based on the design matrix of the correlation between benchmarks. The algorithm starts at the correlation matrix having $N \times N$ size and the bias vector having N length (in orange color) and output the reduced correlation matrix having the $N - o \times N - o$ size and the reduced bias vector having $N - o$ size (in green color).....	64
Figure 22. SI vs. enrichment, water density, burnup, and H/X , based on the Clab decay heat benchmarks. The axes are centered and normalized, having average of zero and unit variance.....	67
Figure 23. H/X vs. enrichment, sample height, burnup, and SI . The plots are based on the PIE benchmarks. The axes are centered and normalized, having average of zero and unit variance.....	68
Figure 24. C/E of the decay heat, calculated for the 262 benchmarks of Clab (top three plots) and GE-Morris (bottom two plots). The BWRs are shown in black color, and the PWRs are in red. The uncertainty bars are experimental uncertainties (2σ).....	71
Figure 25. Same as Figure 24, but for B instead of C/E values.	72
Figure 26. Measured U-235 concentration vs. burnup (left) and the obtained C/E vs. the measured U-235 concentration (right).	73
Figure 27. Measured Pu-239 concentration vs. burnup (left) and the obtained C/E vs. the measured U-235 concentration (right).	74
Figure 28. C/E of the U-235 concentrations. The BWRs are shown in black color (top two plots), and the PWRs are in red color (bottom two plots). The uncertainty bars are experimental uncertainties (2σ), reported for some of the analyzed benchmarks [11].	76
Figure 29. Same as Figure 28, but for B instead of C/E values.	77

Figure 30. C/E of the Pu-239 concentrations. The BWRs are shown in black color (top two plots), and the PWRs are in red color (bottom two plots). The uncertainty bars are experimental uncertainties (2σ), reported for some of the analyzed benchmarks [11].	78
Figure 31. Same as Figure 30, but for B instead of C/E values.	79
Figure 32. C/E of the Cs-137 concentrations. Missing B values are benchmarks lacking experimental measurements (63 PIE samples out of the total 285). The BWRs are shown in black color (top two plots), and the PWRs are in red color (bottom two plots). The uncertainty bars are experimental uncertainties (2σ), reported for some of the analyzed benchmarks [11].	80
Figure 33. Same as Figure 32, but for B instead of C/E values.	81
Figure 34. C/E and B values of Polaris and ORIGEN obtained in this work, along with results from [13,27,28,90]. The bars are 1σ . The listed ND libraries are the primary source of ND.	82
Figure 35. Calculated uncertainties of the decay heat (left), and the FVs of DO origins (right).	85
Figure 36. Same as Figure 35 for the U-235 concentration.	85
Figure 37. Same as Figure 35 for the Pu-239 concentration. Samples of Yankee-1 (PWR) and MOX samples (BWR) are marked with extra “X” symbol.	86
Figure 38. Same as Figure 35 for the Cs-137 concentration.	86
Figure 39. Contribution of uncertainties from ND to decay heat, U-235, Pu-239, and Cs-137 total calculated uncertainties (shaded grey area), and individual contributions of XS, FY, and DD to uncertainties from ND. The SFAs are ordered by burnup (top to bottom). The minimum and maximum cooling times are 2 and 50 years.	88
Figure 40. Same as Figure 39 for selected decay heat relevant nuclides.	89
Figure 41. Perturbed concentrations of U-235 and Pu-239 vs. the burnup perturbation factor – both axes are centered and normalized. Left plot is benchmark A1-I2 (BWR), and the right plot is benchmark G10_4 (PWR).	90
Figure 42. Correlations of the calculated characteristics with the DO parameters. The boxes show the median and the first and third quartiles (Q1 and Q3). The whiskers are at $Q1 - 1.5 \times IQR$ and $Q3 + 1.5 \times IQR$ (IQR is the interquartile range).	92
Figure 43. Relative uncertainty for cases implementing different assumptions on the power and burnup uncertainties (relative to the reference case of SFA 6432 of Ringhals-1). The minimum and maximum cooling times are 2 and 100 years.	94
Figure 44. Correlations between the calculated decay heat values of the Clab and GE-Morris benchmarks (top row), and only the Clab benchmarks (bottom row). The matrices are ordered according to the burnup (top to bottom and left to right). The left column shows correlations due to perturbing the DO parameters, and the right column shows correlations due to perturbing the ND.	97
Figure 45. Correlations between the calculated concentrations of Cs-137, U-235, and Pu-239. The matrices and columns are ordered similar to Figure 44.	98
Figure 46. Bootstrap distributions of the average biases (the red lines are 95% normal CI). The distributions are centered near the observed average biases and testing their significance proceeds by observing whether or not a zero average bias falls within the chosen CI.	101

Figure 47. Decay heat biases calculated using Polaris and ORIGEN (P and O) – shown only for the Clab benchmarks. The BWRs are shown in black color, and the PWRs are in red. The uncertainty bars are experimental uncertainties (2σ).....	103
Figure 48. Calculated decay heat values (DH) using Polaris vs. ORIGEN (left), and vs. the measured values (right). The data belong to both the Clab and GE-Morris benchmarks. Linear regression results in the presented RMSE values. The blue lines have a slope of unity.	103
Figure 49. Permutations distributions of the average biases of Clab benchmarks (first row), and the bootstrap distributions (second row). The corresponding distributions of the GE-Morris benchmarks are in the third and fourth rows. BWRs are left and PWRs are right. Red lines mark the actually observed average biases in the permutation plots, and zero biases in the bootstrap plots.....	106
Figure 50. Z-scores for the decay heat, Cs-137, U-235, and Pu-239 concentrations, obtained using calculated uncertainties. The header of each plot provides the combined z-score (z) (considering correlations between calculations) and the 95% CI on the z-score distribution.	109
Figure 51. Same as Figure 50 for the decay heat benchmarks, considering both the calculated and the experimental uncertainties.	110
Figure 52. Combined z-score (z), obtained using both the calculated and the experimental uncertainties, vs. the experimental correlation. The insignificant bias is within the shaded area.....	111
Figure 53. Observed bias (validation-based) vs. the LM predicted bias (ML-based) of decay heat of the Clab benchmarks. The left plot is based on integral parameters of the benchmarks, using the calculated decay heat value (C), and the right plot is based on the correlation between the benchmarks, implementing an 0.95 correlation cut-off. The redline is a 45° line, indicating equality between the predicted and the observed bias.....	119
Figure 54. Same as Figure 53 for the Pu-239 concentration, based on the interaction between the spectral index and the Pu-239 calculated concentration ($SI \times C$), and an 0.65 correlation cut-off.	119
Figure 55. Observed bias (validation-based) vs. the RF model predicted bias (ML-based) for the decay heat – Clab benchmarks. The left plot is based on integral parameters of the benchmarks, using the spectral index (SI), and the right plot is based on the correlation between the benchmarks. The redline is a 45° line, indicating equality between the predicted and the observed bias. The blue line is the linear regression line of the observed bias on the predicted one.	122
Figure 56. Same as Figure 55 for the KNN model.....	122
Figure 57. Observed bias (validation-based) vs. the RF model predicted bias (ML-based) for all the decay heat benchmarks (Clab data are highlighted in red color). The left plot is based on integral parameters of the benchmarks, using the interaction between the spectral index and the cooling time ($SI \times \text{Decay}$), and the right plot is based on the correlation between the benchmarks.	123
Figure 58. Same as Figure 57 for the KNN model.....	123
Figure 59. Observed bias (validation-based) vs. the RF model predicted bias (ML-based) for the U-235 benchmarks. The left plot is based on integral parameters of the benchmarks, using the calculational-based uncertainty (σ), and the right plot is based on the correlation between the benchmarks.....	125
Figure 60. Same as Figure 59 for the KNN model.....	125

Figure 61. Observed bias (validation-based) vs. the RF model predicted bias (ML-based) for the Pu-239 benchmarks. The left plot is based on integral parameters of the benchmarks, using the hydrogen-to-fissile atom ratio (H/X), and the right plot is based on the correlation between the benchmarks.	127
Figure 62. Same as Figure 61 for the KNN model.	127
Figure 63. Observed bias (validation-based) vs. the RF model predicted bias (ML-based) for the U-235 benchmarks. The left plot is based on integral parameters of the benchmarks, using a single features, the interaction between burnup and the calculated Cs-137 concentration ($BU \times C$), and the right plot is based on the correlation between the benchmarks.	129
Figure 64. Same as Figure 63 for the KNN model.	129
Figure 65. Observed bias (validation-based) vs. the RF model predicted bias (ML-based) for the Clab benchmarks. The left plot is based on integral parameters of the benchmarks, using the spectral index (SI), and the right plot is based on the correlation between the benchmarks.	132
Figure 66. Same as Figure 65 for the Pu-239 concentration bias. The left plot is based on the hydrogen-to-fissile atom ratio (H/X), and the right plot is based on the correlation between the benchmarks.	132
Figure 67. Decay heat biases, both validation-based and ML-based. The ML model is the RF model, and the data are the validation-based bias and the calculated correlations between the benchmarks.	134
Figure 68. Same as Figure 67 for the Pu-239 concentration.	135
Figure 69: Polaris south-east (S-E) models of the Calvert Cliffs-1 assemblies: D101, D047, and BT03 (left to right). Rods having different enrichments are shown in different colors. The analyzed rods are shown in black color.	158
Figure 70: Polaris model of the Genkai-1 assembly JPNNG1SFA1 showing the location of the rods containing the analyzed PIE samples: rod JPNNG1PWR-1 and JPNNG1PWR-2 (in black color). The rods contain samples H01 and H05, respectively.	160
Figure 71: Polaris S-E models of the Mihama-3 assemblies SFA1, SFA2 and SFA3. The assemblies are similar to each other in their pin-layout and slightly differ in their enrichments. The S-E map show the actual position of the analyzed rods or their reflection in the S-E quarter. The analyzed rods are shown in black color.	162
Figure 72: Polaris model of the Neckarwestheim-2 assembly 419. The analyzed rods are shown in purple color.	164
Figure 73: Polaris S-E models of the Obrigheim-1 assemblies: BE210 (left), BE124 (middle), and BE168, BE170, BE171, BE 172, and BE176 (right). The latter assemblies had all of their rods dissolved and analyzed. The analyzed rods in BE210 and BE124 are shown in black color.	167
Figure 74: Polaris S-E models of the Ohi-1 and Ohi-2 assemblies (left to right). The Ohi-2 assembly shows the actual position of the analyzed rods or their reflection into the S-E quarter. The analyzed rods are shown in black color, and the gadolinia-bearing rods are shown in purple color.	169
Figure 75: Axial locations of the analyzed PIE samples of T3 reactor.	171
Figure 76: Polaris S-E model of the Takahama-3 assemblies G23 and G24. The S-E map shows the actual positions of the analyzed rods (or their reflection in the S-E quarter). The analyzed rods are shown in black color, and the gadolinia-bearing rods are shown in purple color.	171
Figure 77: Polaris S-E models of the Three Mile Island-1 assemblies: NJ05YU and NJ070G (left to right). Rods having different enrichments are shown in different colors. Four discrete absorber rods are shown	

inserted in their guide tubes. The analyzed rods are shown in black color (2 in NJ05YU and 3 in NJ070G).	173
Figure 78: Polaris models of the Trino Vercellese-1 assemblies: A32 and A49 (top row, left to right), and A69 and A104 (bottom row, left to right). The analyzed rods are shown in black color. The peripheral rods (in red color) are rods that belong to the control rod follower part, which are fuel rods of 2.72 wt% U-235 enrichment.	176
Figure 79: Polaris S-E models of the Turkey Point-3 assemblies: D01 and D04 and B17 SFA (left to right). The shown rods (in black color) reflect the symmetric reflection of the rods' actual positions into the S-E quarter.	179
Figure 80: Layouts of the analyzed assemblies of Yankee-1 reactor: E5, E6, F4 and F5 with respect to each other and the control rods, based on SFCOMPO [11]. The implemented dimensions and span of the control rod wings are based on the original reference [121].	182
Figure 81: Polaris models of the Yankee-1 assemblies: E5 and F4 (top row) and E6 and F5 (bottom row). The rods in black color are the rods from which RCA samples are analyzed in this study. The peripheral location of the CR follower is shown in different color.	183
Figure 82: Polaris model of the Cooper-1 assembly CZ346. The rods containing the analyzed samples are shown in black color (rod B3 and C3).	187
Figure 83: Polaris models of the Dodewaard-1 assemblies: Y014, Y012 and Y013 (left to right). The Y014 and Y012 SFAs have MOX-based fuel, and the Y013 has UO ₂ fuel. Two PIE samples are analyzed from each rod of the MOX based SFAs (4 MOX PIE samples) and only one samples is analyzed from the rod of the UO ₂ based SFA.	188
Figure 84: Polaris model of the Fukushima Daini-1 9x9-9 assembly design (ZN2 and ZN3 assemblies). The rods positions A9, C2 and C3 are shown in black color.	191
Figure 85: Axial locations of the PIE samples of the SFAs: ZN2 (top row) and ZN3 (bottom row).	192
Figure 86: Polaris models of the Fukushima Daini-2 assemblies. The top row contains the D1 and D2 assemblies. The middle row contains the D3 and D8 assemblies (left to right). The bottom row contains fuel designs of the DN23 assembly. Assembly DN23 had most of its samples based on the middle design (left), and samples 89-1, 99-1 and 99-10 are based on the top and bottom designs (right). The rods hosting the analyzed samples are shown in black color.	195
Figure 87: Axial positions of the PIE samples of the rods 98 and 99 of the DN23 assembly. Different colors indicate differences in enrichment or gadolinia content in the rods.	196
Figure 88: Axial positions of the PIE samples from the D1, D2, D3, and D8 assemblies. The third letter in the sample ID is a number indicating the assembly of origin; 1, 2, 3, and 5 for D1, D2, D3 and D8, respectively. Different colors indicate differences in enrichment or gadolinia content in the rods.	196
Figure 89: Polaris models of the Garigliano-1 assemblies: A-106 (left) and SA-13 (middle). The rods hosting the analyzed samples are shown in black color. The elevation of the samples from the SA-13 assembly are shown in the right plot.	200
Figure 90: Polaris models of the Gundremmingen-1 assemblies B23 and C16 (left to right). The rods containing the analyzed samples are shown in black color.	203
Figure 91: Layout of the Japan Power Demonstration Reactor-1 core showing the three analyzed assemblies based on [133].	205

Figure 92: Polaris models of the Japan Power Demonstrations Reactor-1 assemblies: A20 (left) and both A14 and A18 (right). The rods hosting the analyzed samples are shown in black color. The water gaps are either non-boiling moderator (heavy blue) or a mixture of the moderator and the poison curtain (light blue).....	206
Figure 93. Polaris models of two SFAs: a BWR (left) and a PWR (right). Within each model, the fuel rods are shown in different colors to reflect differences in their densities, enrichments, and gadolinium percentage. The rod containing the analyzed sample is colored in black.	210
Figure 94. Permutation distributions of the average biases (the red lines are the observed values).	221

List of Tables

Table 1: Radioactive waste in Switzerland in m3 (top) and Bq (bottom) for the year 2075 [3,8].	3
Table 2. Summary of the decay heat experimental benchmarks considered in this study, based on [12,13,27,54]. Range of properties, e.g., burnup range, are listed for all benchmarks belonging to particular reactors.	15
Table 3. Uncertainties (2σ) in decay heat measurements at the Clab facility based on Reference [12].	17
Table 4. Uncertainties (2σ) in decay heat measurements at the GE-Morris facility based on Reference [27]. The values correspond to both PWRs and BWRs.	17
Table 5. Summary of the analyzed PIE samples from the SFCOMPO database.	19
Table 6. Specifications of the hardware used to perform the depletion and decay, uncertainty propagation, and the machine learning calculations.	27
Table 7. Uncertainties in design and operational parameters of the analyzed benchmarks, based on [56]. The reference values in [56] are uncertainties and tolerances, whereas the applied uncertainties in this study are standard deviations (1σ).	34
Table 8. Average C/E and B for the decay heat benchmarks, along with two standard deviations (2σ). The parentheses indicate the number of benchmarks in each category.	69
Table 9. Average C/E and B for U-235 concentrations, along with two standard deviations (2σ). The parentheses indicate the number of benchmarks in each category.	73
Table 10. Average C/E and B for Pu-239 concentrations, along with two standard deviations (2σ). The parentheses indicate the number of benchmarks in each category.	74
Table 11. Average C/E and B for Cs-137 concentrations, along with two standard deviations (2σ). The parentheses indicate the number of benchmarks in each category.	75
Table 12. Average along with one standard deviation of the calculated uncertainties (%).	83
Table 13. Average along with one standard deviation of the FVs of the uncertainties of DO origins.	84
Table 14. SFAs considered for the analyses of the uncertainty contributions of XS, FY, and DD.	87
Table 15. p-values of the Shapiro-Wilk normality test conducted on the BWR and PWR bias data.	99
Table 16. C/E and B for the decay heat calculations using Polaris and ORIGEN, along with 1σ .	102
Table 17. p-values of the Shapiro-Wilk normality test conducted on the Polaris and ORIGEN decay heat bias data.	104
Table 18. Simultaneous testing p-values of the permutation tests.	104
Table 19. Simultaneous testing p-values of the bootstrap tests.	105

Table 20. Aggregate z-scores and results of the hypothesis testing conducted on the validation and uncertainty analyses data. A rejection of H_0 implies that the observed bias is significant, given the calculated uncertainties, at an 0.05 significance level.	108
Table 21. Decay heat measurements on the same SFA, along with assumed weights (w).	112
Table 22. Properties of PIE benchmarks at Q1, Q3, and median of the BWR and PWR data.	114
Table 23. Variables included in design matrices (identified with “✓”), implementing an 0.1 cut-off on calculated sensitivity coefficients.	115
Table 24. Aggregate results of the outliers detection and removal procedure, applied on the decay heat benchmarks (left table) and the Pu-239 concentration benchmarks (right table). Both characteristics are analyzed using the RF models, applied on both design matrices: <i>SI</i> for the decay heat, <i>H/X</i> for Pu-239 concentration, and the correlation matrices for both. The decay heat data belong to the Clab benchmarks solely.	131
Table 25. Specifications of rebuild SFAs from the benchmarks of Clab, based on [12].	154
Table 26. Characteristics of the PIE samples of the Calvert Cliffs-1 reactor.	159
Table 27. Characteristics of the PIE samples of the Genkai-1 reactor.	160
Table 28. Characteristics of the PIE samples of the Mihama-3 reactor.	163
Table 29. Characteristics of the PIE sample of the Neckarwestheim-2 reactor.	164
Table 30. Characteristics of the PIE samples of the Obrigheim-1 reactor.	167
Table 31. Characteristics of the PIE samples of the Ohi-1 and Ohi-2 reactors.	170
Table 32. Characteristics of the PIE samples of the Takahama-3 reactor.	172
Table 33. Characteristics of the PIE samples of the Three Mile Island-1 reactor.	174
Table 34. Characteristics of the PIE samples of the Trino Vercellese-1 reactor.	178
Table 35. Characteristics of the PIE samples of the Turkey Point-3 reactor.	180
Table 36. Characteristics of the PIE samples of the Yankee-1 reactor.	184
Table 37. Characteristics of the PIE samples of the Cooper-1 reactor.	187
Table 38. Characteristics of the PIE samples of the Dodewaard-1 reactor.	189
Table 39. Characteristics of the PIE samples of the Fukushima Daini-1 reactor.	192
Table 40. Characteristics of the PIE samples of the Fukushima Daini-2 reactor.	197
Table 41. Characteristics of the PIE samples of the Garigliano-1 reactor.	201
Table 42. Characteristics of the PIE samples of the Gundremmingen-1 reactor.	203
Table 43. Characteristics of the PIE samples of the Japan Power Demonstrations Reactor-1.	207

List of Abbreviations

AC	Actinides
ANL	Argonne National Laboratory
ANSI/ANS	American National Standards Institute/American Nuclear Society
AOA	Area of Applicability
ARIANE	Actinides Research in a Nuclear Element
ATM	Approved Testing Material
ATW	Alpha Toxic Waste
BA	Operational Waste (Betriebsabfälle)
BEPU	Best Estimate Plus Uncertainties
BOL	Beginning of Life
BWR	Boiling Water Reactor
BU	Burnup
B&W	Babcock & Wilcox Company
CI	Confidence Intervals
CO	Cutoff
CR	Control Rod
CRP	Coordinated Research Project
CSA	Criticality Safety Analysis
CV	Cross-Validation
DD	Decay Data
DGR	Deep Geological Repositories
DH	Decay Heat
DO	Design and Operational
DRN	Dose Rate Relevant Nuclides
ECDF	Empirical Cumulative Distribution Function
EDEY	Doctoral Program in Energy
EGADSNF	Expert Group on Assay Data for Spent Nuclear Fuel
ENDF/B-VII.1	Evaluated Nuclear Data File (version B-VII.1)
ENSI	Swiss Federal Nuclear Safety Inspectorate (Eidgenössisches Nuklearsicherheitsinspektorat)
EOL	End of Life
EPFL	Swiss Federal Institute of Technology Lausanne (École polytechnique fédérale de Lausanne)

F/DP	Fission and Decay Product
FV	Fractional Variance
FY	Fission yield
GE	General Electric
GE-Morris	General Electric Morris facilities
GE7	General Electric 7x7 (fuel design)
GE8	General Electric 8x8 (fuel design)
GE9	General Electric 9x9 (fuel design)
GEVNC	General Electric Vallecitos Nuclear Center
GNU	GNU General Public License
H/X	Hydrogen-to-Fissile Atom Ratio
HEDL	Hanford Engineering Development Laboratory
HLW	High Level Waste
HM	Heavy Metal (the mass of metals having atomic number greater than 89)
HPLC-ICPMS	High-Performance Liquid Chromatography coupled to Inductively Coupled Plasma/Mass Spectrometry
IAEA	International Atomic Energy Agency
ID	Identification (<i>e.g.</i> , in SFA ID and Sample ID)
ID-ICPMS	Isotope Dilution Inductively Coupled Plasma/Mass Spectrometry
IDMS	Isotope Dilution Mass Spectrometry
IHM (HMi)	Initial Heavy Metal (at BOL)
IQR	Interquartile Range
IRCh	Institute for Radiochemistry at Karlsruhe
ISF	Interim Storage Facility
ISRAM	Information System for Radioactive Materials
ITU	Institute of Transuranium Elements
JAEA	Japan Atomic Energy Agency
JAERI	Japan Atomic Energy Research Institute
JEFF-3.1	Joint Evaluated Fission and Fusion Nuclear Data Library (version 3.1)
JENDL-3.3	Japanese Evaluated Nuclear Data Library (version 3.3)
JPDR-1	Japan Power Demonstration Reactor-1
KEG	Nuclear Energy Act (Kernenergiegesetz)
KKB	<i>Kernkraftwerk Beznau</i>
KKG	<i>Kernkraftwerk Gösgen-Däniken</i>
KKL	<i>Kernkraftwerk Leibstadt</i>

KKM	<i>Kernkraftwerk Mühleberg</i>
KKNN	Weighted K-Nearest Neighbors
KNN	K-Nearest Neighbors
KS	Kolmogorov-Smirnov
L/ILW	Low- and Intermediate-Level Waste
LM	Linear Models
LOOCV	Leave-One-Out-Cross-Validation
LRS	Laboratory for Reactor Physics and Systems Behaviour
LWR	Light Water Reactor
M&S	Modeling and Simulation
MAE	Mean Average Error
MCC	Material Characterization Center
MG	Multi-Group
MIR	Medicine, Industry, and Research
MIRAM	Model Inventory for Radioactive Materials
ML	Machine Learning
MOX	Mixed Oxides
MS	Mass-Spectrometry
MSE	Mean Square Error
Nagra	National Cooperative for the Disposal of Radioactive Waste (Nationale Genossenschaft für die Lagerung radioaktiver Abfälle)
NBL	New Brunswick Laboratory
ND	Nuclear Data
NEA	Nuclear Energy Agency
NPP	Nuclear Power Plants
NRC	Nuclear Regulatory Commission
O	ORIGEN (code)
OECD	Organization for Economic Co-Operation and Development
OOB	Out of Bag
ORNL	Oak Ridge National Laboratory
OSE	One Standard Error
P	Polaris (code)
PIE	Post Irradiation Examination
PNL	Pacific Northwest Laboratory
PSI	Paul Scherrer Institute

PWR	Pressurized Water Reactor
Q1 and Q3	First and Third Quartiles
RA	Reactor Waste (Reaktoren Abfälle)
RCA	Radiochemical Analysis
REBUS	Reactivity Tests for a Direct Evaluation of the Burnup Credit on Selected Irradiated LWR Fuel Bundles
RF	Random Forest
RFE	Recursive Feature Elimination
RMSE	Root Mean Square Error
RSS	Residual Sum of Squares
S100	SVEA-100 (fuel design)
S64	SVEA-64 (fuel design)
SA	Decommissioning waste
SE	Standard Error
S-E	South-East (a quarter of the SFA)
SFA	Spent Fuel Assembly
SFCOMPO	Spent Fuel Isotopic Composition
SFCOMPO TRG	SFCOMPO Technical Review Group
SI	Spectral Index
SKB	Svensk Kärnbränslehantering AB
SNF	Spent Nuclear Fuel
TIMS	Thermal Ionization Mass Spectrometry
TSS	Total Sum of Squares
W14	Westinghouse 14x14 (fuel design)
W15	Westinghouse 15x15 (fuel design)
W17	Westinghouse 17x17 (fuel design)
WA	Reprocessing waste
WAK	Karlsruhe Reprocessing Plant
WPNCs	Working Party on Nuclear Criticality Safety
XS	Cross-Section
Zr	Zircaloy
Zwilag	Interim Storage Facility (Zwischenlager)
σ	Standard Deviation

List of Vocabulary

The vocabulary used in the current work are based on the guide: “Evaluation of measurement data — Guide to the expression of uncertainty in measurement” [1]. Definitions in the guide refer mostly to measurements, adapted in this work to refer to calculations, explained as following:

1. **Benchmark (or experimental benchmark)**

The word “benchmark” or “experimental benchmark” is used in this work to refer to a measurement conducted on spent nuclear fuel for evaluating one or more of its characteristics. In addition to the measured values, their uncertainties, benchmarks include information necessary for modeling and simulation. The necessary information includes the design of the spent nuclear fuel assembly and irradiation and decay history.

2. **Measurand**

The quantity to be measured. The measurand cannot be specified by a value but only by a description of a quantity – *e.g.*, U-235 concentration.

3. **Characteristic**

The quantity to be calculated. The characteristic cannot be specified by a value but only by a description of a quantity – *e.g.*, U-235 concentration.

4. **Accuracy**

Closeness of the agreement between the result of a measurement or a calculation and a target value. Accuracy is a qualitative concept.

5. **Standard uncertainty (of measurement or calculation) – referred to as "uncertainty" in this work**

Parameter, associated with the result of a measurement or a calculation, characterizing the dispersion of the measurand or characteristic. The parameter may be, for example, a standard deviation (or a given multiple of it), or the half-width of an interval having a stated level of confidence. Uncertainties are evaluated by the statistical analysis of series of observations (type A evaluation), or by other means (type B evaluation).

6. **Correction factor (*e.g.*, isotopic correction factor)**

Numerical factor by which the uncorrected result of a measurement or calculation is multiplied to compensate for a systematic error. Since the systematic error cannot be known perfectly, the compensation cannot be complete.

7. **Variance**

A measure of dispersion, which is the sum of the squared deviations of observations from their average, divided by one less than the number of observations. The variance defined here is more

appropriately designated by the “sample estimate of the population variance”. For n observations x_1, x_2, \dots, x_n with average

$$\bar{x} = \frac{1}{n} \sum_{i=1}^n x_i$$

The variance is

$$\sigma^2 = \frac{1}{n-1} \sum_{i=1}^n (x_i - \bar{x})^2$$

8. Standard deviation

The positive square root of the variance.

9. Statistic

A function of the sample random variables. A statistic, as a function of random variables, is also a random variable and as such it assumes different values from sample to sample. The value of the statistic obtained by using the observed values in this function may be used in a statistical test or as an estimate of a population parameter, such as a mean or a standard deviation.

10. Estimation

The operation of assigning, from the observations in a sample, numerical values to the parameters of a distribution chosen as the statistical model of the population from which this sample is taken.

11. Estimate

The value of an estimator obtained as a result of an estimation.

12. Confidence level

The value $(1 - \alpha)$ of the probability associated with a confidence interval or a statistical coverage interval, whereas α is a significance level. $(1 - \alpha)$ is often expressed as a percentage.

13. Error (of calculation) – referred to as "bias" in this work

A measurement or a calculation has imperfections that give rise to an error in the measured or calculated values. Traditionally, an error is viewed as having two components, namely, a random component and a systematic component. It can be represented as the calculation minus a true value of the measurand (measurement in this work). The error of the result of a calculation may often be considered as arising from a number of random and systematic effects, contributing to individual components of the error of the result.

14. Relative error (of calculation) – referred to as "C/E" in this work

The relative error can be expressed as the value of a calculation divided by a true value of the measurand (measurement in this work).

15. Systematic error – referred to as "systematic component" and "systematic component of the bias" in this work

The systematic error is defined in the present study as the mean that would result from an infinite number of calculations of the same characteristic carried out under repeatability conditions

minus a true value of the characteristic. The systematic error is equal to error minus random error.

Like true value, systematic error and its causes cannot be completely known. Also, the systematic error, like random error, cannot be eliminated but it too can often be reduced. If a systematic error arises from a recognized effect of an influence quantity on a measured or calculated value, hereafter termed a systematic effect, the effect can be quantified. If the systematic error is significant in size relative to the required accuracy of the measurement or calculation, a correction or correction factor can be applied to compensate for the effect. It is assumed that, after correction, the expectation or expected value of the error arising from a systematic effect is zero.

16. Random error – referred to as "random component" and "random component of the bias" in this work

Random error is assumed to arise from unpredictable or stochastic variations of the quantity being measured or calculated, *i.e.*, it results from random effects. Also, it can be expressed as the error minus the systematic error. Because only a finite number of calculations can be made, it is only possible to determine an estimate of the random error.

17. Repeatability and reproducibility (for results of measurements or calculations) – referred to as "precision" in this work

Closeness of the agreement between the results of successive measurements or calculations of the same measurand or characteristic carried out under the same conditions (repeatability), or under changed conditions (reproducibility). The precision may be expressed quantitatively in terms of the dispersion characteristics of the results.

Chapter 1 Introduction

The irradiation of nuclear fuel throughout its operational life results in the accumulation of short and long-lived radionuclides, in majority contained within fuel rods of the spent nuclear fuel (SNF). Besides the radiotoxicity of these radionuclides, they release a substantial amount of heat during their radioactive decay. Such radiotoxicity and heat generation impact activities such as handling, transporting, packing into specific containers, and ultimately the SNF long-term or final disposal. The design, operation, and safety of facilities conducting these activities are ultimately affected, *e.g.*, nuclear waste management and disposal solutions such as interim storage facilities (ISF) and deep geological repositories (DGRs) [2,3]. As required by regulations, safety analyses are intended to demonstrate that the nuclear waste handling and disposal facilities comply with requirements aiming at ensuring the safety of humans and the environment.

For the purpose of safety analyses, upstream inputs such as the radionuclide inventory and decay heat are typically obtained through calculations based on available data (fuel design, irradiation information, and nuclear data). In parallel, the heavy reliance on calculations for characterization of SNF is motivated by the impracticality of their measurements, as well as the difficulty and cost of characterizing SNF in such a way. As a consequence, and prior of using calculated SNF characteristics in subsequent downstream analyses, it is required to establish confidence on such calculations and assess how far these characteristics are from true values or potential measurements. The latter requirement motivated the presented herein research and thesis.

1.1 Worldwide status of spent nuclear fuel

As of 2017, the amount of SNF generated from the operation of nuclear power plants (NPPs) accumulates to approximately 400 kilotons of heavy metals (HM) [4]. It increases on yearly basis by approximately 11 kilotons of HM generated from the operational fleet of the NPPs, being 442 reactors in 30 countries, as of today. Such SNF is one of the most hazardous radioactive wastes being generated from the nuclear power industry, containing most of the radiotoxicity and long-lived radioactive isotopes. Typically, they are radioactive, and the generated heat requires both shielding and cooling. The radioactivity is concentrated such that, the SNF accounts for approximately 3% of the volume of the generated nuclear waste, while it contains approximately 95% of the total radioactivity [5] (depending on the time after discharge). After its end of life (EOL), the SNF is categorized as high-level waste (HLW), and it may be reprocessed to recover fissile and

fertile materials. As such, radionuclides of the dissolved fuel matrix are separated, and the process results in separation of uranium and plutonium, and other higher actinides, used for the fabrication of new nuclear fuel elements. The remaining materials are termed “reprocessed waste”, also containing both long- and short-lived radionuclides.

The SNF is stored in central interim storage, or on-site storage at NPP (both wet and dry). Figure 1 shows recent stored amounts of SNF by country (in metric tons of HM) and future prognostics in year 2050. Both storage options have limited capacities, and efforts are currently made to obtain a long-term solution, such as disposing the SNF in deep geological repositories – sub-surface storage sites with stable geological characteristics. Also, the DGR solution is considered by many countries as one of the safest options for long-term or final disposal. Several countries have already moved forward in this direction, analyzing and planning for a long-term disposal in DGRs, including Finland, France, Sweden, and Switzerland.

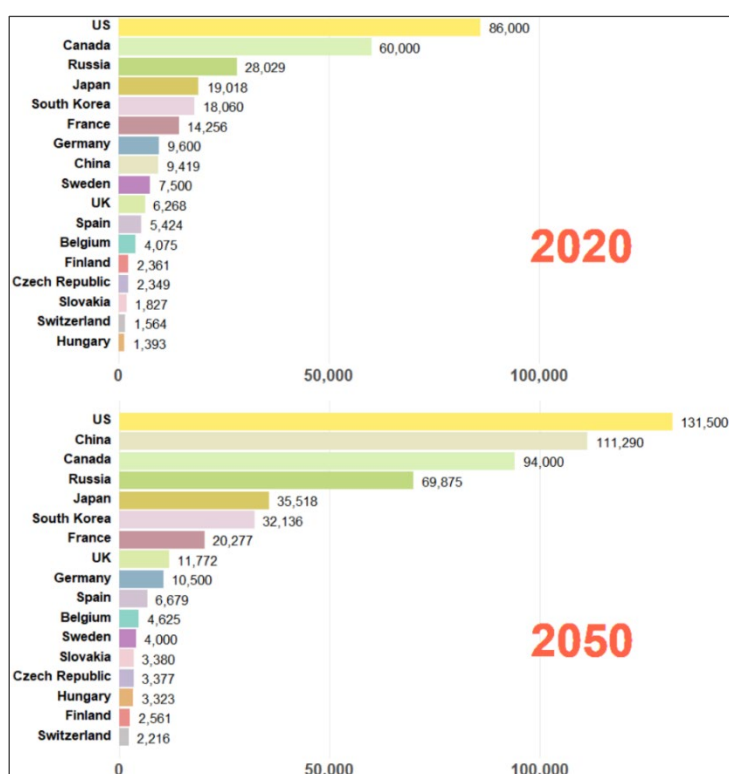


Figure 1. Tons of HM contained in SNF in year 2020 (top), and the prospected amount in year 2050 (bottom) (figure from Reference [4]).

1.2 Status of radioactive waste in Switzerland

The present research is funded by the National Cooperative for the Disposal of Radioactive Waste (Nationale Genossenschaft für die Lagerung radioaktiver Abfälle) (Nagra). Nagra has the mandate on behalf of the Swiss NPPs, research facilities, hospitals and other sources of radioactive waste to prepare and implement solutions for waste management and disposal, ensuring the long-term safety of the population and the environment [3]. According to the Swiss law, the radioactive waste will be deposited in a DGR [6]. Therefore, Nagra will be conducting activities such as planning, designing, construction, and operations of a prospected DGR.

The radioactive wastes in Switzerland arise from the operation of four NPPs (Kernkraftwerk Beznau (KKB), Kernkraftwerk Gösgen-Däniken (KKG), Kernkraftwerk Leibstadt (KKL), and Kernkraftwerk Mühleberg (KKM)), the interim storage facility (Zwischenlager, or Zwiilag), and from medicine, industry, and research (MIR). Most radioactive waste in Switzerland is handled by Zwiilag, an interim storage facility containing both SNF (in dry storage) and reprocessed waste canisters (reprocessed in La Hague and Sellafield plants). Also, it includes facilities for incineration, conditioning, and storage of the low- and intermediate-level waste. The overall nuclear waste in Switzerland can be categorized based on its source as [7]:

1. Operational waste (Betriebsabfälle) (BA) (*e.g.*, ion-exchange resins)
2. Reactor waste (Reaktoren Abfälle) (RA) (*e.g.*, reactor movable pieces such as control rods)
3. Spent nuclear fuel (SNF)
4. Reprocessing waste (WA)
5. Decommissioning waste (SA) (*e.g.*, activated structural components).

Another classification, based on volume and radioactivity, is shown in Table 1 [3,8].

Table 1: Radioactive waste in Switzerland in m³ (top) and Bq (bottom) for the year 2075 [3,8].

Category	SNF	WA	BA	RA	SA	MIR	Total
HLW*	1363	112				1	1476
ATW**		102			24	211	337
L/ILW***			8465	473	23024	21005	52967
Total	1363	214	8465	473	23048	21217	54780
Category	SNF	WA	BA	RA	SA	MIR	Total
HLW*	1.70E+19	1.90E+18				2.10E+10	1.89E+19
ATW**		1.90E+16			3.60E+12	3.40E+15	2.24E+16
L/ILW***			4.30E+14	5.50E+15	6.30E+16	1.00E+16	7.89E+16
Total	1.70E+19	1.92E+18	4.30E+14	5.50E+15	6.30E+16	1.34E+16	1.90E+19

* HLW: high-level waste

** ATW: alpha-toxic waste (conditioned waste containing large amounts of alpha-emitters)

*** L/ILW: low- and intermediate-level waste

In Nagra, the radioactive waste data, such as those listed in Table 1, are managed by the ISRAM database (Information System for Radioactive Materials) [9]. Another database, the MIRAM database (Model Inventory for Radioactive Materials), is also available to manage the total inventory of radioactive waste (including waste predictions according to prognoses or scenarios). Predicting the potential waste in the DGR is necessary since the NPPs are still in operation and the MIR waste is still being produced. The applications of these databases are mainly in safety analyses, repository design and cost studies for the DGR [10].

1.3 International projects addressing SNF characterization

As mentioned, the SNF is a significant component of the nuclear waste, and several international projects were conducted (and are being initiated) to address related-research questions. As early as the nuclear power industry itself, post-irradiation-examinations (PIEs) were performed on irradiated fuel samples. Recent needs to aggregate these information from publicly

available PIE data resulted in the creation of the Spent Fuel Isotopic Composition (SFCOMPO) database under the Nuclear Energy Agency (NEA) of the Organization for Economic Co-operation and Development (OCED/NEA) [11]. The database serves the purpose of providing, in a consistent manner, necessary modelling information and measured characteristics of PIE samples, allowing validation of calculational sequences. Besides the radionuclides, the decay heat generation from the SNF is also gaining major attention. As the phase of packing the SNF into disposal canisters is approaching, it is currently understood that the heat generation is a potential limiting factor and can place constraints on the disposal of such SNF. Projects were initiated earlier in the history of the nuclear power industry to measure the decay heat generated from SNF; in open-source data, two large measurements campaigns were conducted by the General Electric (GE) and Svensk Kärnbränslehantering AB (SKB) [12,13].

Recently, the topic has gained more attention with increasing number of spent fuel assemblies (SFAs) and decommissioned NPPs, and also as the DGR is foreseen in the near future. The EURAD project is an active European research project, including members such as waste management and technical support organizations, as well as research units across Europe. The project aims at addressing the research and development related to the radioactive waste management, and answering common research questions related to the planning, implementation, and safety analysis of DGRs [14]. Parts of the present study were conducted under the EURAD work package 8, related to the SNF characterization. Recently, the work package 8 is extended to include the SNF decay heat analyses. This extension is motivated by the increased interest in the SNF decay heat generation under long-term storage and disposal. Design and irradiation data of about 50 new assemblies measured at Clab have been requested from the SKB [15], covering an extended burnup range compared to the 2006 measurements campaign [12].

Additionally, under the International Atomic Energy Agency (IAEA), a Coordinated Research Project (CRP) is initiated [16]. The CRP, entitled “Spent Fuel Research and Assessment” (SFERA) [17], focuses on questions related to fuel, fuel cladding, and fuel assembly structures, and understanding their behavior and performance under long-term storage. Also, the NEA Working Party on Nuclear Criticality Safety (WPNCS) has coordinated several research programs addressing topics related to SNF, such as criticality safety and burnup credits [18]. A number of WPNCS subgroups are addressing questions and research points similar to parts of the present study, such as the SG7 (focusing on validation of burnup calculations), the SFCOMPO Technical Review Group [19] (focusing on reviews and updates of the SFCOMPO database), and a new subgroup dedicated to the addition of the decay heat benchmarks in SFCOMPO. Finally, a blind test benchmark was organized by SKB for the validation, and comparison between participants, of the decay heat calculations of 5 new assemblies measured at the Clab facility [20].

1.4 Motivation of the current research project

As mentioned, the characteristics of the SNF (radionuclide inventory and decay heat) are typically obtained through modeling and simulation (M&S) of their in-reactor irradiation and the

subsequent cooling, resulting in values such as those listed in Table 1. These characteristics are eventually being used in downstream analyses and for the assessment of a broad range of topics, such as criticality, thermal optimization, SNF integrity, *etc.* Given their reliance on calculations, primary concerns are to improve the accuracy and to establish confidence on these calculated characteristics.

Additionally, from the aspect of regulations, the Swiss Federal Nuclear Safety Inspectorate (Eidgenössisches Nuklearsicherheitsinspektorat) (ENSI) [21] is the supervisory and regulatory authority with respect to the safety and security of the nuclear installations as per the Nuclear Energy Act (Kernenergiegesetz) (KEG – SR 732.1) [22], and the Act on the Federal Nuclear Safety Inspectorate (ENSI-Gesetz) (ENSIG – SR 732.2) [23]. ENSI issues guidelines to regulate the activities in these installations. Regarding the principles and the safety requirements for the DGR, the guideline ENSI-G03 [6] requires quantification of the uncertainties that impact the safety of the DGR, and according to Section 7:

- *“The safety case must be documented in a safety report. This report also has to present and quantify uncertainties and their relevance for safety. This includes uncertainties relating to parameters, scenarios and conceptual models.”*
- *“Analysis of existing uncertainties in data, processes and models and calculation of the resulting range of radionuclide release and doses.”*

Certain uncertainties are inevitable, due to unknowns about processes (*e.g.*, chemical reactions), and uncertainties in physical quantities (*e.g.*, diffusivities). However, it is beneficial to reduce them as far as possible and necessary, and also to estimate (based on conservative assumptions) their radiological consequences, as well as to evaluate their influence on the long-term safety of the DGR. Such relevant regulations necessitated the initiation of several projects, including the present one, to quantify uncertainties associated with the characteristics of the nuclear waste, and to reduce such uncertainties as far as feasible.

1.5 Relevant SNF characteristics

Preliminary safety assessment of the post-closure phase of the DGR showed that a limited number of radionuclides (52 radionuclides) are the main contributors to the surface dose rates [24,25], named dose-rate-relevant-nuclides (DRN). Uncertainty analyses have shown that the dose rate uncertainties from certain radionuclides (*e.g.*, Cl-36 and I-129) are mainly due to uncertainties in their inventory. Accurate evaluation of their inventory and associated uncertainties will directly impact the analyzed long-term surface dose rates. Therefore, selected DRN are the primary focus of the current research.

As mentioned, the heat generation from SNF is also relevant. Based on the DGR host rock properties, an upper limit of decay heat from the SNF canisters is derived. In Switzerland, the current maximum limit is 1500 W per canister at emplacement. Such constraint, combined with large uncertainties in calculated SNF characteristics, can lead to longer storage times in ISFs prior to encapsulation or to partial filling of disposal canisters, options being economically

disadvantageous. Therefore, accurate estimation of the SNF decay heat along with quantification of uncertainties are necessary, whereas these inevitable uncertainties will lead to an additional margin on the maximum heat load constraint.

1.6 Needs of validation

The previous safety and design considerations make it necessary to accurately estimate the SNF characteristics, and also to comply with relevant regulations [6,26]. A growing trend in the nuclear engineering community is called BEPU, or “best estimate plus uncertainties”, which encourages using *best estimate*, or high fidelity, numerical solvers along with quantification of uncertainties associated with the calculational sequence (the method and the data). The former approach can potentially reduce systematic differences between calculations and measurements. The latter approach allows quantification of the remaining systematic part of these differences, along with the inevitable random components. Eventually, the calculated values better resemble the true ones and conservatism (including safety margins) can be potentially reduced.

In the nuclear engineering community, confidence in the calculations is examined through acceptable and routine practice, consisting in comparing the results of calculations with experimental measurements [26,27]. Such practice is referred to as validation of the M&S (see for example Gauld et al. [27], Ilas et al. [28], and others [29–31]). The validation results can be presented as computational biases (B) – differences between calculations (C) and measurements (E):

$$B = C - E. \quad (1.1)$$

Alternative metrics are bias per ton of initial heavy metal, *e.g.*, W/tHMi, and the ratio between calculations and measurements (C/E). The bias B is a useful measure, as it indicates how far a calculation of a particular SNF characteristic is from its measurement. It is a widely used validation metric (see for instance the standard of the American National Standards Institute/American Nuclear Society ANSI/ANS-8.24 [32]).

The bias is not an exact value due to uncertainties in both calculations and measurements, estimated as

$$\sigma_B \cong \sqrt{\sigma_C^2 + \sigma_E^2}, \quad (1.2)$$

assuming that there is no correlation between calculated and experimental uncertainties. Uncertainties of random nature are assumed to exist in both calculations and measurements, resulting in bias uncertainties of random nature, *i.e.*, the observed value of the bias contains a random component. Random uncertainties in calculations can originate from random uncertainties in the data, such as random uncertainties in nuclear cross-sections and fission yields. These uncertainties propagate into calculations, leading to a random component of the calculated values. Random uncertainties in the measurements can be observed in fluctuations of

the measured values, being not attributed to different experimental configurations (*i.e.*, the measured value contains an unexplained component).

However, the bias can also include a systematic difference between calculations and measurements. Differences between calculations and measurements having random origin can be compared to those having a systematic one, using methods such as statistical analyses. Such statistical analyses provide a probabilistic answer to whether the observed difference (the bias) includes a random or systematic nature. The discussed differences between both types of uncertainties are important, since the bias can be represented as two components: a systematic component, and a random component.

Understanding the origins of differences between calculations and measurements of SNF characteristics finally helps to predict the bias in a more reliable way. However, these biases are thought to be intrinsically complex such that it is challenging to derive functions mapping variables in the calculations and the measurements into their differences. The approximate functional form mapping these features into biases is unknown, and the model features that are bias-informative are also unknown. In such cases, data-driven methods can be employed in the attempt to simplify the problem by approximating the target function f , and to select the informative model features X , such that the bias can be expressed as

$$B = f(X) + \epsilon, \quad (1.3)$$

whereas $f(X)$ is the systematic part of the bias and ϵ is the random part of the bias.

Measurements can be systematically different from the true value of the parameter, due to inherent defects or limitations of the methods employed during the measurements. For instance, inefficient dissolution of metallic elements in a PIE sample can result in measured concentrations underestimating the actual values; and un-accounting for escaping gaseous fission products can result in the opposite effect. Also, calculations can be systematically biased as they are an imperfect representation of nature; only a few physical phenomena are being included in the models such as neutron-induced reactions, and other phenomena are potentially excluded from the model (such as material diffusion) to ease the calculational requirements. In performing calculations, relevant physical phenomena are modelled in a reduced volume of space, and regions beyond this volume are assumed to induce negligible effect on the target solution. Alternatively, when the physics beyond the interesting model space are important but not modelled, boundary conditions are often used to approximate them. Calculations also use data, such as fuel design and irradiation information and nuclear data, containing inaccuracies and imprecisions to some degree, which eventually propagate through the calculations.

Large biases mean that more conservative assumptions or safety margins are needed to penalize the calculated SNF characteristics. Knowledge of the origin and possible improvement of these discrepancies, captured by B , can help reducing over-conservatism. Such improvements potentially result from using high-quality measurements, high-fidelity calculational sequences, detailed modelling, and using accurate and precise data (*e.g.*, improved nuclear data, precise and

detailed operational data, *etc.*). However, the bias is expected to persist to some degree, optimistically in a possible representation of two components being a systematic and a random one, as presented earlier.

1.7 Needs of explaining and predicting the bias

Different approaches are being followed in literature to extract aggregate measures and to explain the observed differences between calculations and measurements of characteristics of SNF. Using a similar calculational approach and different nuclear data evaluations can explain sources of discrepancies related to nuclear data. This approach was followed in a study on criticality safety benchmarks, differentiating between various nuclear data libraries: JEFF-3.1, ENDF/B-VII and JENDL-3.3 [33]. Another approach relies on modeling the same benchmark with different codes and code users. This method was followed in various benchmarks conducted by the OECD/NEA on depletion calculations and burnup credit criticality safety [34–36]. Other solutions rely on modeling large numbers of benchmarks using the same calculational methods and nuclear data, so that systematic deviations can be analyzed. The latter approach was followed in various studies conducted in the Oak Ridge National Laboratory on decay heat calculations, depletion calculations, and criticality safety analyses [27,37,38]. The present study falls into the latter category.

The measurements on the SNF characteristics are expensive, such that the available measurements represent a small fraction of the overall assemblies. The publicly available SNF decay heat measurements stand at few hundreds; large scale measurements campaigns such as those conducted by the SKB at the Clab facility [12] and the GE at the GE-Morris facility [13] resulted in measurements of less than three hundreds SFAs. As of 2017, there are over a million of SFAs. The situation of the measured isotopic concentrations is even more challenging; typical PIE samples are just about 1 cm length section of a fuel rod. The fuel assembly itself is typically a few hundreds of fuel rods, mostly standing at 3-5 meters long [11]. Knowledge about how accurate and precise calculational tools and data characterize this large number of SFAs relies on knowledge about how accurate and precise they perform on the available limited measurements.

The M&S tools and data (information about fuel design and irradiation, and nuclear data) are validated within ranges of properties of the validation benchmarks (*e.g.*, a range of material compositions, burnup, and other quantities). The relevant characteristics of the measurements, and therefore the benchmarks, define what is referred to as the area-of-applicability (AOA). However, when the M&S tools and data are used for a target application (*e.g.*, realistic calculations of SNF), the properties of the application are not necessarily identical to those of the benchmarks used for validation. The considered SNF can share some properties with a number of measurements, such as their enrichment or burnup. However, they can also differ from any of the available measurements. Additionally, it is not always straightforward to know which particular SNF properties are critical in defining the AOA and informing about the similarities to available benchmarks. Again, predictive modelling can be employed herein to obtain relevant

properties of the validation data and to define how distant the practical calculations exist from the AOA.

Different areas of analyses of nuclear fuel and SNF are at different stages of developments in this aspect – defining relevant properties and AOA of validation benchmarks and establishment of prediction techniques from the validation data. In the case of criticality safety analysis (CSA), techniques of predicting the bias in a target application from sets of neutronicallly similar benchmarks are well established [39]. The predicted biases are then used to justify necessary margins of subcriticality in the intended applications. Standards, such as the ANSI/ANS-8.24 [32], allow bias and bias uncertainty to be predicted from validation benchmarks, *e.g.*, using linear or power models. The models rely on independent variables such as the hydrogen-to-fissile atom ratio (H/X) or similarity index (c_x). However, there is no consensus on which variables can be used for predictions, and such predictions are routinely aggregated over models relying on different features, preferably those showing notable trends with the bias [40,41].

Other areas of safety analyses and characterizations of SNF face similar challenges, where relevant properties and AOA of validation data need to be defined, and bias prediction techniques need to be furtherly developed. Literature related to bias predictions in SNF calculations, other than CSA, are scarce and techniques are not as developed. Examples of bias inference of the SNF decay heat from validation benchmarks were previously analyzed in studies such as the work of Gauld and Murphy [26] and Hermann et al. [42]. Statistics of the decay heat biases, *e.g.*, averages and standard deviations, form a basis for safety factors on calculated decay heats in the Regulatory Guide 3.54 of the US Nuclear Regulatory Commission (NRC) [43]. Also, in studies by Gauld and Mertzyurek [37] and Radulescu et al. [44] on depletion calculations of SNF, bias averages and standard deviations of selected isotopes were used as correction factors on the isotopic concentrations in downstream criticality calculations – CSA that credits the fuel burnup. However, for the present applications, the bias prediction methods are not yet developed as in the case of CSA, and statistics are still being used to inform about the bias in target calculations.

1.8 Predictive modelling paradigm

The goal of predictive modelling is to understand how selected SNF features are mapped into the response, the bias in this case. The predictive modelling can rely on given or assumed hypotheses about these features and the relation between these features and the bias. Additionally, and more importantly, the goal of predictive modelling is to be able to use the data-driven final models to make predictions on realistic, or target, calculations. As an example, in the present study, models that rely on information from similar benchmarks will be used to predict the bias of a benchmark of interest. The hypothesis in this case is that similarity allows prediction of the bias. The quantity “similarity” is not adequately defined, and a hypothesis is analyzed in the present study that the correlation between benchmarks contains information about their similarity. Other integral features, such as the H/X , might also inform about the similarities

between benchmarks. Finally, some models can show that they have promising predictive performance of the bias. They can be used in future to provide a bias estimate of a realistic calculation on SNF, given its correlation with a number of validation benchmarks with known biases. Alternatively, integral features found to be informative about the bias can be used for such predictions relying on similar benchmarks in the features space.

As mentioned, the predictive modelling is not yet well-developed for the quantities of interest, even if a number of recent approaches in literature are exploring such direction. Recently, Random Forests (RF) were used by Grechanuk *et al.* [45] to predict the bias in the neutron multiplication factor k_{eff} from its sensitivity to nuclide-wise reactions. Neudecker *et al.* [46] have used RF models to understand the contributions of nuclear data into biases of criticality calculations, using also k_{eff} sensitivity to nuclide-wise reactions. Ebiwonjumi *et al.* [47] have used neural networks and gaussian processes, to predict the decay heat measured values. Finally, Solans *et al.* [48] have used neural networks to predict the Monte Carlo-based k_{eff} of SFAs packed in disposal canisters, given model features such as the isotopic composition of the depleted fuel.

1.9 The research questions and hypotheses

The present research aims at validating a calculational sequence based on the SCALE code system [49] on a large number of validation benchmarks. Particularly, the calculations rely on the Polaris code of the SCALE code system (version 6.2.3) along with SCALE nuclear data primarily based on the ENDF/B.VII.1 nuclear data library [49]. The validation data are two categories: SNF decay heat, and radionuclide concentrations of PIE samples (namely: Cs-137, U-235, and Pu-239). Then, uncertainties and correlations of the calculated values are to be evaluated. The biases, their uncertainties, and the calculated correlations are to be used to investigate ML models and algorithms enabling predictions of the bias in realistic calculations of SNF characteristics.

Two main hypotheses are analyzed in the present research. The first one is that the observed biases are not significant, given uncertainties. These uncertainties, based on calculations only (or along with the measurements), can indicate that the observed bias between calculations and measurements is not significant, such that

$$C - E \sim N(0, \sigma). \quad (1.4)$$

The bias is assumed to follow a normal distribution, zero-centered, parameterized by the variance of the calculations only (or along with the variance of the measurements). The hypothesis is tested using the collected validation and uncertainty analyses data.

The second hypothesis of the present research is that the bias of SNF characteristics can be predicted using ML models and algorithms. The bias is represented as two components: a systematic one, targeted to be predicted using the ML models, and a random and unexplained component. Validation data (bias and potentially informative SNF features), hypotheses on the ML models, and learning, testing, and validation procedures are assembled in ML algorithms such that a solution is obtained for Equation 1.3 for the bias (restated herein):

$$C - E = f(X) + \epsilon. \quad (1.5)$$

The design matrix X contains informative model features (unknown *a priori*) and f is a function that maps X into the bias (also unknown *a priori*). The function $f(X)$ is intended to capture the systematic part of the bias (the explained bias), and ϵ is intended to capture the random part of the bias (the unexplained part of the bias). As in the case of CSA, X can be the correlation between benchmarks, and f can be the linear model that regresses the bias of the benchmarks onto their correlations. A class of functions, namely neighborhood-schemes, is analyzed. The chosen class of functions is related to an assumption that neighboring benchmarks are informative in predicting the bias. The ML models are the random forests and the weighted k-nearest neighbors. In such model types, predictions are driven from “neighbors” or highly similar benchmarks to the target application.

The scope of the present research is also to analyze different types of SNF features, potentially informative into predicting the bias (*e.g.*, features defining the neighborhood or similarity). Features such as those driven from sensitivity analysis, integral features such as spectral indices and uncertainties, and calculated correlations are to be analyzed. The structure of the neighborhood, *e.g.*, the number of neighboring benchmarks and their weights, is also to be driven from the validation data. Finally, an estimate of the error ϵ , in providing new predictions using the ML models and algorithms, should be obtained using techniques such as cross-validations.

Lastly, the novelty of the present study is in method development of data-driven bias prediction techniques, *e.g.*, using large sets of validation data and machine learning (ML) models and algorithms, applied on characteristics of SNF such as decay heat and radionuclide concentrations.

1.10 Potential applications

If successful, the developed data-driven models will explain a fraction of the original bias variance, resulting in less variability of the bias. The variance reduction of the bias is not guaranteed to be meaningful or significant, using the applied techniques in the present study. Alternatively, and given the analyses of a significantly large number of benchmarks, the calculated bias can be justified using laws of probability to estimate confidence intervals.

The applications potentially benefitting from bias prediction techniques are such as packing of SFAs in disposal canisters and calculations of temperatures inside storage casks. To adhere to safety limits, calculations can be penalized with a bias and a bias uncertainty. Also, criticality calculations on SNF which credit the fuel burnup can rely on predictions of biases of isotopic concentrations. Also, experimental measurements on SNF are expensive and sparse, and development of these techniques will help in maximizing their usage and allowing data-driven predictions on applications not fully covered by their AOA.

1.11 Structure of the Thesis

The thesis is structured as following:

- Chapter 2 describes the analyzed decay heat and PIE benchmarks.
- Chapter 3 introduces the codes and computer hardware used in the present study.
- Chapter 4 describes the relevant M&S assumptions.
- Chapter 5 presents the hypotheses tests: the parametric z-test, and the non-parametric permutation and bootstrap tests.
- Chapter 6 describes relevant techniques and models of ML. Selected methods of model validation and data resampling are provided. Then, descriptions are provided for the procedures followed in the present study for predicting the bias using integral features of the benchmarks, and their correlations, and also the applied methods of extracting properties of the benchmarks.
- The results are presented in Chapter 7 to 11:
 - Chapter 7: the validation results.
 - Chapter 8: the uncertainty analyses results.
 - Chapter 9: results of the non-parametric tests applied using the validation data.
 - Chapter 10: results of the z-tests applied using the validation and uncertainty analyses data.
 - Chapter 11: results of the ML application on predicting the bias. Firstly, the extracted features are presented. Then, the predictions of the ML models are presented, starting with the linear models separately, given their limitations. The results of the RF and KNN models are then presented, based on integral features of the benchmarks, *e.g.*, H/X , and their correlations. Lastly, the predictive performance along with outliers removal is presented for the decay heat and Pu-239 concentration biases.
- Chapter 12 concludes and summarizes the present study, along with potential applications of the present study and future work.

Chapter 2 Validation Benchmarks

The present study focuses on two SNF characteristics, namely, the decay heat and radionuclide concentrations (Cs-137, U-235 and Pu-239). These characteristics were chosen given their importance for the economics and long-term safety of the DGR. The SNF decay heat is an important parameter affecting the number of disposal canisters required to encapsulate the SNF assemblies for their final disposal. Accurate evaluations of the SNF decay heat would result in using less safety margins on the calculated values, reducing the number of required canisters, which is economically advantageous. The chosen radionuclides are important for the long-term safety of the repository and the calculated dose rates, being part of the DRN list defined by Nagra [50], and also other WMO organizations such as SKB and Posiva [51,52]. The DRNs are more than the analyzed radionuclides, however, the chosen ones are the most abundantly measured in open literature addressing PIE of LWR fuel samples. Relatively large number of benchmarks would improve the subsequent data-driven analyses. Particularly, with respect to other fission products, Cs-137 has the highest number of measurements in the analyzed PIE data (except for Nd-148). Also, U-235 and Pu-239 are particularly important for other SNF applications, such as burnup credit implementation in criticality safety analyses [37].

Experimental benchmarks, hereinafter benchmarks, of these characteristics are selected from open-source literature for generation of the validation database, described in the following sections.

2.1 Decay heat benchmarks

Decay heat measurements for various light water reactor (LWR) fuel assembly designs, enrichments, burnups, and cooling times have been selected for validating the M&S sequences. The modeled SFAs are listed in

Table 2. All assemblies are based on UO_2 fuel. The data are 262 measurements on 160 SFAs, split into 85 measurements on pressurized water reactors (PWRs) and 177 on boiling water reactors (BWRs). Particular SFAs have multiple measurements at various cooling times, assumed independent in this work. Such assumption is motivated by the unavailability of experimental correlation values between the reported measurements. Therefore, each individual measurement is considered a benchmark, including the multiple measurements on the same SFA. The influence of the correlation assumptions on the hypothesis testing is also analyzed in this study.

The data are based on measurements conducted by GE and SKB [12,13], along with details about the irradiation history and the design specifications of the SFAs. The measurements covered assembly discharge burnups up to 51 and 47 GWd/tHMi for PWRs and BWRs, respectively, and cooling times up to 27 years.

The data are selected from the open-source literature, and other measurement campaigns which are limited in size are excluded. Specifically, the measurements on 4 assemblies conducted at the EMAD facility by the Hanford Engineering Development Laboratory (HEDL) were excluded [53]. They represent less than 2% of the total analyzed data, and it was decided that excluding these 4 SFA is a negligible reduction. Also, excluding these data allowed splitting the analyzed data based on the laboratory conducting the measurements (*i.e.*, GE and SKB) and the SFA reactor of origin (*i.e.*, BWR and PWR). The analyzed categories are:

1. Clab PWRs
2. Clab BWRs
3. GE-Morris PWRs
4. GE-Morris BWRs

2.1.1. Measurements at the GE-Morris facility

Calorimetric measurements were conducted by GE at the Morris facilities (Illinois, USA) on 77 full-length PWR and BWR SFAs discharged from the following reactors: San Onofre 1, Point Beach 2, Dresden 2, Cooper, and Monticello [13,54]. The measurements were conducted using a pool-type calorimeter that evaluates the rate of the water temperature rise in the calorimeter where the SFA is located. The decay heat is evaluated using a calibration curve, established between the thermal output of an electric heater and the corresponding rise in the water temperature. The measurements account for the heat loss through gamma leakage using gamma-ray detectors. The GE-Morris benchmarks cover a range of cooling times down to approximately 2 years, burnups down to approximately 5 GWd/tHMi, and also SFAs with high decay heat.

2.1.2. Measurements at the Clab facility

Calorimetric measurements were conducted between 2003 and 2004 by SKB at the Clab facility (Oskarshamn, Sweden) on 83 SFAs, reported in SKB report no. R-05-62 [12]. The measurements were conducted also using a pool-type calorimeter. However, the experimental uncertainties are lower than that of the GE measurements. The measurements involved SFAs spanning higher discharge burnups and are measured at longer cooling times than the GE measurements [12]. The SFAs measured in Clab contain 18 “rebuilt” SFAs: some of their fuel rods were removed at the EOL or in between cycle downtime. Such cases are still considered in this work, and their specifications are provided in Appendix I.

2.1.3. Fuel assembly designs and irradiation data

Table 2 lists the SFAs modeled in the present study, and selected Polaris models are shown in Figure 2. The SFAs have various fuel assembly designs, enrichments, discharge burnups and cooling times, being useful for assessing the performance of the computational tools over a wide range of applications. The SFAs discharged from a reactor belong to a particular design, except for the Forsmark and Oskarshamn SFAs. Additionally, major SFA designs include subcategories such as the GE 8x8 in Ringhals-1 and W 15x15 in Ringhals-2. The SFA design subcategories reflect differences in the assembly enrichment layouts, the number of burnable absorbers, and the design specifications. Many of the BWR SFAs contain integral absorbers, gadolinia-bearing fuel rods, summing to 157 benchmarks out of the total of 262.

The PNL-577 Vol. I and II reports [13,54] provided the basis for the data implemented for the Cooper SFAs (GE measurements). However, the enrichment layout (and other design data) of the Cooper GE 7x7 assembly type was not detailed in the reports and was supplemented from the NUREG report CR-6972 [27]. The latter report also provided data for the remaining benchmarks of the GE measurements. The SKB report R-05-62 [12] was used for the SFA design and irradiation history data of the measurements carried out at the Clab facility.

Table 2. Summary of the decay heat experimental benchmarks considered in this study, based on [12,13,27,54]. Range of properties, *e.g.*, burnup range, are listed for all benchmarks belonging to particular reactors.

Facility	Reactor type	Reactor ^I	Measured value (W)	Burnup ^{II} (GWd/tHMi)	Decay time (years)	No. of SFAs	No. of measurements
GE-Morris (GE)	PWR	SO-1	359 – 934	27 – 32	3 – 8	8	8
	PWR	PB-2	724 – 934	32 – 39	4	6	6
	BWR	D-2	20 – 30	5	8	1	2
	BWR	C	62 – 392	12 – 28	2 – 7	56	81
	BWR	M	46 – 155	9 – 21	10 – 11	6	13
Clab (SKB)	BWR	B-1, 2	83 – 240	20 – 41	11 – 25	7	9
	BWR	F-1,2,3	85 – 218	20 – 38	11 – 15	11	12
	BWR	O-2,3	56 – 283	15 – 47	12 – 27	14	15
	BWR	R-1	88 – 211	21 – 45	13 – 24	17	45
	PWR	R-2	357 – 692	34 – 51	16 – 27	18	33
	PWR	R-3	210 – 714	20 – 47	13 – 26	16	38
Total	PWR		210 – 934	20 – 51	3 – 27	48	85
	BWR		20 – 392	5 – 47	2 – 27	112	177

^I SO, PB, D, C, M, B, F, O, and R are abbreviations for: San Onofre, Point Beach, Dresden, Cooper, Monticello, Barsebäck, Forsmark, Oskarshamn, and Ringhals, respectively.

^{II} Assembly discharge burnup

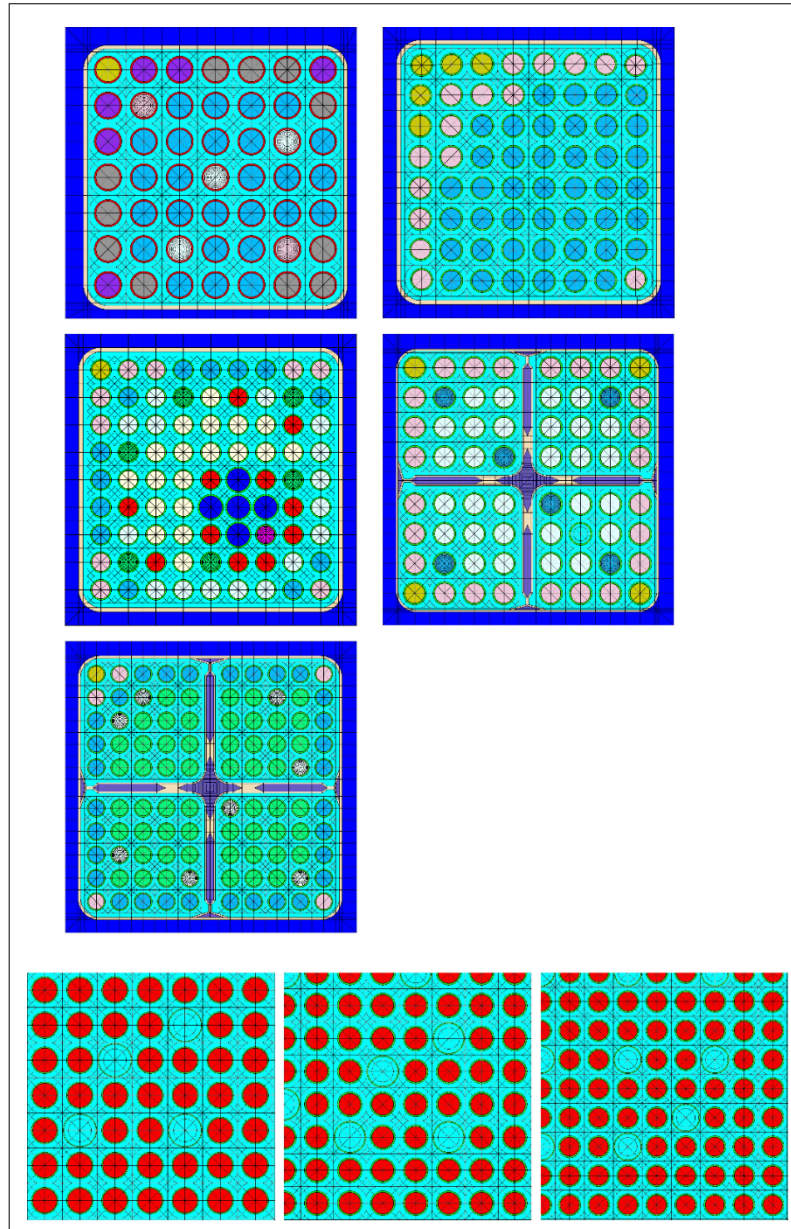


Figure 2. Selected Polaris models of BWR SFAs (top 3 rows) and PWR SFAs (bottom row). The BWR models are asymmetric, while the majority of the PWRs have quarter symmetry. The models are (from left to right, top to bottom): GE7, GE8, GE9, SVEA-64, SVEA-100, W14x14, W15x15, and W17x17. Fuel rods are shown in different colors to reflect differences in densities, enrichments, and gadolinium content.

2.1.4. Decay heat experimental uncertainties

The uncertainties in the measurements reported by SKB are based on [12] (summarized in Table 3), and they are based on estimates of Gauld et al. [27] for the GE measurements (summarized in Table 4) – both are two standard deviations (2σ). The values in Table 3 and Table 4 are plotted in Figure 3. The uncertainties are reported at specific upper and lower power, and uncertainties at intermediate decay heat values are not reported in the original reports. In the present study, uncertainties at intermediate decay heat values are obtained by linear interpolations between the values in Table 3 and Table 4. The uncertainties are higher at low

decay heat values for both laboratories. As observed, uncertainties of the GE measurements are significantly higher than the ones of SKB.

Table 3. Uncertainties (2σ) in decay heat measurements at the Clab facility based on Reference [12].

SFA	Power (W)	Uncertainty (W)	Uncertainty (%)
BWR	50	4.2	8.4
	350	6.2	1.8
PWR	250	9.2	3.7
	900	18.8	2.1

Table 4. Uncertainties (2σ) in decay heat measurements at the GE-Morris facility based on Reference [27]. The values correspond to both PWRs and BWRs.

SFA	Power (W)	Uncertainty (W)	Uncertainty (%)
GE	200	16	8
	700	28	4

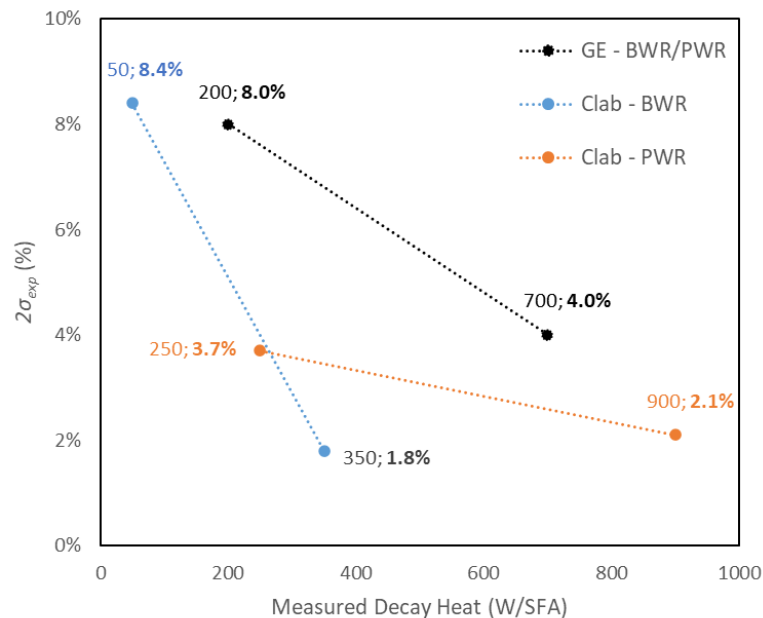


Figure 3. Uncertainties in the decay heat measurements [12,27]. Uncertainties are reported at upper and lower values, marked at the ends of each line along with values of both the measured decay heat and the corresponding uncertainty. Uncertainties are interpreted as 2σ , and intermediate values are linearly interpolated between the listed upper and lower values.

2.2 Post-irradiation-examination benchmarks

The analyzed PIE benchmarks in the present study are obtained from the SFCOMPO database. SFCOMPO (version 2.0) is a relational database of experimental assay data of SNF isotopic composition [11,55]. The database is maintained and evaluated by OECD/NEA' SFCOMPO TRG [19] of the Working Party on Nuclear Criticality Safety (WPNCS) of the NEA Nuclear Science Committee [56]. The database is composed of publicly available (*i.e.*, published) data of PIE benchmarks. The data include the radiochemical analyses (RCA) of measured isotopes (*e.g.*, their inventory, methods of measurements, and experimental uncertainty). Additionally, other details are included to allow validating calculational methods of fuel burnup calculations. The latter details are primarily reactor operational data (*e.g.*, dates of active and down cycles), PIE irradiation history (*e.g.*, cycle-wise power densities), and assembly design information (*e.g.*, enrichment layout and rod dimensions). Additional relevant information is also included, such as references to the original experimental lab reports and publications analyzing the PIEs. The summary of the analyzed PIEs in the present study is provided in Appendix II. Also, Appendix III provides selected Polaris input files of two PIEs having a BWR and a PWR origin.

2.2.1. Characteristics of the PIE Benchmarks

The present study focuses on PIE samples irradiated in light water reactors (LWR), considering PIEs from 12 PWRs and 7 BWRs (summarized in Table 5). Most PIEs are from assemblies based on UO_2 fuel (281 PIEs) and 4 PIEs are MOX-type fuel, totaling 285 samples. The PIE data are more diverse than the decay heat data, they have different fuel assembly designs, burnups, enrichments, operational conditions, and multiple laboratories that conducted the measurements. Detailed descriptions of the analyzed PIE samples and their host assemblies are provided in Appendix II, along with main modelling assumptions used to generate the Polaris models. Such assumptions include methods used to interpolate the moderator temperature in PWRs vs. the axial height of the samples. Specific modelling assumptions for particular samples, such as cruciform control rods in Trino Vercellese-1 and Yankee-1 PIEs, are discussed within the subsections of each reactor data.

Figure 4 shows selected characteristics of the considered PIE benchmarks. The axial height is the ratio of the axial position of the sample to the total active height of the fuel rod. The benchmarks are well distributed over the active length of the fuel rods, ranging from axial positions of 0.0 to 1.0. The coolant density is the density of the water in the vicinity of the sample, excluding water that might exist in, for instance, water gaps. Water density changes significantly with the axial height for BWR, considering the increased void fraction with the axial height upon the onset of boiling. In PWRs, the change in the coolant density over the axial length is smaller, due to the rise in the water temperature without boiling. The enrichment is the ratio of the U-235 mass the total uranium mass initially present in the sample (unlike the decay heat benchmarks which have their assembly average enrichments). Enrichments as low 0.24 and 0.70 wt% are encountered, whereas the former belongs to MOX samples (4 PIE samples from the

Dodewaard-1 reactor). The 0.7 wt% enrichment belongs to fuel samples at top and bottom blankets of BWR, having natural uranium loading. The range of enrichments spans up to relatively high values of 4.94 wt% U-235 (regarding LWR fuel enrichments).

Table 5. Summary of the analyzed PIE samples from the SFCOMPO database.

Reactor name	Reactor type	No. of samples
Calvert Cliffs-1	PWR	9
Genkai-1	PWR	2
Mihama-3	PWR	9
Neckarwestheim-2	PWR	1
Obrigheim-1	PWR	25
Ohi-1 and Ohi-2	PWR	6
Takahama-3	PWR	16
Three Mile Island-1	PWR	13
Trino Vercellese-1	PWR	31
Turkey Point-3	PWR	13
Yankee-1	PWR	21
Cooper-1	BWR	6
Dodewaard-1	BWR	5
Fukushima Daini-1	BWR	13
Fukushima Daini-2	BWR	44
Garigliano-1	BWR	26
Gundremmingen-1	BWR	15
Japan Power Demonstration Reactor-1	BWR	30
Total	PWRs	146
	BWRs	139

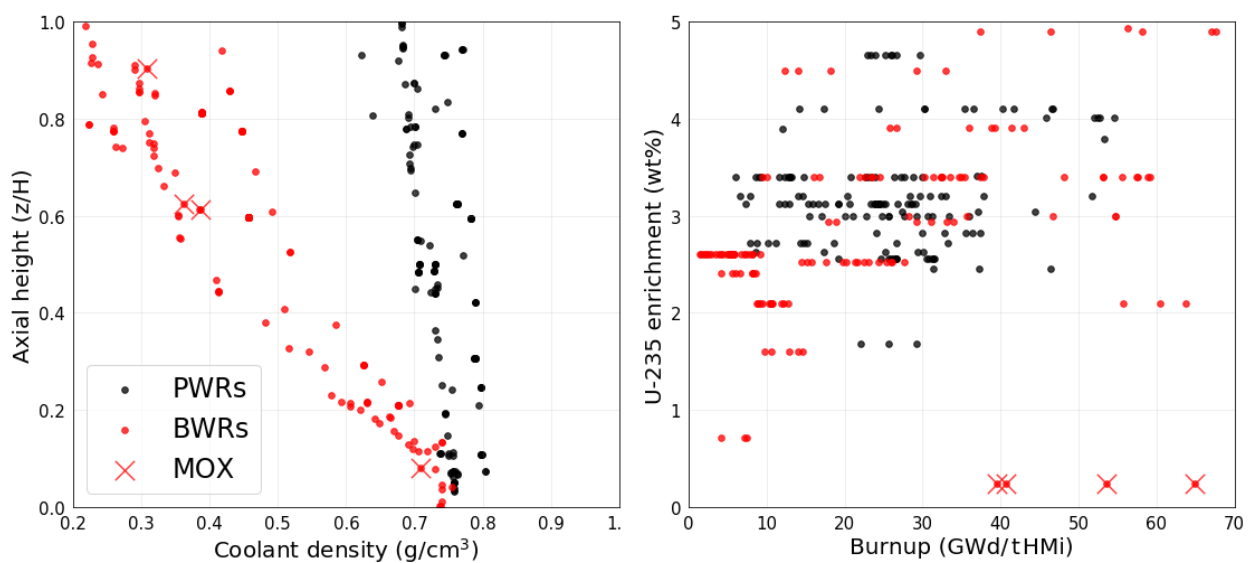


Figure 4. Characteristics of the considered PIE samples. Left: the axial height of the sample (z) with respect to the active length of the fuel rod (H) vs. the coolant density. Right: the sample enrichment vs. the sample given burnup. Additionally, BWR MOX samples are marked with “X”.

2.2.2. Burnup values for the PIE samples

Few samples are having burnup values higher than 60 GWd/tHMi, which is lower than recently discharged fuels. The largest burnup value in the current dataset is 67 GWd/tHMi, belonging to samples from the Fukushima Daini-1 reactor. Very low burnup values are also encountered in the current dataset. The lowest burnup is 1.4 GWd/tHMi, from the Japan Power Demonstration Reactor-1 samples (JPDR-1). All the samples of the JPDR-1 have relatively low burnup values, ranging from 1.4 to 9.1 GWd/tHMi, which is a relevant extension in the low burnup region. The PWRs cover narrower burnup range compared to the BWRs, ranging from 6.0 up to 54.6 GWd/tHMi.

An implemented assumption regarding the sample burnup is that the calculated burnup values are adjusted such that the calculated Nd-148 concentration matches the measured value (within $\pm 0.05\%$ of the measured value). The adjustments proceed by scaling the power in all irradiation cycles by a specific factor. The burnup values shown in Figure 4 are the ones from SFCOMPO, not corrected to match the Nd-148 concentration measurements. Typically, they are different from the actually implemented burnup values. Figure 5 shows the applied corrections on the burnup values. As observed, significant corrections to the given burnup values were applied. Only 52% of the samples have their estimated burnup within 1% of the given values. 95% of the corrections lie within 0.8 and 1.15, and the minimum and maximum applied correction factors are 0.49 and 1.34.

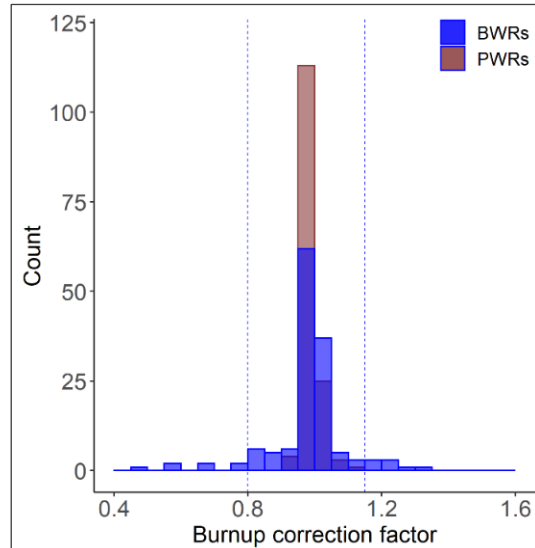


Figure 5. Correction factors applied on the burnup of the PIE samples. The dashed blue lines are the 2.5% and 97.5% percentiles (*i.e.*, an interval that contains 95% of the observations).

2.2.3. Measurements of the radionuclide concentrations

The measured concentrations of U-235 and Pu-239 are reported for the analyzed 285 samples. Cs-137 measurements are reported only for 222 of the analyzed samples. 5 samples have their U-235 and Pu-239 measured multiple times, using different methods or at different laboratories. Also, 33 samples have their Cs-137 measured multiple times. Duplicate measurements are not

considered in the analyses, *i.e.*, only one value out of the multiple measurements is selected for further analyses. For instance, for samples that have “cross-check” measurements at different laboratories (SCK.CEN and PSI), such as PIE DU1 and DM1 of the Dodewaard-1 reactor, only the measurements at SCK.CEN are considered, as other samples from Dodewaard-1 were only measured at SCK.CEN.

The reported measurements are in different units. For instance, U-235 and Pu-239 have their measured values (or measurements-driven values) reported in the following units:

1. mass per initial uranium mass
2. mass per initial U-238 mass
3. mass per final uranium mass
4. mass per final U-238 mass
5. moles per final uranium moles

The Cs-137 has other units of measurements (in addition to the above-mentioned units):

1. activity (Bq) per final uranium mass
2. activity (Ci) per initial uranium mass

In the present study, all units are converted into mass per initial heavy metal mass (*e.g.*, mg/gHMi), including the MOX samples. The initial HM mass is the initial mass of elements having their atomic number $Z > 89$. The conversion is motivated by the need to have the same unit for the bias, and therefore the calculated and the measured values. Mass per initial HM mass is chosen since most U-235 and Pu-239 measurements are reported in this unit. The conversion factors into the initial HM mass are based on the calculations.

In addition to the measured concentrations, the majority of the measurements have their experimental uncertainties reported:

1. for U-235: 235 samples out of 285,
2. for Pu-239: 218 samples out of 285, and
3. for Cs-137: 146 samples out of 222.

As noticed, a significant number of samples lack information about uncertainties. Figure 6 shows histograms of the reported experimental uncertainties, based on the SFCOMPO database [11]. Whenever experimental uncertainties are not reported, they are assigned to zero in this figure. Additionally, the reported uncertainties are often different in different methods of measurements, and also for different laboratories using the same method of measurements.

Figure 7 shows the measured U-235, Pu-239 and Cs-137 concentrations vs. the given burnup values of the PIE samples. The burnup is chosen for the plots since the considered isotopes change monotonically in low and medium burnup ranges, albeit non-linear, with the burnup.

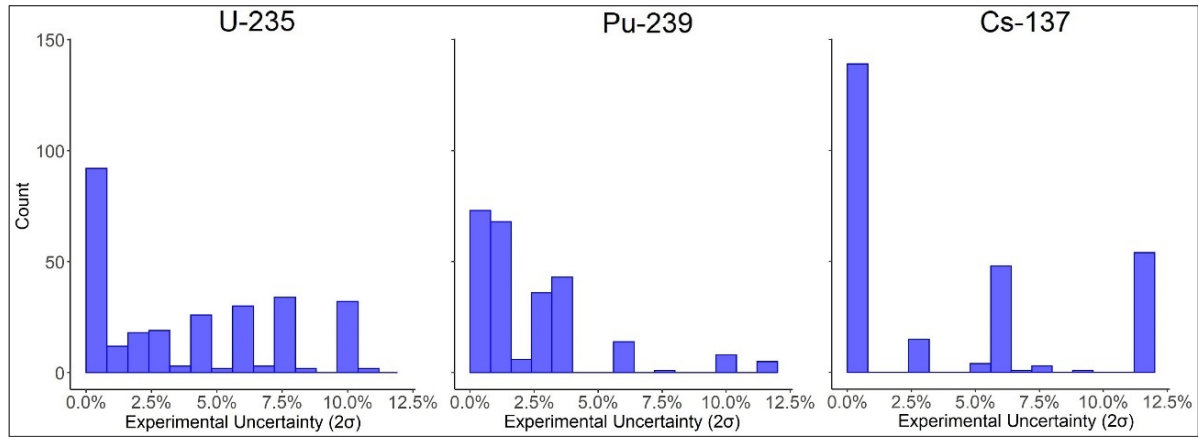


Figure 6. Experimental uncertainties (2σ) for the PIE samples, based on SFCOMPO [11].

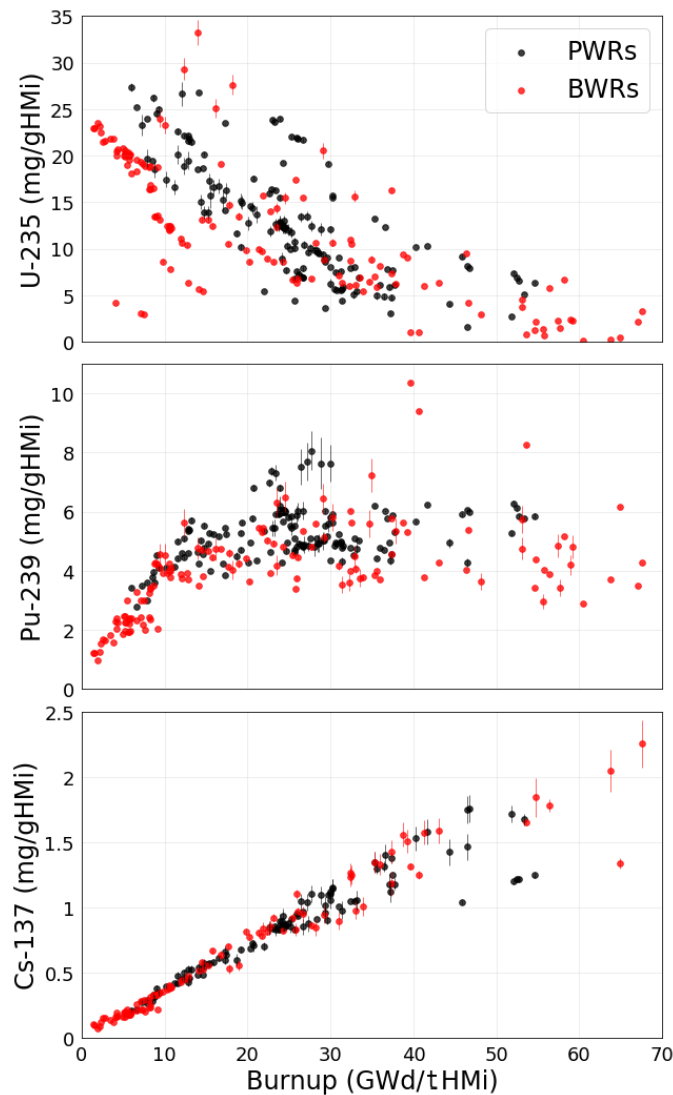


Figure 7. Measured U-235, Pu-239, and Cs-137 concentrations vs. the sample given burnup. The plotted bars are experimental uncertainties (2σ).

2.2.4. Excluded SFCOMPO benchmarks

The analyzed PIEs in this work are 285 samples, less than the number of LWR samples in the SFCOMPO. Several samples were excluded from the present study, based on analysis of their

provided data in SFCOMPO. Benchmarks that have incomplete description of their lattice design and operational data are excluded, such as the benchmarks of Fukushima Daiichi-3, Tsuruga-1 and Quad Cities-1. Often, benchmarks have incomplete description of their details, and assumptions are used to complete the necessary modelling information. However, missing information can be essential. Other excluded PIE benchmarks belong to fuel rods that were relocated in different positions during irradiation, such as Gösgen-1 and Vandellors-2. Modelling the relocated samples requires additional assumptions compared to non-relocated PIEs. Such assumptions are significant, potentially resulting in significant differences in calculated concentrations.

Chapter 3 Modelling and Simulations Codes

Three types of calculations are performed in the present study:

1. Validation, *i.e.*, modelling of SNF benchmarks to calculate their measured characteristics.
2. Uncertainty propagation, *i.e.*, propagating uncertainties in the inputs and data of the calculational models into uncertainties and correlations of the calculated characteristics.
3. Machine learning, *i.e.*, applying algorithms on the validation and uncertainty analyses data to derive models for predicting the bias of the calculated characteristics.

The SCALE nuclear modeling and simulation code system [49] (version 6.2.3) is primarily used for validation and uncertainty propagation. It is developed by Oak Ridge National Laboratory (US) and is chosen for its widely usage for nuclear system design and safety analyses such as criticality safety, shielding calculations, and LWR analyses. The current validation and uncertainty propagation rely mainly on two SCALE codes: the Polaris module and the Sampler super-sequence. The Polaris lattice physics code (coupled to ORIGEN depletion and decay code) is used for validation. Sampler stochastic sampling super-sequence is used for uncertainties propagation. The R language [57], along with the Caret package [58], are primarily used for Machine Learning.

Cross-section libraries are available in SCALE in a 252- and 56-group structure for use if calculations with Polaris. The 252-group library is for general-purpose reactor physics and criticality safety applications and the 56-group library is intended for light water reactor analysis [49]. In the present study, Polaris and Sampler are implemented using the SCALE “56g” multi-group (MG) library. Choosing the 56g MG library is mainly motivated by its reduced computational requirements compared to the more refined 252g library, and its suitability for the intended application, *i.e.*, depletion, and decay calculations.

3.1. Validation tools

3.1.1. Polaris code

Polaris is a 2D lattice physics module used for the analysis of LWR fuel assemblies, based on the Embedded Self-Shielding Method for evaluating the self-shielded multigroup cross-sections and a Method of Characteristics transport solver [59,60]. The Polaris module performs the lattice calculations, coupled with ORIGEN for depletion and decay calculations, leading to time-dependent isotopic concentrations, and subsequently decay heat. The decay and fission yield data are based on the ENDF/B-VII.1 nuclear data library, while the MG cross-section libraries are

based primarily on ENDF/B-VII.1 along with supplementary data from the JEFF-3.0/A nuclear data library, as recommended for general-purpose reactor physics and LWR analysis [49].

3.1.2. *ORIGEN code*

The decay heat benchmarks are re-calculated using different codes than Polaris. The purpose of the multiple calculations will be explained in Section 5 (Hypothesis testing on the bias). The second calculational sequence (ORIGEN hereinafter) consists of three steps: generation of lattice-specific irradiation-dependent cross-section data using TRITON [49,61], followed by multiple cross-section data interpolations using the ARP interpolator utility and the actual SFA design and irradiation data, followed by depletion and decay calculations using ORIGEN [49,62]. Similar to Polaris, TRITON also uses the SCALE 56g library. The approach has been selected to have differences from the Polaris calculations – differences in the methods and data, such that systematic differences of different calculations from the measurements could be identified.

3.2. Uncertainty propagation

The uncertainty propagation is performed using the SCALE Sampler super-sequence. Sampler performs stochastic uncertainty propagations, by generating and running hundreds of input files of sub-sequences (Polaris) and analyzing the outputs [63]. The inputs are generated by random sampling from nuclear data covariances (available in SCALE) and joint probability distributions of uncertain design and operational variables of the SFA. The outputs are statistical analyses of distributions of Polaris calculated values, which include estimations of the uncertainties and correlations between the calculated values. The nuclear data covariances are primarily based on the ENDF/B-VII.1 nuclear data library. ENDF/B-VII.1 covariance data along with other supplementary data are sources for the cross-section, spectra and nubar covariances. Fission yield variances (combining independent and cumulative yields) are sources for the fission yields covariances. Decay variances along with imposed sum of unity for branching ratios are sources for decay data covariances.

3.3. Machine learning

The application of the machine learning models and algorithms is performed using the R language and environment. R is an open-source language and environment for statistical computing, developed at Bell Laboratories [57], available under the terms of the Free Software Foundation's GNU General Public License in source code form. R is chosen since it is a widely used tool in statistical analysis related research, and also due to its inclusion of a wide range of statistical models, tests, and algorithms, data analysis and manipulation capabilities, together with generation of publication-quality plots. R also serves as a programming language, which allowed developing algorithms tailored to the hypotheses of the current research. R packages are extensions of R itself, allowing lengthy operations to be integrated in functions. In the current research, the Caret package [58], which stands for "Classification And REgression Training" is

mainly used for developing the investigated ML models, *i.e.*, data splitting, pre-processing, feature selection, model training and testing, tuning using resampling, and variable importance estimation, as well as other functionality.

3.4. Computational requirements

All calculations were performed on the workstations listed in Table 6. The depletion and decay calculations of the PIE benchmarks spanned 9.5 hours (on average). The corresponding calculations of the decay heat benchmarks spanned 1.6 hours (on average). The PIE benchmarks required approximately 1.8 million core-hour for completions, whereas the decay heat benchmarks required approximately 0.3 million core-hour. The length of an individual calculation depends mainly on the number of materials being depleted, the presence of gadolinia (which requires ring-wise material specifications), and the number of irradiation steps.

An additional 0.35 million core-hour were required to run the machine learning models for all the data (excluding testing times). The runtime of the individual ML models significantly depends on the type of the model being regressed, the initial number of variables in the model, and the size of the grid being searched for the optimal model parameters. The KNN-type models are computationally intensive, which required between 32-48 runtime hours on a 128-thread workstation. RF models required less time, between 6-9 runtime hours on the same workstations.

Table 6. Specifications of the hardware used to perform the depletion and decay, uncertainty propagation, and the machine learning calculations.

Host	Workstation-H	Workstation-I	Workstation-J	Workstation-K
Architecture	x86_64	x86_64	x86_64	x86_64
CPU name	AMD Ryzen Threadripper 2990WX	AMD Ryzen Threadripper 2990WX	AMD Ryzen Threadripper 3990X	AMD Ryzen Threadripper 3990X
CPU clock speed	3.0 GHz	3.0 GHz	2.9 GHz	2.9 GHz
CPU cores / threads	32/64	32/64	64/128	64/128
RAM	128 GB	128 GB	256 GB	256 GB
Operating System	Ubuntu 18.04 LTS (64-bit)	Ubuntu 20.04 LTS (64-bit)	Ubuntu 20.04 LTS (64-bit)	Ubuntu 20.04 LTS (64-bit)

Chapter 4 Validation and Uncertainty Propagation Schemes

The implementation of Polaris and Sampler on the present study is described in this chapter. As mentioned, the current data are two categories, SNF decay heat and isotopic concentrations (Cs-137, U-235, and Pu-239). Firstly, sections 4.1 and 4.2 provide the implementation of Polaris for the validation of the two categories of SNF characteristics, respectively. However, the descriptions of the PIE benchmarks include reactor and sample specific modelling assumptions, thoroughly described in Appendix II. Afterwards, Section 4.3 provides the implementation of Sampler for the uncertainty propagations.

4.1. Implementation of Polaris on the decay heat benchmarks

The input data for the selected benchmarks, *e.g.*, SFA design and irradiation information, are described in Section 2. These data are converted into individual Polaris inputs for each benchmark. For each model, the following assumptions are applied:

1. The 2D model represents the assembly as a whole (the active section of the assembly) – *i.e.*, average enrichment (per rod), burnup, and operational history are axially average values.
2. The water density values of the Clab benchmarks are similar to the values reported in literature [27,28]. Seven SFAs are not reported in the mentioned references, being rebuilt. Four assemblies belong to the Barsebäck-1 reactor, and three belong to the Oskarshamn-2 reactor. The description of the Barsebäck-1 assemblies provided in Reference [12] do not include the moderator density or void fraction. The water density was assumed to be the average water density for other SFAs irradiated in the same reactor. The description of the Oskarshamn-2 assemblies provided in Reference [12] include nodal values of the void fraction. Void fractions were averaged into assembly average values and interpolated into densities using the water and steam densities at the given reactor pressure.
3. The water density value for all the GE benchmarks is 0.4343 g/cm^3 , similar to the value provided in [27] (Table 4.10).
4. The irradiation histories are average cycle powers and operational variables (*i.e.*, cycle-wise averages are implemented).

5. The 2D axially symmetric models include reflective boundary conditions (radially) and exclude the neighboring assemblies.

These approximations (implementing 2D models and approximating the radially neighboring assemblies with boundary conditions) stem from the properties of the used version of the Polaris code (being a 2D code). The approximation of implementing cycle-wise irradiation data stem from the resolution of the available irradiation data. Particular SFAs have their irradiation data in a high resolution (including cycle variations), which necessitated using their cycle-wise averages such that they are consistently modelled with the other SFAs.

6. Modeling control rods was excluded due to absence of their design data.
7. Impurities in the fuel and structural material were implemented whenever data were available – *e.g.*, for the Cooper benchmarks.
8. The activation of the cladding and structural materials (*e.g.*, spacers) was considered. Spacers were included in the models as an additional thickness of the cladding (implementing the specific material for the spacers). The total mass of the spacers was assumed to be uniformly distributed over the active length of the SFA, conserving the moderator-to-fuel ratio in the model – the 2D model represent the whole SFA.
9. The default predictor-corrector method is implemented.
10. SFA quarter symmetry was considered only for symmetric PWR cases.
11. 18 SFAs from Clab were “rebuilt” (following the wording in Reference [12]), *i.e.*, fuel rods were removed at the end of life (EOL) or during cycle downtimes. The actual rebuild of the SFAs proceeds by removing fuel rods at the end of life or during cycle downtimes and replacing them with other non-active rods. The rebuilt SFAs were modelled similarly to the typical SFAs – *i.e.*, in a single depletion and decay simulation without rearrangement of the lattice layout. The decay heats of the rebuilt SFAs were calculated by considering decay heat from the non-replaced rods, *i.e.*, the decay heat per SFA excludes the rebuilt rods. The assumption of modelling the rebuilt SFAs in this method is that the decay heat per the non-replaced rods is not significantly different between two models where the rebuilt rod is a fuel or a Zr-homogenous rod. As an example, the difference in the decay heat per SFA of one of the rebuilt SFA, no. 5829 of the Ringhals reactor, is <0.2% of the calculated value, which is considered not significant. Further description of the modelling of the rebuilt SFAs is provided in Appendix I.

4.2. Implementation of Polaris on the PIE benchmarks

The PIE data are more heterogeneous than the decay heat data, including various fuel designs and irradiation conditions, necessitating specific modelling assumptions. Detailed descriptions of the PIEs and modelling assumptions are provided in Appendix II. Herein this section, only generic

descriptions of the implementation of Polaris and generic modelling assumptions are provided. Also, the descriptions are provided whenever they are different from the Polaris implementation for the decay heat benchmarks. The following assumptions are applicable to the PIE samples:

1. The Polaris models represent a 2D horizontal slice of the lattice at the location of the PIE sample. The lattice design and the irradiation history are assumed or interpolated at the location of the sample. A few measurements are reported for the whole assemblies or fuel rods (5 SFAs of the Obrigheim-1 reactor and 5 full-length fuel rods of Turkey Point-3 reactor). The latter models implement the assembly average enrichment and operational history.
2. The irradiation histories are implemented as provided in SFCOMPO or in the original references of the PIE samples. Whenever average cycle powers and operational variables are provided, the irradiation histories are discretized to approximately the resolution of a maximum of 2 GWd/tHMi.
3. Modeling the control rods were implemented whenever the PIE samples are reported to have active control rod movements neighboring their host assemblies. 33 Samples were modeled along with active control rod movements, representing 11% of the PIE data.
4. Assemblies having their fuel rods relocated during their irradiation are excluded from the PIE data. These include benchmarks of Gösgen-1 and Vandellós-2.
5. The BWRs are modelled as a whole (no symmetries are applicable to BWR models in the current version of Polaris). Only the south-east quarter is modelled in PWRs when the assemblies have quarter symmetries. PWRs lacking symmetry, either due to the layout of the guide types or the presence of a cruciform-like control rod, are modelled as a whole.
6. Fuel temperatures are not provided for all of the analyzed PIEs. In case the fuel temperature is not provided, it is assumed to be 900 K.

Reference [64] presents a sensitivity study conducted on fuel samples from Trino Vercellese reactor, showing that the concentrations of the currently analyzed isotopes have low sensitivity to the fuel temperature. For a perturbation of 10% of the fuel temperature (in Kelvin), the changes in the concentrations of Cs-137, U-235, and Pu-239 are: 0.0%, <0.3% and 1.0%, respectively. A similar observation is also noted in other literature studies such as Reference [65], indicating that the fuel temperature has little significance on the analyzed isotopes. Uncertainties in the concentrations of the analyzed isotopes are within 0.3% due to uncertainties in fuel temperatures.

Additionally, sensitivity analysis to the fuel temperature was performed on selected pin-cells (Table 22). The fuel temperatures were perturbed by $\pm 1\%$ in these pin-cell models, and the maximum change in the analyzed characteristics are (in the analyzed six pin-cells):

- Decay heat: 0.02%
- Cs-137: <0.01%

- U-235: 0.09%
- Pu-239: 0.13%

Such sensitivity and uncertainty values would justify approximating the fuel temperature (herein this study) in the prescribed manner to allow inclusion of a larger number of samples. In total, fuel temperatures in 16 PIE samples of PWR origin were set equal to 900 K, and 113 for the BWRs (total PWR and BWR samples are 146 and 139, respectively). Indeed, most of the BWR PIEs lack their fuel temperature information.

Information about whether the fuel temperature is given or assumed is also recorded for each sample as a dummy variable in the ML models. Binary values are used; recording one for “given” fuel temperatures and zero for “assumed” fuel temperatures.

7. Gadolinium rods, $\text{UO}_2\text{-Gd}_2\text{O}_3$, are modelled as rings to capture the ring-wise, gradual depletion of the gadolinia with irradiation. Each rod is discretized into 10 rings and 8 radial sectors.
8. Side water gaps and water channels in BWRs contain water (*i.e.*, moderating water). Moderating water has the same temperature of the cooling water at the non-boiling section of the assembly and has the saturation temperature for the remaining upper section of the assembly in which the cooling water is in a boiling state.
9. Guide and instrument tubes in PWRs are filled with the same cooling water in-between the fuel rods.
10. The only part of the fuel assembly modelled with air is the gap between the fuel and the cladding.
11. For PWRs, whenever the moderator temperature is not provided in SFCOMPO or the references of the PIE samples, it is assumed to have a cosine shape along the active length of the SFA. The assumption is based on a simplification of the power profile in the active fuel section to follow a sinusoidal shape function, based on Reference [66]. The power density in the fuel would peak in the center of the axial length, and the moderator temperature peaks at the end of the active length. The following equation is used to obtain the moderator temperature as a function of the axial length from the bottom of the active fuel:

$$T_z = T_{in} + \frac{T_{out} - T_{in}}{2} \left(1 - \cos \frac{\pi z}{H} \right). \quad (4.1)$$

Using the water inlet and outlet temperatures (T_{in} and T_{out}), water temperatures (T_z) are obtained at the axial locations (z) of the sample.

12. For BWRs: whenever the temperature of the cooling water is not provided in SFCOMPO or the references of the PIE, it is set to the boiling temperature at the given reactor pressure. The density of the cooling water is the sum of two components: the water and steam at the location of the PIE sample.

13. A boron letdown curve is assumed for PIE samples having only their cycle average boron values. The boron concentration is assumed to decrease linearly achieving the given cycle-wise average values.

4.3. Implementation of Sampler for uncertainty analyses

Calculated uncertainties are obtained through stochastic propagation of the calculational model input uncertainties: SFA design and operational variables (DO) and nuclear data (ND). The latter are uncertainties in the fission yields (FY), cross-sections (XS) (also fission spectra, neutron yield (ν -bar), and scattering distributions), and decay data (DD). They arise from uncertainties in experimental nuclear data measurements, as well as uncertainties in the evaluation process itself, combining differential experimental information with nuclear physics theory to generate evaluated nuclear data like the ENDF/B-VII.1 library. These uncertainties are available in the SCALE code system (version 6.2.3), based primarily on ENDF/B-VII.1 nuclear data [49].

The DO uncertainties are not available for the majority of the analyzed benchmarks, neither the decay heat benchmarks nor the PIE samples. The DO uncertainties are implemented in the present study based on recommended literature values, which are reported in the “*Evaluation Guide for the Evaluated Spent Nuclear Fuel Assay Database (SFCOMPO)*” [56].

The DO variables are assumed to be normally distributed, and the implemented standard deviations (σ) of their distributions are listed in Table 7. The total mass of the SFA is assumed to be precise, *i.e.*, the SFA heavy mass has zero variance, and a full correlation between the total cross-sectional area of all fuel rods and the fuel density is implemented. Fuel densities are not correlated to irradiation parameters in the present study (*e.g.*, fuel temperatures and burnups). Fuel enrichments of all rods are assumed to be fully correlated. Fuel temperatures, water densities and temperatures, void fractions and the boron content in the water are the same throughout the lattice. In different cycles, these properties are assumed to be fully correlated. No information is available regarding the burnup uncertainties in the analyzed SFAs. The cycle-wise powers of the SFAs are assumed to be normally distributed with a standard deviation of 1.67%. The SFA cycle-wise average powers are assumed to be fully correlated between cycles. Finally, burnup uncertainties are assumed to originate from uncertainties in the cycle-wise average powers.

Additional correlations were established between water density and temperature for the PWRs, and between SFA power and fuel temperature in both PWRs and BWRs. The water temperatures in the PWRs, for example, are sampled from their distribution with a correlation of -1 with the perturbed water density. Similarly, the fuel temperatures are sampled from their distribution with a correlation of +1 with the perturbed SFA power.

Upper and lower limits were imposed on the distributions of the parameters, limiting unphysical values, such as an upper water density value in the BWR models corresponding to the non-boiling water density.

Table 7. Uncertainties in design and operational parameters of the analyzed benchmarks, based on [56]. The reference values in [56] are uncertainties and tolerances, whereas the applied uncertainties in this study are standard deviations (1σ).

Parameter ^I	Uncertainty/Tolerance [56]	1σ (this work)
Cladding/tube thickness	$\pm 40 - 50 \mu\text{m}$	$16.7 \mu\text{m}^*$
Cladding/tube diameter	$\pm 200 \mu\text{m}$ (PWR) / $\pm 300 \mu\text{m}$ (BWR)	$67 \mu\text{m} / 100 \mu\text{m}^*$
Fuel pellet density	$< 2\%$ the theoretical density	$0.67\%^*$
Fuel pellet diameter	$\pm 20 \mu\text{m}$	"
Enrichment (U-235 wt%)	$\pm 0.05\%$	$0.0167\%^*$
SFA powers	-	1.67%
Water temp. (PWR only)	$\pm 2^\circ\text{C}$	2 K
Water density (PWR only)	$\pm 0.005 \text{ g/cm}^3$	0.005 g/cm^3
Void fraction (BWR only)	$\pm 6\%$	6%
Fuel temp.	$\pm 50^\circ\text{C}$	50 K
Boron content (PWR only)	$\pm 10 \text{ ppm}$	10 ppm

^I The parameters in reference [56] not included in this list are assumed to be precise.

^{II} Full correlation with fuel density.

* The reported uncertainties in reference [56] are tolerances, and it is assumed in the present study that a two-sided tolerance interval contains 99.7% of the observations, *i.e.*, the tolerance interval corresponds to $\pm 3\sigma$ of a normal distribution.

The burnup can be a significant variable impacting the resulting uncertainties of DO origin, and the accuracy of the burnup estimation depends on various factors, such as the reactor and core management codes [56]. Also, it can depend on the location in the core, *i.e.*, whether the assembly is located at the periphery of the core or at its center. For this reason, cases are analyzed in addition to those listed in Table 7. For these cases, the assumptions of the burnup and power uncertainties are assessed for their relevance to the resulting uncertainties. The following cases are analyzed:

- 1- Case 1: the SDs of all variables are increased by 50%.
- 2- Case 2: all variables are uniformly distributed. The variance of each distribution for each variable is set equal to the variance of the normal distribution of the variable in the reference case. For example, the burnup value is uniformly distributed between 0.971 and 1.029 of its nominal value, instead of normal distribution with a σ of 1.67%.
- 3- Case 3: the burnup uncertainty is considered, and all other variables are assumed precise.
- 4- Cases 4 and 5: the uncertainty in the cycle-wise powers depends on the burnup, *i.e.*, instead of a fixed σ of 1.67% in the nominal case, the variance of the cycle-wise power depends on the current burnup value. Assemblies are relocated to different regions of the core in different irradiation cycles and, as noted in reference [56], uncertainties in powers and burnups could be larger in peripheral locations of the core. In-out, out-in, and in-out-in (along with other patterns [67]) are fuel-loading strategies that allocate the assemblies in the core based on their reactivities and burnup; this can result in assemblies

having uncertainties in their powers, depending on their current location in the core and their current burnup value.

Two cases are considered: the first case has zero variance in the SFA power at BOL (beginning of life), and the variance in the cycle-wise powers increases linearly with burnup up to discharge. The second case has a maximum variance in the SFA power at BOL, and the variance in the cycle-wise powers decreases linearly with burnup down to zero variance at discharge. In both cases, the SFA discharge burnup has the same σ of 1.67%. For example, for the first case of zero variance in the power at BOL, the σ of the cycle-wise powers are 0.2% and 3.2% for the first and the last irradiation cycles, respectively.

- 5- Case 6: the cycle-wise powers are sampled from their distributions independently from each other, *i.e.*, correlations are not enforced. The discharge burnup does not necessarily have the nominal σ of 1.67%.

4.4. Validation and uncertainty measures

Common measures are being used in validating M&S tools and data in literature [27,28,68], such as the bias between the calculated and the measured values ($B = C - E$), the normalized bias ($B_n = C - E / M_{HM}$), and their ratio (C/E). The present study focusses on using the bias (B) and the ratio (C/E) in representing the validation results.

Uncertainties of the calculated isotopic concentrations are direct outputs of Sampler, along with perturbation-wise calculated isotopic concentrations. Uncertainties of ND origin and those of SFA DO origin are propagated in separate runs. Calculated uncertainties from both separate calculations are combined together to obtain total calculated uncertainties, summed in quadrature. The uncertainties from ND origin are assumed to be uncorrelated with the ones from DO origin, and the total uncertainty for nuclide j is calculated as:

$$\sigma_{C,j}^2 \cong \sigma_{ND,j}^2 + \sigma_{DO,j}^2. \quad (4.2)$$

The total calculated and experimentally measured values are assumed to be uncorrelated with each other. Uncertainty of the bias B of benchmark i is calculated from calculated and measurement uncertainties as:

$$\sigma_{B,i}^2 = \sigma_{C,E,i}^2 \cong \sigma_{C,i}^2 + \sigma_{E,i}^2. \quad (4.3)$$

Uncertainties in the DO variables and their correlations are discussed in Section 4.3. The uncertainties of ND origin (XS, FY and DD) are propagated together in the same runs.

The perturbation-wise calculated values allow obtaining correlations between them, and between the calculated values and the perturbed DO variables. The correlations between the calculated values of the benchmarks result from using the same perturbed ND or perturbation factors for the DO variables in numerous runs. The Pearson correlation between the calculated values of benchmarks i and j is calculated as:

$$\rho_{ij} = \frac{1}{N-1} \sum_{k=1}^N \frac{(C_k^i - \bar{C}_i)(C_k^j - \bar{C}_j)}{\sigma_i \sigma_j}, \quad (4.4)$$

where C_k^i and C_k^j are the calculated values in benchmarks i and j in the k^{th} perturbation. The \bar{C}_i and \bar{C}_j are the average values of the calculated quantities in benchmarks i and j .

Polaris models are run N times using various perturbed inputs, *e.g.*, perturbed ND and DO variables, where N is 400 for the decay heat benchmarks and 335 for the PIE samples. The latter values are selected considering computational requirements and also to ensure that the results are sufficiently precise, *i.e.*, they have low standard errors (SE). The SE of σ and correlation coefficients are calculated as [69]:

$$SE(\sigma_i) = \frac{\sigma_i}{\sqrt{2N}}, SE(\rho_{ij}) = \frac{1 - \rho_{ij}^2}{\sqrt{N-1}}. \quad (4.5)$$

The SE of σ and correlation coefficients depend on their values. *E.g.*, the calculations with assembly F32 lead to a value of 2σ of 49.0 W for its total decay heat due to uncertainties in ND. The SE value of the latter uncertainty will be 1.7 W (3.5% of the calculated uncertainty value). The total decay heat of the same assembly shows correlations of 0.67 and 0.98 with the total decay heats of assemblies 5A3 and 0E2, respectively. The latter correlations will have SE values of 2.7% and 0.2%, respectively.

Chapter 5 Hypothesis Testing on the Bias

Hypothesis testing can be used to analyze whether the observed mean bias between the calculations and the measurements is significant or not. In particular, the following null and alternative hypothesis can be tested:

$$H_0: C - E = 0, \quad (5.1)$$

$$H_a: C - E \neq 0. \quad (5.2)$$

In other words, the alternative hypothesis is that the calculations and measurements are significantly different: $H_a: C \neq E$. Different statistical tests can be used, broadly categorized into parametric and nonparametric tests. In the present study, statistical tests are conducted at a threshold p -value of 0.05.

5.1 Non-parametric tests

Nonparametric tests can assess the significance of differences between the calculations and measurements without assumptions on their distributions, *e.g.*, they do not rely on normality assumptions of the data [70]. Once the distributions of the biases under the null hypothesis are obtained, statistical tests are conducted (*e.g.*, at a significance level of 0.05). Under the assumption that the null is true, the null distribution of the chosen test statistic is generated, and the observed bias is compared to the null distribution to evaluate the probability of observing equal or more extreme values [70]. The null hypothesis in this case implies that the differences between the calculations and the measurements are random differences, *i.e.*, due to chance, and the alternative hypothesis implies systematic, or statistically significant differences.

Permutations and bootstrapping are randomization tests [69], used to generate the null distributions of the biases. In permutations, under the null hypothesis, the calculations and the measurements are equal, and calculated values are reassigned as measured values in numerous permutations (inter-shuffled in all possible rearrangements). Permutation is possible assuming “paired data” — *i.e.*, the calculations and the corresponding measurements are conducted on the same unit, individual benchmarks. Sampling in permutation tests is performed without replacement. Random sampling is implemented using Monte Carlo, considering the extensive number of all possible permutations of the present data, increasing the computational requirements to calculate the exact permutation distribution. The average difference between the permuted calculations and measurements is calculated in each permutation – namely the permutation bias. The permutation distributions are used to calculate p -values of the actually observed mean bias, and therefore its significance, by calculating the biases that are equal or

more extreme than the observed mean bias. The null hypothesis is rejected, and the alternative is accepted if less than 5% of the observations are equal or more extreme than the observed mean bias in a two-sided test setting.

Alternatively, in bootstrapping, the distributions of the mean biases are approximated by simulating from the present datasets. Unlike the permutations, bootstrap sampling is with replacement, *i.e.*, numerous sampled datasets of biases are obtained by random sampling from the original dataset (both of equal sizes) with replacements. Once obtained, inference about the observed biases is performed from the bootstrap distributions. The bootstrap distributions are centered around the observed mean bias, and the alternative is tested by constructing 95% normal bootstrap confidence intervals on the bootstrap distribution of the bias. The null hypothesis is rejected, and the alternative is accepted if the 95% bootstrap confidence interval does not contain a mean bias of zero.

5.2 Parametric z-test

The parametric tests rely on assumptions regarding the underlying distribution from which the data are drawn. The bias is assumed to follow a normal distribution that is parameterized by the variance of the calculations only (or along with the variance of the measurements):

$$C - E \sim N(0, \sigma). \quad (5.3)$$

The z-test is an example of a parametric test. It is used to test the hypothesis regarding the significance of the observed bias, given uncertainty. In the present study, two cases of uncertainties are considered: (1) uncertainties in the calculated values, and (2) combined uncertainties from both the calculated and the measured values. The former case is the default for all of the analyzed characteristics, and the latter case will be additionally analyzed for the decay heat data.

The calculated and measured values are converted into z-scores [69,71]. The z-score of benchmark m is calculated as:

$$z_m = \frac{C_m - E_m}{\sigma}. \quad (5.4)$$

For multiple benchmarks, the z-scores are correlated to some extent, due to correlations between the calculations and between the measurements, resulting in correlations between the biases. The correlations between these scores affects the applied hypothesis testing, and they are combined into a single figure using a combined weighted z-transform [72,73]. The following transformation is implemented to obtain the combined z-score:

$$\bar{z} = \frac{\sum_{m=1}^M w_m z_m}{\sqrt{\sum_{m=1}^M w_m^2 + 2 \sum_{m < n}^M w_m w_n \rho_{mn}}}, \quad (5.5)$$

where w_m is a weight for z_m , and ρ_{mn} is the correlation between z_m and z_n . The m and n are different benchmarks, and the summation in Equation 5.5 is over every multiple combination of

benchmarks in the analyzed data. Equal weights are assigned to the benchmarks, and other weights are investigated in Chapter 10. The correlations between the z-scores could be obtained from the covariances between the biases and the standard deviations of the combined measurements and calculations (σ) as following:

$$\rho_{mn} = \frac{\text{cov}(B_m, B_n)}{\sigma^m \sigma^n} = \frac{\text{cov}(E_m, E_n) + \text{cov}(C_m, C_n)}{\sigma^m \sigma^n}. \quad (5.6)$$

The measurements and calculations are assumed independent from each other. The covariance between the biases is pinned down to the sum of two covariance terms: the covariance between the calculations and the covariance between the measurements. The latter is not available for the analyzed measurements, and only the covariance between the calculations will be evaluated given the applied perturbations. Equation 5.6 will be approximated based on the calculations solely, such that:

$$\rho_{mn} \cong \frac{\text{cov}(C_m, C_n)}{\sigma_c^m \sigma_c^n}. \quad (5.7)$$

The covariance between the biases is assumed to result only from the covariance between the calculations. Incorporation of experimental uncertainties and different levels of correlations between the measurements allows to analyze their effect on the hypothesis testing, investigated in Chapter 10.

Chapter 6 Machine Learning Schemes

Machine learning and statistical inference are branches of science addressing predictions and inference using data. They both intersect with the data science field; however, data science is usually used to describe many other paradigms such as artificial intelligence and big data. Within the data-driven methods, a different emphasis is placed upon inference and prediction, whereas machine learning emphasizes more on predictions [74]. A way to interpret the difference is that inference focuses on using data and on finding out how the output is generated as a function of such data. Whereas for prediction, the interest is on using the existing data to derive models that accurately estimate the output for a new observation.

6.1 Description of the chapter

This chapter is structured as following: Section 6.2 provides a general description of the aims of applying ML on the current data. Section 6.3 introduces the distinctions between two cultures in ML: placing emphasis on predictive performance and placing emphasis on interpretability. Section 6.4 to 6.6 provide descriptions of statistics used to assess the predictive performance of models and choosing such models in a conservative manner. Section 6.7 describes the ML models applied in the present study, while Section 6.8 emphasizes on data resampling techniques. Sections 6.9 to 6.12 present the ML algorithms applied on two types of benchmark features: integral features and correlation matrices, along with outliers removal approach. Finally, section 6.13 presents the applied approach for extracting features from the benchmarks.

6.2 Application of predictive modelling of the bias

The generic problem in ML is that, for an observable variable Y , we assume that it depends on several variables $X = (X_1, X_2, \dots, X_3)$. The dependency of Y on X is then written as

$$Y = f(X) + \epsilon, \quad (6.1)$$

where, f is an arbitrary function of X ; X are independent variables and ϵ is a random error term, independent of X and has a mean zero. Y consists of two components: a systematic component $f(X)$ and a random component ϵ .

Predictive modelling involves solving Equation 6.1, given sets of data and possibly a hypothesis about the underlying model that generated these data. The exact function f that maps input variables X into the response Y is unknown. Additionally, there is an infinite number of possible forms of such function. Placing a hypothesis on this function can narrow down the search space.

The exact parameterization of the chosen function, *e.g.*, the slopes in linear regression, are driven from the data using appropriate optimization algorithms.

The variables X are also unknown. Features extraction is employed, enhanced by prior field-knowledge, to extract potentially informative variables (or features) from the data. Features selection follows to narrow down the features space. *I.e.*, features extraction refers to the process of obtaining many features of the data, such as burnup, obtained through sensitivity analysis in the present study. Whereas features selection refers to the process of selecting a few informative features from several extracted features, such as the spectral index in decay heat models, selected through recursive features elimination in the present study.

Lastly, a residual error remains, unexplained by the driven model. The error term measures the unexplained or the unpredictable part of Y by the model, which is also an expected error of using the model to derive new predictions.

In the present study, the dependent variable is the bias between calculations and measurements of SNF characteristics, *i.e.*, the aim is to solve the following equation

$$C - E = f(X) + \epsilon. \quad (6.2)$$

The paired X and $C - E$ are obtained from the validation and uncertainty analyses data. Solving Equation 6.2 will result in the part of the bias that could be explained using variables of the benchmarks, namely $f(X)$, along with the random component of the bias, the unexplained bias ϵ . All parts are unknown *a priori*.

The application of ML in the present study aims at pinning down variables of the calculations (set of X s) that can be informative about the difference between these calculations and measurements – *e.g.*, burnup, spectral index, and other variables. Additionally, ML functions (possible f s) that rely on “neighborhood” or “similarity” between benchmarks are analyzed for their predictive performance of the bias.

6.3 Prediction vs. inference

Different approaches exist in ML: either emphasizing prediction or inference. In the prediction case, given that the error term averages to zero, Y is being predicted as (based on [75]):

$$\hat{Y} = \hat{f}(X), \quad (6.3)$$

where \hat{Y} is the prediction of Y , and \hat{f} is an approximate form, an estimate of f which is the unknown function mapping X into Y . The motivation is to obtain an \hat{f} that provides accurate and precise predictions of Y . There are no bounds on the complexity of \hat{f} , and even black-box type functions (such as deep neural networks [76]) can be used to obtain the predictions.

Equation 6.3 approximates Equation 6.1, and the prediction error of using Equation 6.3 is two parts: a reducible error and an irreducible error. The reducible error results from using \hat{f} which approximates f . It can be minimized using techniques to derive functions \hat{f} approximating well

the unknown target function f . The irreducible error results from that Y depends also on ϵ , which is random and unexplained by X . Unmeasured variables, hidden variables, not contained in X or errors of random nature (*e.g.*, from physical measurements) can result in ϵ . The irreducible error represents an upper bound on the prediction's accuracy, which is unknown. However, the unexplained part of the response Y should always be calculated for the used set of explanatory variables X and the approximate function \hat{f} used in making predictions. In the present study, the prediction error is specific to the calculational tools and the validation data (*e.g.*, to Polaris and the SCALE nuclear data, and the validation benchmarks). Also, the error is specific to the applied ML models and algorithms – *e.g.*, the procedure of selecting the informative model features.

The total prediction error can be written as:

$$Error^2 = Bias^2 + Variance. \quad (6.4)$$

The bias results from the reducible error, and the variance results from the irreducible error. The total error is quantifiable, however, the breakdown into its two components is usually unknown.

The other approach in ML is to understand which X s affect Y , and how X s affect Y . In this case, inference is the main objective; data are used to obtain a small subset of X used in the explanation of the target response Y . Smaller subsets of features are preferred in this case, providing more “explainable” association between the X s and Y . Interpretable (usually simple) functions \hat{f} help in understanding the relationship between X and Y . Less features and simpler models are preferred even if they might result in less accurate predictions. On the contrary, the ML models of black-box nature are not preferred for being more difficult to interpret or explain.

The described options place the ML model between models that are highly interpretable, and those that are highly predictive. For example, the choice of the models from the types of available ML models, as shown in Figure 8, favors either higher interpretability or higher predictive performance. Models that have both characteristics are the ultimate quest in the ML paradigm. Historically, readily interpretable models such as the linear model existed first, and the need for higher predictive performance motivated the introduction of more complex and highly predictive models such as neural networks. However, models can be complex enough such that any meaningful interpretation are not foreseen, and such models are termed “*black-box*” models.

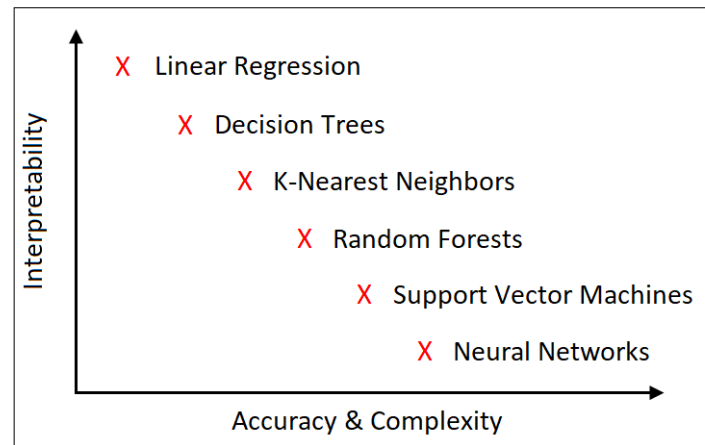


Figure 8: A subjective view of the placement of various ML model types between interpretability and predictive performance.

Figure 8 represents a subjective view of the tradeoff between model interpretability and model accuracy and complexity. Other representations can be found in literature, such as in Reference [75]. Additionally, within each model type, the complexity is also different based on the number of variables. Models relying on a large number of variables are seen as more complex, and less interpretable, than those containing fewer number of variables. The interplay between model complexity and accuracy is affected by the tradeoff between error components, namely the bias and the variance components. The former is usually high for relatively simpler models, indicating that the models have low flexibility to fit the data, *i.e.*, they suffer from under-fitting. For relatively complex models, flexibility is higher, and their associated variance is higher as well. Models with higher variance indicate that they fit to some degrees to the random part of the error (the noise), *i.e.*, they suffer from over-fitting. The trade-off between both the bias and the variance, as shown in Figure 9, results in optimally performing models, usually obtained using optimization algorithms.

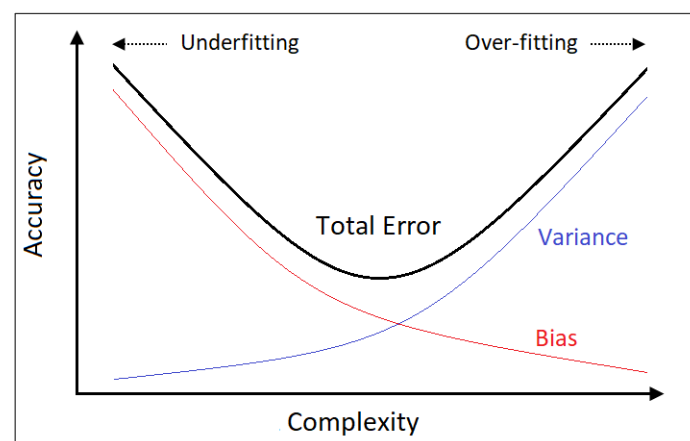


Figure 9: Trade-off between the bias and variance of a machine learning model. Simpler models have higher bias, which indicates under-fitting. Complex models have higher variance, which indicates over-fitting. Both are model defects increasing the total error of the model.

6.4 Predictive performance evaluation

The following measures are commonly used in literature to evaluate the predictive performance of a particular ML model, such as mean-square-error (*MSE*) and mean-average-error (*MAE*):

$$MSE = \frac{1}{n} \sum_{i=1}^n (y_i - \hat{y}_i)^2, \quad (6.5)$$

$$MAE = \frac{1}{n} \sum_{i=1}^n |y_i - \hat{y}_i|, \quad (6.6)$$

where i denotes the i th observation, and n is the total number of observations.

The closer the model predictions to the original observations, the lower the error measures *MSE* and *MAE*. *MAE* has the same unit as y . The square root of *MSE*, the root-mean-square-error (*RMSE*), also has the same unit as y . The main difference between them is that the *MAE* considers all observations to have similar weights, and their individual error contributes equally to the total error. On the contrary, the *RMSE*, considering squaring the errors before their addition, will place more weights to observations having large errors. In the latter case, outliers could significantly penalize the models. If the data are justifiably containing outliers, choosing *MAE* will reduce their influence on the overall procedure of model selection.

6.5 Model validation

Model validation refers to techniques of assessing the predictive performance of the models, and how well the model predicted values simulate the original observations. In addition to the error indices discussed in Section 6.4, other measures are employed in the present study to thoroughly analyze the predictive performance of the chosen models.

Scatter plots of the model predictions vs. true observations (or vice versa) provide qualitative means of assessing the model predictive performance and helps to identify possible erroneous computations [77]. They are the first mean of conducting a qualitative and comparative data description and analysis. Then, summary univariate measures are employed, such as aggregate statistical measures. Models could be validated by quantitatively measuring the association between the predicted and the observed bias, based on literature recommendations [77]. Several indices are employed for such purpose:

1. Two-sample Kolmogorov-Smirnov (KS) test [78],
2. Index of agreement (d),
3. The slope and the intercept of an ordinary least-squares regression between the predicted and the observed bias,
4. Systematic and unsystematic components of the *RMSE* ($RMSE_s$ and $RMSE_u$), where $RMSE = RMSE_s^2 + RMSE_u^2$.

In the non-parametric two-sample Kolmogorov-Smirnov (KS) test [78], the association between the predicted and the observed biases is quantified through statistical testing, *e.g.*, testing whether they originate from the same distribution. It does not rely on assumptions regarding the underlying distributions generating both samples and it tests their similarities by comparing their empirical cumulative distribution functions (ECDFs). Specifically, the KS test compares the maximum distance between the ECDFs of the two samples, to a distribution of distances between ECDFs generated under the null hypothesis that these samples originate from the same distribution. An *a priori* significance level needs to be defined. There is no objective reason for a choice of a significance level, and the results of the present study will be presented often at a significance level of 0.05.

The index of agreement (d or IOA) is also used to measure how well the model predictions follow the original observations, or the accuracy the predicted bias has estimated the observed one. It was originally proposed by Willmott [77], and is recommended over common correlation based metrics. It varies between 0 and 1, whereas 0 indicates complete lack of agreement and 1 indicates perfect agreement. The index of agreement is calculated as

$$d = 1 - \frac{\sum_{i=1}^n (y_i - \hat{y}_i)^2}{\sum_{i=1}^n (|y_i| + |\hat{y}_i|)^2}. \quad (6.7)$$

Following this third measure [77,79], the observed bias is regressed onto the predicted one, since this form of regression will be more beneficial in future applications of the models. The developed ML models would allow obtaining an estimate of the bias (a prediction), and it is beneficial to use a bias prediction to obtain other estimates of the observed bias along with a chosen prediction interval. This measure also allows a qualitative assessment of the model.

Finally, model predictions are not error-free, and the *RMSE* provides a measure of the errors produced from the models. Its systematic and random components are beneficial in the assessment of the final models, and whether they suffer from large systematic errors.

6.6 The law of parsimony: one-standard-error rule

Test here.

Models are compared to each other to optimize the described performance measures. For instance, models and features space could be searched for models that minimize the *MAE* (*e.g.*, finding the minimum in Figure 9). The one-standard-error (OSE) rule can be additionally used in the model selection process, allowing to deliberately obtain simpler models. The OSE is an application of the Law of Parsimony, also known as the Occam's Razor. The chosen models will be more interpretable, with less predictive performance – hence more conservative. The application of the OSE rule in ML is well described in literature [75,80–82].

The *MAE* of different models is calculated along with the standard errors (SE). The chosen model is not the model with the minimum *MAE*, rather, it is a model that has its validation error within an error margin (*e.g.*, 1 SE) of the model with the minimum *MAE*, located to the left side

in Figure 9. The error margin of the validation error of the best performing model is used to allocate an interval containing the errors of other models that are more or less equally good to the best performing model. Selecting models following this rule favors simpler and more interpretable models. Also, following this rule will be at the expense of some loss of the predictive performance (*e.g.*, higher *MAE*). The loss in the predictive performance is still acceptable, given the gained interpretability.

In the present study, the application of the OSE rule is in selecting between models that differ in the number of their features, as presented in Figure 10. First, the optimum subset of features is chosen based on the model performance on validation sections of the data, based on the minimum *MAE*. Then, a model is chosen such that it has fewer features, and its predictive performance is within 1 SE of the optimum model having the minimum *MAE*.

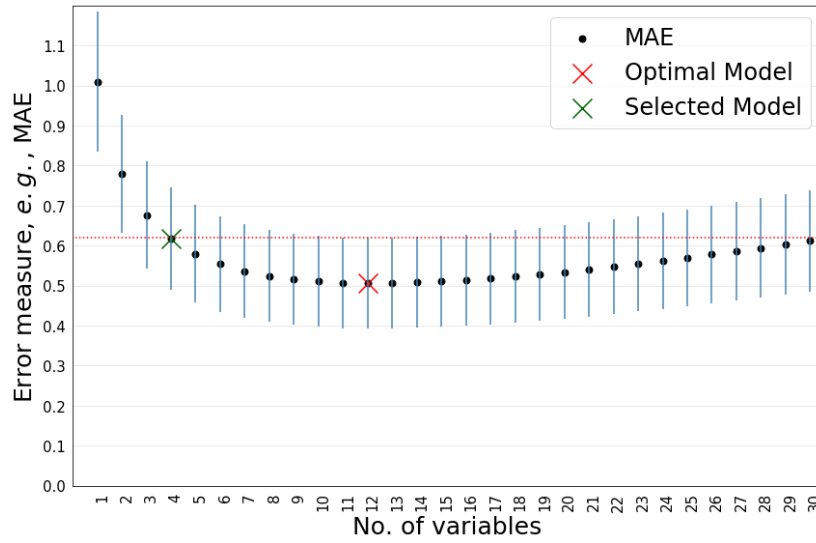


Figure 10: Application of the OSE rule. The optimal model contains 12 variables. A simpler model is chosen following the OSE rule, containing lower number of variables (4 variables).

6.7 Machine learning models

Two broad classifications can be assigned to learning from data: supervised and unsupervised learning (SL and USL). In SL each data point has:

1. a label: $y_i \in Y$.
2. a vector of features of length m : $x_i = (x_1, x_2, \dots, x_m) \in X = (X_1, X_2, \dots, X_m)$.

Both X and Y can be continuous or discrete. The aim in SL is to estimate Y using one or more of the X s. ML models are fit to the data, such that the response is predicted accurately (emphasizing prediction). Also, fitting the data allows understanding which features contain information about Y and the characteristics of the relationship between X and Y (emphasizing inference).

In USL, the data points do not have a label, only a vector of features. Model fitting is not possible since no response is available to supervise the learning process. The aim in USL is to use the data to derive information about relationships between the variables and structures of the

data [75]. In the present study, the learning is supervised, proceeding from observations consisting of features of the benchmarks and the target response, the bias.

In the following sections, ML models applied in the present study are described. The considered models are linear, weighted k-nearest neighbors, and random forests [75,82], which are widely used in literature. These are relatively simple ML models, having the advantage that the final models are more interpretable than other “*black-box*” type of models. Simple and interpretable models can be more useful in critical applications related to SNF characterization than complex models – even that the latter can have better predictive performance.

6.2.1. Linear models

The linear model (LM) is historically one of first and mostly used models. It is analyzed in the present study given its application in the validation of CSA [41]. Also, the LM is the first term approximation of a function f in its neighborhood, which may work reasonably well in approximating a complex target function. The LM implies an assumption that the response is linearly dependent on the features, which can be written as

$$Y = \beta_0 + \sum_{j=1}^p \beta_j X_j. \quad (6.8)$$

The term β_0 is an intercept, and $\beta_1, \beta_2, \dots, \beta_p$ are coefficients associated with each predictor. The value p is the number of predictors or features of the data. Introducing a constant predictor of value 1 allows writing the above expressions as an inner product (a vector form):

$$Y = \sum_{j=0}^p \beta_j X_j = X^T \beta. \quad (6.9)$$

The LM is fitted to the data to obtain the coefficients β , commonly using least-squares regression, *i.e.*, minimizing the residual sum of squares (RSS).

The LM is applied separately on learning from features of the benchmarks and on learning from their correlation. In the former, a linear relation is assumed between the bias of the benchmarks and one or more of the features of the benchmarks. The regression follows Equation 6.8, whereas Y is the bias of the benchmarks, X is one or more features of the benchmarks. In the second learning setting, a linear relation is assumed between the bias of the benchmarks and their correlation. A major difference between this learning setting and the former, is that the final models based on correlations between the benchmarks will always be used for predictions at $\rho = 1$. The LM regression onto the correlation between benchmarks is shown in Figure 11, for the application on CSA. The C/E of the benchmarks is regressed on the correlation; however, predictions are only meaningful at unit correlation. Similar to the application of bias prediction techniques in CSA based on the correlation between benchmarks, the unit correlation marks the target benchmark, or a neutronically identical benchmark, given the applied perturbations.

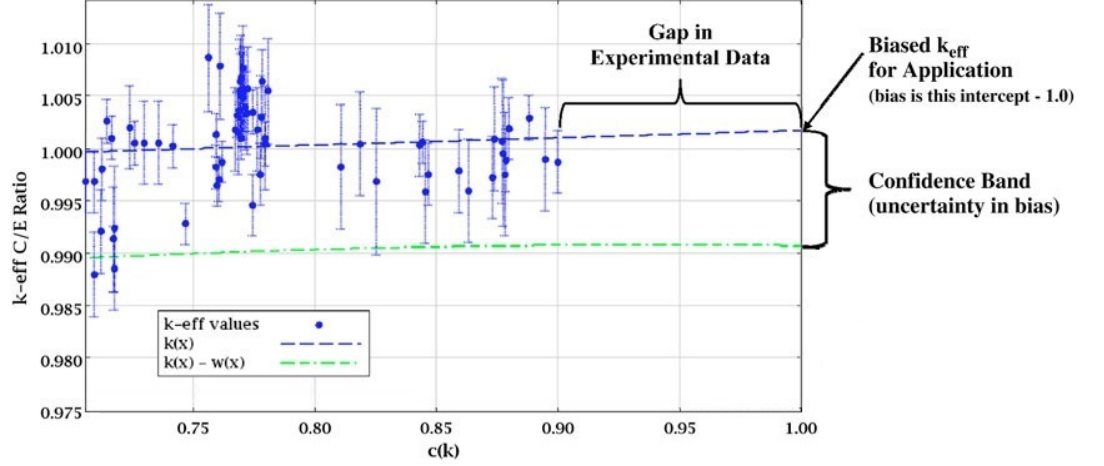


Figure 11: Linear model in CSA using the correlation between benchmarks (figure from Reference [83]). A target application is fully correlated with benchmarks at unit correlation.

The assumption of linearity can be a large simplification. Introducing flexibility in the LM can be achieved assuming that the model is valid in the range of highly similar benchmark. By introducing cutoffs on the correlations with the target benchmark, only those highly correlated, or highly similar, benchmarks to the target benchmark will contribute to the predictions from the LM. The model based on the correlation between benchmarks, applying correlation cutoffs, can be expressed as

$$B_{(\rho=1)} = \hat{Y}_{(\rho=1)} = \beta_0 + \hat{I}_{\rho > co}(\rho) \hat{\beta} \rho, \quad (6.10)$$

where \hat{I} is an indicator function, equal to 1 above a correlation cutoff (co), and zero otherwise:

$$\hat{I}_{\rho > co} = \begin{cases} 1 & \text{if } \rho > co \\ 0 & \text{if } \rho < co. \end{cases} \quad (6.11)$$

6.2.2. The weighted k -nearest neighbors (KKNN)

The nearest-neighbor method (KNN) is common in ML, which is a non-parametric method. Unlike the LM, no assumptions are made in the KNN method about the underlying function generating the data. Predictions are made using observations close in their input space to the target data point. The response of the data points in the neighborhood of the target data point are averaged such that

$$\hat{Y}(x) = \frac{1}{K} \sum_{k=1}^K y_k. \quad (6.12)$$

The prediction is at x , and K is a number of data points closest to x . Closeness could be measured using distances from the neighboring benchmarks to x , such as the Euclidean distance (squared difference) and the Manhattan distance (absolute difference). Equation 6.12 equally weights the data points in the neighborhood of x , *i.e.*, localized method. The weighted k -nearest neighbors method (KKNN) is also a weighted neighborhood scheme similar to the KNN method. However, the neighboring observations are weighted, usually using their closeness to x . The predictions using the KKNN model can be obtained as following

$$\hat{Y}(x) = \sum_{k=1}^K w_k y_k. \quad (6.13)$$

Differences between the KNN and the KKNn are considered minor, and only the KKNn results will be analyzed in the present study. The localization in the KKNn model is achieved by using kernels, and the weights can resemble a Gaussian kernel. The weights increase the importance of an observation on the prediction of the target observation the smaller the distance between them. Gaussian weights are the focus of the present study, calculated as

$$w_k = C e^{-\frac{(x_k - x)^2}{2\sigma^2}}. \quad (6.14)$$

The weights are required to be normalized, *i.e.*, $\sum_{k=1}^K w_k = 1$. Also, the weight of a benchmark depends on its Euclidean distance to the target benchmark, and the variance of the Gaussian density function. The model is explained in Figure 12.

The bias prediction based on the correlation between benchmarks proceeds by averaging the bias of the benchmarks with highest correlations (highest similarity) to the target benchmark. Averaging in KKNn is obtained using Gaussian weights, that depend on the value of correlation between each benchmark and the target benchmark. The predicted bias at unit correlation is obtained as following

$$B_{(\rho=1)} = \sum_{k=1}^K w_k B_k. \quad (6.15)$$

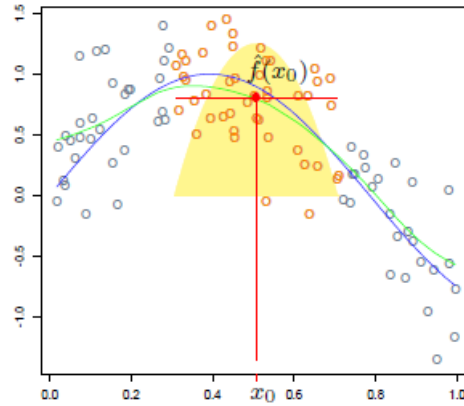


Figure 12: KKNn model using Gaussian weights. The red points are used for predictions at x_0 , and the yellow area is the scale of the weights assigned to these points (figure from Reference [82]). The blue line is the underlying model generating the data, and the green line is the KKNn model prediction.

6.2.3. Decision tree and random forest

To obtain a tree, the input space is recursively partitioned (or split) in a top-down approach. Starting from the initial data, a predictor and a cutpoint are selected such that the *RSS* is minimized. The cutpoint splits the input space into two regions. The predicted value of the response in each region of the predictor space is the average response value in each region. The process is repeated, selecting a predictor and a cutpoint minimizing the *RSS*. However, not all the space is split, rather, one of the previously created regions from the upstream splitting. The

process is repeated until a criterion is met, *e.g.*, attaining a maximum number of splits or a maximum tree depth. An example of a tree on a 2-dimensional predictor space is presented in Figure 13.

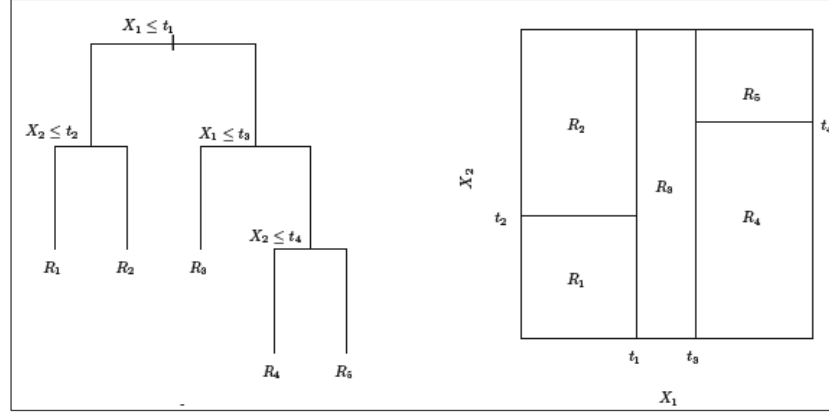


Figure 13: A tree build on a 2D predictor space (left). Making predictions of the response using the tree proceeds by averaging the response of the observations located in the same terminal node (R_1, R_2, \dots, R_5). The terminal nodes are intervals on the predictor space (right) (figure from Reference [75]).

Predicting the response of an observation proceeds by averaging the response values of the observations located in the same terminal node, *i.e.*, performing localized regression in each leaf. A leaf (or a terminal node) is an interval on one or several model features, *e.g.*, a burnup interval, where the target bias is approximated to have a constant value. Predicting the response of x located in a terminal node R , which contains K observations, proceeds as following

$$\hat{Y}(x) = \frac{1}{K} \sum_{k=1}^K y_k \cdot I_{X \in R}(X). \quad (6.16)$$

Equation 6.16 shows that the prediction of a target observation depends on the observations located in its neighborhood, *i.e.*, a localized method. X are features that are informative, *i.e.*, they define the neighborhood of the observation. However, the structure of the neighborhood in trees (and later on random forest) differs from its structure on other neighborhood-based schemes such as KNN and KNNN. Trees are some of the most interpretable ML models, however they suffer from low predictive performance and high variance of their predictions [75].

The random forest (RF) is also a weighted neighborhood scheme [84], *i.e.*, a localized regression model. The RF is built using multiple trees, *i.e.*, it is an ensemble model which outperform single trees at the expense of some loss of interpretability. Averaging observations reduces the variance, and in RF, these observations are averaged from different trees. Multiple training datasets are usually bootstrapped from the original dataset, creating S bootstrap samples. The predictions are averaged from the predictions of S trees regressed on the bootstrap samples such that

$$\hat{Y}(x) = \frac{1}{S} \sum_{s=1}^S y_s(x), \quad (6.17)$$

where y_s are predictions of individual trees, obtained using Equation 6.16. Bootstrapping the dataset results in approximately two-thirds of the original data in the bootstrap training data. The remaining one-third of the original data, referred to as the out-of-bag (OOB), is not used in training and can be readily used for testing the regressed tree. Usually, the test error of the tree is evaluated on the OOB observations, without the need to have separate test data. The RF improves the method further, by decorrelating the bootstrapped training data. In each split, a random sample of a subset of all predictors is considered, rather than considering all the predictors in each split. Typically, the number of the predictors is set to the square root of the number of all predictors. In each split, different random set of predictors are considered for a potential split, being a small fraction of the original number of predictors. Averaging the predictions from various trees could also use weights for each tree, whereas these weights are based on the OOB test errors. Trees that perform well in the OOB sample have higher weights in the final predictions of the RF.

In the learning setting based on the correlation between the benchmarks, the leaf containing the unit correlation is always used for prediction of the bias of the target benchmark (the target benchmark is always located at unit correlation). The predicted bias is therefore the average bias of highly similar benchmarks located within a correlation interval based on the target benchmark. The predicted bias of the target benchmark is then the weighted average of the biases predicted from numerous trees, from leaves of these trees containing the unit correlation (the leaves do not necessarily have the same interval width). The bias is predicted as following from N trees, based on the correlation between the benchmarks

$$B_{(\rho=1)} = \frac{1}{N} \sum_{n=1}^N w_n B_n \cdot I_{\rho \in [c_0, 1]}(\rho). \quad (6.18)$$

6.8 Resampling methods

The data are used to obtain the parameters of the models (*e.g.*, the slopes in the linear regression models) and to identify informative features. Both are not known *a priori*. The former process is referred to as training the model, and the latter is referred to as features selections. Both are parts of the overall ML process. However, once a learning process is followed on a model or several models, it is required to test the process and evaluate the predictive performance on data that have not been used in training or feature selection. The latter is indeed a must to avoid having overly optimistic test error of the developed ML models.

Testing the ML process can be performed by splitting the original data, keeping aside a test section, used later on to assess the predictive performance of the developed ML process. This is not an ideal procedure since it reduces the size of the data available for training and validation of the model. Additionally, data are usually expensive and limited, such that making efficient use of them is required. In this section, common methods of splitting the data for training, validation, and testing are discussed. The original dataset is usually split, or resampled, to yield two sections:

1. A training and a validation section: the application of this section is to select between models, or features, and to train models (*i.e.*, to tune their parameters).
2. A test section: the application of this section is to test the models and features selection procedure applied on the training and validation section.

Several methods of resampling could be employed to split, or resample, the data. Some of the common methods are shown in Figure 14, and described in the following [81]:

1. Repeated Holdout validation: the data are randomly split into a training and a validation section, and a test section. The holdout validation is repeated k times, using different random seeds, and the performance on the test sections is averaged over the different splits.
2. Bootstrapping: a training and validation section of the data, usually having the same size as the original dataset, is sampled with replacement. Approximately two-thirds of the original observations will be sampled in the training and validation sections. The remaining one-third of the data is used as a test section.
3. k -fold cross-validation: the data are split into k folds, *e.g.*, into 10 folds resulting in 10-fold cross-validation. Recursively, for each fold in the data, the fold is set aside for testing and the remaining folds are used for training and validation. A special case of k -fold cross-validation is the leave-one-out-cross-validations (LOOCV). In LOOCV, k is equal to the number of data points n . Recursively, each data point is set aside for testing, and training and validation is performed on $n - 1$ data points. A model that is trained on the training and validation section of the data is used to predict the set aside test observation. The process is repeated for every data point.

The LOOCV procedure is computationally expensive compared to other methods [81], being encouraged for small data sizes. Models are selected and fit n times, which can be computationally expensive specially if the data size is large and the fitting and model selection process is slow (*e.g.*, large number of predictors or wide grid search space). However, the procedure has low bias since the training is conducted on $n - 1$ data points (which is almost the same size of the original data). The procedure is also not affected by randomness in splitting or sampling the data, such as in k -fold cross validation and bootstrapping. The test result is the same if the process is repeated, allowing the results to be exactly reproduced. Also, the test error is approximately unbiased, however, it has high variance since it is driven from single observations.

6.9 Model selection

In the previous section, splitting the dataset into a training and validation section and a test section was introduced. The former split serves two purposes: selecting between models and training a selected model. For example, Equation 6.15 is used to make predictions using KNN method on the test section of the data. The number of the nearest neighbors to be used in making these predictions is not known *a priori*. Also, the neighborhood is not defined, *e.g.*, which features define the Euclidean distance between the observations. One of the widely used approaches is to further split the training and validation section into two sections: a training

section and a validation section. Such splitting follows any of the splitting and resampling techniques described in Section 6.8. Following this procedure, the data is recursively split into three sections (as shown in Figure 15):

1. a training section,
2. a validation section, and
3. a test section.

A common approach in ML is to search for the model optimal parameters, *e.g.*, the optimal number of nearest neighbors, based on the performance of models using these parameters on separate sections of the data – the validation sections. For a grid of k -values, models with different k nearest neighbors are fitted to the training data. The performance of each model is evaluated by calculating their prediction error on the validation section of the data. The model having the lowest validation error is then selected. The model is re-trained on the combined training and validation sections. The fitted model is used to predict the test data.

Additionally, features are also being selected on the training and validation data concurrently with the model selection. Various features selection techniques are available, including techniques that are well suited to LM such as shrinkage methods (*e.g.*, Ridge Regression and the Lasso) and dimensionality reduction methods (*e.g.*, Principal Component Analysis). Other methods can work with all types of models, such as resampling methods (*e.g.*, cross-validation and bootstrapping). Such procedures are commonly referred to as Subset Selection [75]. Models of different sizes, different numbers of features, are trained on the training data. The performance of models having different sizes is evaluated on the validation data, and the optimal model size is chosen to minimize the validation error.

The nested cross-validation (two nested LOOCV) is the main splitting procedure being followed in the present study. The selection of the procedure is motivated by the relatively small size of the current data, the availability of computational power, and to exclude randomness resulting from the randomness of splitting or resampling the data. An outer LOOCV loop is used to split the original data into a training and validation section, and a test section. An inner LOOCV loop is used to split the training and validation section into a training section and a validation section.

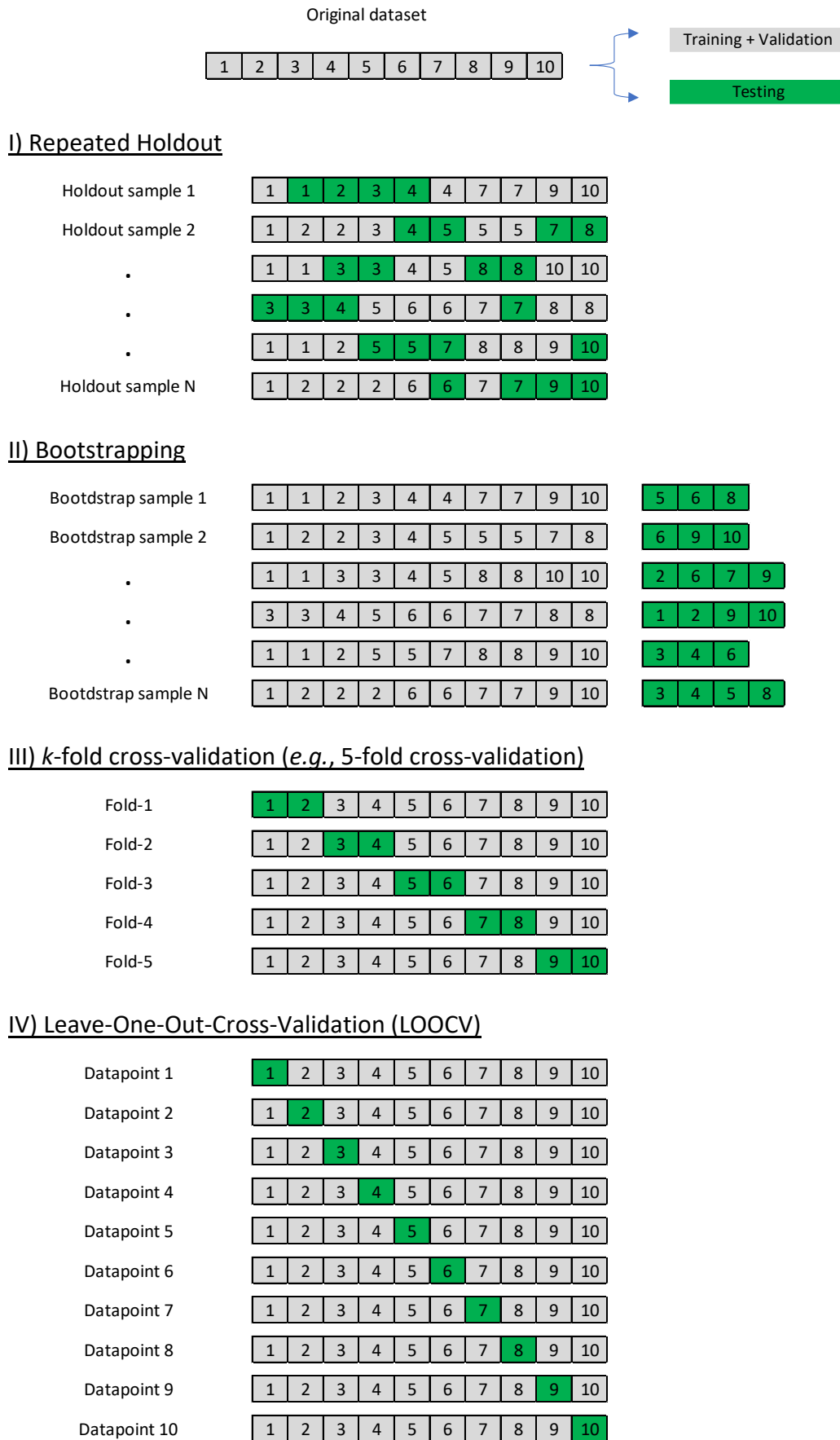


Figure 14: Illustration of common sampling techniques on a dataset of size 10. The splits of the holdout, bootstrapping and the 5-fold cross-validation are random.

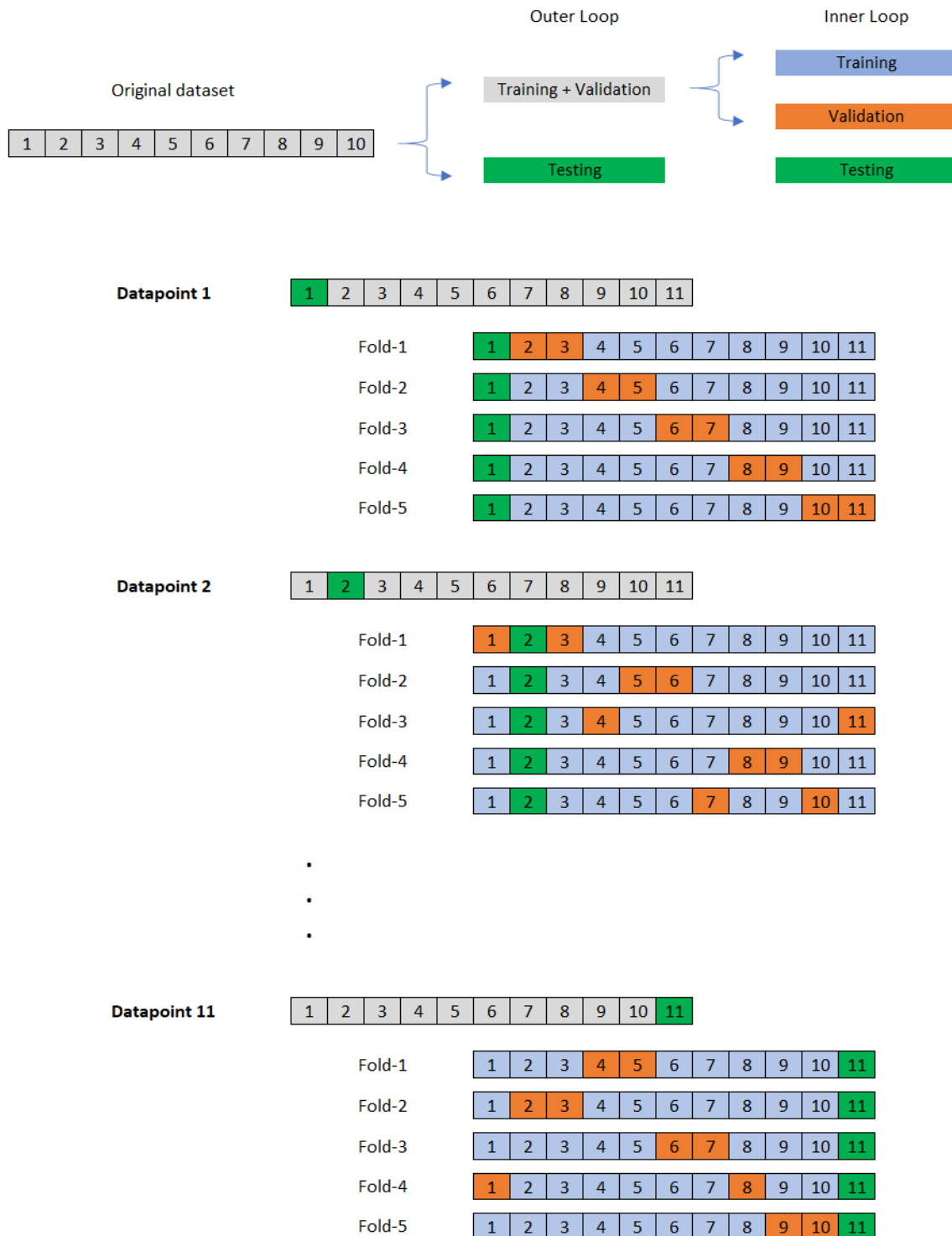


Figure 15: Illustration of a nested cross-validation. A 5-fold cross-validation (inner loop) is nested within a LOOCV (outer loop). The inner loop performs model selection and training, and the outer loop is for performance assessment of the model selection and training procedure. Testing results are not random, being LOOCV, and the selection and training results depend on the random splitting of the data.

6.10 Predicting the bias from validation benchmarks

In the present study, two learning procedures of the bias are developed based on two types of data. The first procedure relies on a design matrix composed of integral parameters or features of the benchmarks. Integral parameters are properties of the benchmarks, based on the calculations solely. The second relies on a design matrix based on correlations between the calculated values. The following subsection discusses the two learning procedures developed for these two types of data.

6.10.1. Predicting the bias based on integral parameters of the benchmarks

Two nested cross-validations (nested CV) are used for both features and model selection as well as for the assessment of the model performance. The nested CV is described in the literature [36, 37], and discussed in sections 6.8 and 6.9. The flowchart of the applied learning procedure is shown in Figure 16, showing the inner and outer LOOCV loops. The outer loop is used to evaluate the performance of the models (*i.e.*, estimating the test error). The two inner loops are used for features and model selection (*i.e.*, selecting informative features and model sizes, and tuning the model hyperparameters).

Recursive feature elimination (RFE) [85], is used for feature selection. The method is wrapper-based, belonging to the Best-Subset selection approach discussed in Section 6.9. In RFE, many models with different subsets of all the features, or model sizes, are iteratively trained on sections of the data (*i.e.*, training sections). Specifically, a model is built using all predictors, and an importance score is calculated for each predictor. The least important predictor is removed, and a model is built using the remaining predictors. An importance score is then recalculated for the remaining predictors, and the least important predictor is removed, once again. The chosen number of predictors is the model size achieving the lowest validation error.

Model selection applies the OSE rule, *i.e.*, choosing a smaller model size containing fewer number of predictors that has its validation error within an error margin (*e.g.*, 1 SE) of the best performing model size. As mentioned, the chosen model will be simpler and easier to interpret at the expense of an acceptable loss of its predictive performance. In addition to a better interpretability, it would fit less to the noise in the data. The bias is affected by experimental uncertainties (and its random component), and the bias in the present data can contain large random uncertainties, *i.e.*, large noise. The learning algorithm is designed to reduce the impact of this noise on the final models. The optimum model hyperparameters (tuning of the model parameters) are also chosen using LOOCV and based on the model performance on validation sections of the data. The hyperparameter search is re-conducted for the final selected model once the number of features is chosen based on the preceding RFE steps.

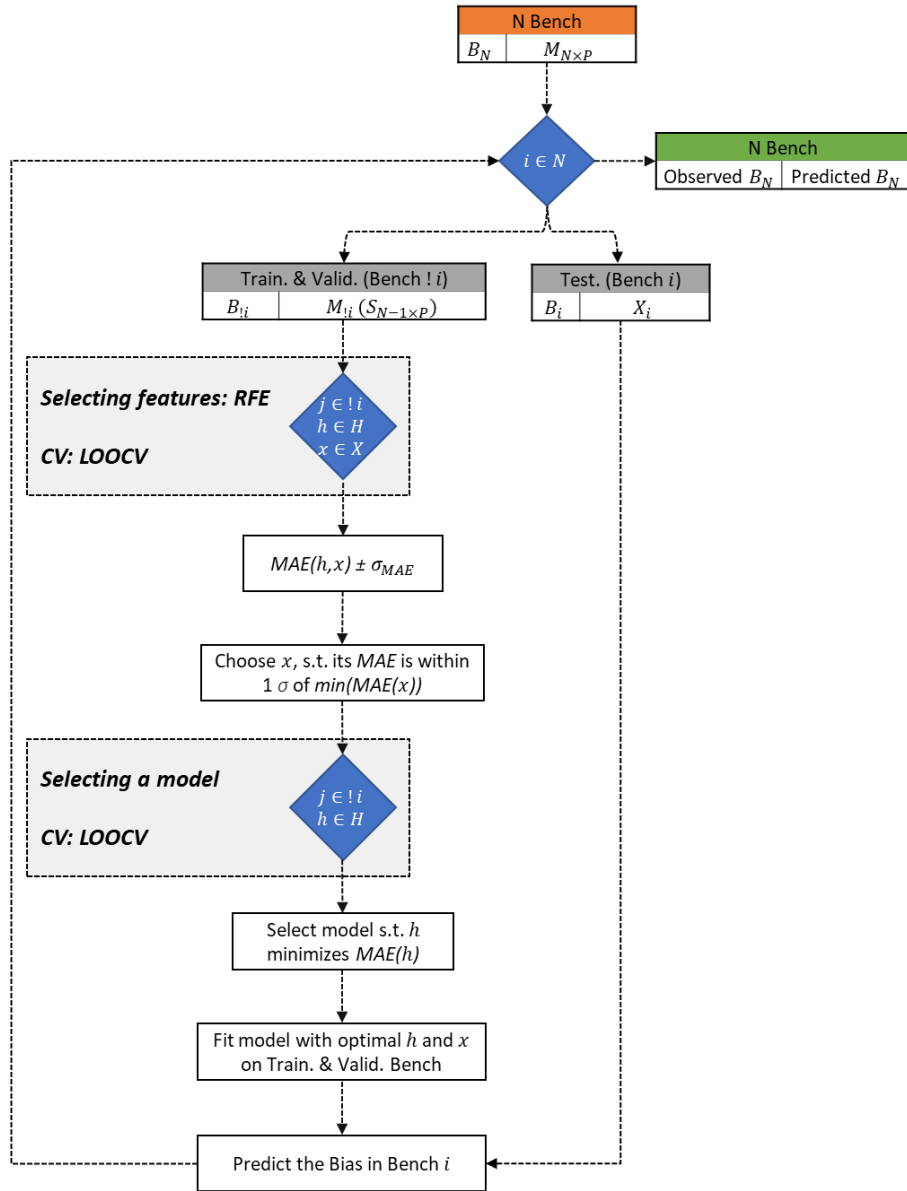


Figure 16. Flowchart of performance assessment of features and model selection procedure applied for learning from integral benchmark parameters. The size of the design matrix is $N \times P$, where N is the number of benchmarks and P is the number of predictors (*i.e.*, features). Also, B is the bias, x and X are subset and all benchmark features, h and H are subset and all model hyperparameters, and j is a single benchmark. The algorithm starts at the design matrix (in orange color) and output the paired prediction/observation data (in green color).

6.10.2. Predicting the bias based on the correlation between benchmarks

Predicting the bias from the correlation between benchmarks is conceptually different from the procedure based on features of the benchmarks. This has motivated splitting the bias learning process into two distinguished procedures, relying on two distinguished design matrices. The procedure starts with a correlation matrix of size $N \times N$ (where N is the number of benchmarks), and a bias vector of length N . The procedure is designed to mimic the bias prediction of a target application. As the calculation of a SNF characteristic in a target application is conducted, its correlation vector with validation benchmarks is also calculated, whereby the

bias in these validation benchmarks is known *a priori*. A correlation vector between the target application and the validation benchmarks along with the bias vector of the validation benchmarks are used to estimate the bias in the target application. The learning procedure is designed similarly. Therefore, the correlation matrix is decomposed into N correlation vectors and, along with the bias vector, they generate N separate design matrices for each benchmark, as shown in Figure 17 and Figure 18. Each design matrix contains a correlation and a bias vector as the independent and the dependent variables, respectively.

Model testing follows a LOOCV approach. However, model validation, selection of optimal model parameters such as the optimal number of k nearest neighbors, follows two different approaches. In the first approach (Figure 17), model validation is applied on the submatrix. Optimal parameters are selected based on the models' performance on predicting the bias of the benchmarks located at the diagonal of the submatrix, also using the correlation data of the submatrix. In the second approach (Figure 18), model validation is applied on the training and validation section of the correlation vector of the test benchmark. Optimal model parameters are selected based on the models' performance on predicting the bias of the benchmarks located on the same correlation vector of the test benchmark. The latter method is the default in the present work.

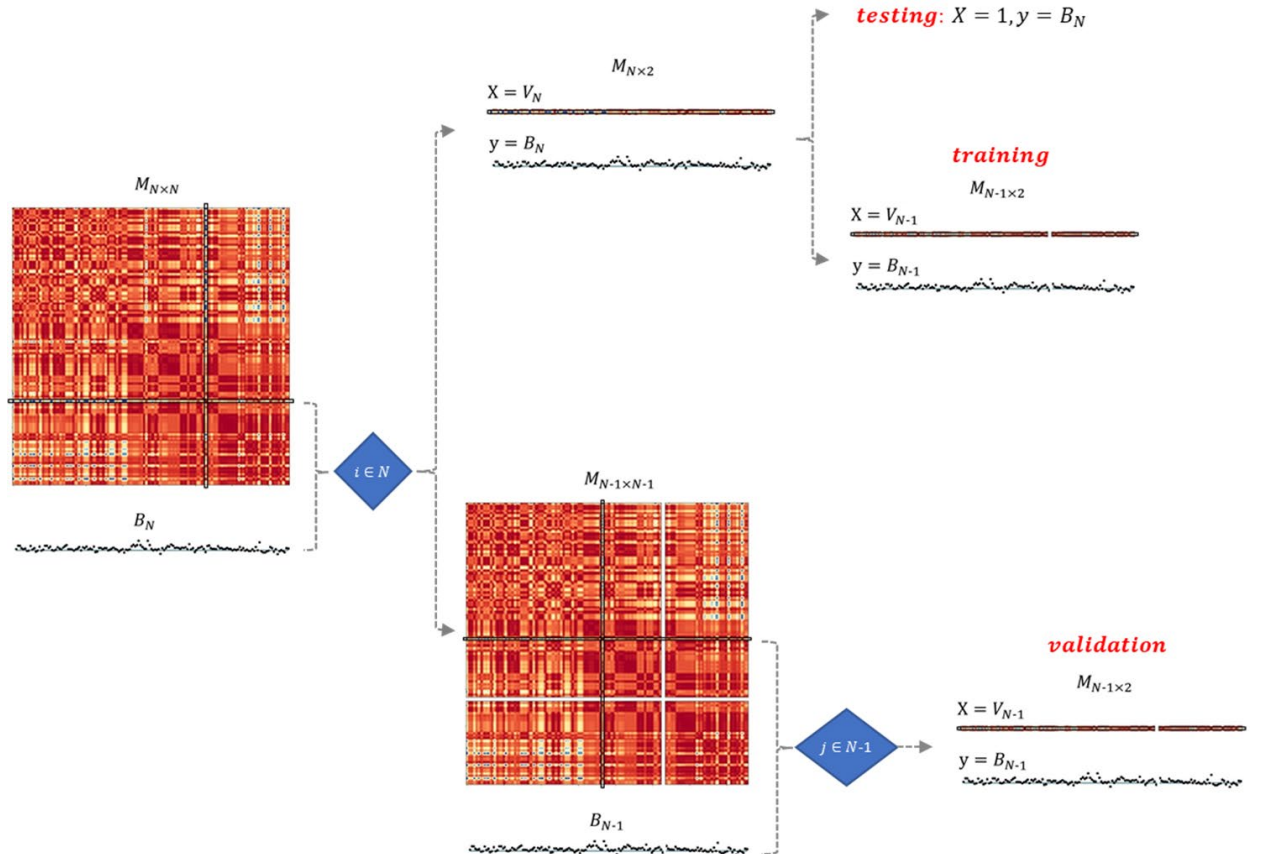


Figure 17. Decomposition of the correlation matrix of size $N \times N$ into N individual correlation vectors (for training and testing), along with submatrices of size $N - 1 \times N - 1$ for validation. The correlation and bias data are combined to result in the design matrices.

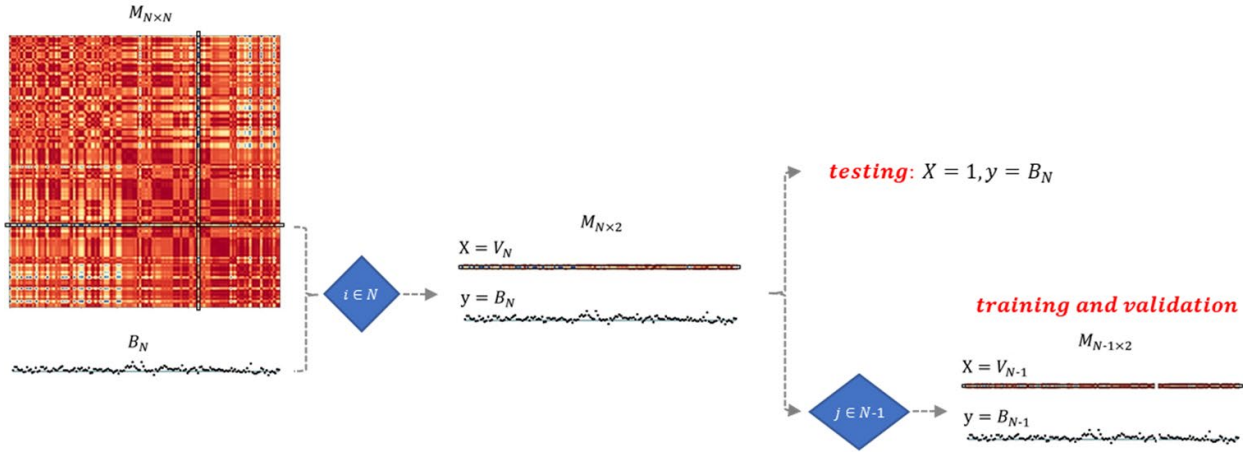


Figure 18. Similar to Figure 17, implementing matrix decomposition for validation, training, and testing. Unlike the approach described in Figure 17, the validation relies on data resampling (e.g., using LOOCV) on the correlation vector – along with the bias vector, optimizing model parameters for their performance on the validation section of the correlation vector.

No feature search is conducted as there is only one predictor, *i.e.*, the correlation between benchmarks. Once the correlation matrix is decomposed into N design matrices, the LOOCV procedure is applied on each design matrix for model selection (tuning the model hyperparameters). The test error of the chosen model is evaluated on a single hold-out sample, the target benchmark, which is the benchmark at unit correlation (the diagonal element in the correlation matrix). The scheme of the procedure is shown in Figure 19.

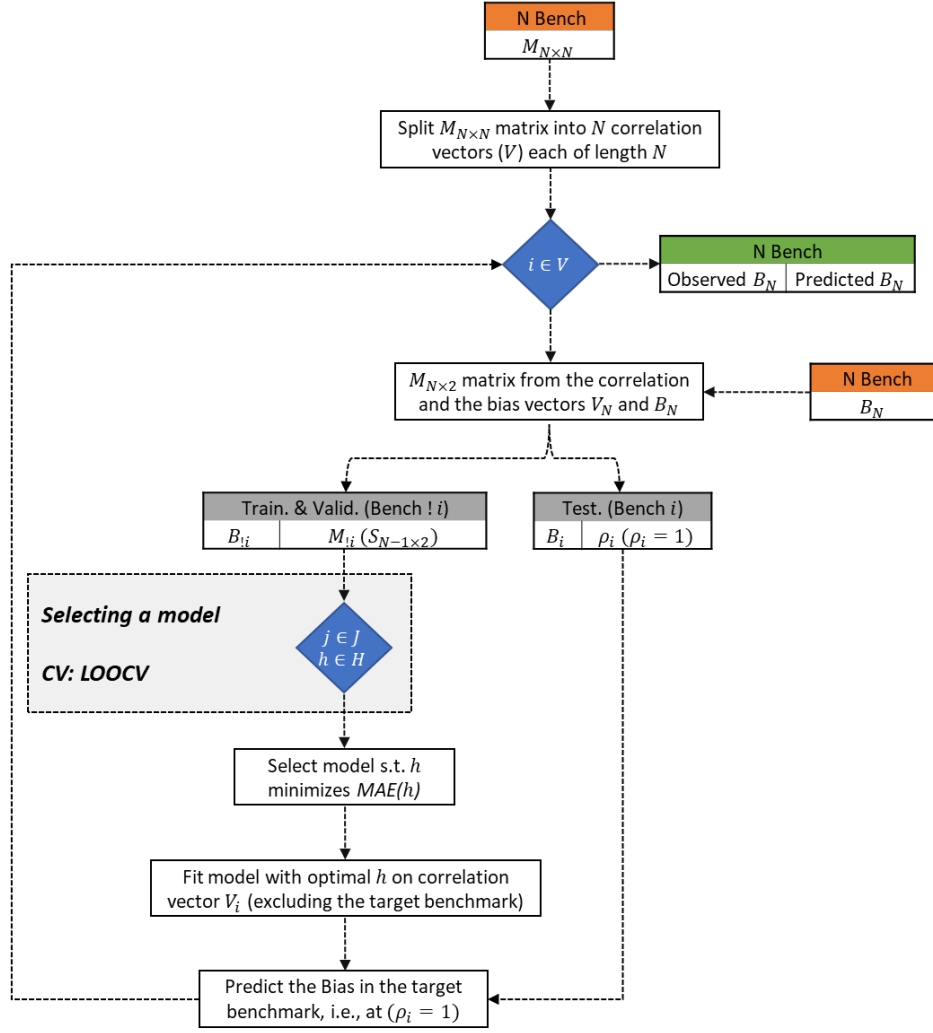


Figure 19. Flowchart of the performance assessment of the model selection procedure applied for learning from the correlation between the benchmarks. N is the number of benchmarks, B and ρ are their biases and correlations, M and S are the correlation matrix (all data) and a subset correlation matrix, h and H are subset and the entire model's hyperparameters, J is a correlation vector, and j is a single benchmark. The algorithm starts at the correlation matrix and the bias vector (in orange color) and output the paired prediction/observation data (in green color).

6.11 Detection and removal of outliers

Outliers are referred to as abnormalities, deviants, or anomalies in the data mining and statistics literature [86]. They are data points that differ significantly from other observations, which can occur due to random uncertainties or erroneous data – either erroneous calculations or measurements in the present validation data. Several methods can be employed to detect potential outliers in the data, including descriptive statistics (such as boxplots), measures of influence (such as Cook's distance), and hypothesis testing (such as *Chi*-square test and *z*-test). Data points are outliers with respect to the data and the model employed, *i.e.*, other models and data could result in different conclusions about the abnormality of a datapoint. Also, outliers

detected using statistical methods should be followed by specific analyses of the observation, for justifying its exclusion from the data.

The application of the outliers detection and removal in the present study proceeds as following; as models are being trained and validated using the inner-most loop of the algorithms described in Section 6.10, the selected model is regressed onto the training and validation section of the data. Outliers are detected with respect to the regressed model, choosing the z-test in the present study. Since the process is repeated through a LOOCV procedure for N benchmarks, the outliers detection process is repeated N times excluding a test benchmark in each iteration. For each iteration, the p -value of the observations in the training and validation section of the data are recorded, and at the end of the LOOCV procedure, these p -values are aggregated to result in a single value for each benchmark being tested as an outlier at a chosen significance level.

The scope of the present study is mostly in data analyses, rather than analyzing particular measurements for their extremity or abnormality. Also, the benchmarks detected as outliers following the preceding discussion will be outliers with respect to given statistical models and data, *e.g.*, the RF model and the correlation between Clab benchmarks. For such reasons, outliers detection and removal from the current data will be selectively conservative, *i.e.*, resulting in removal of a small number of benchmarks. The following criteria will be applied:

1. outliers should have a z-value >3 (corresponding to a probability of 0.0027),
2. aggregation of the p -values from different data (different training and validation data) assumes that these data are un-correlated, requiring that the median p -value to be significant at threshold $\alpha/2$, *i.e.*, the aggregate significance level is 0.00135.

The preceding criteria should lead to a significantly small number of benchmarks being excluded as outliers. The procedures, applied on both design matrices, are shown in Figure 20 and Figure 21. The procedures are similar to those being used to test the model performance, except that the inner-most loops are being used to detect outliers and finally aggregate this information. The procedures result in design matrices having equal or less dimensions than the original ones, which are then used for the predictive performance assessment following the algorithms described in Section 6.10.

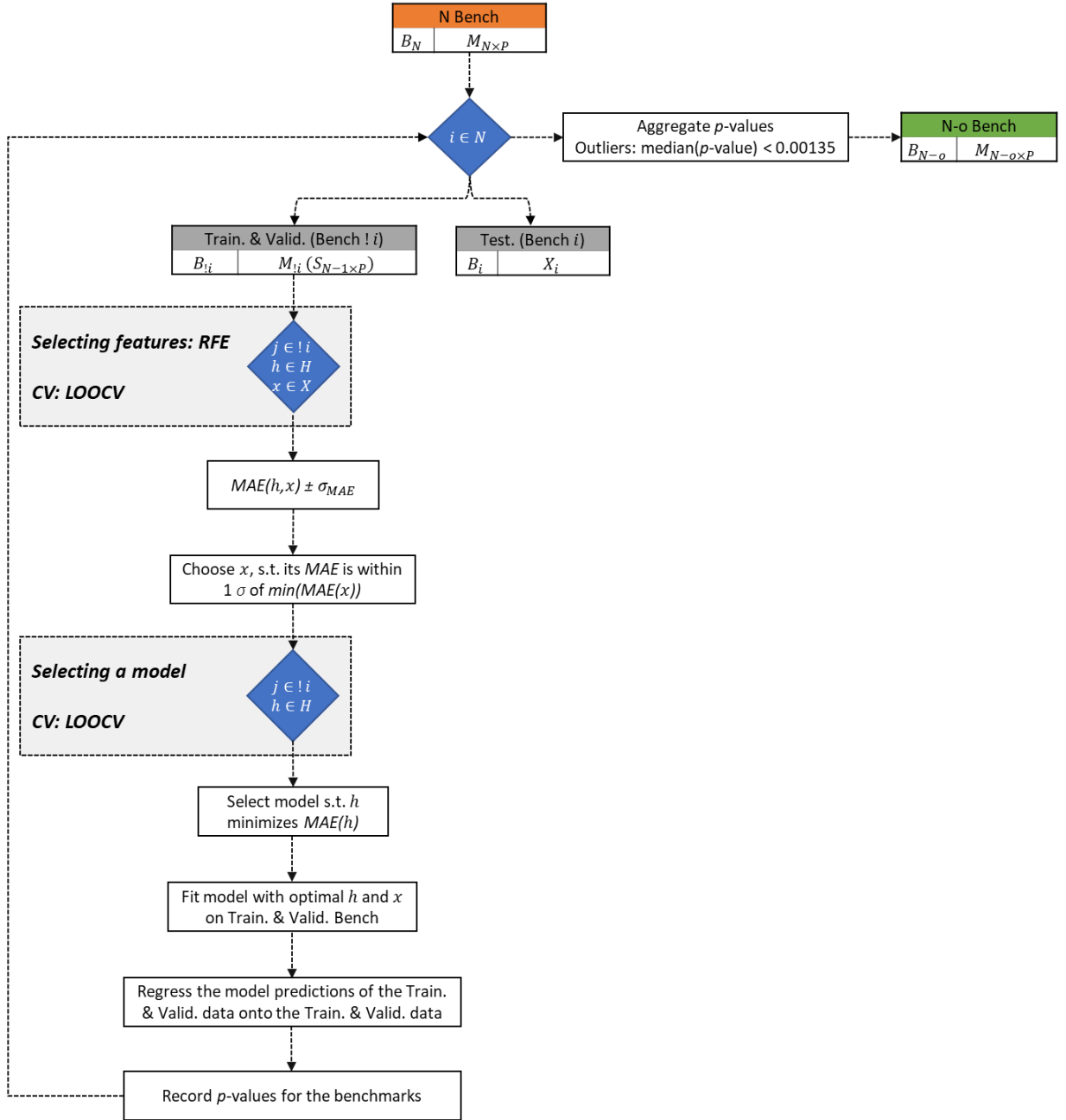


Figure 20. Flowchart of outliers detection and removal based on the design matrix of the integral benchmark parameters. The algorithm starts at the design matrix having $N \times P$ size (in orange color) and output the reduced design matrix having the $N - o \times P$ size (in green color).

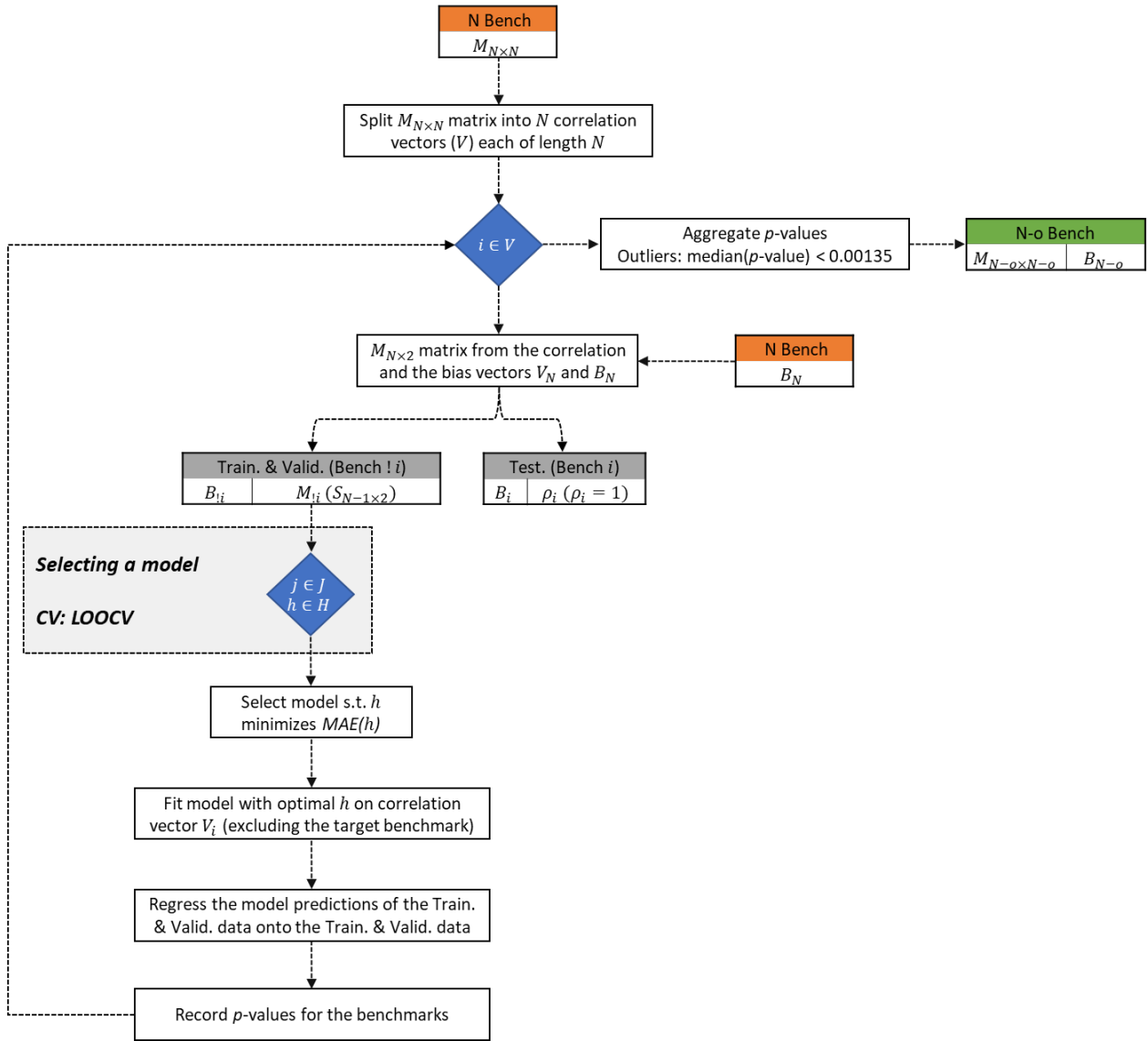


Figure 21. Flowchart of outliers detection and removal based on the design matrix of the correlation between benchmarks. The algorithm starts at the correlation matrix having $N \times N$ size and the bias vector having N length (in orange color) and output the reduced correlation matrix having the $N - o \times N - o$ size and the reduced bias vector having $N - o$ size (in green color).

6.12 Final models of the bias predictive procedures

Final models are models fitted to the whole data, readily used for prediction of the bias in target applications. The final models based on the first learning procedure are obtained by repeating the steps for features and model selection on the full data, *i.e.*, excluding the iterative data splitting into a test section and a training and validation section (the outer LOOCV loop in Figure 16). Once obtained, the final models can be used for bias predictions on realistic calculations. The final models consist of selected features of the benchmarks and learned functional forms that can map these features into the target bias. For the RF and the KNN models, the final models will also use the entire validation data to obtain the bias prediction, *e.g.*, biases and features of a few neighboring benchmarks will be applied to predict the bias in the target benchmark. For both the RF and the KNN models, the entire validation benchmarks are also part of the final model.

Alternatively, learning from the correlations between the benchmarks does not necessarily result in final models that can be readily used for bias predictions of a target application. A target application will probably have a correlation vector with the validation benchmarks that is different from any of the present correlation vectors. Therefore, final models await the correlation vector of the target application with the present benchmarks. Indeed, the latter argument is the motivation and rationale for splitting the learning process so that it is based on two types of matrices: integral parameters of the benchmarks and correlations between the benchmarks.

The quality of the final models, how well the predicted bias simulates the originally observed one, will be also assessed using the R^2 . The R^2 statistic is a measure of the quality of the fit. The ML model will explain, or reduce, part of the original variance of the bias using the driven systematic part $f(x)$. The unexplained part of the variance will be contained in the error term ϵ . The R^2 is the proportion of the variance explained by the model – *i.e.*, explained or reduced by $f(x)$. It takes values between 0 and 1, where a perfect model results in R^2 value equal to 1, and a model that does not explain any of the variance of the original data results in R^2 value equal to 0. The R^2 is calculated as

$$R^2 = 1 - FVU, \quad (6.19)$$

where FVU is the fraction of the variance unexplained by the model, calculated as

$$FVU = RSS/TSS = \sum (y_i - \hat{y}_i)^2 / \sum (y_i - \bar{y})^2, \quad (6.20)$$

where RSS and TSS stand for residual sum of squares and total sum of squares, respectively. The former residual originates from the remaining error after the application of the ML model, and the latter residual originates from the initial error in the data.

6.13 Features extraction

In the present section, possible ML features are discussed. The ML algorithms usually start with a relatively large number of features that can be informative. Informative features contain information that allow predicting the bias, given the ML model and the validation data. The data are used to allocate those features that are actually informative through a features selection process.

The features may belong to both the calculations and the measurements. In the present study, only features of the calculations are considered, *i.e.*, it is aimed to explain the bias using only calculational-based features. The rationale is to obtain ML models that allow predicting the bias, without reference measurements. These models are developed from validation benchmarks, and their target applications are realistic SNF calculations without reference measurements. This is a necessary approximation, since learning the bias using potential features of both calculations and measurements can result in models that do not have an application on calculations, lacking reference measurements. Even if the latter approach might incorporate more informative features in the learning process, the resulting models are certainly less useful given the foreseen application of the ML models. As an example, calculated uncertainties are considered a possible model feature, but experimental uncertainties are excluded since, even if they are potentially informative for the bias prediction, they will not be available for a target application.

The analyzed features include ones commonly used in validation of CSA. In CSA, a trending analysis of the bias using the similarity index (c_x) is used [41]. The similarity index is the Pearson correlation coefficient between the calculated values, obtained when parameters and data are perturbed. Benchmark parameters (*e.g.*, burnup) and data (*e.g.*, nuclear data) are uncertain and, when they are perturbed, the calculated values respond with some degree of similarity, measured using the Pearson correlation coefficient. Trending analysis assumes that uncertainties in parameters and data result in differences between calculations and measurements. Additionally, benchmarks share, to some degree, similar parameters and data-induced uncertainties, measured through their similarity index. Differences between calculations and measurements can be regressed on the similarity index to predict the bias. The regression models could be linear, implementing cutoffs on similarities. As a result, benchmarks showing weak similarities with the application are excluded from the regression models [87].

In the present study, predicting the bias using the correlation between benchmarks is being analyzed. The correlations are calculated, and experimental correlations are excluded given their unavailability. Also, these correlations would not be available for a target application. As described in Chapter 6, the structure of the learning algorithm based on the correlation between benchmarks is distinguishable from learning from other integral parameters, and therefore it is treated in a separate learning setting.

Other integral features can be informative, namely:

1. calculated value of the SNF characteristic

2. hydrogen-to-fissile atom ratio (H/X)
3. reactor type (PWR vs. BWR)
4. spectral index (SI)
5. calculated uncertainty of both ND and DO origins

Only three of these features appear in literature. The calculated value (no. 1) is being used in reference [46], addressing ML for the validation of nuclear data. The H/X (no. 2) is commonly used in validation of CSA [32], along with the previously discussed similarity index. As in Reference [26], the validation driven safety factors on calculated decay heat values are classified per reactor type (no. 3). Including these three features assumes that they are informative in the current application, and whether they are informative features (or noninformative) is to be based on the data.

The SI , which provides information about the neutron flux spectra, is calculated as the ratio between the fast and the total flux, with an 0.625 eV as the lower energy bound of the fast flux. The H/X also provides information about the enrichment, water density, and burnup. These variables, SI and H/X , are labelled “integral parameters” in the current study, implying their correlation with several SNF properties. Two different sections of the validation data are selected to demonstrate potential correlations between the SI and H/X , and several SNF properties. The Clab section of the decay heat data is used for the SI , and the PIE data are used for the H/X .

Figure 22 shows plots of the SI versus enrichment, water density, burnup, and H/X for the Clab decay heat benchmarks (both BWRs and PWRs), indicating potential correlations between these variables. Higher enrichment is associated with higher SI and lower H/X values. Higher water density, PWRs in this case, are relatively under-moderated with respect to BWRs, showing lower H/X values. Lower H/X values in the PWRs result in harder neutron flux spectra, and higher SI values. Higher burnup values are also associated with higher SI and lower H/X values, however to a weaker extent. The correlation of SI with burnup results from changes in the flux spectra as burnup progress (typically the flux becomes harder at higher burnup values).

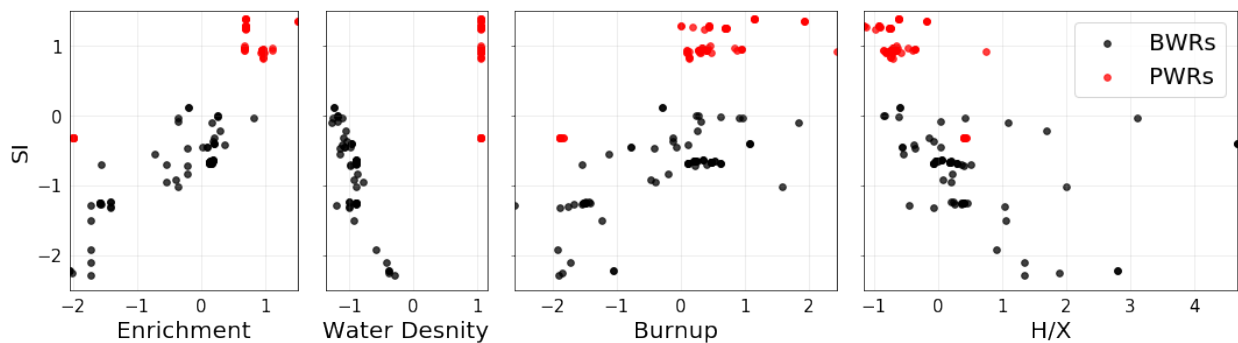


Figure 22. SI vs. enrichment, water density, burnup, and H/X , based on the Clab decay heat benchmarks. The axes are centered and normalized, having average of zero and unit variance.

Figure 23 shows corresponding plots for the H/X versus enrichment, sample height, burnup and SI for the PIE benchmarks (both BWRs and PWRs). Lower H/X values are generally observed in samples that have higher initial enrichments and are located at elevated positions in their host

assemblies. The correlation of H/X with burnup results from gradual depletion of the fissile material with burnup, resulting in an increasing trend for H/X with burnup. Both SI and H/X tend to show negative trend with each other, as shown in both Figure 22 and Figure 23. Higher H/X , moderator-to-fuel atom ratio, tends to soften and increase the moderation of the flux.

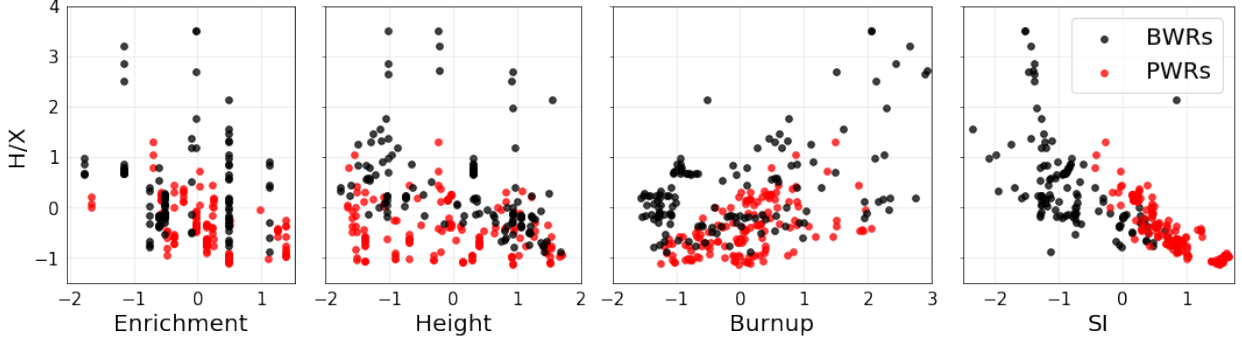


Figure 23. H/X vs. enrichment, sample height, burnup, and SI . The plots are based on the PIE benchmarks. The axes are centered and normalized, having average of zero and unit variance.

These variables change during irradiation, and a single value for each benchmark was obtained implementing cycle-wise burnup weighting, applied as following:

$$SI = \frac{\sum_1^n (BU_i \times SI_i)}{\sum_1^n (BU_i)}, \quad (6.21)$$

$$H/X = \frac{\sum_1^n (BU_i \times H/X_i)}{\sum_1^n (BU_i)}. \quad (6.22)$$

For n irradiation steps, the SI and H/X of each step (SI_i and H/X_i) are weighted using the step-wise burnup change (BU_i), resulting in a burnup weighted average value for each benchmark.

Additional features can be included in the learning process, based on sensitivity analysis. Sensitivity analysis in features engineering is mostly applied in features selection to identify highly influential features toward the response [88,89]. In predicting the bias of CSA calculations, sensitivity coefficients are used as features in the learning process [45]. In this study, it is assumed that sensitivity analysis can identify influential or informative features. A sensitivity coefficient of the bias to model input x is obtained as

$$S_{B,x} = \frac{\partial B/B}{\partial x/x}. \quad (6.23)$$

Ideally, the aim is to identify influential parameters through sensitivity analysis on the bias. However, Equation 7.3 requires evaluating sensitivities on the measurements too, which is not feasible. It is assumed that influential variables on the calculations can be as well influential on the difference between calculations and measurements. The calculated values are used instead of the bias in Equation 7.3.

Chapter 7 Validation Results

The validation results are ratios between the calculated values (C) and the measurements (E), abbreviated hereafter as C/E , and also biases ($B = C - E$), discussed in the following sections. The biases and C/E values presented in this chapter are based on Polaris code, described in Section 3.1.1.

7.1 SNF decay heat

The decay heat values have been calculated for the 262 benchmarks of Clab and GE-Morris; the obtained C/E s and B s are shown in Figure 24 and Figure 25, respectively. Averages of C/E s and B s along with two standard deviation (2σ) are listed in Table 8, categorized by the reactor of origin and the measurement laboratory. The reported standard deviations are calculated from the variance of the data, without considering the variance of each individual observation (*i.e.*, without considering uncertainty in calculations and measurements).

Based on the measurement laboratory and the reactor of origin, averages of the obtained C/E s are within 1.5% from unity, however, the variances are large. The standard deviations are within 5% in the Clab benchmarks, and up to 23% in the GE-Morris benchmarks. The GE-Morris benchmarks have relatively larger experimental uncertainties compared to the ones from Clab. Also, a large number of C/E s of the GE-Morris benchmarks are outside the experimental uncertainty bands.

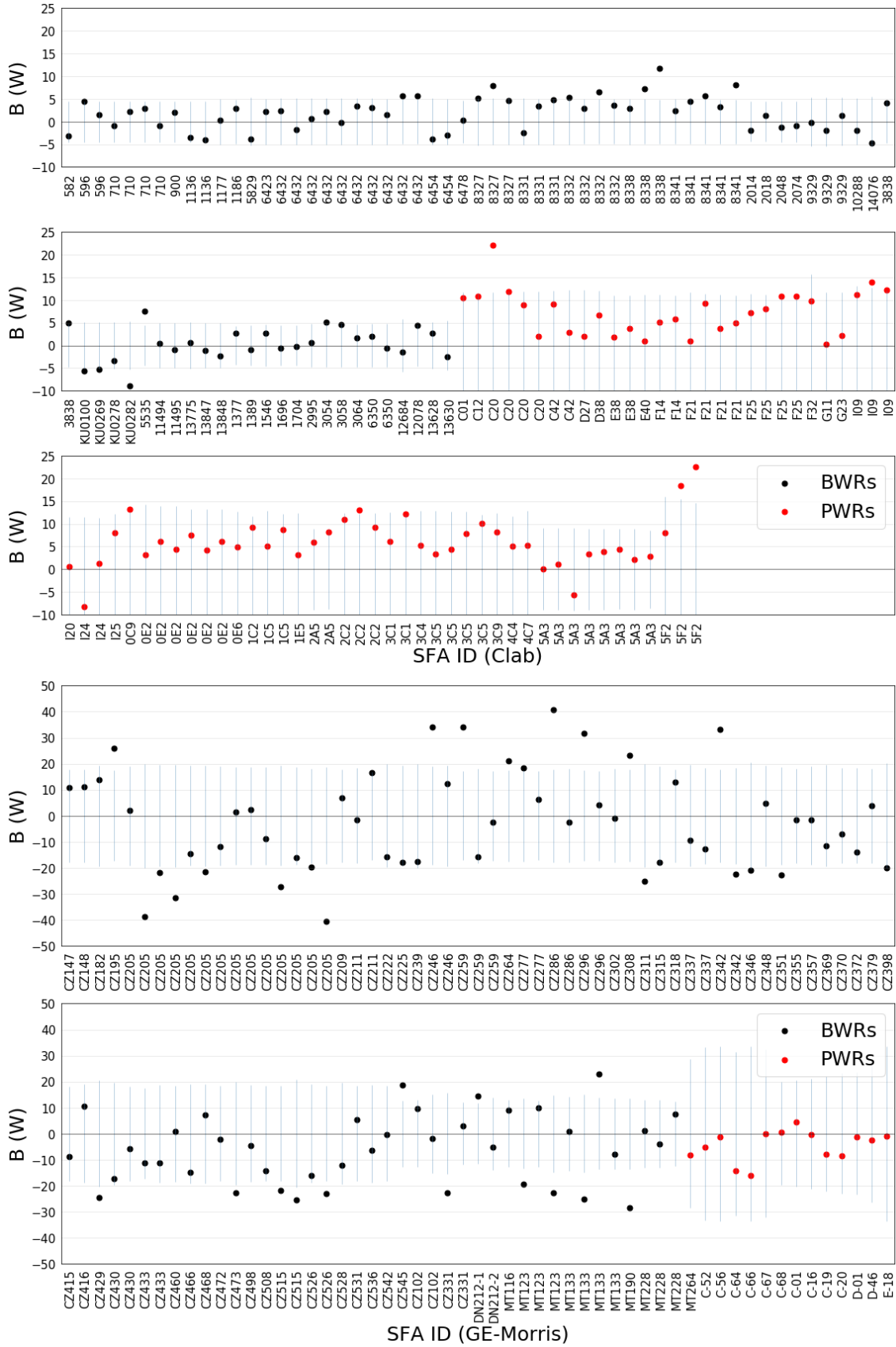
Table 8. Average C/E and B for the decay heat benchmarks, along with two standard deviations (2σ). The parentheses indicate the number of benchmarks in each category.

Dataset (number)	$\overline{C/E}$	\overline{B} (W)
Clab: BWR (81)	1.010 ± 0.051	1.3 ± 7.3
Clab: PWR (71)	1.015 ± 0.023	6.5 ± 10.3
GE-Morris: BWR (96)	1.000 ± 0.229	-4.2 ± 34.2
GE-Morris: PWR (14)	0.994 ± 0.017	-4.3 ± 11.4
BWRs (177)	1.005 ± 0.172	-1.7 ± 26.2
PWRs (85)	1.012 ± 0.027	4.7 ± 13.2
Clab (152)	1.012 ± 0.041	3.7 ± 10.3
GE-Morris (110)	0.999 ± 0.214	-4.2 ± 32.2

Also, the variance of the C/E s of the PWRs tend to be lower than that of the BWRs, and large variance of the B s in the PWRs does not necessarily correspond to large variance of the C/E s. BWRs have more complex designs than PWRs, also their operational parameters are more

intricate. As shown in Table 7, uncertainties in certain DO parameters of the BWRs are larger than those of the PWRs, such as external cladding radius and moderator density. Such differences could eventually lead to larger differences between calculations and measurements in the BWRs. Also, the measured decay heat values of the PWR assemblies are typically larger than the BWRs, for closely similar cooling times. For example, the average measured decay heat value in the Clab PWRs is 428 W, whereas it is 153 W for the BWRs. As shown in Table 3 and Table 4, uncertainties in the measured decay heat values tend to be lower in relative units (percentage) at higher measured decay heat values – typically PWRs in this case. Whereas the higher measured decay heat values tend to have larger uncertainties in absolute units (W). Such uncertainties could result in lower variances for PWR assemblies, presented in relative units, compared to larger variances when presented in absolute units. Also, as shown in Table 12, uncertainties in the calculated decay heat values tend to be similar between the PWRs and BWRs, presented in relative units (percentage). However, noting also that PWRs tend to have relatively larger calculated decay heat values than BWRs for closely similar cooling times, the uncertainties in the calculated decay heat value of PWRs tend to be larger, presented in absolute units (W).

71

Figure 25. Same as Figure 24, but for B instead of C/E values.

7.2 U-235 concentration

The U-235 concentrations have been calculated for the 285 benchmarks selected from SFCOMPO; the obtained C/E s and B s are shown in Figure 28 and Figure 29, respectively. Averages of the C/E and B along with two standard deviations are listed in Table 9.

The calculated values are overestimated (with respect to the measured values) in both BWRs and PWRs, by 1.7% and 2.5%, respectively. In general, the variability is high in both C/E and B . Also, the BWRs tend to have larger variability in the C/E and B , measured by the standard deviation, compared to the PWRs. For clarity, the range of the C/E and B (Figure 28 and Figure 29) for the BWRs are 100% and 50% wider than the ones for the PWRs. The latter figures show uncertainty bars corresponding to reported experimental uncertainties ($2\sigma_{meas.}$), and a significant number of the benchmarks have their C/E and B located outside the experimental uncertainties.

Table 9. Average C/E and B for U-235 concentrations, along with two standard deviations (2σ). The parentheses indicate the number of benchmarks in each category.

Dataset	$\overline{C/E}$	\overline{B} (mg/gHMi) $\times 10^3$
BWR (139)	1.017 ± 0.176	110 ± 1423
PWR (146)	1.025 ± 0.085	245 ± 848
Total (285)	1.021 ± 0.138	179 ± 1170

The present data span wide range of properties, significantly impacting the measured concentration of U-235. 95% of the burnup values in the present data are within 3.5 and 58.1 GWd/tHMi, and 95% of the measured U-235 concentrations are within 1.3 and 25.2 mg/gHMi, both being relatively wide ranges. Burnup, as will be discussed in the Chapter 8, is a relevant parameter affecting the calculated U-235 concentration. Also, as shown in Figure 26, the measured U-235 concentration shows a decreasing trend with burnup, as expected. The U-235 concentration reaches quite low values for several high burnup samples. The large standard deviations of the C/E in Table 8 are primarily attributed to samples having high burnup and significantly low measured values of U-235 concentration, as shown in Figure 26.

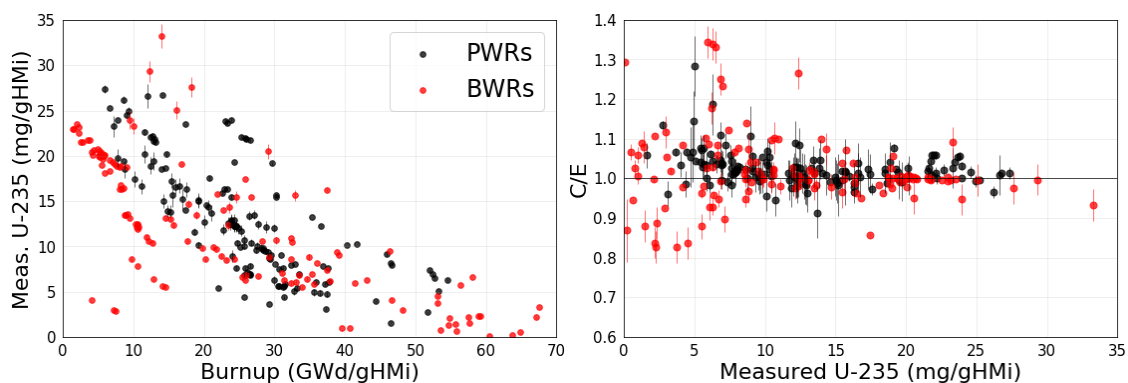


Figure 26. Measured U-235 concentration vs. burnup (left) and the obtained C/E vs. the measured U-235 concentration (right).

7.3 Pu-239 concentration

The Pu-239 concentrations have been calculated for the 285 benchmarks selected from SFCOMPO; the obtained C/E s and B s are shown in Figure 30 and Figure 31, respectively. Averages of C/E and B along with two standard deviations are listed in Table 10.

Similar to the U-235 results, the calculated values are overestimated (with respect to the measured values) in both BWRs and PWRs. The overestimations are 1.3% and 3.9%, respectively. In general, the variability is high in both C/E and B . Also, similar to the U-235 case, the BWRs tend to have larger variability in the C/E and B , measured by the standard deviation, compared to the PWRs. For clarity, the range of the C/E and B (Figure 30 and Figure 31) of the BWRs are 100% and 50% wider than the ones for the PWRs. Also, a significant number of benchmarks have their C/E and B located outside the experimental uncertainties ($2\sigma_{meas.}$).

Table 10. Average C/E and B for Pu-239 concentrations, along with two standard deviations (2σ). The parentheses indicate the number of benchmarks in each category.

Dataset	$\overline{C/E}$	\overline{B} (mg/gHMi) $\times 10^3$
UO ₂ BWR (135)	1.011 \pm 0.164	-9 \pm 740
MOX BWR (4)	1.087 \pm 0.126	709 \pm 1089
PWR (146)	1.039 \pm 0.129	208 \pm 644
Total (285)	1.026 \pm 0.149	112 \pm 741

The Pu-239 concentration is affected by several parameters, including the burnup. The range of the measured Pu-239 concentrations is not as wide as the U-235 case, 95% of the measured Pu-239 concentrations are within 1.7 and 7.5 mg/gHMi. As shown in Figure 27, the measured Pu-239 concentration increases significantly with burnup in the low burnup range and plateaus at higher burnups, as expected. At medium and high burnup ranges, the Pu-239 concentration is nearly balanced between its production from U-238 and removal from absorption – both capture and fission. The large standard deviations of the C/E in Table 10 are being attributed to samples at different burnup ranges. Significantly large C/E and B values (compared to the rest of the data) are attributed to the 4 MOX samples of the Downward-1 reactor. Their measured Pu-239 concentrations are also relatively high compared to the UO₂-based samples.

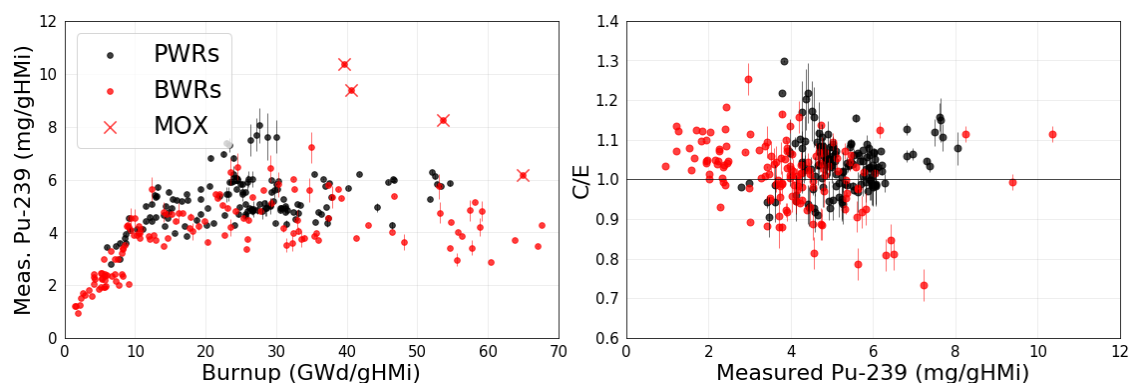


Figure 27. Measured Pu-239 concentration vs. burnup (left) and the obtained C/E vs. the measured U-235 concentration (right).

7.4 Cs-137 concentration

The Cs-137 concentrations have been calculated for only 222 benchmarks of SFCOMPO (out of the selected 285 ones); the obtained C/E s and B s are shown Figure 32 and Figure 33, respectively. Averages of C/E s and B s along with two standard deviations are listed in Table 11.

The calculated values are slightly underestimated (with respect to the measured values) in both BWRs and PWRs. In general, the variability is high in both C/E and B . Also, similar to the U-235 and Pu-239 cases, the BWRs tend to have larger variability in the C/E and B , measured by the standard deviation, compared to the PWRs. Also, a significant number of the benchmarks have their C/E and B located outside the experimental uncertainties ($2\sigma_{meas.}$).

Table 11. Average C/E and B for Cs-137 concentrations, along with two standard deviations (2σ). The parentheses indicate the number of benchmarks in each category.

Dataset	$\overline{C/E}$	\overline{B} (mg/gHMi) x 10^3
BWR (105)	0.996 ± 0.160	-10 ± 180
PWR (117)	0.993 ± 0.078	-6 ± 69
Total (222)	0.995 ± 0.124	-8 ± 133

76

77

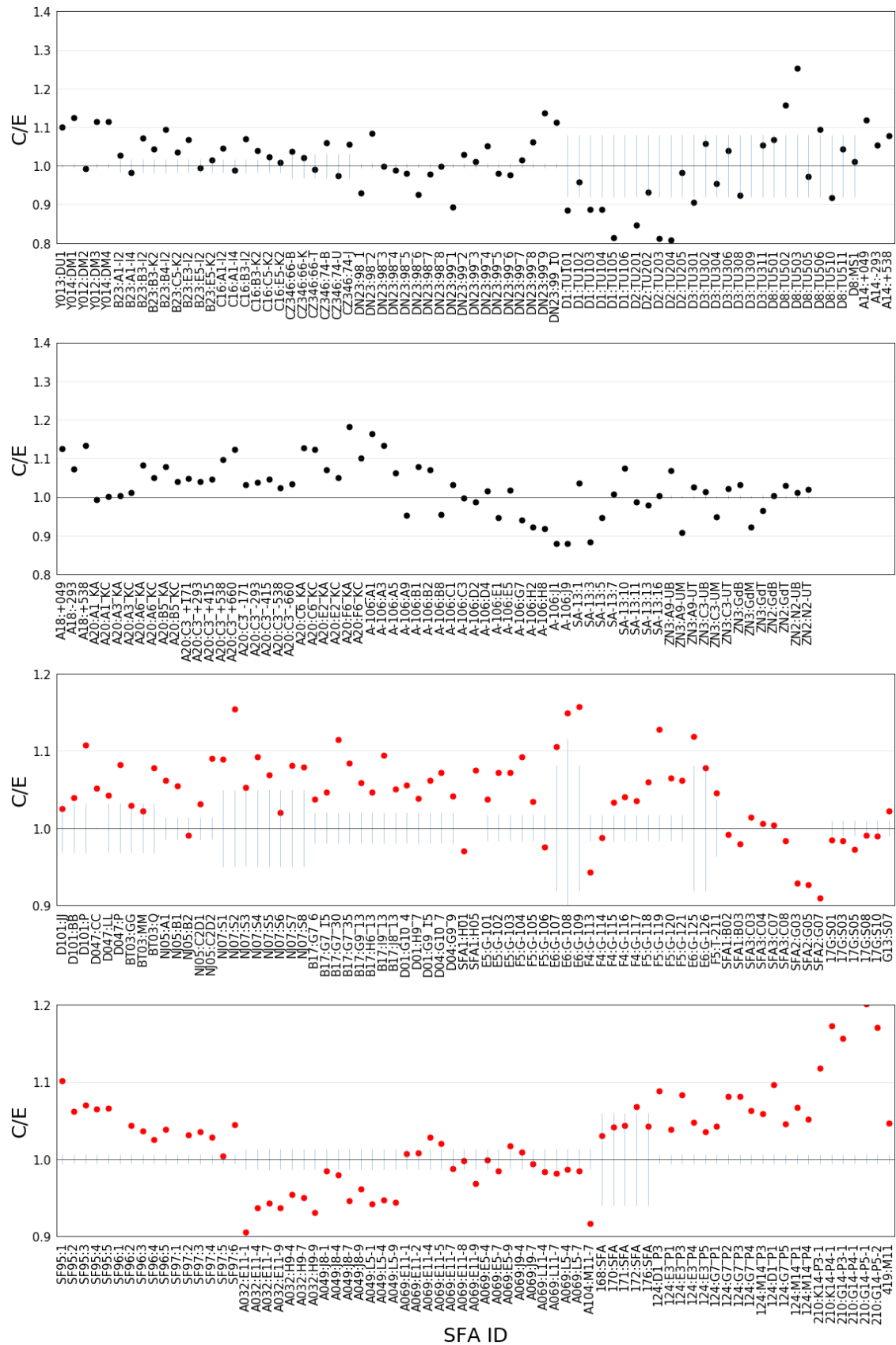
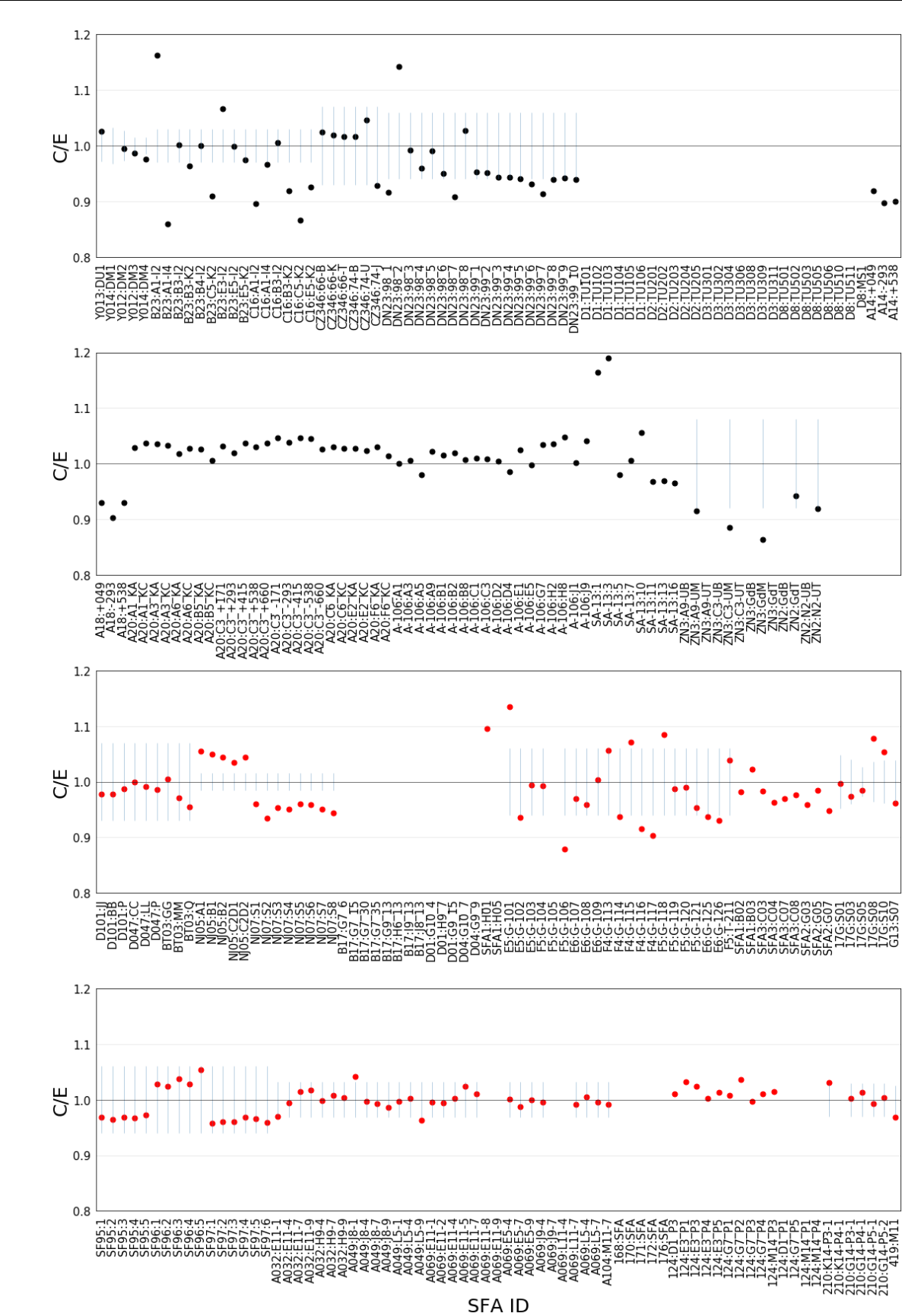


Figure 30. C/E of the Pu-239 concentrations. The BWRs are shown in black color (top two plots), and the PWRs are in red color (bottom two plots). The uncertainty bars are experimental uncertainties (2σ), reported for some of the analyzed benchmarks [11].



81

7.5 Comparison with literature

In this section, a comparison with literature is presented for the decay heat benchmarks. The decay heat benchmarks are selected, given that several literature studies consistently present bias and C/E values for large numbers of decay heat benchmarks, analyzed in this work. As will be explained in Chapter 9, the decay heats are also calculated using ORIGEN (SCALE 6.2.3), in addition to Polaris. The B and C/E values of the decay heat are shown in Figure 34, categorized by the measurement laboratory and the reactor type. Figure 34 shows the present results along with the results of Gauld et al. [27], Yamamoto and Iwahashi [90], Ilas et al. [28], and Wiles et al. [13]. The results presented are not necessarily based on the same number of benchmarks as for the present work. For example, the analyzed benchmarks in [28] exclude the GE benchmarks, and the benchmarks in [13] do not include any Clab benchmarks. The B and C/E values from Polaris and ORIGEN are comparable to the ones from the references. The B s are having less variance in the Clab benchmarks, particularly for the BWRs. For the Clab benchmarks, the B s and C/E s tend to be higher on average in the PWRs compared to the BWRs, *i.e.*, the calculations in the PWRs overestimate the decay heat values (with respect to the measured values), compared also to the BWRs. For both the Clab and GE-Morris benchmarks, the C/E s of the PWRs tend to have less variance compared to the BWRs.

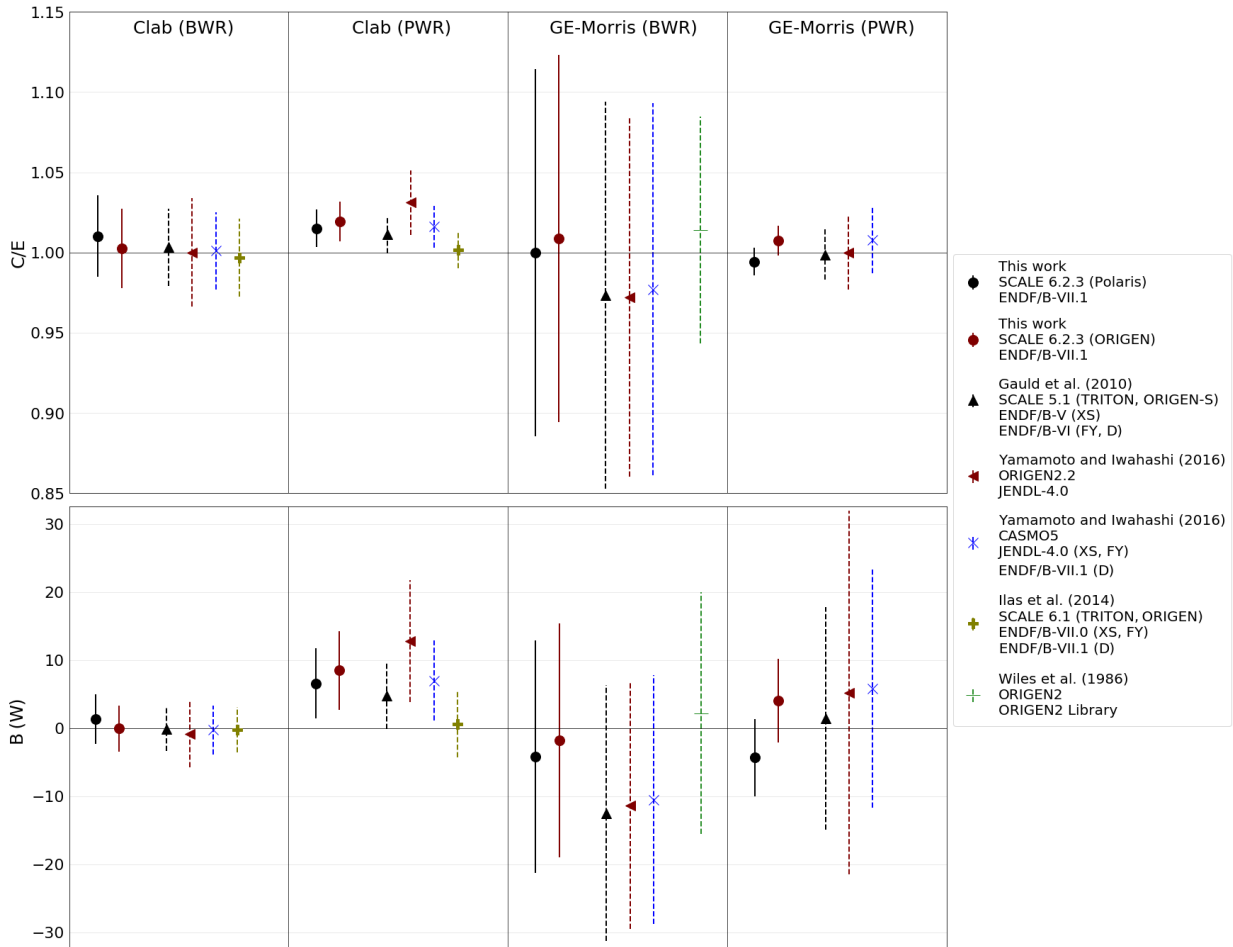


Figure 34. C/E and B values of Polaris and ORIGEN obtained in this work, along with results from [13,27,28,90]. The bars are 1σ . The listed ND libraries are the primary source of ND.

Chapter 8 Uncertainty Analyses

Uncertainties of ND and DO origins were individually propagated in the calculational models for all benchmarks, using 400 perturbations for the decay heat benchmarks and 335 for the PIE samples (individually for ND and DO perturbations). Then, ND and DO uncertainties were combined together (through summation of quadrature) to obtain the total calculated uncertainties. The uncertainty propagation method and the propagated uncertainties were discussed in sections 4.3 and 4.4. The uncertainties presented in this chapter are based on both Polaris and Sampler codes, described in Section 3.1.1.

The fractional variance (FV) is used to quantify the contributions of ND and DO uncertainties in the total calculated uncertainties, and also the contributions of uncertainties in XS, FY, and DD to the uncertainties of ND origin. The XS contributions to uncertainties of ND origin are calculated as

$$FV_{XS} = \frac{\sigma_{XS}^2}{\sigma_{ND}^2} = \frac{\sigma_{XS}^2}{\sigma_{XS}^2 + \sigma_{FY}^2 + \sigma_{DY}^2}. \quad (9.1)$$

The ND contributions to the total calculated uncertainties are evaluated as

$$FV_{ND} = \frac{\sigma_{ND}^2}{\sigma_C^2} = \frac{\sigma_{ND}^2}{\sigma_{ND}^2 + \sigma_{DO}^2}. \quad (9.2)$$

8.1 Calculated uncertainties and fractional variances

The calculated uncertainties are summarized in Table 12, represented as one standard deviation (%) of the calculated values. No significant differences are noted between the PWRs and the BWRs. The uncertainties of the decay heat and Cs-137 concentration are approximately 2.3% and 1.7-1.8%, respectively. Both uncertainties have low variances around their averages. In contrast, uncertainties in the U-235 and Pu-239 concentrations are largely varying around their averages, particularly for the former isotope. The uncertainties of the U-235 concentration are 2.5-3.0% whereas they are 2.4-2.6% for the Pu-239 concentration.

Table 12. Average along with one standard deviation of the calculated uncertainties (%).

Parameter	PWR	BWR
Decay Heat	2.3 ±0.2	2.3 ±0.2
U-235	2.5 ±1.0	3.0 ±2.5
Pu-239	2.6 ±0.6	2.4 ±0.7
Cs-137	1.8 ±0.1	1.7 ±0.1

The calculated uncertainties have two origins: ND (*e.g.*, XS, FY, and DD) and DO parameters. The contributions of uncertainties of DO origins into the calculated uncertainties are listed in Table 13, measured as fractional variances. Similar to the total uncertainties, differences between the PWRs and the BWRs are not significant. The uncertainties of DO origins contribute largely to the calculated uncertainties. They contribute more than 80% to the total variances of the calculated decay heat values, U-235, and Cs-137, particularly for the latter isotope where the FV is 97-98%. The Pu-239 FVs show large variances around their average, however, the FVs are considerably large, being between 55% and 59% of the total variances.

Table 13. Average along with one standard deviation of the FVs of the uncertainties of DO origins.

Parameter	PWR	BWR
Decay Heat	0.84 \pm 0.05	0.85 \pm 0.04
U-235	0.87 \pm 0.07	0.89 \pm 0.08
Pu-239	0.59 \pm 0.16	0.55 \pm 0.19
Cs-137	0.98 \pm 0.01	0.97 \pm 0.01

The observed variations in the calculated uncertainties and the FVs, listed in Table 12 and Table 13, can indicate their dependency on benchmarks features. As will be discussed in Section 8.3, the perturbed SNF characteristics correlate differently with various benchmark features. The burnup will show high correlations with all of the analyzed SNF characteristics. Therefore, the calculated uncertainties and the FVs listed in Table 12 and Table 13 are plotted against the burnup, see Figure 35 to Figure 38. On average, the calculated uncertainties and the FVs of DO uncertainties of the decay heat and U-235 concentration show noticeable trend with the burnup: the higher the SFA burnup, the higher the calculated uncertainties. The uncertainties (1σ) for the decay heat are less than 3% of the calculated values (at maximum). Whereas uncertainties for U-235 concentration reach higher values, approximately 6% for the PWRs and 12% for the BWRs (at maximum). Trends can also be observed in the FVs of DO origins into the calculated uncertainties. On average, for both the decay heat and the U-235 concentration, the FVs of DO origins decreases at higher burnups, *i.e.*, uncertainties of ND origin increasingly contribute at higher burnup.

The calculated uncertainties and the FVs of DO origins of the Pu-239 and Cs-137 concentrations do not behave similarly, *i.e.*, they do not exhibit noticeable trends with the burnup as for the decay heat and the U-235 concentration. As will be discussed in Section 8.3, the Pu-239 concentration is affected by other parameters than the burnup, *e.g.*, parameters inducing large spectral changes such as the moderator density. Additionally, several benchmarks cluster together, such for the Yankee-1 reactor. Calculated uncertainties for the Cs-137 concentration and the FVs of DO origins also do not show noticeable trends with the burnup. However, these uncertainties and FVs are constrained within small interval, being 1.67-1.75% for the former, and 0.97 to 1.00 for the latter. The Cs-137 concentration is therefore mostly affected by uncertainties of DO origin, and the most influencing parameter is the burnup, as expected.

The burnup uncertainties are implemented as percentages of the burnup, and as listed in Table 7, burnup uncertainty is 1.67%, close to the calculated uncertainties of the Cs-137 concentration.

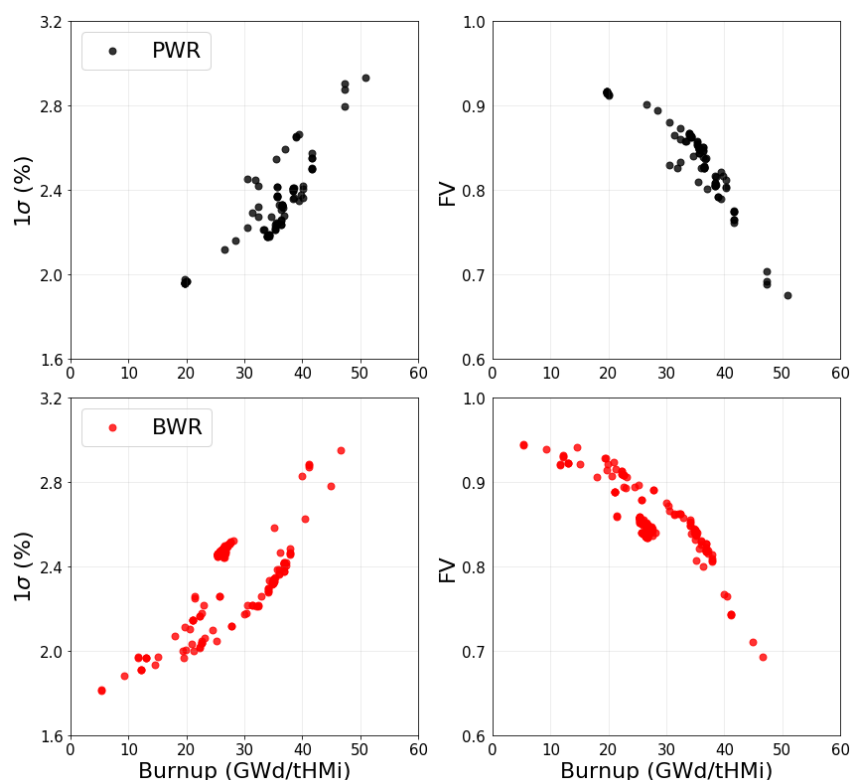


Figure 35. Calculated uncertainties of the decay heat (left), and the FVs of DO origins (right).

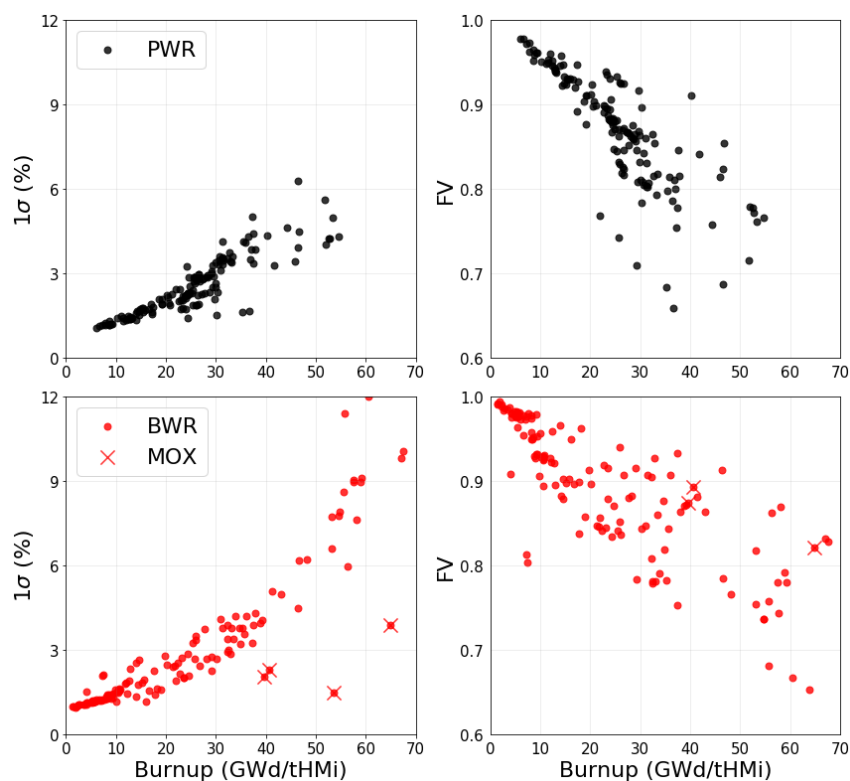


Figure 36. Same as Figure 35 for the U-235 concentration.

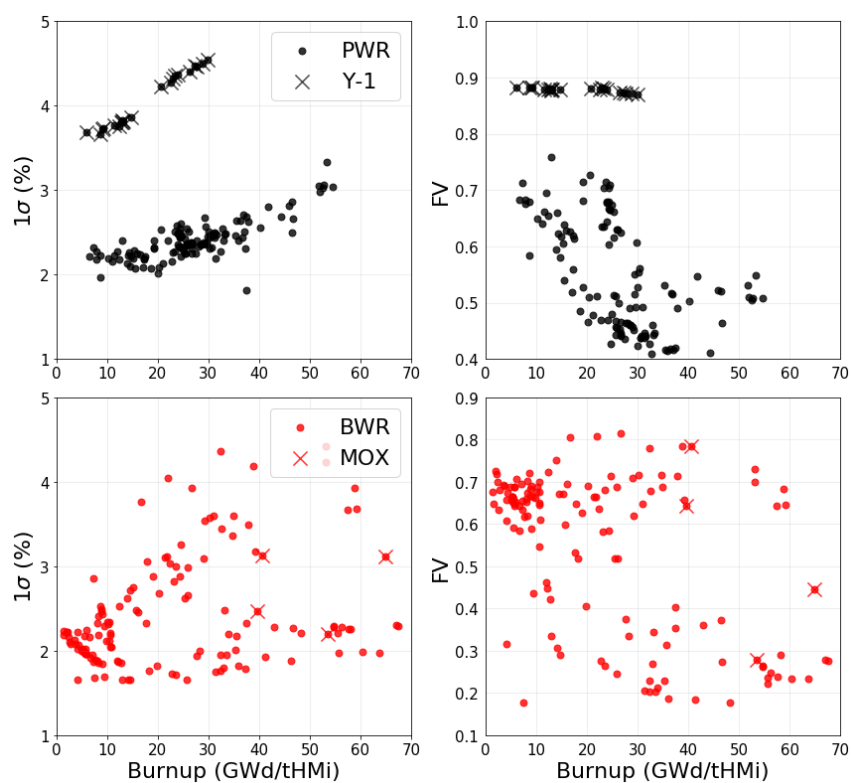


Figure 37. Same as Figure 35 for the Pu-239 concentration. Samples of Yankee-1 (PWR) and MOX samples (BWR) are marked with extra “X” symbol.

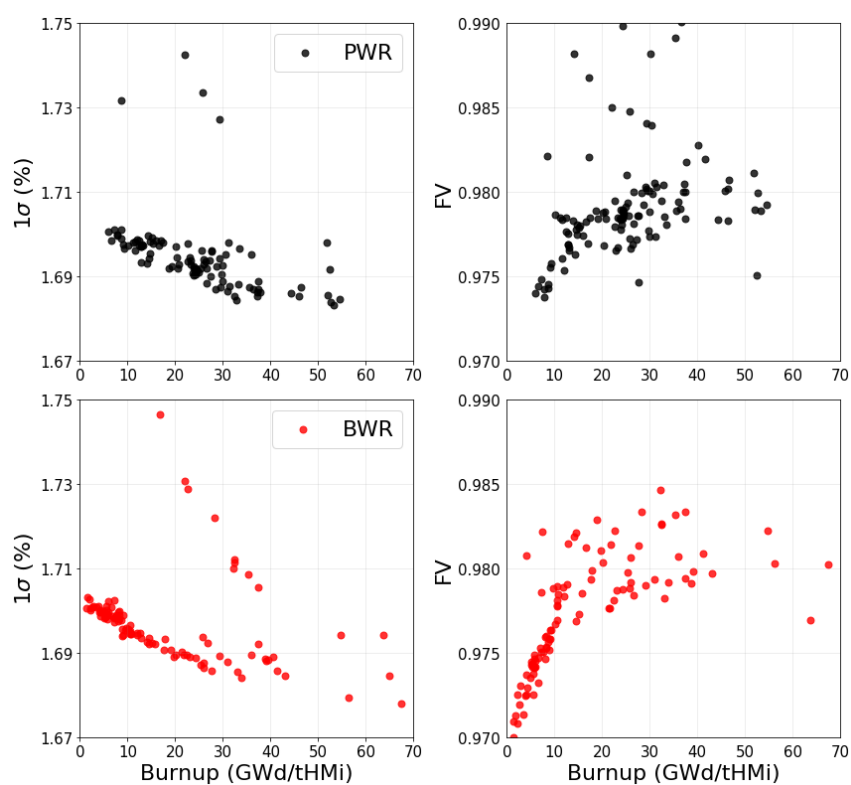


Figure 38. Same as Figure 35 for the Cs-137 concentration.

8.2 Uncertainties from nuclear data and fractional variances of XS, FY and DD

In the previous section, calculated uncertainties were decomposed into their two components, ND and DO origins. In this section, uncertainties from ND are further decomposed into their components. However, unlike the previous section in which all the benchmarks are analyzed, only 4 SFAs are analyzed in the following. They were selected to show differences in their burnup values and enrichments, coming from both BWRs and PWRs, see Table 14.

Table 14. SFAs considered for the analyses of the uncertainty contributions of XS, FY, and DD.

Reactor of origin	SFA ID	SFA Design	U-235 wt%	Burnup (GWd/tHMi)
PWR	F32	15x15	3.20	51.0
PWR	OE2	17x17	3.10	41.6
BWR	6432	GE 8x8	2.89	36.9
BWR	11495	SVEA-64	2.91	32.4

Uncertainties in XS, FY, and DD are propagated individually in the calculational models. Their FVs are shown in Figure 39, between 2 and 50 years after discharge. The uncertainties due to ND are smaller than the ones due to DO for the decay heat, U-235, and Cs-137 concentrations. The Pu-239 concentration show varying level of contributions of both ND and DO uncertainties, whereas the contributions of the former are higher at higher burnup. XS dominates the ND uncertainties for the decay heat, U-235, and Pu-239 concentration. The uncertainties in the Cs-137 concentration are mostly originating from the DD (74-76%) and FY (23-25%).

Uncertainties in the calculated U-235 and Pu-239 concentrations are dominated by uncertainties in neutron cross-sections. U-235 is mostly being removed through absorption reactions, both radiative capture and fission reactions. Pu-239 is mostly being produced through radiative capture in U-238, followed promptly by beta decay. Also, Pu-239 is mostly being removed through absorption reactions like the U-235. The mentioned reactions are neutron XS reactions, and uncertainties in the final concentrations of both U-235 and Pu-239 are dominated (>99%) by those uncertainties – measured using the FV. Cs-137 is a fission and decay product being affected by uncertainties in the FY and DD.

The decay heat has a different characteristic than the mentioned nuclides, as it results from the contribution of several decay heat producing nuclides. Decomposition of the uncertainties from ND into their components in a list of decay heat relevant nuclides is analyzed, focusing on the 14 most decay heat producing nuclides between 5 and 100 years after discharge. At these cooling times, the selected nuclides contribute more than 95% to both the calculated decay heat values and decay heat uncertainties in the analyzed SFAs. The FVs of the XY, FY, and DD in the uncertainties from ND are shown in Figure 40. Differences between the production routes of decay heat relevant nuclides result in different contributions of XS, FY and DD to uncertainties due to ND. For the actinides (AC), ND variances are largely due to XS (0.97-0.99) and, to a minor extent, to DD (0.01-0.03). For the fission and decay products (F/DPs), they show large contributions from FY and DD uncertainties. Isotopes such as Cs-134 and Eu-154 show

pronounced contributions from XS uncertainties compared to the other F/DPs, and almost no dependence on FY and DD uncertainties. The production of the latter nuclides results mainly from neutron capture in Cs-133 and Eu-153 [91]. In general, the F/DP are shorter lived compared to the AC. Their concentrations to the calculated decay heat values decrease at longer the cooling times, and also their contributions to the calculated decay heat uncertainties.

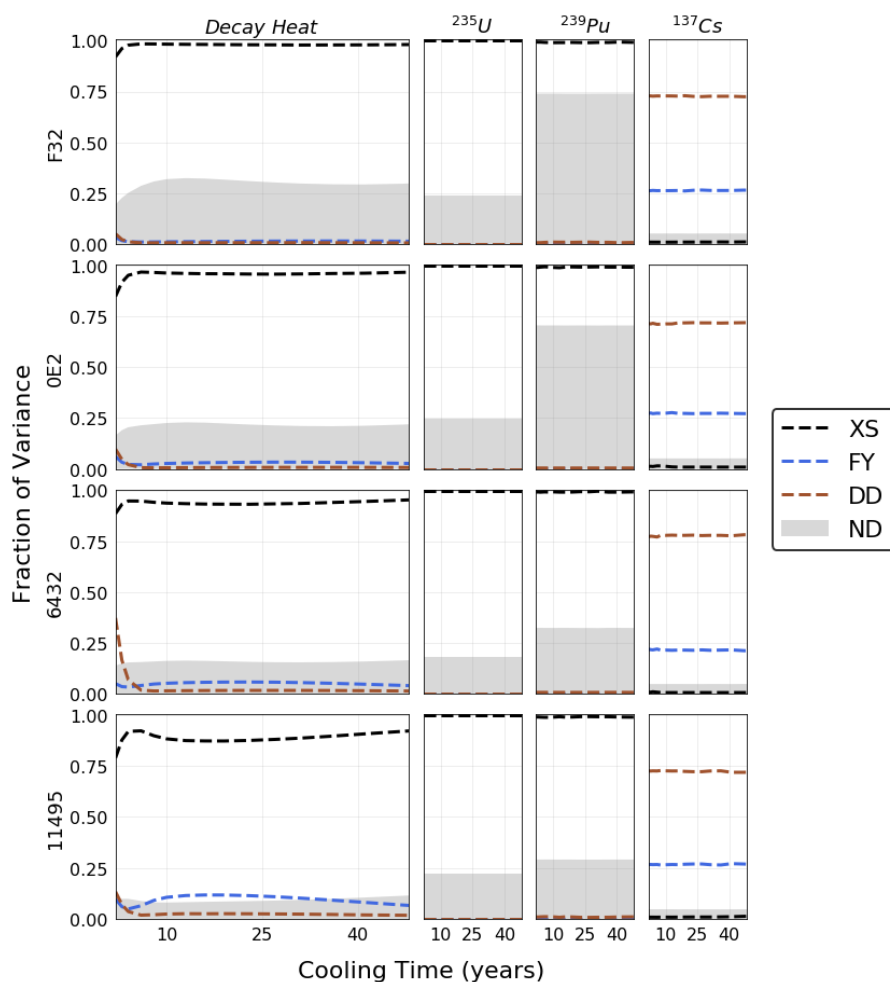


Figure 39. Contribution of uncertainties from ND to decay heat, U-235, Pu-239, and Cs-137 total calculated uncertainties (shaded grey area), and individual contributions of XS, FY, and DD to uncertainties from ND. The SFAs are ordered by burnup (top to bottom). The minimum and maximum cooling times are 2 and 50 years.

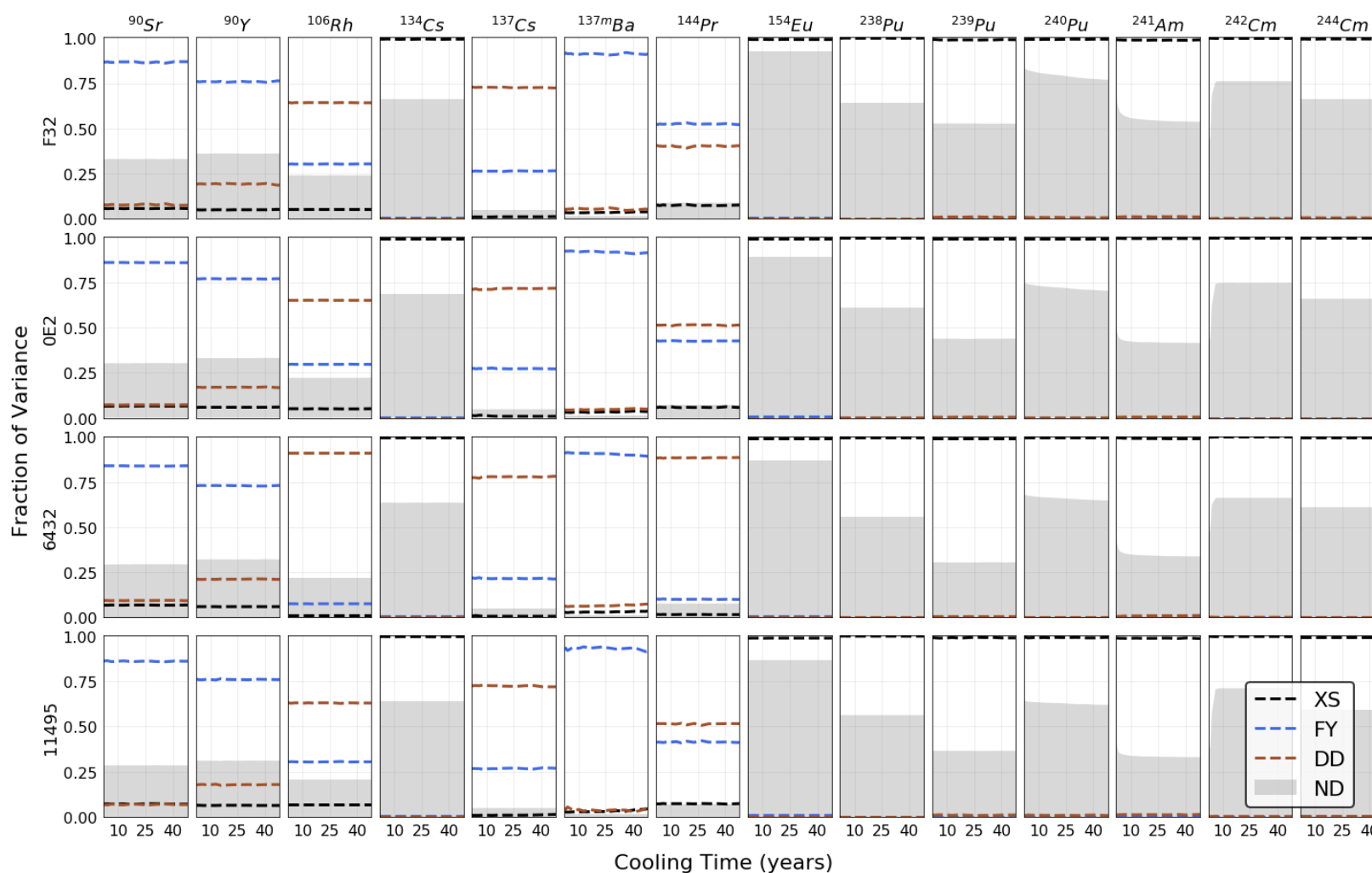


Figure 40. Same as Figure 39 for selected decay heat relevant nuclides.

8.3 Relevant design and operational parameters

In the previous section, the relevant ND uncertainties were presented, and in this section the relevant DO parameters are presented. The previous analyses of ND uncertainties using the FV is computationally intensive, it requires perturbing each component individually. For such a reason, the previous analyses were conducted on selected benchmarks. Instead of the FV, the relevant DO parameters are analyzed through their correlations with the calculated characteristics.

In each benchmark, DO parameters in the Polaris model are perturbed altogether using Sampler as described in Section 4.3. Then, the correlation is calculated between each perturbed DO parameter and the perturbed calculated value, resulting in the correlation coefficient for each DO parameter, also in each benchmark. As shown in Figure 41, perturbing the burnup results in perturbations in the calculated U-235 and Pu-239 concentrations. The benchmarks in Figure 41 are A1-I2, assembly B23 of the Gundremmingen-1 reactor (BWR), and G10_4, assembly D01 of the Turkey Point-3 reactor (PWR). Changes in the burnup in a perturbed Polaris model are also accompanied by changes in other DO parameters, such as water density. The altogether perturbation of the DO parameters causes significant scatter of the calculated concentrations, being affected by multiple DO parameters. Also, benchmarks have different characteristics, *e.g.*, BWRs vs. PWRs and also burnup values. These differences change the levels of correlations between the calculated concentrations and the perturbed DO parameters, resulting in a distribution of the correlation values for the same DO parameter in different benchmarks.

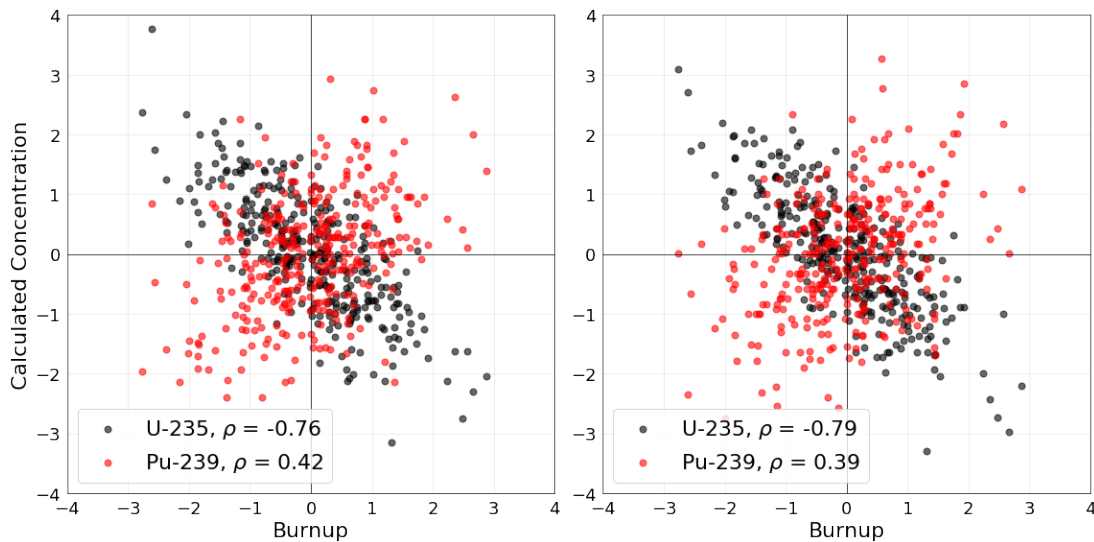


Figure 41. Perturbed concentrations of U-235 and Pu-239 vs. the burnup perturbation factor – both axes are centered and normalized. Left plot is benchmark A1-I2 (BWR), and the right plot is benchmark G10_4 (PWR).

Following this approach allowed conducting the analyses without repeating the calculations, perturbing individual components. However, the interpretability of the results is limited compared to evaluating the FVs. The calculated characteristics are sensitive to several DO parameters, being perturbed all together at once and independently from each other.

Figure 42 shows plots of the Pearson correlation between the calculated characteristics and the DO parameters. Other DO parameters, not presented in the figure and mentioned in Section 4.3, correlate with the plotted DO parameters, and are excluded (such as the coolant temperature, which correlates with the coolant density in the PWRs). One can observe that the burnup is a highly relevant or influential parameter, being correlated with all of the analyzed characteristics. For the decay heat and Cs-137 concentration, they largely and positively correlate with the burnup and the variations of the resulting correlation coefficients are constrained in narrow ranges. For the U-235 and Pu-239 concentrations, the resulting correlations with the burnup span wider ranges, whereas they are mostly negative for U-235 concentration and positive for Pu-239 concentration. The decay heat and Cs-137 concentration tend to show significantly lower correlations with the other DO parameters. Whereas, for the U-235 and Pu-239 concentrations, various levels of correlations are observed with the other DO parameters. The initial enrichment is a relevant DO parameter for the calculated final U-235 concentration, showing largely positive correlations. Parameters inducing neutron spectral changes such as the coolant density and the cladding outer radius (*i.e.*, inner radius and thickness) affect the Pu-239 concentration as well. The effects on the correlation of both the coolant density and the cladding radius tend (on average) to be on the opposite side of the correlation plots. The coolant density has a larger impact on both the U-235 and Pu-239 concentrations in the BWRs compared to the PWRs. The implemented uncertainties in the coolant density in the BWRs are significantly larger than the PWRs (see Section 4.3). In the PWRs, the uncertainty in the water density is usually less than 1%, whereas it is 6% for the void fraction in the BWRs.

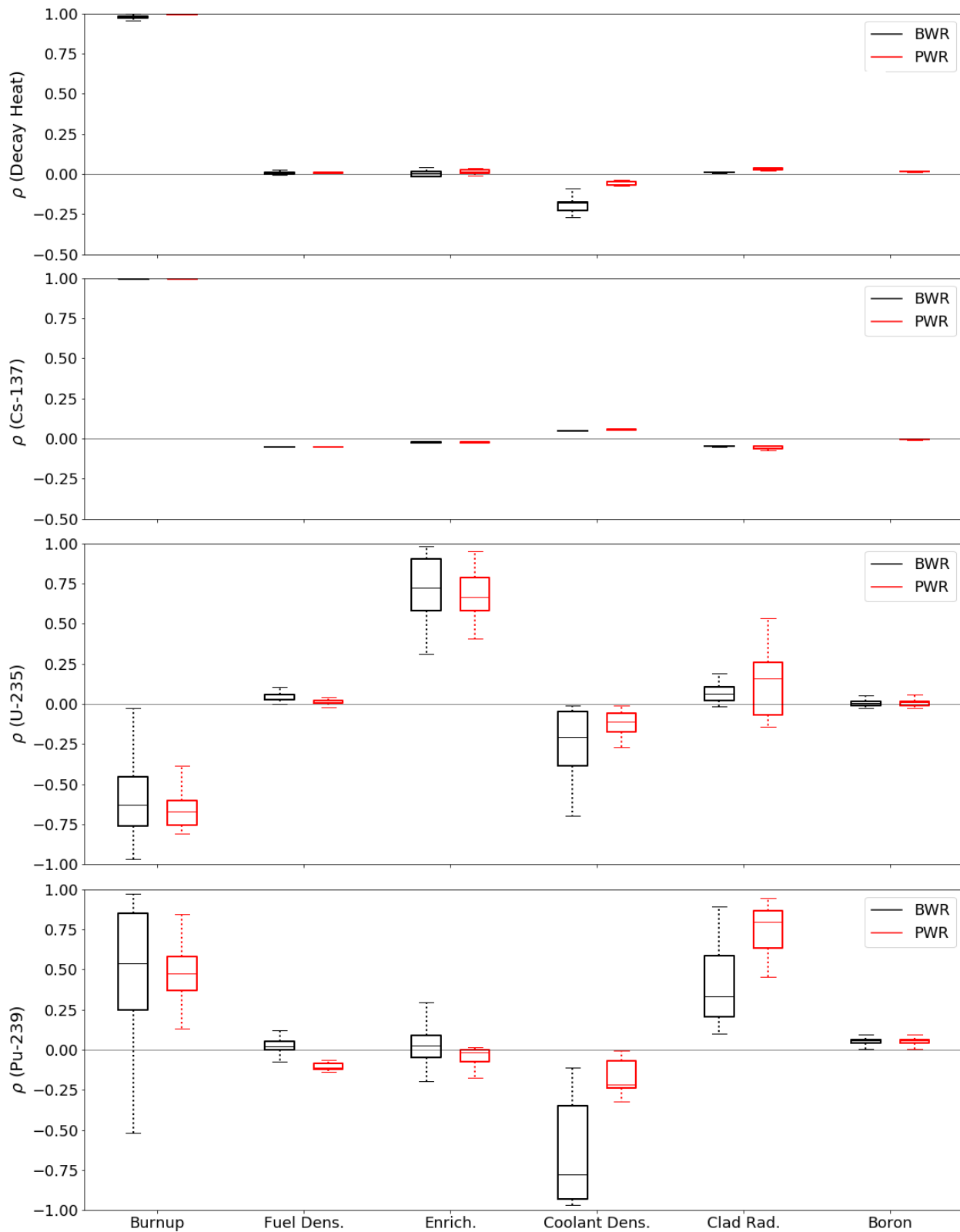


Figure 42. Correlations of the calculated characteristics with the DO parameters. The boxes show the median and the first and third quartiles (Q1 and Q3). The whiskers are at $Q1 - 1.5 \times IQR$ and $Q3 + 1.5 \times IQR$ (IQR is the interquartile range).

8.4 Assumptions of burnup uncertainties

The burnup has shown large correlations with all of the analyzed characteristics. In this section, the assumptions on the burnup uncertainties are analyzed on a selected benchmark from the decay heat data (SFA 6432 of Ringhals-1). The results are presented for cooling times between 2 and 100 years after discharge. Several cases implementing different assumptions on the burnup uncertainties are described in Section 4.3, and in the following, the resulting standard deviations are compared to the ones from the reference assumptions (listed in Table 7). The number of perturbations implemented in the models discussed in this section is 400. Such number of perturbation results in a standard error of 5% for the presented standard deviations.

Case 1 represents a 50% increase in the SD of all variables (including the burnup), resulting in an increase in the SD of all characteristics by approximately 50%, *i.e.*, the final variances increased by almost the same percentage as the initial variances. The other cases (cases 2 to 6) are shown in Figure 43. Case 2, considering a uniform distribution instead of the reference normal one, shows approximately the same SD for all the calculated characteristics, *i.e.*, both have the same variance.

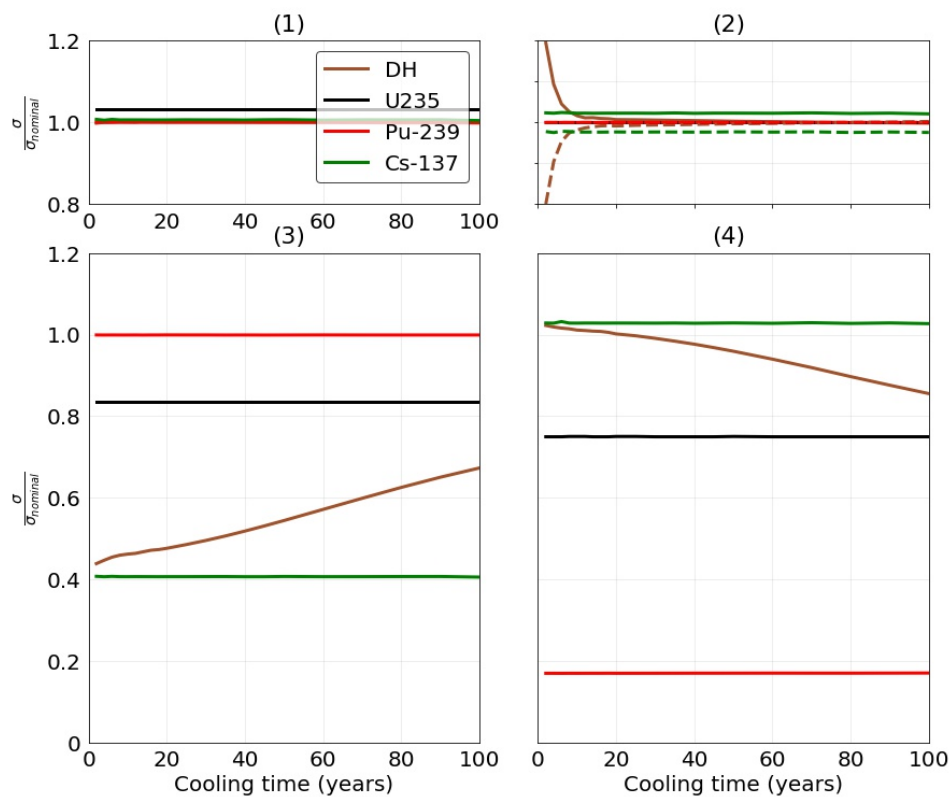
The cases 3 and 4 have the same burnup uncertainties, originating largely from uncertainties in the power in later cycles (case 3), and in earlier cycles (case 4). Case 3 shows increased uncertainties in the decay heat for short-term decay, and vice versa for case 4. In both cases, for longer decay time, uncertainties of the calculated characteristics approach the reference case.

In case 5, where cycle-wise average powers are sampled independently of each other, one can observe that the variance of the final burnup is also lower than the reference case, where correlations between cycle-wise powers ensured the final burnup variance. The decay heat uncertainties are significantly lower than the reference case for short cooling times, where the contribution of decay and decay heat uncertainties largely come from F/DP. At longer cooling times, the contributions of AC to decay heat and decay heat uncertainty increase, being sensitive to other perturbed parameters, in addition to the burnup. Pu-239 uncertainties are nearly unaffected. U-235 and Cs-137 uncertainties, which correlate significantly with burnup, are significantly reduced, particularly for the latter isotope.

Considering only uncertainties in the power and the fuel temperature (case 6) results in a gradual decrease in the decay heat uncertainty the longer the decay time. The decrease in uncertainty mainly results from the decrease in uncertainties of the AC, being sensitive to other variables that induce spectral changes (excluded in this case). The uncertainty of Pu-239 concentration is significantly reduced in this case, and the uncertainties for the U-235 and Cs-137 concentrations (which correlate significantly with burnup) are not strongly reduced. U-235 uncertainties are 0.75 of the reference values, and Cs-137 uncertainties are approximately similar to the reference case.

The power uncertainty is a significant contributor to the resulting uncertainties in the analyzed characteristics. Assumptions on these power uncertainties are relevant, however, to different

extents. The assumption on the form of the distributions (normal vs. uniform), while maintaining the same variance, has shown to be insignificant on the resulting uncertainties. Different allocations of the power variances along the irradiation history, while maintaining the same variance in the burnup, also have shown insignificance effect on the uncertainties. The assumption that cycle powers do not correlate leads to reduced overall burnup uncertainties. As a conclusion, the most relevant assumption on the power is the variance of the burnup. Accurate power history and reduction of uncertainties in the SFA burnup would result in a significant reduction in the calculated-related uncertainties of the decay heat, U-235, and Cs-137 concentrations. The Pu-239 concentration is mostly affected by parameters inducing spectral changes, and burnup uncertainties contribute less significantly to its uncertainty compared to the other isotopes.



- (1) Uncertainties have a uniform distribution with a variance equal to the reference case.
 (2) Power uncertainties are allocated in later irradiation cycles (solid line), or earlier cycles (dashed line).
 (3) Uncorrelated cycle powers.
 (4) DO uncertainties originate from power and fuel temperature only.

Figure 43. Relative uncertainty for cases implementing different assumptions on the power and burnup uncertainties (relative to the reference case of SFA 6432 of Ringhals-1). The minimum and maximum cooling times are 2 and 100 years.

8.5 Correlations between benchmarks

In this section, the correlations between benchmarks are introduced, based on perturbations in the ND and the DO parameters. Also, these correlation matrices later on form the design matrices used to predict the bias of the benchmarks (see Chapter 11). As discussed in Section

8.3, the burnup is a relevant DO parameter that correlates significantly with all of the calculated characteristics, and the discussed correlation matrices are ordered according to the burnup (in a descending order from top to bottom and left to right). For example, the top-left corner of the correlation matrix will show the correlation between high burnup benchmarks, and the bottom-left corner will show the correlation between high and low burnup benchmarks.

9.4.1. *Decay heat correlations*

The correlations between the calculated decay heat values in both the Clab and GE-Morris benchmarks are shown in Figure 44. All correlations between the decay heat values are positive. Various levels of correlations are observed, which are significantly high due to perturbations in the DO parameters (the lowest value is 0.96). The corresponding correlations due to perturbations in the ND are lower, down to 0.24. These correlation matrices are obtained between the calculated decay heat values at the times of measurements, spanning wide ranges (the GE-Morris benchmarks are measured between 2 and 11 years after discharge, whereas Clab benchmarks are measured between 11 and 27 years after discharge). As discussed in Section 8.2, the decay heat results from the contribution of various nuclides. At short cooling times, various short-lived F/DPs are decaying at different rates, contributing more to the decay heat than the actinides. At longer cooling times, the contribution increases from the longer-lived actinides. The contributions to the calculated decay heat values from the analyzed decay heat relevant nuclides change in the range of the analyzed cooling times [92]. The Clab benchmarks are also plotted separately in Figure 44, showing decreased correlations between benchmarks having differences in their burnup (based on the ND perturbations) and still significantly high correlations based on perturbations of the DO parameters. The lowest correlations in the Clab benchmarks are 0.96 and 0.45, for both correlation matrices based on the DO and ND perturbations, respectively. Also, the benchmarks are highly correlated (with respect to the calculated decay heat) due to combined perturbations in both the ND and DO parameters. Differences between these SFAs, such as their burnup and cooling times, can change the correlations, as they differently impact nuclide-wise contributions to the decay heat.

9.4.2. *Correlations of the Cs-137, U-235, and Pu-239 concentrations*

The correlation matrices of the calculated isotopic concentrations show variable levels of correlations between the benchmarks, as shown in Figure 45. The followings are the minimum correlations in each correlation matrix (DO and ND matrices, respectively):

1. U-235: (0.01, 0.43),
2. P-239: (-0.97, 0.59),
3. Cs-137: (-0.04, 0.01).

Correlations in U-235 and Pu-239 concentrations resulting from perturbing the DO parameters are significantly lower than the ones from ND. The U-235 matrices show that benchmarks having similarity in their burnups correlates largely with each other, due to perturbations in both the DO

parameters and the ND. The Pu-239 matrix based on perturbations in the ND shows similarity to the U-235 matrices, however, the DO-based matrix shows variable levels of correlations. In perturbing the DO parameters, several parameters correlate with the Pu-239 concentration, as explained in Section 8.3. The Pu-239 correlation matrix based on the DO perturbations is ordered by burnup; other parameters highly correlated with the Pu-239, such as water density and cladding radius, can also change the observed levels of correlations in benchmarks having similarities in their burnups. Very low correlations are observed between the concentrations of Pu-239 in the MOX-based samples and the rest of UO₂-based samples, due to perturbations in either ND or DO parameters. The Cs-137 matrix based on the ND perturbations shows similarity in the burnup trend to the U-235 matrices. However, the matrix based on the DO perturbations shows excessively high and skewed distribution of the correlation values. The minimum observed correlation in the latter matrix is around zero, however, approximately 95% of the observed correlations are above 0.97. The Cs-137 matrix based on ND perturbations show similar skewness, however to a lesser extent, and approximately 95% of the observed correlations are above 0.72. Also, very low correlations are observed between the concentrations of Cs-137 in the MOX-based samples and the rest of UO₂-based samples, due to perturbations in either ND or DO parameters.

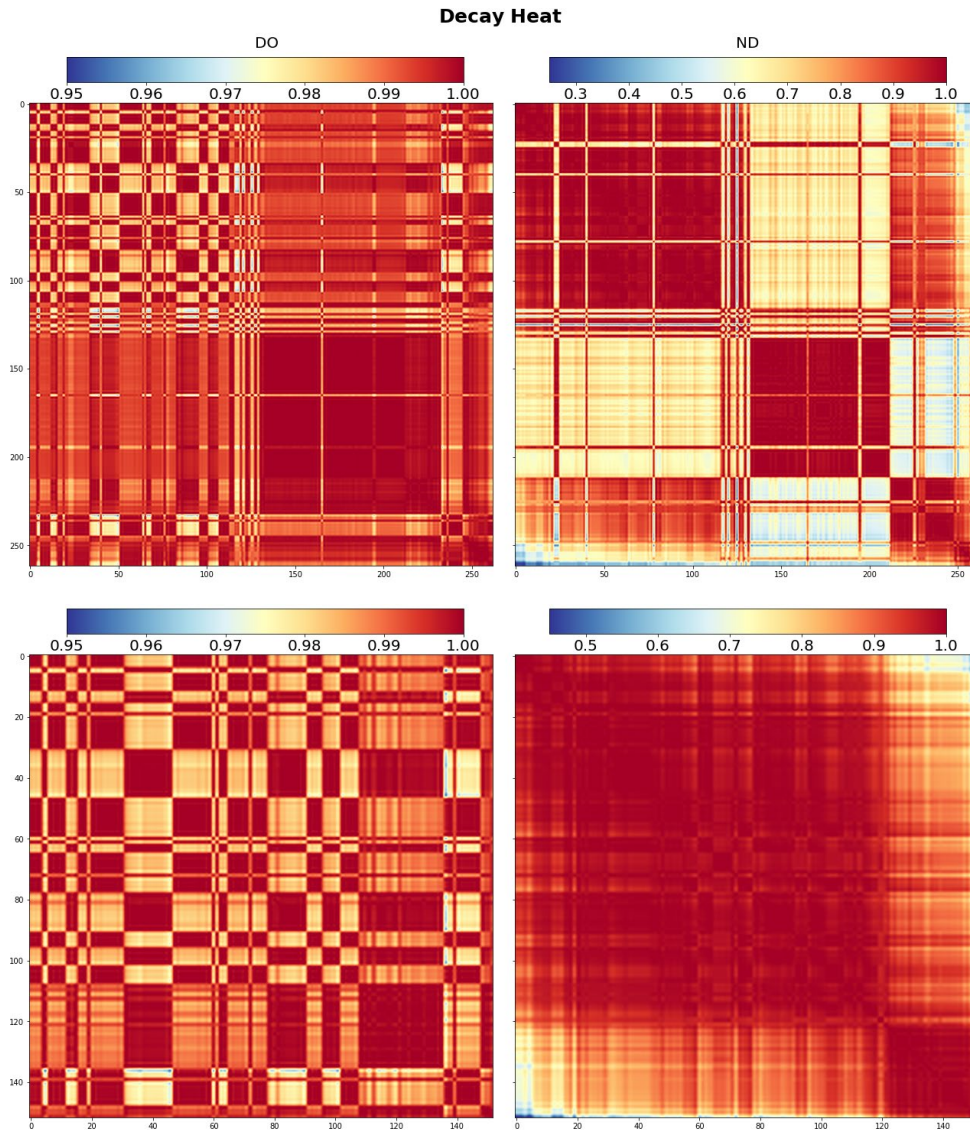


Figure 44. Correlations between the calculated decay heat values of the Clab and GE-Morris benchmarks (top row), and only the Clab benchmarks (bottom row). The matrices are ordered according to the burnup (top to bottom and left to right). The left column shows correlations due to perturbing the DO parameters, and the right column shows correlations due to perturbing the ND.

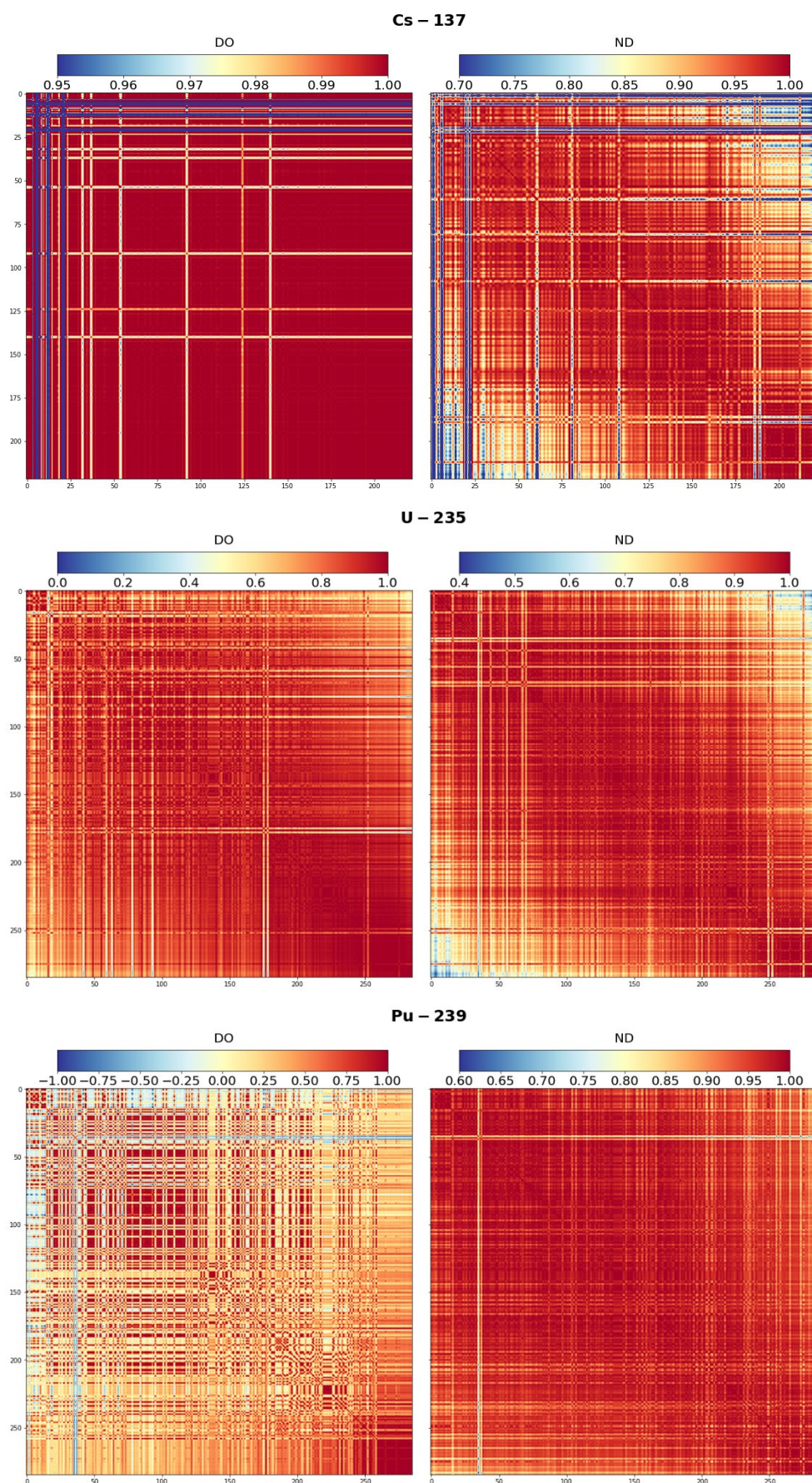


Figure 45. Correlations between the calculated concentrations of Cs-137, U-235, and Pu-239. The matrices and columns are ordered similar to Figure 44.

Chapter 9 Significance of the Bias Based on the Validation Data

The significance of the average bias is analyzed using non-parametric tests, as described in Section 5.1. The null hypothesis implies that differences between calculations and measurements are random differences, *i.e.*, due to chance, whereas the alternative hypothesis implies systematic differences. The statistical analyses in this chapter use the validation results of the Polaris code, except for Section 9.1, which are based on both Polaris and ORIGEN codes.

The benchmarks have properties potentially leading to differences between the biases. It is assumed in this study that differences in between PWRs and BWRs can lead to differences in the bias. The BWRs are typically more challenging in their modelling, given their geometrical complexity and neutronic heterogeneity. Also, some of their DO parameters can be more uncertain than the PWRs [56], such as the coolant density, eventually leading to higher uncertainties in the biases. A generic observation from sections 7.1 to 7.4: the bias variance of the BWRs is larger than that of the PWRs. The data are then split based on the reactor type. The Shapiro-Wilk normality test was conducted on the bias of each category, and the p -values show that the biases are not normal at a significance level of 0.05, as listed in Table 15. Nonparametric tests are applicable in this case [70].

Table 15. p -values of the Shapiro-Wilk normality test conducted on the BWR and PWR bias data.

Characteristic	BWR	PWR
Decay Heat	0	0.014
Cs-137	0	0.016
U-235	0	0
Pu-239	0	0.001

The null distributions generated using bootstrapping on the bias data are shown in Figure 46, showing also the 95% normal confidence intervals (CI). The null hypothesis is rejected when the defined CI do not contain a zero bias. For all of the observed biases of the PWR sections, the p -values are approximately zero. Therefore, the null hypothesis is rejected, and the alternative is accepted that the PWR calculations are systematically or significantly different from the measurements. These observed average biases are extreme with respect to these null distributions (*i.e.*, they are statistically significant). Alternatively, the observed average biases of all the BWR sections have p -values greater than the significance threshold. Therefore, the tests

failed to reject the null hypothesis. The calculations on the BWRs are not systematically or significantly different from the measurements and the observed biases are likely to be due to chance or result from randomness in the data. The BWR data show that it is likely to have a random component, large enough, to prevent an identification of systematic difference (if existing). Permutation tests were also conducted, and the results are provided in Appendix IV. The conclusions are similar to those of the bootstrap tests, however, at slightly different p -values.

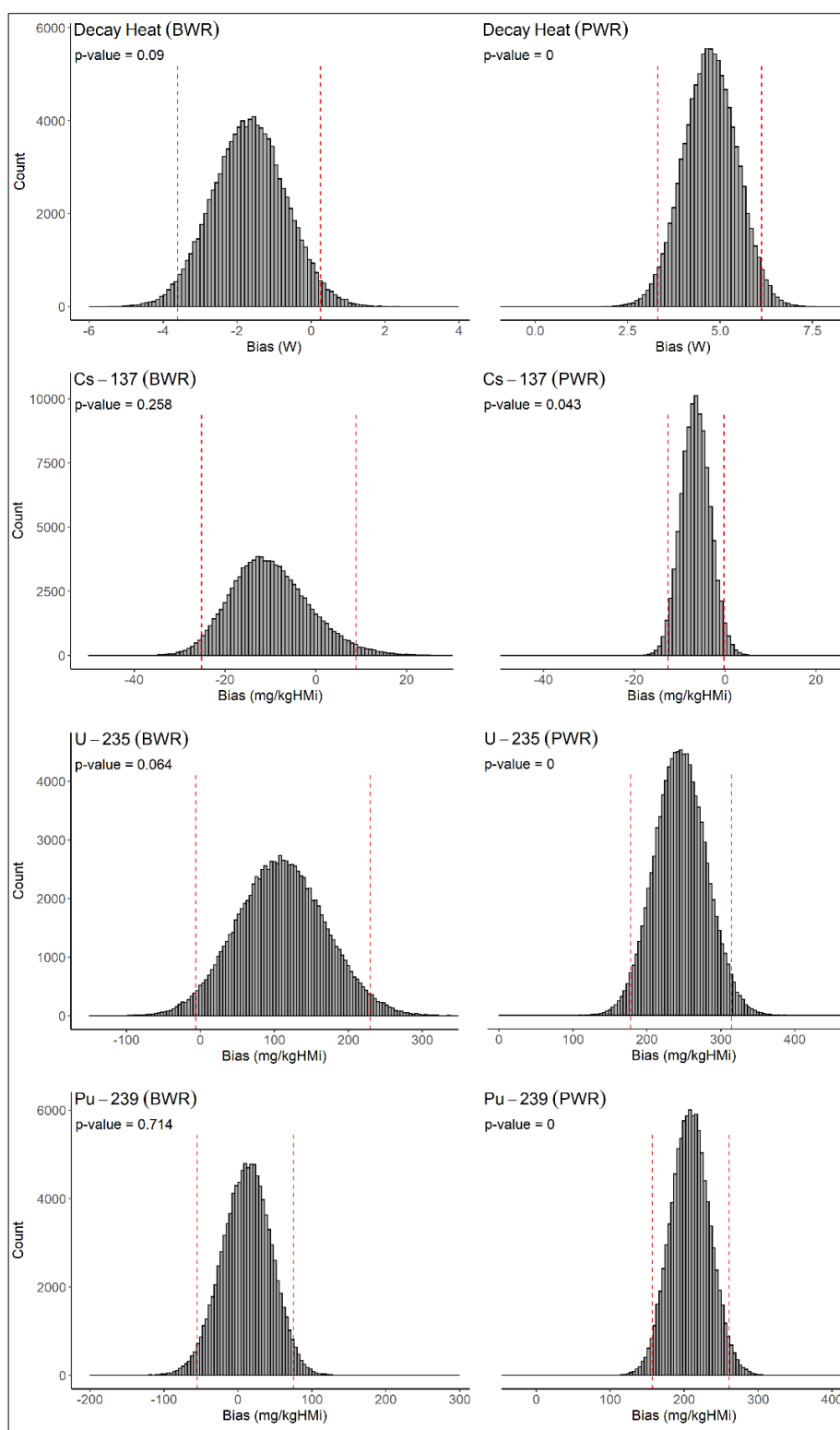


Figure 46. Bootstrap distributions of the average biases (the red lines are 95% normal CI). The distributions are centered near the observed average biases and testing their significance proceeds by observing whether or not a zero average bias falls within the chosen CI.

9.1 Significance of the bias based on simultaneous testing

The significance of the conducted non-parametric tests can be increased through setting a lower value for the significance threshold, such that the null is rejected, and the alternative is accepted at more extreme observations. However, the choice of the significance threshold is arbitrary.

A different approach is analyzed, requiring more evidence from the data against the null-hypothesis, through multiple hypotheses testing. The significance of the biases obtained using two codes is simultaneously analyzed. The simultaneous hypothesis testing is applied on the decay heat data only. The first calculations are based on the Polaris code (as previously analyzed), and the second calculations are based on the ORIGEN code (SCALE 6.2.3), described in Appendix V. The results are shown in Figure 47. The calculations of Polaris and ORIGEN show some degree of similarity, *i.e.*, possible trends in their calculations. Also, Figure 48 shows that the Polaris and ORIGEN calculations are more similar to each other than the similarity between the Polaris calculations and the measured values. The RMSE between the Polaris and ORIGEN values is 3 W, compared to 12 W between the Polaris calculations and the measured values. The averages of the B s and C/E s of the calculations of both Polaris and ORIGEN are listed in Table 16.

The ORIGEN code is different from Polaris, such that they are independent to some extent. However, the differences are in the calculational method and the modelling assumptions. The two calculational sequences still have large similarities, *e.g.*, both use the same SCALE ND libraries, and the same evaluations of the irradiation data and the measurements. Inclusion of an additional code relying on different ND, and access to irradiation data and measurements evaluated independently can allow further improvements to the method by reducing the dependencies between the results.

The alternative hypothesis that the calculations are systematically or significantly different from the measurements is accepted only when the two calculations show such evidence. The null hypothesis in this case implies that the differences between the measurements and the calculations are random differences (simultaneously in the calculations of the two codes). Again, the tests are conducted at a significance level of 0.05.

Table 16. C/E and B for the decay heat calculations using Polaris and ORIGEN, along with 1σ .

Dataset	Code	$\overline{C/E}$	\overline{B} (W)
Clab: BWR (81)	Polaris	1.010 ± 0.026	1.3 ± 3.6
	ORIGEN	1.003 ± 0.025	-0.1 ± 3.4
Clab: PWR (71)	Polaris	1.015 ± 0.012	6.5 ± 5.2
	ORIGEN	1.019 ± 0.012	8.5 ± 5.8
GE-Morris: BWR (96)	Polaris	1.000 ± 0.114	-4.2 ± 17.1
	ORIGEN	1.009 ± 0.115	-1.9 ± 17.2
GE-Morris: PWR (14)	Polaris	0.994 ± 0.009	-4.3 ± 5.7
	ORIGEN	1.007 ± 0.009	4.0 ± 6.2

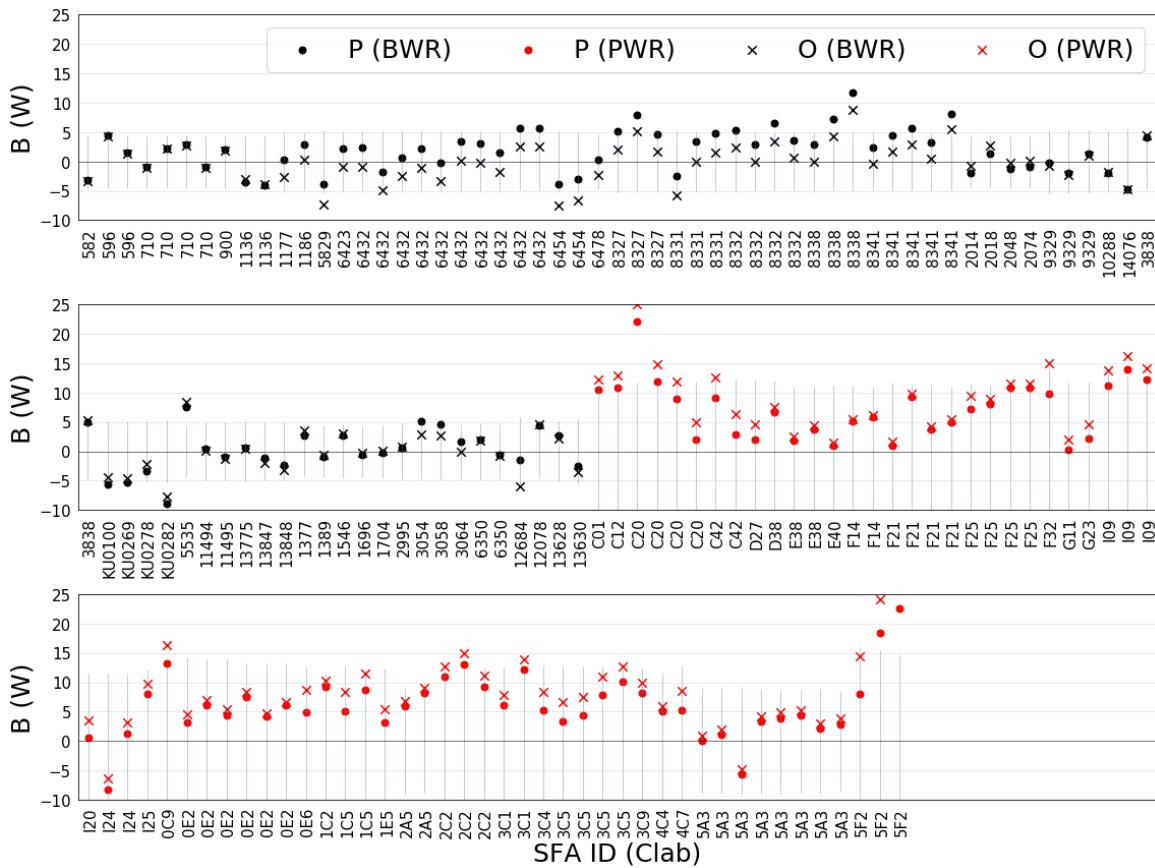


Figure 47. Decay heat biases calculated using Polaris and ORIGEN (P and O) – shown only for the Clab benchmarks. The BWRs are shown in black color, and the PWRs are in red. The uncertainty bars are experimental uncertainties (2σ).

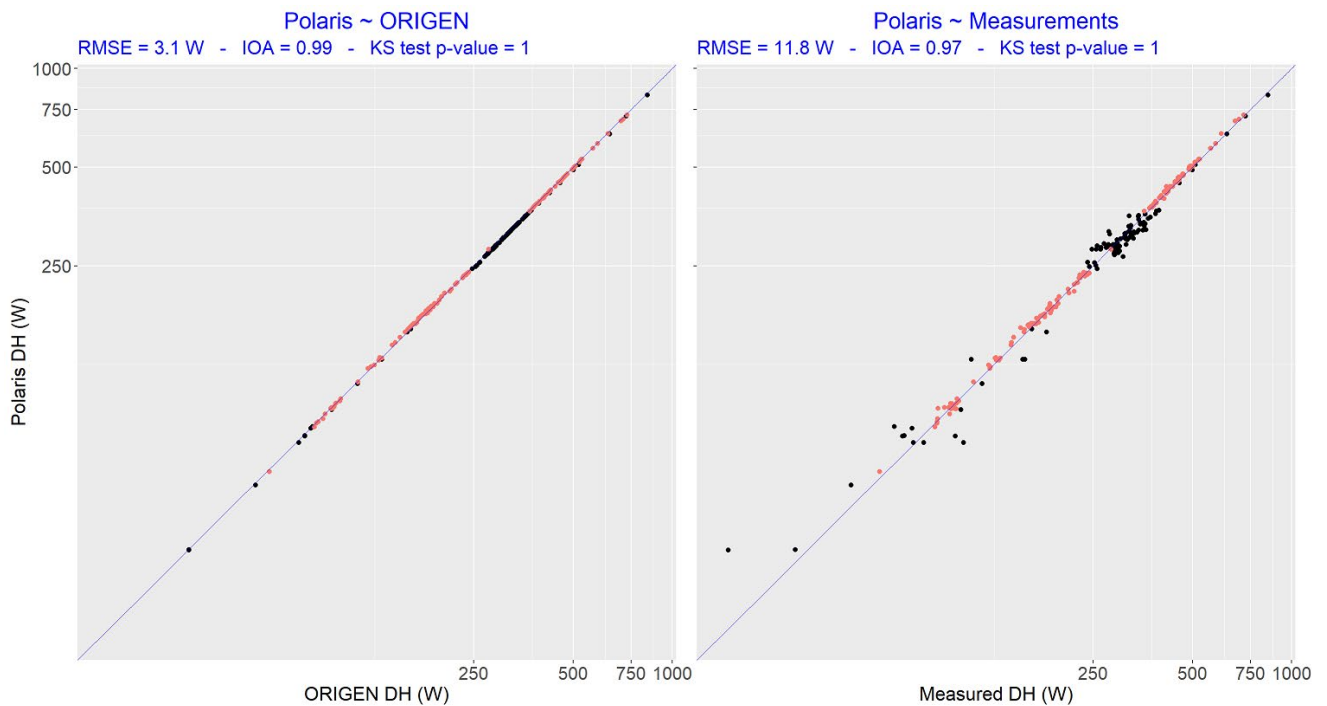


Figure 48. Calculated decay heat values (DH) using Polaris vs. ORIGEN (left), and vs. the measured values (right). The data belong to both the Clab and GE-Morris benchmarks. Linear regression results in the presented RMSE values. The blue lines have a slope of unity.

The p -values of the Shapiro-Wilk normality test are listed in Table 17. Similarly, the biases in each category are not consistently normal using both codes at a significance level of 0.05.

Table 17. p -values of the Shapiro-Wilk normality test conducted on the Polaris and ORIGEN decay heat bias data.

Lab.	Reactor	Polaris	ORIGEN	Normality test
Clab	PWR	0.01	0.01	Reject H0
	BWR	0.97	0.63	Fail to reject H0
GE	PWR	0.21	0.75	Fail to reject H0
	BWR	0.11	0.09	Fail to reject H0

The analyzed data are interpreted as paired data—*i.e.*, the two calculations and the corresponding measurements are conducted on the same units. This interpretation allows to conduct the permutations in the two datasets simultaneously. For example, in a random permutation, sampled calculations of the two codes are simultaneously assigned the corresponding measured values. Both distributions are centered near zero, and the alternative is tested by counting the observations that are at least more extreme than the observed average biases for both codes (*i.e.*, two-sided test setting). The null hypothesis is rejected, and the alternative is accepted if less than 5% of the observations on the joint distribution are more extreme than the observed biases. Alternatively, in bootstrap testing, the null hypothesis is rejected, and the alternative is accepted if the two codes show that their 95% bootstrap CI do not contain an average bias of zero at the same time. The applied technique belongs to simultaneous testing techniques [70].

The permutation distributions of the average biases are shown in Figure 49 (first and third rows), plotted as joint distributions. The red lines mark the observed average biases by both codes on each validation category. The overall (*i.e.*, the simultaneous testing) p -values for the PWR benchmarks of both Clab and GE-Morris are less than the set threshold, meaning that the null hypothesis is rejected, and the alternative is accepted that the two codes (simultaneously) are systematically or significantly different from the measurements. In contrast, the BWR sections of the data yield p -values > 0.05 , meaning that the test failed to reject the null hypothesis and there is no evidence from the BWR data that the two calculations are simultaneously different from the measurements. The p -values of the permutation tests are listed in Table 18.

Table 18. Simultaneous testing p -values of the permutation tests.

Lab.	SFA type	Polaris	ORIGEN	Combined test	Simultaneous test result of H0
Clab	BWR	0.002	0.872	0.872	Fail to reject H0
	PWR	0	0	0	Reject H0
GE-Morris	BWR	0.020	0.295	0.295	Fail to reject H0
	PWR	0.014	0.037	0.049	Reject H0

The bootstrap distributions of the average biases are also shown in Figure 49 (second and fourth rows). The shaded regions are 95% normal CI. Similar to the permutations, the null

hypothesis is rejected for the PWRs, and it is failed to reject it for the BWRs. The conclusions drawn from the bootstrap tests are similar to those from the permutation tests, however with differences in the p -values (listed in Table 19).

Table 19. Simultaneous testing p -values of the bootstrap tests.

Lab.	SFA type	Polaris	ORIGEN	Combined test	Simultaneous test result of H0
Clab	BWR	0.001	0.874	0.872	Fail to reject H0
	PWR	0	0	0	Reject H0
GE-Morris	BWR	0.018	0.290	0.302	Fail to reject H0
	PWR	0.001	0.018	0.018	Reject H0

The average biases for the two codes in the Clab and GE-Morris PWRs are systematically different from zero, and less likely to be due to random effects. In contrast, the BWRs show that the average biases can be due to random effects. Such observation of the distinction of the PWRs from the BWRs can originate from using experimental measurements having low uncertainties in the PWRs (which typically have larger values of the measured decay heat and lower relative uncertainties). Also, the calculated biases of the PWR categories can have a large systematic component with respect to the random component such that this systematic difference can be identified. The BWR sections of the data are likely to have a random component, large enough, to prevent identification of systematic difference (if any) at the chosen significance level.

Testing the Polaris data alone would have resulted in rejection of the null hypothesis for all validation categories, *i.e.*, Polaris data show that the calculated values are systematically different from the measurements. However, simultaneous testing based on both Polaris and ORIGEN requires more evidence from the data to reject the null hypothesis, and only the PWRs show such evidence.

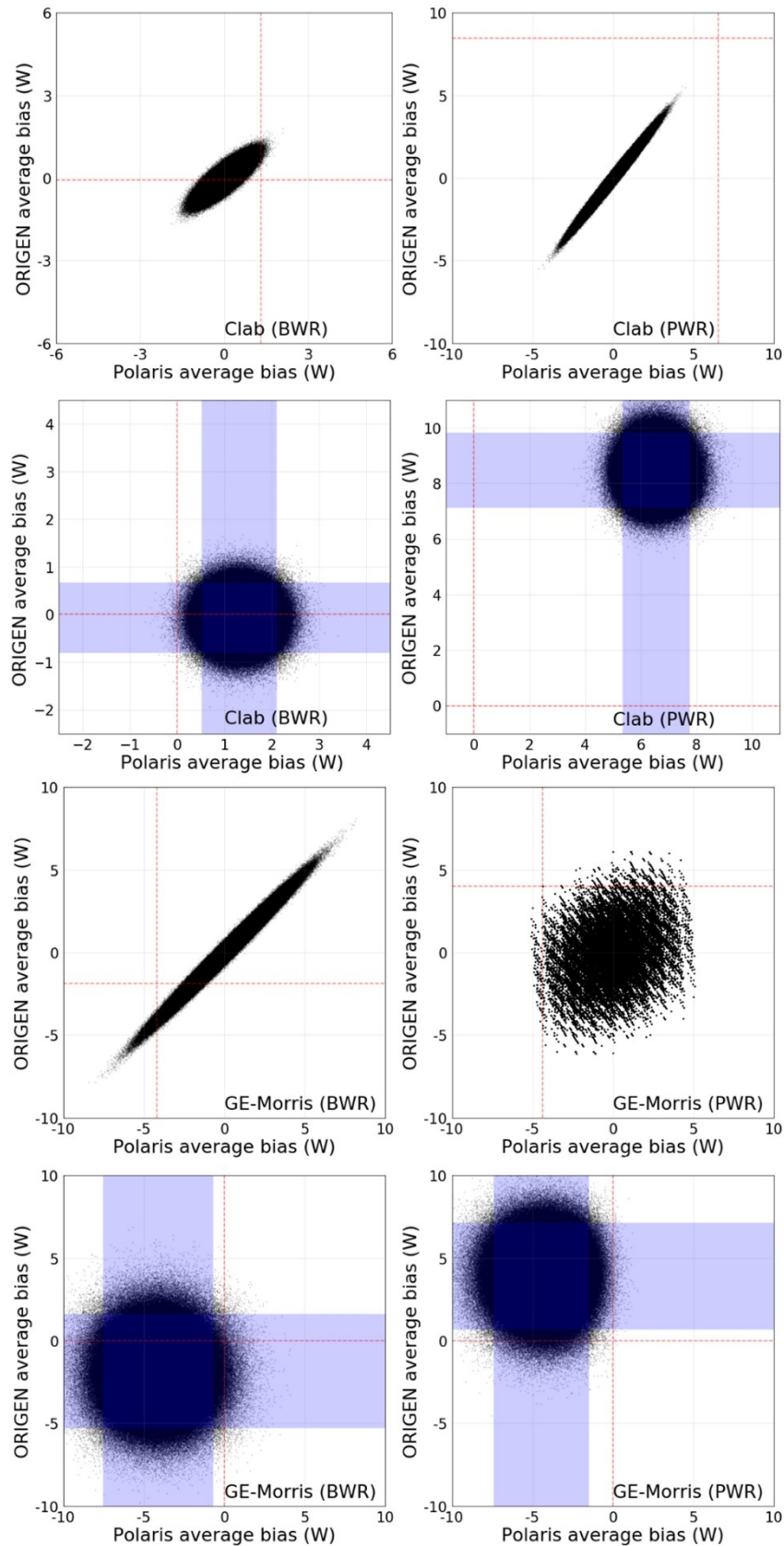


Figure 49. Permutations distributions of the average biases of Clab benchmarks (first row), and the bootstrap distributions (second row). The corresponding distributions of the GE-Morris benchmarks are in the third and fourth rows. BWRs are left and PWRs are right. Red lines mark the actually observed average biases in the permutation plots, and zero biases in the bootstrap plots.

Chapter 10 Significance of the Bias Based on the Validation and Uncertainty Data

Comparing the observed bias to uncertainty allows testing a hypothesis that the bias is insignificant (given the uncertainty). Standardizing the bias can be based on the calculated uncertainties only, or combined uncertainties of the calculations and the measurements. The former is straightforward since they are obtained for all benchmarks in this study. The analysis based on the latter uncertainties will be feasible only for the decay heat benchmarks since experimental uncertainties are not available for all of the PIE benchmarks. The statistical analyses in this chapter use the validation and uncertainty analyses results of the Polaris code, described in Section 3.1.1.

The bias of a benchmark is standardized into a z-score using Equation 5.4, and since these z-scores are correlated to some extent, they are aggregated using Equation 5.5. The higher the correlation between two benchmarks the lesser the information their multiple testing has. In the following, two types of correlation will be analyzed, based on calculations only, and based on combined calculations and measurements. The former is obtained in the present study between all benchmarks. The latter is not available for the analyzed measurements, and the analyses will be based on assumptions, also for the decay heat benchmarks only.

10.1 Significance testing of the bias using calculated uncertainties

The bias is standardized with the calculated uncertainty only, *i.e.*, the combined z-scores are based on calculated uncertainties and calculational-based correlations. Distributions of the z-scores are shown in Figure 50. The z-scores of the decay heat benchmarks present extreme values, noted by an interval containing 95% of the observed z-scores. The majority of the biases of the BWRs are between -6.3 and 6.4 standard deviations of the calculations. These biases are relatively extreme with respect to calculated uncertainties. Using the combined z-score, the BWRs have a combined z-score greater than the significance threshold of 1.96, and the null hypothesis is rejected, and the alternative is accepted: observed biases are significant, given the calculated uncertainties. For the PWRs, the combined z-score is less than the significance threshold and the test failed to reject the null hypothesis: the calculated uncertainties can show that the observed biases are insignificant.

For the U-235 concentration, it is concluded that the observed biases are not significant, given the calculated uncertainties – the tests failed to reject the null hypothesis for both PWRs and

BWRs. In contrast, for the Pu-239 concentration, both the PWRs and BWRs and at least for the Cs-137 BWRs, the null hypothesis is rejected in favor of the alternative, given the extremity of the combined z-scores. The biases are significant, given the calculated uncertainties. This indicates that calculated uncertainties alone might not be enough to show that the observed biases are not significant. A summary of the above results is provided in Table 20.

Table 20. Aggregate z-scores and results of the hypothesis testing conducted on the validation and uncertainty analyses data. A rejection of H0 implies that the observed bias is significant, given the calculated uncertainties, at an 0.05 significance level.

Characteristic	Reactor of origin	\bar{z}	Test result on H0
Decay Heat	BWR	2.14	Reject H0
	PWR	0.64	Fail to reject H0
Cs-137	BWR	3.05	Reject H0
	PWR	1.76	Fail to reject H0
U-235	BWR	1.80	Fail to reject H0
	PWR	1.31	Fail to reject H0
Pu-239	BWR	3.46	Reject H0
	PWR	2.42	Reject H0

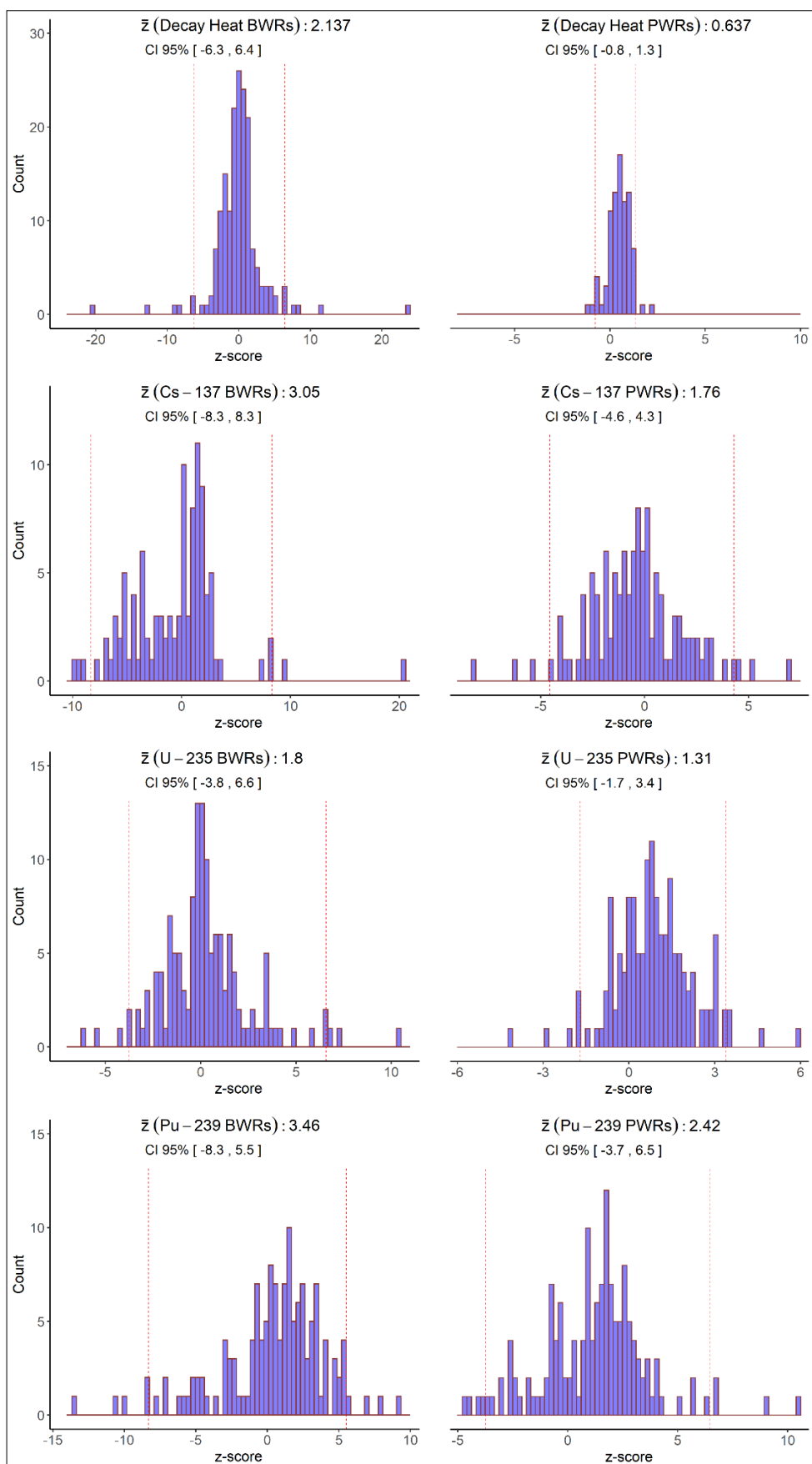


Figure 50. Z-scores for the decay heat, Cs-137, U-235, and Pu-239 concentrations, obtained using calculated uncertainties. The header of each plot provides the combined z-score (\bar{z}) (considering correlations between calculations) and the 95% CI on the z-score distribution.

10.2 Significance testing of the bias using calculated and experimental uncertainties

The so far discussion includes only calculated uncertainties into the hypothesis testing, which is a conservative approach since a small uncertainty in Equation 5.4 leads to a higher z-score and therefore potentially rejecting the null hypothesis. In this section, both the calculated and the experimental uncertainties are considered in the hypothesis testing.

A large number of PIE benchmarks do not have experimental uncertainties. Also, large inconsistencies are observed in the reported experimental uncertainty values. Several measurements of U-235 and Pu-239 concentrations have uncertainties as low as 0.1% and 0.2%, respectively. Other PIE samples measured using similar experimental methods have experimental uncertainties as large as 4.2% and 5.8%, respectively. Therefore, the analyses in this section exclude the PIE benchmarks and focus only on the decay heat ones. The z-scores were recalculated for the decay heat benchmarks, and their distributions are shown in Figure 51. The combined z-scores are calculated assuming that the correlations between the biases originate only from correlations between the calculations, *i.e.*, measurements are assumed uncorrelated. The latter assumption will lead to lower correlations between the biases and conservative combined z-scores.

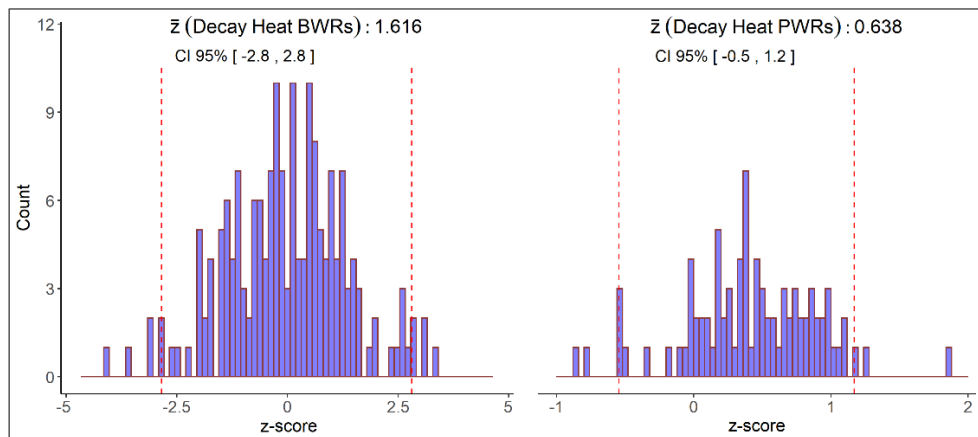


Figure 51. Same as Figure 50 for the decay heat benchmarks, considering both the calculated and the experimental uncertainties.

The distributions of the z-scores based on both the calculated and experimental uncertainties have less variance than those based on the calculated uncertainties only. Extreme z-scores for the BWRs are also observed (beyond -2.8 and 2.8 standard deviations), however, to a lower extent compared to the case of the calculated uncertainties only. The combined z-score for the BWRs is within the significance threshold. The combined z-score for the PWRs is not significantly different from the previous case, implying that the uncertainties in the PWRs are dominated by calculated uncertainties. In conclusions, using both the calculated and experimental uncertainties in the hypothesis testing leads to failure to reject the null hypothesis regarding the significance of the bias.

10.3 Correlations between the decay heat measurements

Calculating a combined z-score using the transformation presented in Equation 5.5 requires calculating and accounting for the correlations between the biases. The denominator includes a summation of the off-diagonal elements of the correlation matrix between the benchmarks. So far, the discussion considers that the correlation matrix between the benchmarks to originate only from calculated correlations. This is a conservative case that would lead to lower correlations between the biases, and therefore potentially larger combined z-score.

The other source of a correlation between the benchmarks is the correlation between the measurements, unfortunately not available for the current data (both the PIE and the decay heat data). In this section, assumptions on experimental correlations are analyzed, focusing again on the decay heat benchmarks. Two categories of measurements are available: the Clab and GE-Morris measurements. Within each category, all measurements are conducted using the same calorimeter. The measurements conducted in each laboratory are assumed to correlate with each other with a correlation of ρ_E . Measurements at different laboratories are assumed independent from each other. For simplicity, the same value of correlation will be assumed between all the Clab benchmarks, and also between all the GE-Morris benchmarks. A grid of ρ_E is analyzed (between -1 and 1), and the combined z-score is plotted vs. the assumed experimental correlation in Figure 52.

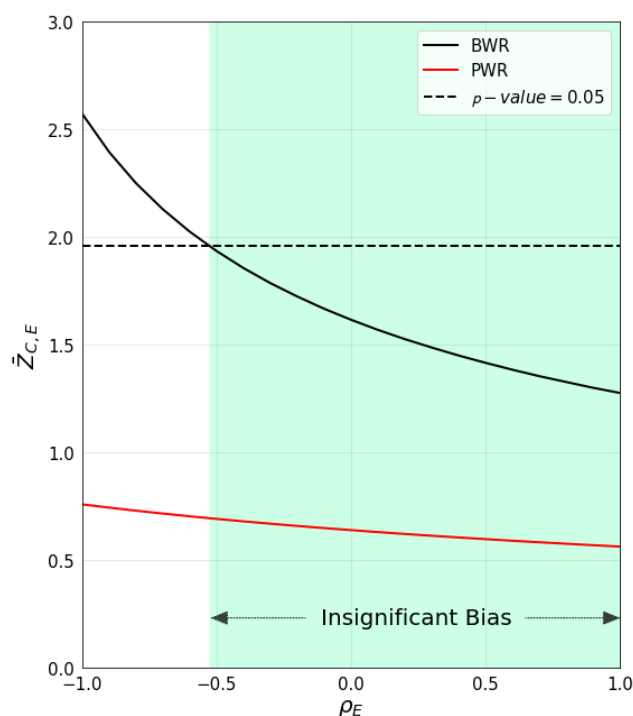


Figure 52. Combined z-score (\bar{z}), obtained using both the calculated and the experimental uncertainties, vs. the experimental correlation. The insignificant bias is within the shaded area.

Compared to the reference cases, the correlations between the measurements reduced the combined z-scores, in both the BWRs and PWRs. The reference cases have combined z-scores of 1.62 and 0.64, for both the BWRs and PWRs, respectively. Assumed correlations between the

BWR measurements resulted in a z-score that is higher than the significance threshold at correlations less than approximately -0.5. For the PWRs, the correlations between the measurements do not alter the results of the hypothesis testing. Negative values of the correlation, anticorrelation, are not apparently physical, however they are shown for completeness.

10.4 Weights of the decay heat benchmarks

The PIE benchmarks are unique samples, *i.e.*, there is a single measurement per benchmark. However, the decay heat benchmarks contain some SFAs that were measured multiple times at different cooling times. Table 21 lists the number of measurements on the SFAs of the decay heat data. The majority of the SFAs were measured once only (111 SFAs) and decreasing numbers of SFAs are having multiple measurements. The SFA CZ205 of the GE-Morris data is the one having the greatest number of measurements (14 measurements at different cooling times).

Table 21. Decay heat measurements on the same SFA, along with assumed weights (w).

No. of meas.	No. of SFA	w
1	111	1
2	25	1/2
3	10	1/3
4	7	1/4
5	1	1/5
6	1	1/6
8	1	1/8
10	1	1/10
14	1	1/14

The so far presented analyses assume that each measurement is a benchmark, assigning a weight of unity to each benchmark. Different benchmark weights are analyzed in this section, assuming that the weight of each SFA is the same, distributing the weight of each SFA on the multiple measurements conducted on it. Such assumption does not increase the weight of the SFAs having multiple measurements on conducting the hypothesis testing. These SFAs will also have equal weights to the SFAs only measured once. As an example, SFA 6432 of the Ringhals-1 reactor has 10 repeated measurements, which will have a weight of 0.1 for each of these measurements, and a unity weight for the whole SFA. The weights for the SFAs having multiple measurements are listed in Table 21. The hypothesis testing is then reconducted under the current assumptions and the obtained combined z-scores of the BWRs and PWRs are:

- 1- 1.47 (BWRs)
- 2- 0.56 (PWRs)

Compared to the above figures, the z-scores calculated using unit weights for the benchmarks were 1.62 and 0.64 for both the BWRs and PWRs, respectively. The tests failed also to reject the null hypothesis; however, the obtained z-scores are less conservative than considering each measurement as an individual benchmark.

Chapter 11 Predicting the Bias of SNF Characteristics

In this chapter, the results of the bias predictive modelling are discussed. Firstly, the extracted features from the decay heat and PIE benchmarks are discussed (Section 11.1). Then, the application of the ML models and algorithms on the validation data is provided (Section 11.2). The presented ML results in this chapter are based on Polaris code, described in Section 3.1.1.

11.1 Features extraction

The features of the benchmarks are based on their correlations. Other features, namely integral features such as those extracted using sensitivity analyses, are also discussed in this chapter.

11.1.1. Design matrix based on correlations between the benchmarks

Description of the method used to calculate the correlation matrices are provided in Chapter 4. The obtained correlation matrices are presented in Chapter 8, based on perturbations of both the ND and DO parameters. As mentioned, the correlations considered are calculational-based, and experimental correlations are excluded.

11.1.2. Design matrix based on integral features of the benchmarks

Sensitivities were used to identify features potentially informative in the bias predictive models, *e.g.*, their burnup. Literature surveys were used to identify features used in other neutronic calculations, such as the validation of CSA. Lastly, features were included based on assumptions that they can be informative in the bias predictive models. It is important to stress here that these approaches allow obtaining features potentially informative in the bias predictive models. However, whether they are informative or not is explicitly based on the data and a conservative features selection algorithm.

Pin-cell models based on selected DO parameters were used for the sensitivity analyses. The pin-cell models use DO parameters at the first and third quantiles (Q1 and Q3) and the median values of the BWR and PWR sections of the PIE data, listed in Table 22. Six pin-cell models were used, 3 based on the data of the PWRs and 3 based on the BWRs. For example, the DO parameters under the right-most column in Table 22 were used to make the 6th pin-cell model (Model 6), whereas these DO parameters belong to the third quantile of the PWR section of the PIE data.

The purpose of using several pin-cell models is to allow exclusion of DO parameters from the subsequent ML studies, if the calculated characteristics show low sensitivity to the parameter in all of these models which are based on different DO parameters.

The pin-cell models were used to calculate perturbed characteristics, given a perturbation of $\pm 0.1\%$ (individually to each parameter). The isotopic concentrations were extracted at discharge, whereas the decay heat was extracted at the median cooling time in the decay heat data (15 years after discharge).

From the six pin-cell models, the highest sensitivity coefficient is used to identify whether the characteristic is sensitive to the perturbed parameter or not. The following variables were considered: burnup, fuel temperature, fuel radius, fuel density, coolant temperature, coolant density, enrichment, gadolinia content, boron, cladding outer radius, lattice pitch, and the cooling time. The calculated characteristics showed different sensitivities toward these parameters and implementing cut-offs allowed reduction of their number.

Table 23 lists parameters exceeding a cut-off value of 0.1 on the sensitivity coefficient, considered in the present study. As an example, the design matrix for the bias of Cs-137 concentration will include only the sample burnup and gadolinia fraction from the parameters analyzed in the sensitivity study. Also, the benchmark burnup will be included in all of the ML models.

Table 22. Properties of PIE benchmarks at Q1, Q3, and median of the BWR and PWR data.

Parameters		BWR			PWR		
		Model 1 Q1	Model 2 Median	Model 3 Q3	Model 4 Q1	Model 5 Median	Model 6 Q3
Design	U-235 wt%	2.41	2.6	3.4	2.83	3.13	3.4
	Gadolinia wt%*	0	0	0	0	0	0
	Fuel density (g/cm ³)	10.23	10.40	10.41	10.05	10.20	10.41
	Fuel radius (cm)	0.5179	0.5955	0.6250	0.4025	0.4450	0.4645
	Cladding radius (cm)	0.615	0.678	0.706	0.475	0.489	0.537
	Lattice pitch (cm)	1.630	1.730	1.930	1.260	1.303	1.430
Irradiation	BU (GWd/tHMi)**	8.1	17.8	34.3	17.8	25.5	30.6
	No. of cycles	4	5	5	4	5	5
	Coolant temp. (K)	554	559	559	549	564	582
	Coolant dens. (g/cm ³)	0.6254	0.4572	0.3560	0.7697	0.7442	0.7059
	Fuel temp. (K)	900	900	900	859	897	922
	Average boron (ppm)	0	0	0	450	489	660
	CR usage (BU %)	0	0	0	0	0	0

* Gadolinia wt% is the weight percent of Gd₂O₃ in the PIE sample.

** estimated value of the burnup after burnup correction.

Table 23. Variables included in design matrices (identified with “✓”), implementing an 0.1 cut-off on calculated sensitivity coefficients.

Parameter	U-235	Pu-239	Cs-137	Decay heat
Burnup	✓	✓	✓	✓
Fuel temperature	–	✓	–	–
Fuel radius	✓	✓	–	✓
Fuel density	✓	✓	–	✓
Coolant temperature	✓	✓	–	–
Coolant density	✓	✓	–	✓
Enrichment	✓	✓	–	✓
Gadolinia	✓	✓	✓	✓
Boron	–	–	–	–
Cladding radius	✓	✓	–	✓
Lattice pitch	✓	✓	–	✓
Cooling time	–	–	–	✓

Additional features were included, namely: calculated values (*e.g.*, calculated U-235 concentration), SI , H/X , reactor type (PWR vs. BWR), calculated uncertainties of both ND and DO origins, and interaction terms. Only three of these features were found in literature (described in Chapter 6), and the others are based on assumptions. The mentioned parameters (including those in Table 23) were extracted for all benchmarks. Some variables change during irradiation, and cycle-wise burnup weighting is implemented to aggregate these cycle-wise values into an integral value of the benchmark.

As mentioned previously, the bias depends on measurements containing noise due to uncertainties of random nature. The scale of this noise can have a detrimental impact on the learning performance from the current data. Also, the number of the available benchmarks in the present study is limited, *i.e.*, the data size is relatively small. Consequently, to minimize overfitting to the design matrix, several steps are followed to reduce its size, such as excluding some of the least sensitive variables and averaging parameters that vary during irradiation.

Additional measures were implemented, such as removing highly correlated variables (those having mutual correlation between their vectors > 0.90), given their detrimental impact on the learning process. Also, these variables were excluded using an unsupervised approach, *i.e.*, the correlations between the features and the bias are not considered, and the mutual correlations between these features were used. For example, in the decay heat design matrix, the lattice pitch is highly correlated with the cladding radius (both pointing to the assembly design, *e.g.*, GE8), and only one variable was used. Also, the reactor type, water temperature, water density, and the IHM have high mutual correlations. Only one of these variables should be kept in the design matrix containing information about the other variables. In the present study, the IHM is used. The reactor of origin is a simple binary variable, and the water density and temperature are almost invariant in either one of the two reactor types. The water density is almost invariant in the PWRs, and the water temperature is invariant in the BWRs.

Additional features are included in the design matrices of the PIE benchmarks. Information about whether the fuel temperature is given or assumed is also recorded for each sample as a dummy variable. The variable record how reliable the implemented fuel temperatures is, using binary values: zero for assumed fuel temperatures and one for given fuel temperatures. Also, several PIE samples experience control rod (CR) usage during their irradiations. A variable containing information about the usage of the CR is included in the design matrices. The variable records the fraction of the burnup during which the assembly containing the sample was controlled. A variable including information about the axial position of the sample is also included. The latter variable stems from an assumption that the PIE irradiation histories in middle regions of the assembly are more accurate than that at the axial peripheries, which might as well affect the bias. The latter variables are included assuming that they contain information about the bias, and again, whether or not they are informative into the bias predictions is based on the data and a conservative features selection algorithm.

11.2 Predictions of the ML models

Firstly, the predictive performance of the linear model (LM) is shown only for the bias of the decay heat and Pu-239 concentration – given its limited applicability on the other SNF characteristics. Discussing the LM firstly intends to highlight its limitations on the current applications. Then, for each of the validated SNF characteristics, the bias predictions are discussed based on using both the Random Forests (RF) and weighted k-nearest-neighbors (KNN) models (using both design matrices). The results of latter models are discussed separately, given that, as they are promising and provide bias predictions (ML-based bias) that have similarity to the initially observed ones (validation-based or already known bias). Then, the predictive performance is discussed along with outliers detection and removal from the data.

11.2.1. Linear models based on integral parameters of the benchmarks

The LM was applied following the algorithm described in Chapter 6. The algorithm is designed to select a model with a lower number of features and a validation error being within the error margin of the validation error of the best performing model (following the OSE rule). For all of the analyzed characteristics, the selected models contain only a single feature (one predictor). The outer testing loop is based on a LOOCV procedure, therefore for each characteristic there is a number of fitted and tested models equal to the original number of the benchmarks. Indeed, in all these models, and for all of the analyzed characteristics, the algorithm tends to select only models based on a single feature. Plots of the observed biases and the LM-predicted biases for the test sections of the data obtained using LMs containing only a single feature are shown in Figure 53 and Figure 54 (left plots). Figure 53 shows these predictions for the decay heat, based on the Clab data. The predictions are based on the calculated decay heat values (C). Figure 54 shows these predictions for the Pu-239 concentration, based on an interaction term between the spectral index and the Pu-239 calculated concentration ($SI \times C$).

Based on the validation measures described in Chapter 6, the predicted bias is not similar to the observed one and based on the KS-test statistic, the null hypothesis is rejected (the predicted bias originates from the same distribution as the observed one), and the alternative is accepted. The latter result is obtained for all of the analyzed characteristics – Figure 53 and Figure 54 show only the decay heat and the Pu-239 concentration, and the other characteristics also provide non-satisfactory bias predictions. Also, in all models, the variance of the predicted bias is not significantly lower than that of the original one, showing the limited usefulness of the models. The limited capacity of the LM is noted comparing the training-based predictions to the original biases, *i.e.*, including the test benchmark in the LMs trying to predict it. In the latter case, the models were still not able to provide useful bias predictions, highlighting their low flexibility and high model bias.

Analyses of the statistical significance of the slopes of the LMs, the median p -values of all the regression lines used to generate the predictions, are listed in the subtitles of Figure 53 and Figure 54. At a threshold p -value of 0.05, the LMs of the decay heat and Pu-239 concentration are statistically significant. Indeed, none of the LMs had a p -value more than the significance threshold. The statistical significance of the slopes of the LMs alone can not indicate the usefulness of the resulting models and their predictive performance. The models were statistically significant, however, they provided bias predictions constrained in narrow ranges, showing low association and non-acceptable low similarity to the observed ones.

11.2.2. Linear models based on correlations between the benchmarks

The decay heat and the Pu-239 concentration biases are regressed onto the correlation between benchmarks (*i.e.*, the second design matrix), following a grid of correlation cut-offs. For each cut-off value, the bias of each target benchmark is predicted based on its correlations with every other benchmark exceeding the cut-off, excluding the target benchmark from the training process. The correlation grid for the decay heat spans between 0.90 and 0.99. The correlation grid for the Pu-239 concentration spans up to 0.71. These values are selected such that there are enough observations for all benchmarks to make predictions using the LM. Correlations cut-offs above these values were excluded given that not all benchmarks will be included in the regression models. Figure 53 and Figure 54 (right plots) show the observed bias vs. the predicted one for the test sections of the data. The predictions are at the target benchmark having unit correlation – recursively for each benchmark. None of the analyzed models have shown satisfactory predictions (along the cut-off grid), and the figures show these predictions at selected cut-off values.

The KS-test statistics are below the 0.05 significance threshold. The latter result is observed at all correlation cut-off values for the analyzed characteristics. Again, the null hypothesis is rejected, and the alternative is accepted. None of the predicted samples are concluded to be similar to the observed ones. Also, looking at the p -values of the regression lines of the LMs that generated the bias predictions in Figure 53 and Figure 54, one can see that the LMs are also

statistically significant, based on the correlation between benchmarks. However, none of these models have generated satisfactory bias predictions. The variances are not significantly reduced, or explained, and the predicted bias does not have similarity in its distribution to the original one. Again, the LM exhibit low flexibility and provide unsatisfactory bias predictions constrained in a narrow range, showing low association with the observed biases.

These results show that the LM is not adequate for bias predictions of the mentioned characteristics, either using integral features of the benchmarks or their correlations. Also, the results show that using the statistical significance of the LM regression lines is not an adequate approach of validating models predicting the bias. These models provided bias predictions that failed other statistical tests aimed at assessing the predictive performance of the models. The results highlight the limitations of the LM, particularly looking at the training-based predictions, and their low flexibility and underfitting (*i.e.*, unacceptable large bias). The limitations of the LM can also originate from their incapacity of approximating the underlying relation that maps the bias.

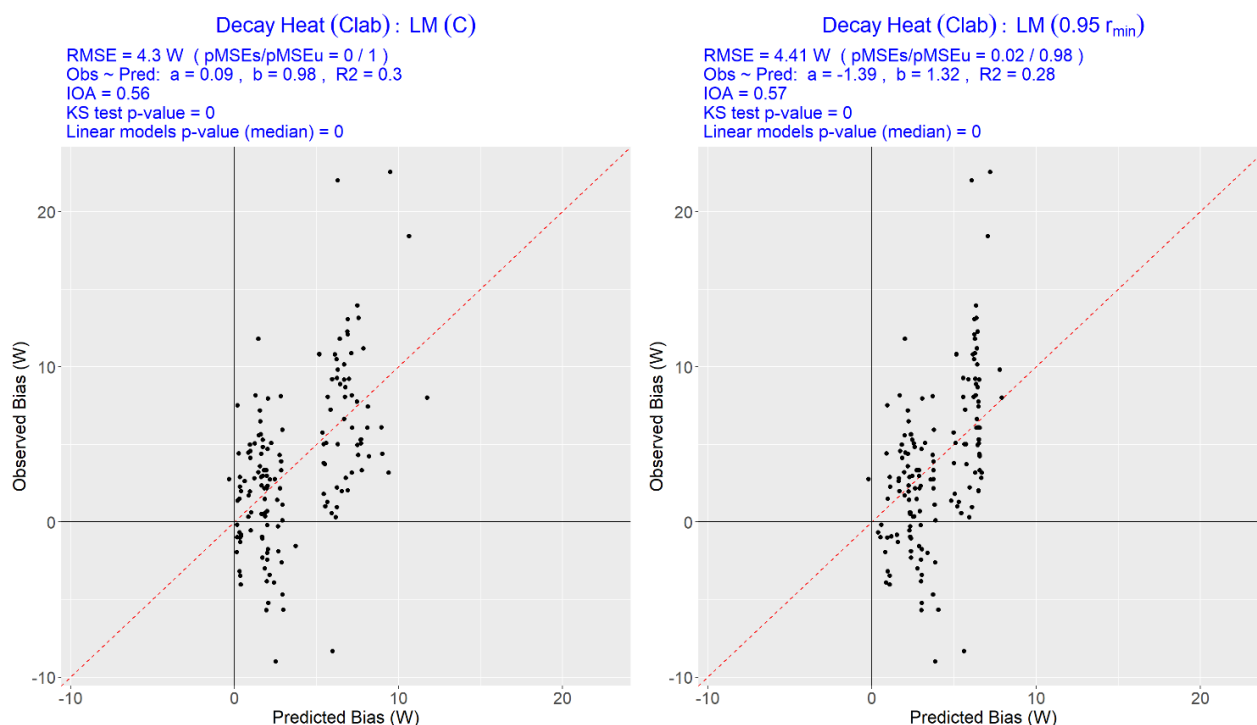


Figure 53. Observed bias (validation-based) vs. the LM predicted bias (ML-based) of decay heat of the Clab benchmarks. The left plot is based on integral parameters of the benchmarks, using the calculated decay heat value (C), and the right plot is based on the correlation between the benchmarks, implementing an 0.95 correlation cut-off. The redline is a 45° line, indicating equality between the predicted and the observed bias.

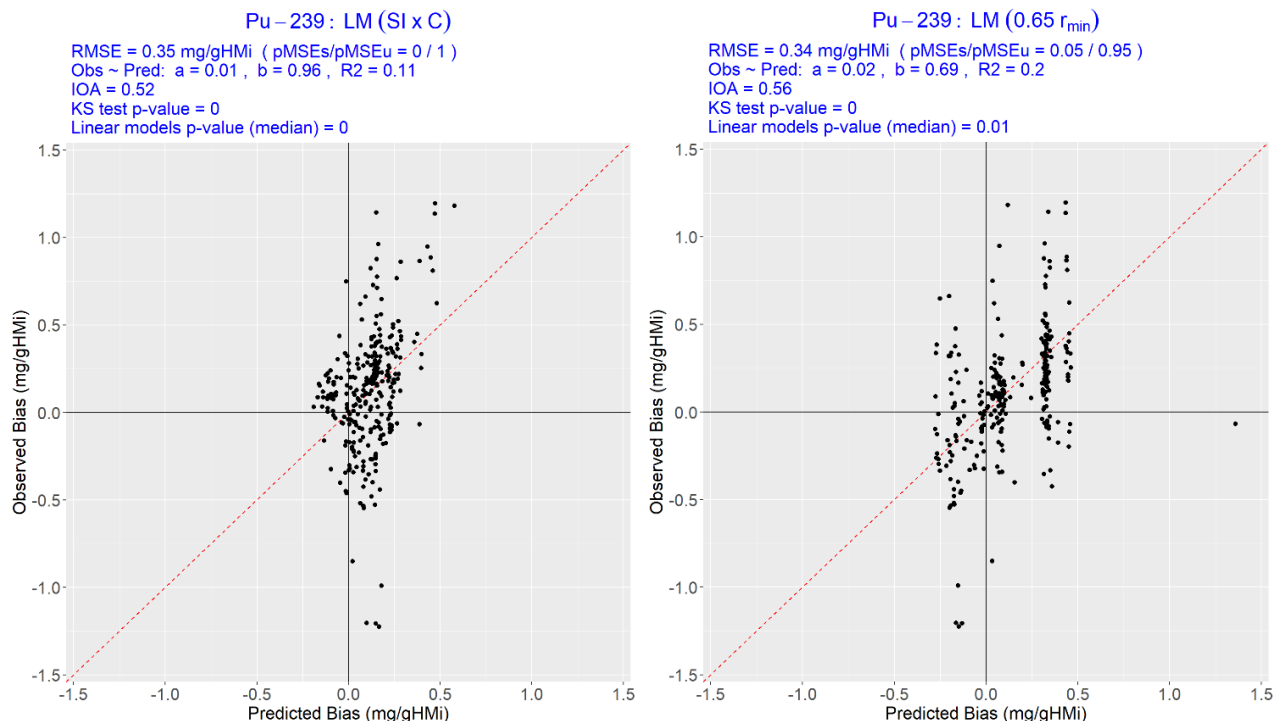


Figure 54. Same as Figure 53 for the Pu-239 concentration, based on the interaction between the spectral index and the Pu-239 calculated concentration ($SI \times C$), and an 0.65 correlation cut-off.

11.2.3. Predictive performance of the decay heat bias

The decay heat benchmarks are two broad categories of measurements: measurements performed at the Clab facility, and measurements performed at the GE-Morris facility. As described in Chapter 2, the former measurements have significantly lower uncertainties compared to the latter measurements. Also, as discussed in the Chapter 7, the validation-based biases of the former data show significantly less scatter (less variance around the average) compared to the latter. In this section, decay heat bias predictions are presented for two types of decay heat data differing in their experimental uncertainty. The first is based on the Clab data only. The second is based on all the decay heat data, including the GE-Morris data which have larger experimental uncertainty. The rationale is that the decay heat benchmarks based only on the Clab data can be selected solely for validating calculational sequence, given their low measurements uncertainty for example. Also, they can be used solely, aside from the older GE-Morris measurement, for bias predictions based on the same rationale.

The RF and the KNN models are applied on the design matrices of the Clab data. Both the integral parameters of the benchmarks (the first design matrix) and their correlations (the second design matrix) are used following the algorithm described in Chapter 6. As shown in Figure 55 and Figure 56 (left plots) for the first design matrix, both the RF and the KNN models select the spectral index (SI) as the informative model feature. A single integral feature, the SI , is consistently being selected by both models of all Clab benchmarks, allowing satisfactory bias predictions. The predictions show 0.46 and 0.47 reductions of the original variances (explained variances), based on the RF and the KNN models, respectively. Both reductions in the variances are promising in the current application, and also the test error of both models is approximately 3.8 W. The validation results of the Clab benchmarks (Table 8), show an average bias of 3.7 W along with 1σ of 5.1 W. The ML models provide bias predictions that has a systematic component depending solely on the SI of the benchmarks, along with an estimated test error of approximately 3.8 W.

The resulting bias predictions show also acceptable IOA values, and KS-test results. The p -values of the KS-test for both models are above the threshold, and it is failed to reject the null hypothesis – the null hypothesis is that the observed bias and the predicted one originate from the same distribution. Such results show that both models are promising in their bias predictions, providing biases that bear statistically significant similarity to the observed ones, the validation based ones, along with acceptable reduction, or explanation, of the variance of the data.

The predictions based on the correlation matrices are shown in the right plots of Figure 55 and Figure 56. The variance of the original bias is reduced, or explained, by 0.44 and 0.40 using the RF and the KNN models, respectively. Both models result in KS-test p -values that fail to reject the null hypothesis. Again, both models are promising in their bias predictions based on learning the bias using the correlation between the benchmarks, providing biases that bear statistically significant similarity to the observed ones, along with acceptable reduction in the

variance of the data. The reductions, or the explanation, of the variances are less than those based on the *SI*, however, they are still acceptable in the current application. The test error of both models is approximately 4.0 W, meaning that the RF and the KNN models using the correlations between the benchmarks provide bias predictions that systematically depend on these correlations, along with an estimated test-error of 4.0 W of using these models to predict the bias. One can observe, with both the RF and KNN models, also based on the two design matrices, that certain benchmarks tend to be significantly mis-predicted in all cases. Treatment of outlier observations, like these ones, is presented in Section 11.2.7.

The bias prediction process is repeated on all the decay heat data, using both the RF and the KNN models applied on both design matrices. The results of the analyses are shown in Figure 57 and Figure 58, highlighting the Clab benchmarks in red color. Unlike the models based on the Clab benchmarks solely (which selected the *SI* as the informative model features), the models based on all the decay heat data selected the interaction term between the *SI* and the cooling time (*SI x Decay*) as the informative model feature. The additional information about the cooling time of the benchmark indeed provides more differentiation between the Clab benchmarks, and the rest of the data. The range of cooling times of the Clab measurements is 11 to 27 years after discharge, whereas it is 2 to 11 years after discharge for the GE-Morris measurements. For all models, and learning cases, the KS-test *p*-values result in failure to reject the null hypothesis. However, other statistics indicate that the reduction in the variances are small, not potentially promising in the current application (the test errors of the models are between 10 and 12 W).

The preceding discussion highlights differences between the two datasets, having differences in their experimental uncertainties. Learning based on the Clab benchmarks solely, which have low experimental uncertainties, provides promising models in terms of the similarities between predictions and observations, reduced variances, and lower test errors. Learning based on all the decay heat benchmarks includes measurements that have significantly high experimental uncertainty, resulting in larger random component of the bias. The latter learning setting has shown less promising predictive performance, with small reductions in variances and higher test errors.

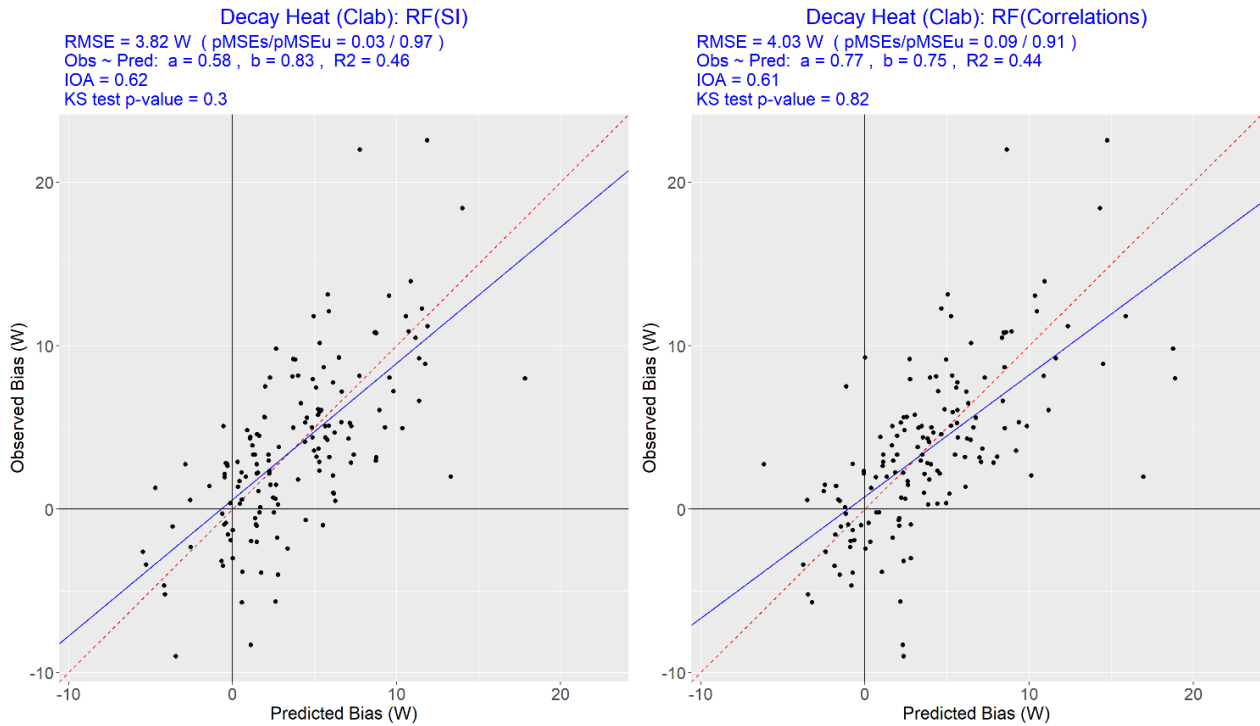


Figure 55. Observed bias (validation-based) vs. the RF model predicted bias (ML-based) for the decay heat – Clab benchmarks. The left plot is based on integral parameters of the benchmarks, using the spectral index (SI), and the right plot is based on the correlation between the benchmarks. The redline is a 45° line, indicating equality between the predicted and the observed bias. The blueline is the linear regression line of the observed bias on the predicted one.

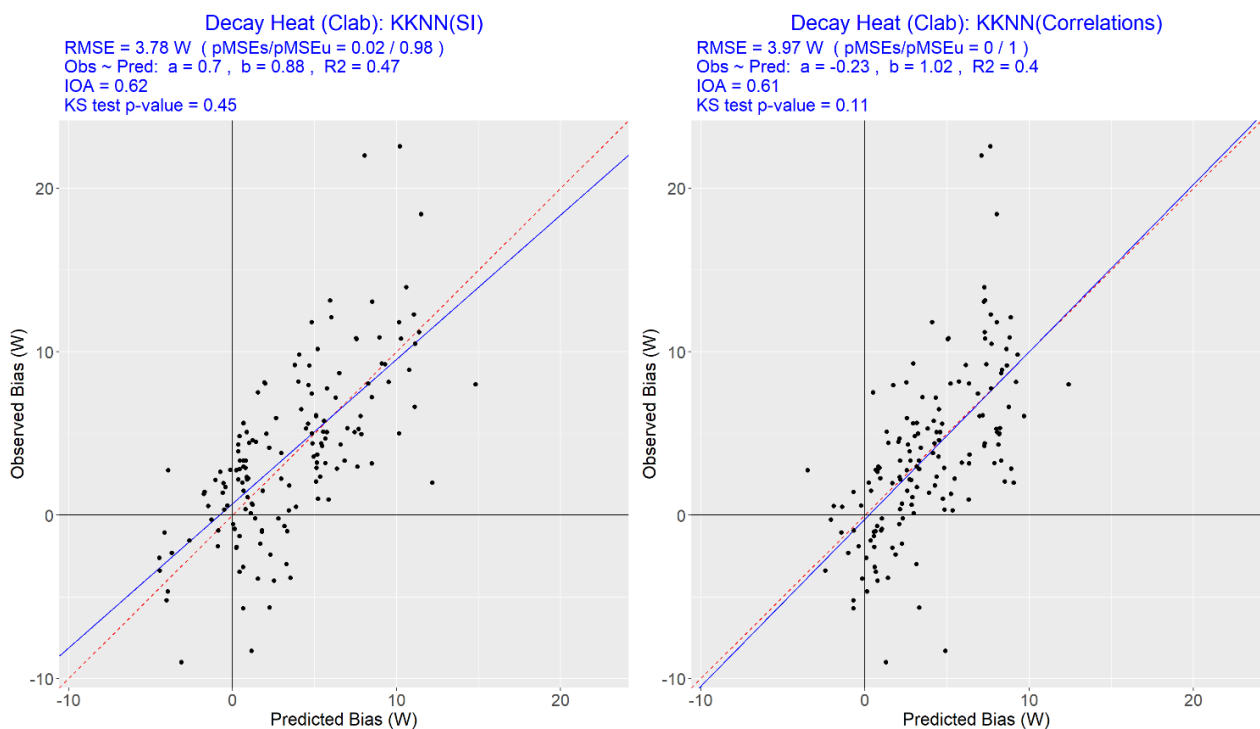


Figure 56. Same as Figure 55 for the KNN model.

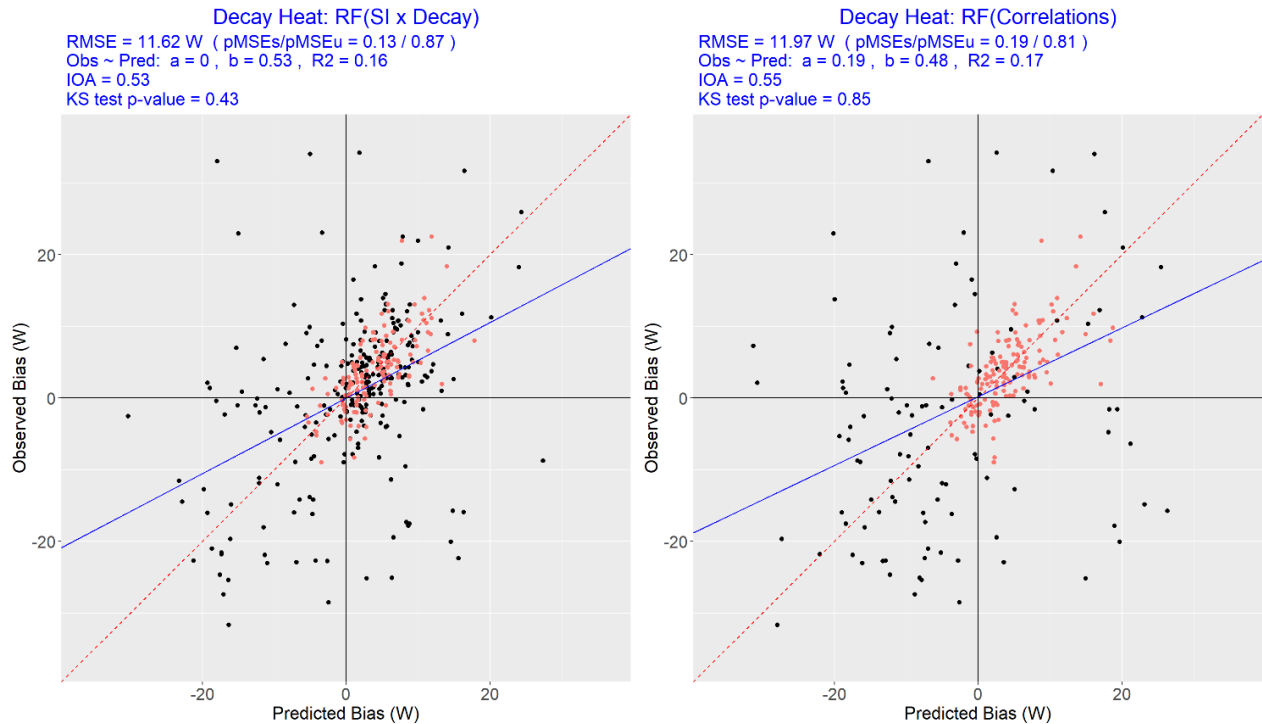


Figure 57. Observed bias (validation-based) vs. the RF model predicted bias (ML-based) for all the decay heat benchmarks (Clab data are highlighted in red color). The left plot is based on integral parameters of the benchmarks, using the interaction between the spectral index and the cooling time ($SI \times Decay$), and the right plot is based on the correlation between the benchmarks.

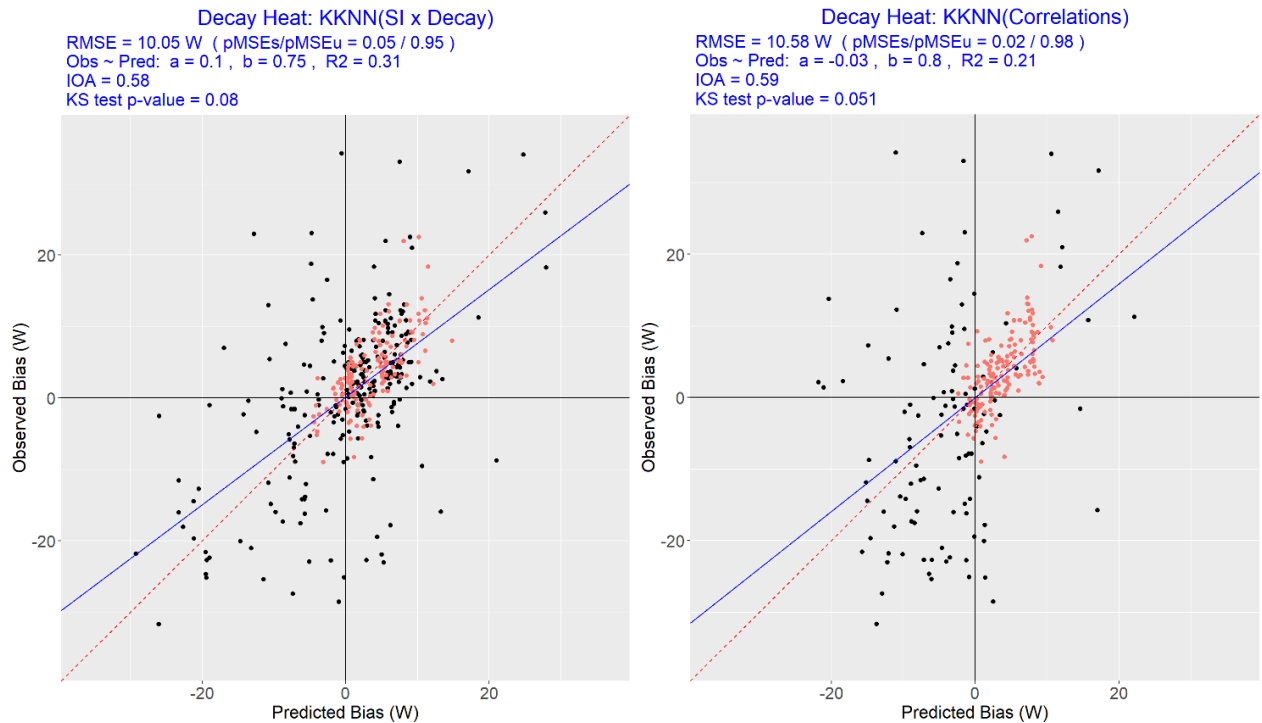


Figure 58. Same as Figure 57 for the KNN model.

11.2.4. Predictive performance of the U-235 concentration bias

The bias prediction process is applied on the U-235 concentration benchmarks, using both the RF and the KNN models with both design matrices, and the results of the analyses are shown in Figure 59 and Figure 60. The models based on the integral parameters of the benchmarks selected the calculated uncertainties (σ) as the informative model feature, for both the RF and the KNN models. The predictions based on the former models show low p -values of the applied KS-tests, and the null hypothesis is rejected, and the alternative hypothesis is accepted. Applying the RF and the KNN models on the U-235 correlation matrix shows acceptable p -value of the KS-test for the predictions of the former, and rejectable one for the latter. However, for both models applied on both design matrices, the explained variances are small and not potentially promising in the current application. The test errors of the models are between 0.55 and 0.61 mg/gHMi, which are not promising in the current application also.

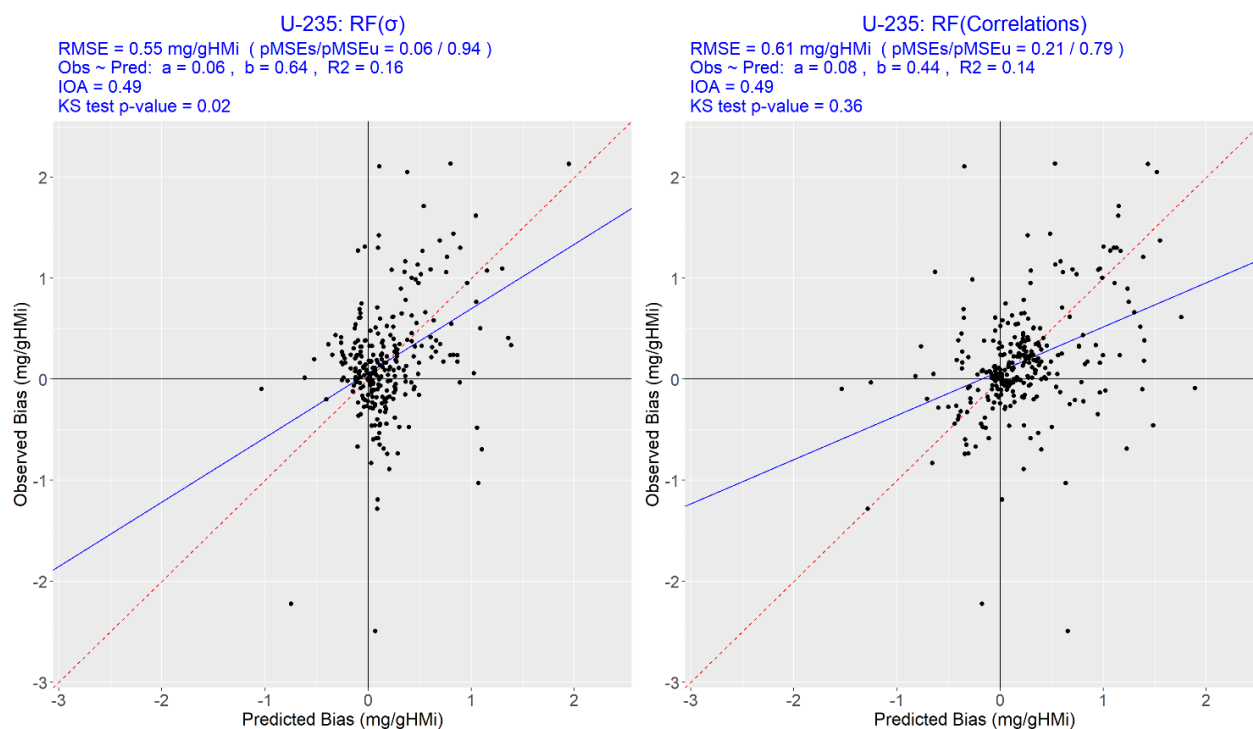


Figure 59. Observed bias (validation-based) vs. the RF model predicted bias (ML-based) for the U-235 benchmarks. The left plot is based on integral parameters of the benchmarks, using the calculational-based uncertainty (σ), and the right plot is based on the correlation between the benchmarks.

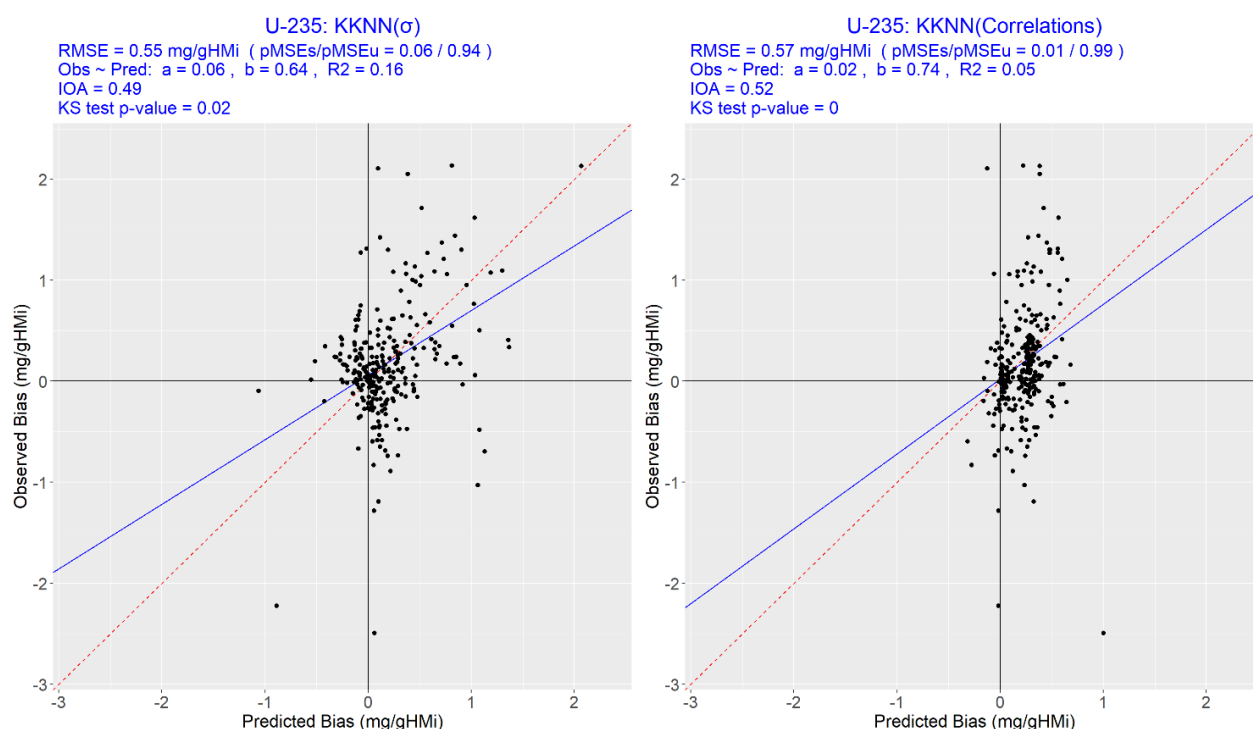


Figure 60. Same as Figure 59 for the KNN model.

11.2.5. Predictive performance of the Pu-239 concentration bias

The bias prediction process is applied on the Pu-239 concentration benchmarks, using both the RF and the KNN models along with both design matrices, and the results of the analyses are shown in Figure 61 and Figure 62. The models based on the integral parameters of the benchmarks selected the hydrogen-to-fissile atom ratio (H/X) as the informative model feature, for both the RF and the KNN models. The predictions based on the former KNN model show low p -values of the applied KS-test, and the null hypothesis is rejected, and the alternative hypothesis is accepted. The predictions based on the RF models show acceptable p -value of the KS-test, and it is failed to reject the null hypothesis. However, learning the bias using the H/X and either the RF or the KNN models result in small reduction of the original variance of the bias.

On learning the bias based on the correlation between the benchmarks, the prediction results of both the RF and the KNN models lead to p -values of the KS-test that are above the threshold, and it is failed to reject the null hypothesis. For both models applied on the correlation matrix, the explained variances are potentially promising in the current application. The fractions of the explained variances are 0.47 and 0.41 for both the RF and KNN models, respectively. The test errors of the models are between 0.28 mg/gHMi, on learning the bias from the correlation between benchmarks, and between 0.34 and 0.36 mg/gHMi on learning from the H/X feature.

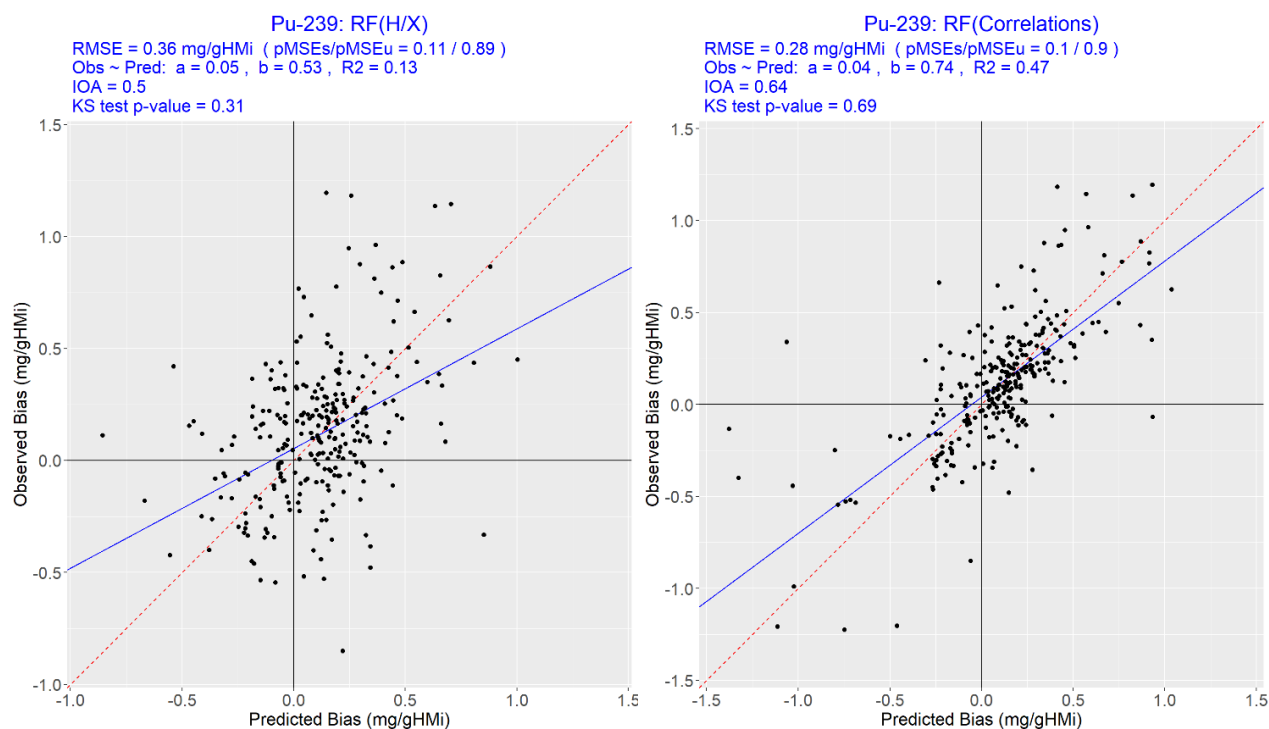


Figure 61. Observed bias (validation-based) vs. the RF model predicted bias (ML-based) for the Pu-239 benchmarks. The left plot is based on integral parameters of the benchmarks, using the hydrogen-to-fissile atom ratio (H/X), and the right plot is based on the correlation between the benchmarks.

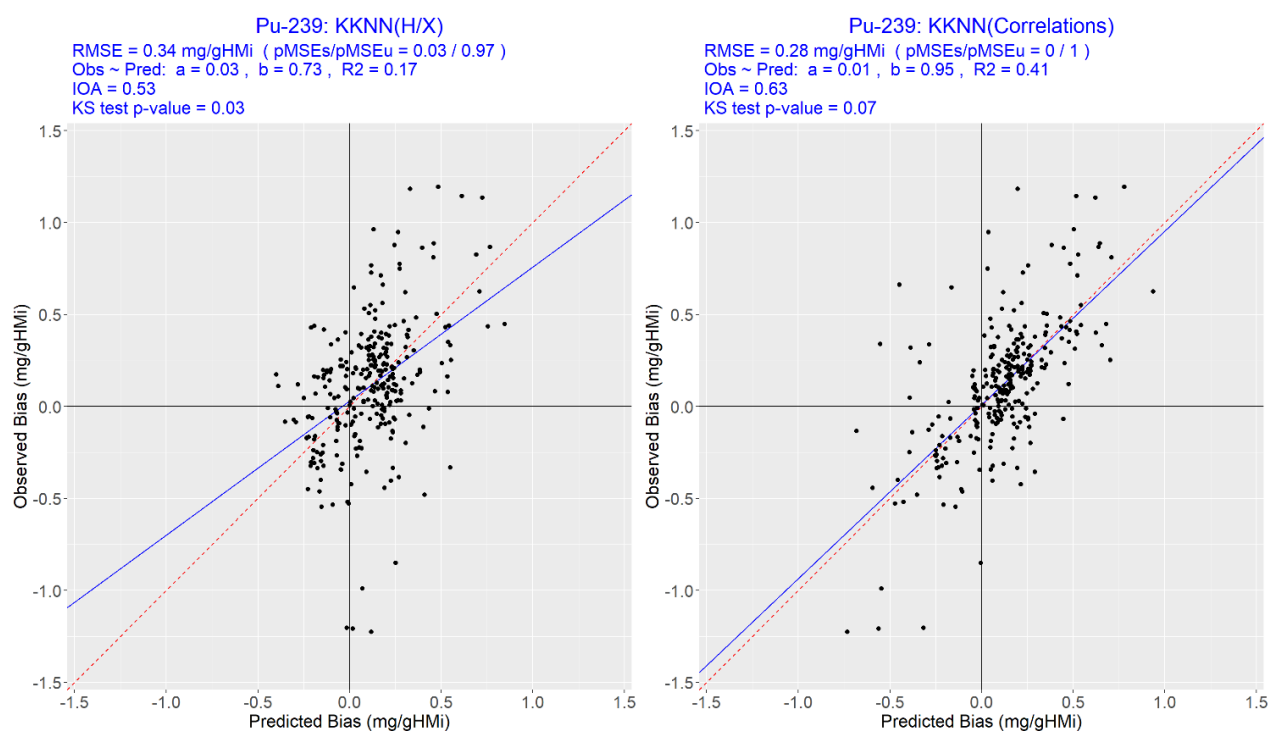


Figure 62. Same as Figure 61 for the KNN model.

11.2.6. Predictive performance of the Cs-137 concentration bias

The bias prediction process is applied on the Cs-137 concentration benchmarks, using both the RF and the KNN models with both design matrices, and the results of the analyses are shown in Figure 63 and Figure 64. The models based on the integral parameters of the benchmarks selected the interaction between the burnup and the calculated concentration of the Cs-137 ($BU \times C$) as the informative model feature, for both the RF and the KNN models. The predictions based on both models show low p -values of the applied KS-test; the null hypothesis is rejected, and the alternative hypothesis is accepted. Learning the bias using the $BU \times C$ and either the RF or the KNN model results in significantly small reductions of the original variance of the bias. The models are not promising to provide useful bias predictions, given integral parameters of the benchmarks. On learning the bias based on the correlation between the benchmarks, the results of both the RF and the KNN models show that the explained variances are negligible. All of the analyzed models learning the bias of the Cs-137 concentration show non-satisfactory reductions of the original variances, being only within 0.03.

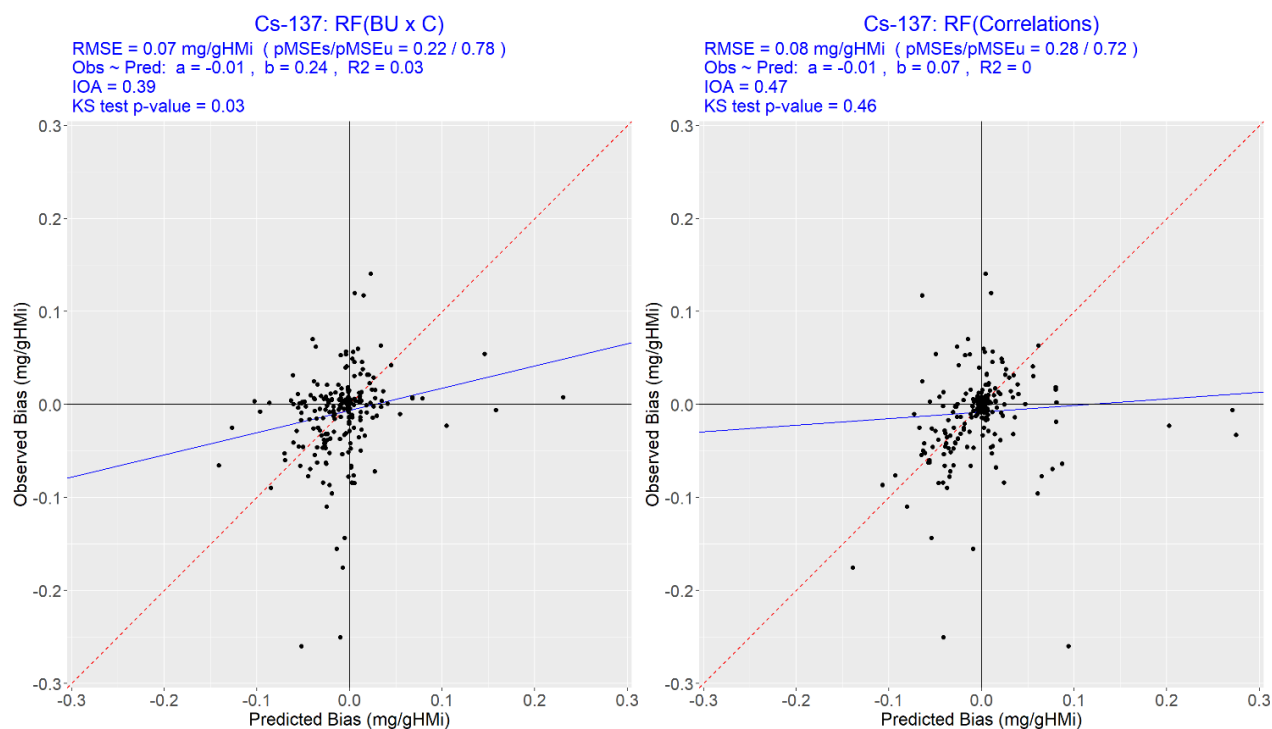


Figure 63. Observed bias (validation-based) vs. the RF model predicted bias (ML-based) for the U-235 benchmarks. The left plot is based on integral parameters of the benchmarks, using a single features, the interaction between burnup and the calculated Cs-137 concentration ($BU \times C$), and the right plot is based on the correlation between the benchmarks.

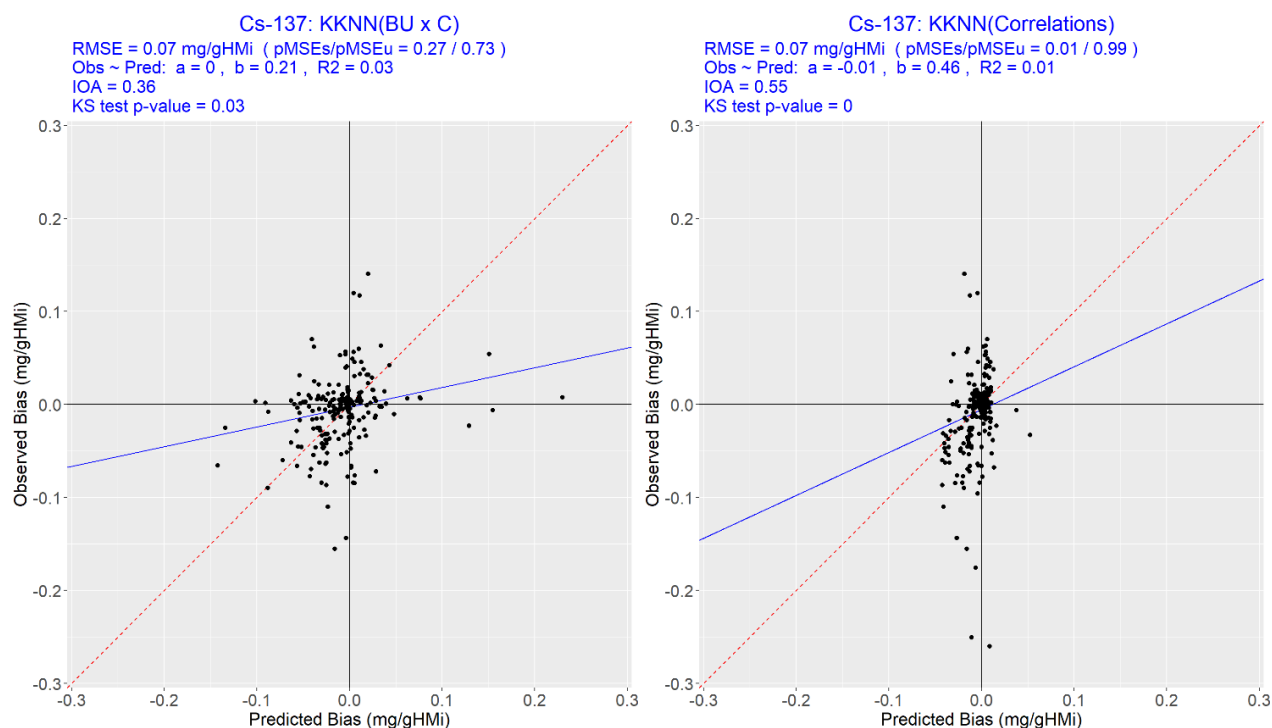


Figure 64. Same as Figure 63 for the KNN model.

11.2.7. Predictive performance along with outliers detection and removal

Sections 11.2.3 and 11.2.5 have shown promising ML models predicting the bias of the decay heat and Pu-239 concentration, based on SI for the former and H/X for the latter, and the correlation between benchmarks for both. The RF model is promising in both applications. In this section, further optimization is applied, based on the RF model. The outliers detection and removal procedures, described in Section 6.11, are applied on both design matrices of the decay heat (Clab benchmarks solely) and the Pu-239 concentration. The results are summarized in Table 24, indicating the benchmarks detected as outliers in the inner-most loops of the algorithms, their count, and the results of the aggregate z-tests.

For the decay heat benchmarks, 2 and 3 outliers are detected based on application of the RF model on the SI and the correlation matrices, respectively. The detected outliers show similarities of 2 benchmarks between both models. For the Pu-239 benchmarks, 8 and 6 outliers are detected based on application of the RF model on the H/X and the correlation matrix, respectively. The detected outliers show similarities of 6 benchmarks between both models. The design matrices of each data are reduced, excluding the detected outliers (at 0.00135 significance level), and the bias predictive performance is recalculated. The predictions of the RF models learning the bias using these reduced matrices are shown in Figure 65 and Figure 66. The measures in these figures include the reduction, or explanation, of the variances using the RF models applied on the reduced design matrices with respect to the original data without removal of outliers. The latter measure is the explained variance (EV), calculated as

$$EV = 1 - \frac{\sigma_{final}^2}{\sigma_{initial}^2} \quad (13.1)$$

The decay heat models show reductions in the original variances of approximately 0.5, resulting from removal of 2 and 3 outliers (based on both the SI and correlation matrix), approximately 2% the size of the initial data. Initially, without outliers removal, the reduced variances are 0.46 and 0.44 (as shown in Figure 55) and removing only few outliers results in an improvement of both values. The results of the Pu-239 concentration bias show significantly larger improvements, reaching reductions in the original variances of 0.48 and 0.63, as shown in Figure 66. Compared to the initial reductions in variances of 0.13 and 0.47, shown in Figure 61, the outliers removal resulted in significant improvements in the predictive performance of the RF models, learning the bias using the H/X and the correlation between the benchmarks, particularly for the former. These improvements result from removing observations detected as outliers with a significance level of only 0.00135, corresponding to 2 to 3% of the original size of the Pu-239 validation data. Again, the outliers detection and removal procedures are selectively conservative, resulting in removal of small fractions of the original data. However, significant improvements are obtained.

Table 24. Aggregate results of the outliers detection and removal procedure, applied on the decay heat benchmarks (left table) and the Pu-239 concentration benchmarks (right table). Both characteristics are analyzed using the RF models, applied on both design matrices: SI for the decay heat, H/X for Pu-239 concentration, and the correlation matrices for both. The decay heat data belong to the Clab benchmarks solely.

Decay heat					Pu-239 concentration				
Features	SI		Correlations		Features	H/X		Correlations	
SFA	Count	Outlier	Count	Outlier	Benchmark	Count	Outlier	Count	Outlier
C12	47	-	46	-	TMI-1 - S2	-	-	3	-
C20-1	104	✓	104	✓	D-1 - DU1	-	-	2	-
C20-2	1	-	-	-	D-1 - DM1	-	-	18	-
I20	-	-	3	-	D-1 - DM2	-	-	17	-
I24	-	-	2	-	D-1 - DM3	39	-	106	-
5F2-1	-	-	84	✓	D-1 - DM4	243	✓	198	✓
5F2-2	116	✓	128	✓	FD2 - 99_8	-	-	3	-
5F2-3	36	-	36	-	FD2 - 99_9	-	-	6	-
10288	-	-	1	-	FD2 - TU104	85	-	44	-
3838	-	-	3	-	FD2 - TU105	285	✓	143	✓
KU0278	-	-	16	-	FD2 - TU106	285	✓	242	✓
KU0282	-	-	2	-	FD2 - TU201	197	✓	119	-
Total	2		3		FD2 - TU202	89	-	66	-
					FD2 - TU203	285	✓	227	✓
					FD2 - TU204	194	✓	158	✓
					FD2 - TU308	97	-	96	-
					FD2 - TU309	187	✓	187	✓
					FD2 - TU311	-	-	1	-
					FD2 - TU501	-	-	41	-
					FD2 - TU502	-	-	69	-
					FD2 - TU503	-	-	3	-
					FD2 - TU510	-	-	4	-
					Y-1 - G-107	-	-	1	-
					Y-1 - G-108	115	-	16	-
					Y-1 - G-109	168	✓	23	-
					M-3 - G07	-	-	1	-
					T3 - SF95_5	-	-	1	-
					T3 - SF96_1	-	-	1	-
					T3 - SF96_5	-	-	81	-
					T3 - SF97_1	-	-	31	-
					OG1 - G14-P3	-	-	18	-
					OG1 - G14-P4	-	-	3	-
					Total	8		6	

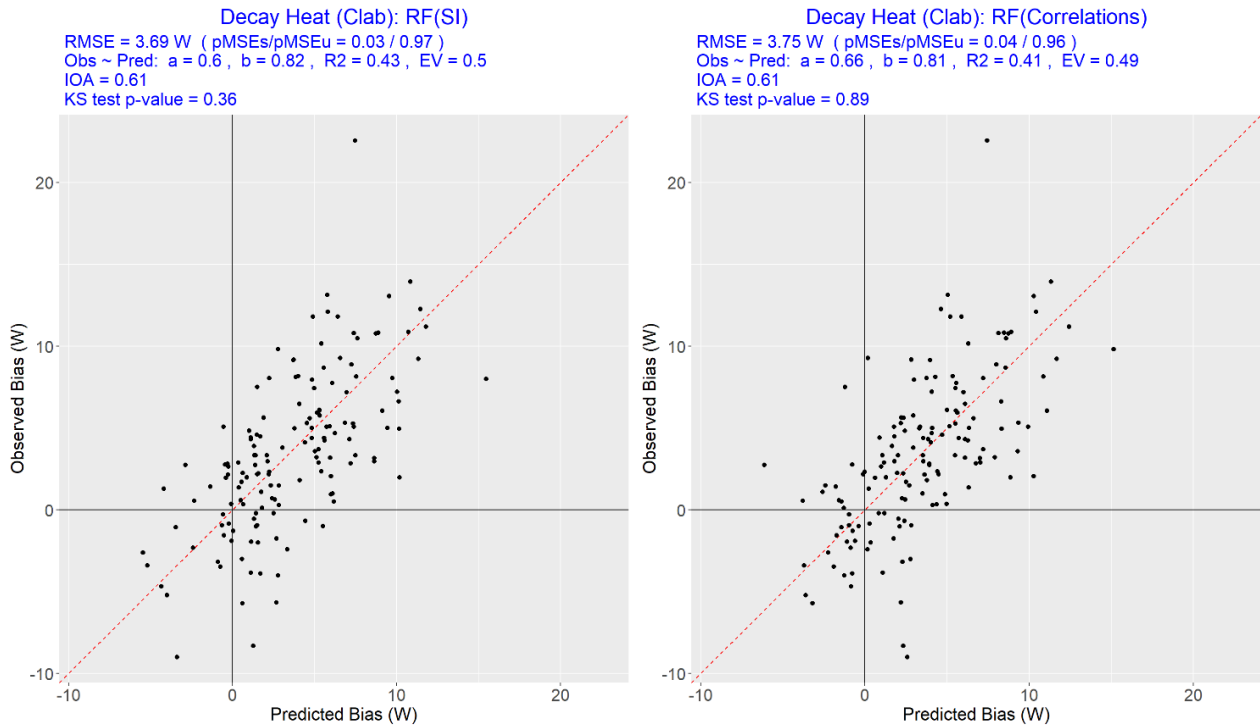


Figure 65. Observed bias (validation-based) vs. the RF model predicted bias (ML-based) for the Clab benchmarks. The left plot is based on integral parameters of the benchmarks, using the spectral index (SI), and the right plot is based on the correlation between the benchmarks.

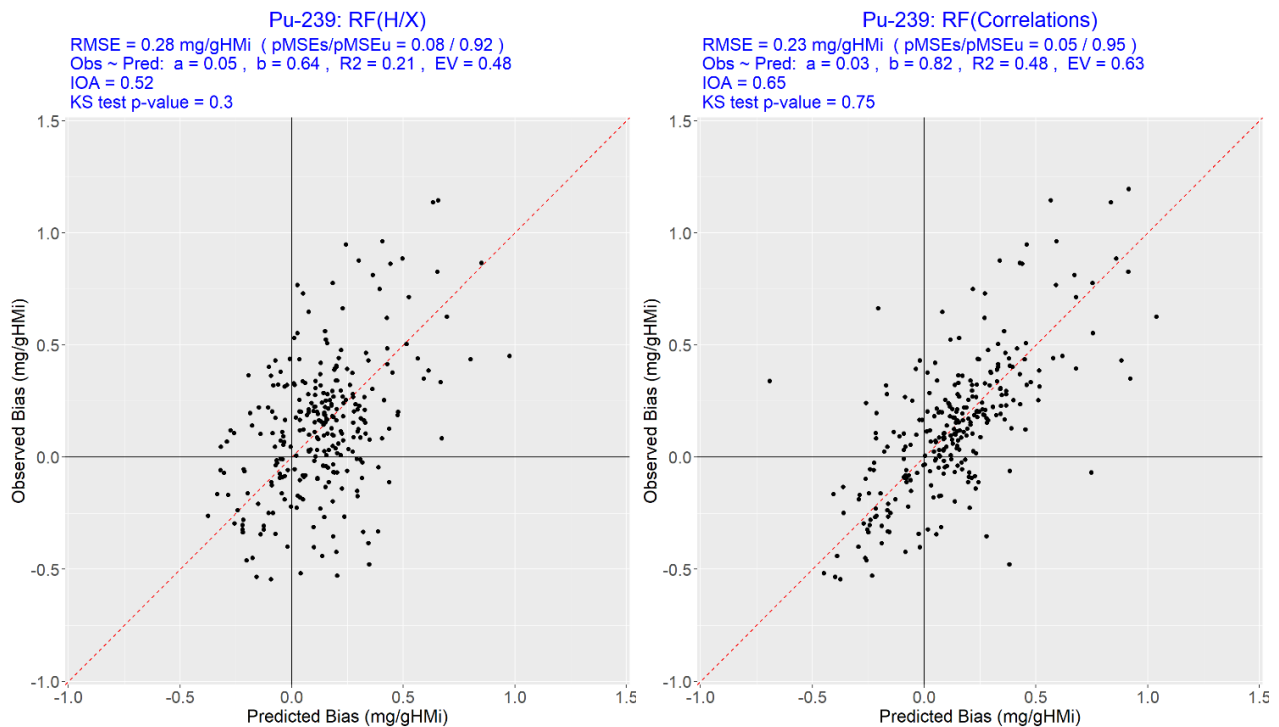


Figure 66. Same as Figure 65 for the Pu-239 concentration bias. The left plot is based on the hydrogen-to-fissile atom ratio (H/X), and the right plot is based on the correlation between the benchmarks.

11.2.8. Final models

The present research analyzed a hypothesis that the bias of SNF characteristics can be predicted using ML models and algorithms, along with validation data. The research starts with a validation process to obtain the bias for validation benchmarks, followed by collecting features of these benchmarks such as their correlations. Then, hypotheses on the ML models, such as using neighborhood schemes (*e.g.*, RF models), and learning, testing, and validation procedures are assembled to obtain a solution for Equation 1.5 ($C - E = f(X) + \epsilon$). The bias is represented as two components: $f(X)$, intended to capture the systematic part of the bias using the ML model (the explained bias), and ϵ , intended to capture the random part of the bias (the unexplained part of the bias). Both components of the bias were unknown *a priori*.

Certain ML models and data have shown promising bias predictive performance, *e.g.*, the RF models have shown promising bias predictive performance, applied on the decay heat and Pu-239 concentration biases, and design matrices based on the correlation between benchmarks. Alternative interpretation of the results is discussed in this section.

The validation bias of the decay heat (*i.e.*, $C - E$ in Equation 1.5) and the ML predicted bias (*i.e.*, $f(X)$ in the same equation) are shown in Figure 67. The ML model is the RF model, predicting the bias using the calculated correlation between the benchmarks along with the validation bias. Outliers removal is applied (3 benchmarks, listed in Table 24). The systematic part of the bias $f(X)$ reduces the original variance in the validation bias by 49%. Using the validation procedure, Polaris overestimates the measured decay heat by 3.7 ± 5.1 W – as shown in Table 8. Then, the RF model application on the decay heat correlation data results in bias predictions (represented as $f(X) \pm 3.7$ W), indicating the following:

1. The predicted bias is not necessarily an overestimation. Unlike the validation-based average bias, $f(X)$ is negative for several benchmarks.
2. The average fluctuation of the error around the $f(X)$ for the ML-predicted bias is lower than its fluctuation around the average bias for the validation data, measured using the standard deviation. The standard deviation (1σ) of the error from the ML model is 3.7 W compared to 5.1 W from the validation procedure, corresponding to a variance reduction of 0.49.

Similar analysis is provided for the Pu-239 concentration, based also on the RF model, as shown in Figure 68. The data are based on the calculated correlation between the benchmarks and the validation bias along with outliers removal (6 PIE samples, listed in Table 24). The systematic part of the bias $f(X)$ reduces the original variance in the validation bias by 63%. Using the validation procedure, Polaris overestimates the measured Pu-239 concentration by 11 ± 0.37 mg/gHMi – as shown in Table 10. Then, the RF model application on the correlation data of the Pu-239 concentration results in bias predictions (represented as $f(X) \pm 0.23$ mg/gHMi), indicating the following:

1. Similar to the decay heat case, the predicted bias is not necessarily an overestimation. Unlike the validation-based average bias, $f(X)$ is negative for several benchmarks.

2. Also, the average fluctuation of the error around the $f(X)$ for the ML-predicted bias is lower than its fluctuation around the average bias for the validation data. The standard deviation (1σ) of the error from the ML model is 0.23 mg/gHMi compared to 0.37 mg/gHMi from the validation procedure, corresponding to a variance reduction of 0.63.

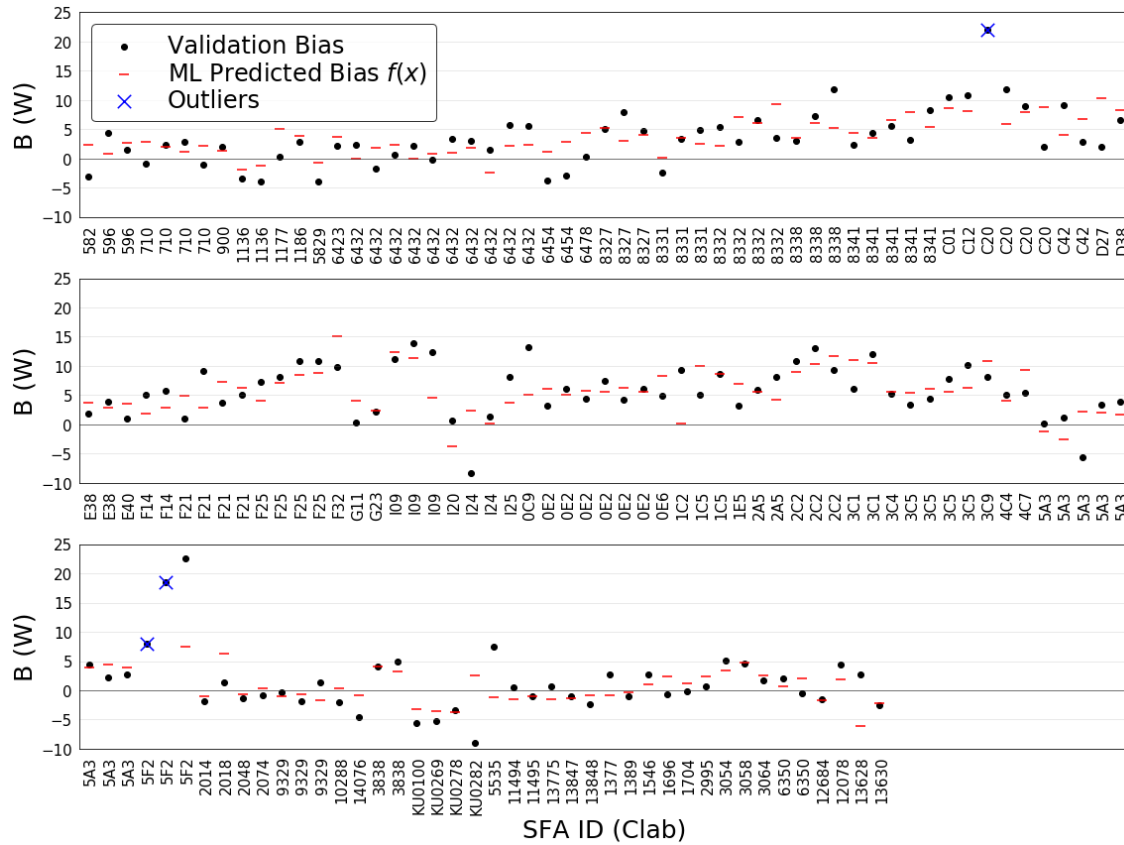


Figure 67. Decay heat biases, both validation-based and ML-based. The ML model is the RF model, and the data are the validation-based bias and the calculated correlations between the benchmarks.

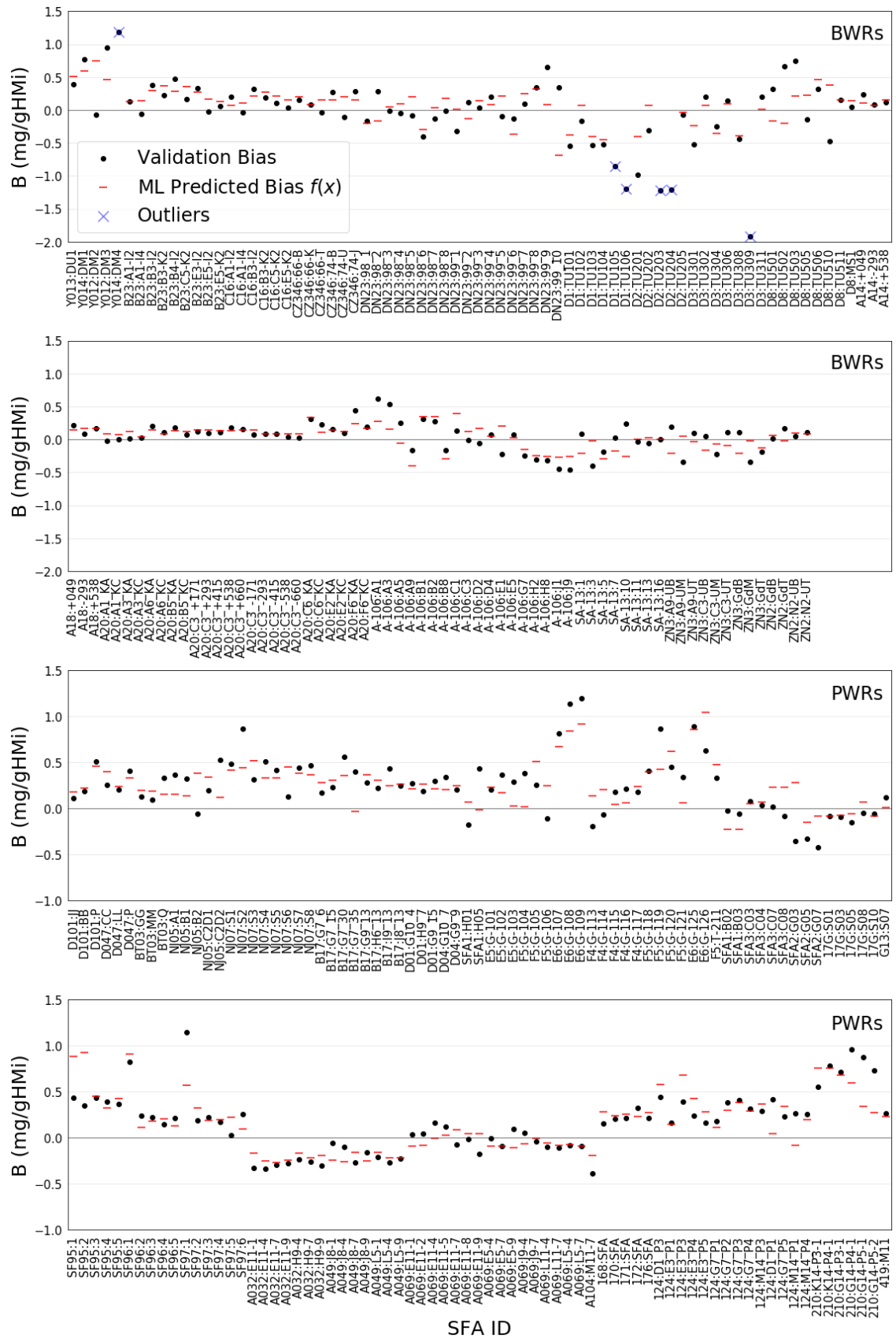


Figure 68. Same as Figure 67 for the Pu-239 concentration.

Chapter 12 Conclusions

The presented research started with a well-defined target: analyzing methods that can allow predicting the difference between calculations of characteristics of spent nuclear fuels (SNF) and their measurements, namely the bias ($C - E$). The research focused on SNF decay heat and concentrations of the following radionuclides: Cs-137, U-235, and Pu-239, being important for the economics and long-term safety of the DGR. The SNF decay heat is an important parameter for the number of disposal canisters required to encapsulate the SNF assemblies for their final disposal, affecting the economics of the DGR. The chosen radionuclides are important for the long-term safety of the repository and the calculated dose rates. Also, they are the most abundantly measured isotopes in open literature addressing PIE of LWR fuel samples, allowing to obtain relatively large datasets to be used in the subsequent data-driven analyses.

Data-driven methods were analyzed, machine learning (ML) models and algorithms, relying on validation benchmarks. The research proceeded in three phases: (1) collecting data, *i.e.*, decay heat and post-irradiation-examination (PIE) benchmarks, along with performing calculations of the measured characteristics, (2) propagating uncertainties in nuclear data (ND) and SNF design and operation (DO) history to the calculated quantities, (3) analyzing the validation and uncertainty analyses results, using statistical hypothesis testing on the significance of the observed biases, and finally (4) applying ML models and algorithms, and analyses of their predictive performance for biases. The last step of this work is a novelty, applying data-driven methods potentially promising in predicting the bias of SNF characteristics. These steps are detailed in the following discussion, starting from chapter 7 up to 11.

Chapter 7 – Validation Results: Validation benchmarks are collected from open-literature, *i.e.*, SNF design and irradiation specifications, as well as the measurements of their characteristics. The data are 262 decay heat measurements, conducted by Svensk Kärnbränslehantering AB (SKB) and General Electric (GE), at the Clab and the GE-Morris facilities, and 285 PIE samples, obtained from the SFCOMPO 2.0 database. Then, these benchmarks were modelled using the Polaris code of the SCALE code system (SCALE 6.2.3), and the calculated values were compared to the measured ones.

The decay heat bias has large variance in the GE-Morris benchmarks compared to the Clab ones, and also for the BWRs compared to PWRs. However, the average bias is small, being within ± 5 W, corresponding to 0.5% and 1.2% for the BWR and PWR sections of the data. . The concentration biases of the analyzed isotopes show large variances in SFAs originating from both reactor types. However, the biases are small on average. The U-235 concentration biases are 0.11 and

0.25 mg/gHMi in the BWRs and PWRs, respectively (corresponding to 1.017 and 1.025 for the C/E). The Pu-239 concentration biases are 0.01 and 0.21 mg/gHMi in the BWRs and PWRs, respectively (corresponding to 1.013 and 1.039 for the C/E). The Cs-137 concentration biases are within ± 0.01 mg/gHMi in both the BWRs and PWRs on average (corresponding to 0.996 for the C/E). Again, these biases show large variances around their averages.

Chapter 8 – Uncertainty Analyses: Uncertainties of ND and DO origins were propagated to the calculated quantities, relying on SCALE-based ND for the former, and literature values along with additional assumptions for the latter [56]. Uncertainties in the calculated decay heat values are $\sim 2.3\%$ (1σ). Uncertainties in the U-235 and Pu-239 concentrations are between 2.5-3.0% for the former and 2.4-2.6% for the latter. The Cs-137 concentration uncertainties are between 1.7-1.8%.

The uncertainties showed increasing trend with burnup for both the decay heat and U-235 concentration, also along with increasing contributions from ND uncertainties. The Pu-239 concentration, being significantly affected by several parameters, showed various levels of uncertainties and contributions from ND. For the Cs-137 concentration, the uncertainties are mainly due to DO uncertainties. The burnup uncertainties largely contribute to uncertainties of the analyzed characteristics. For the U-235 and Pu-239 concentrations, uncertainties in other parameters also show large effects on the uncertainties, such as enrichment for the former, and coolant density for the latter.

The correlations between the calculated decay heat values are high, being >0.96 due to perturbations of DO parameters and >0.24 due to perturbations of ND. The U-235 correlation matrices showed that benchmarks having similarities in their burnup values correlate largely with each other, due to perturbations in both ND and DO parameters. The Pu-239 correlation matrix based on ND shows similarities to the corresponding U-235 matrix, and the one based on DO parameters shows different levels of correlations. Both matrices span wider correlation ranges than the U-235 matrices. The Cs-137 correlations matrices also show significantly high correlations.

Chapter 9 – Significance of the Bias Based on the Validation Data and Chapter 10 – Significance of the Bias Based on the Validation and Uncertainty Data: The significance of the biases was assessed using two techniques: (1) randomization tests on the validation data, and (2) parametric z-tests on both the validation and uncertainty analyses data. Firstly, randomization tests were applied using both bootstrapping and permutations. The conclusions drawn are: (1) the calculations for the PWRs tend to be systematically biased for all of the analyzed characteristics, and (2) the calculations for the BWRs do not show such conclusion. The results of the bootstrapping and permutations tests are similar, however at slightly different p -values. The null hypothesis is

$$H_0: C_P = E. \quad (14.1)$$

Simultaneous hypotheses testing was applied on the decay heat data, using ORIGEN in addition to Polaris, requiring more evidence against the null hypothesis. The conclusions drawn from

the Polaris calculations were confirmed also by the application of ORIGEN: the PWR data tend to be systematically biased in the calculations of both codes simultaneously, and the BWR data do not show such evidence in both Polaris and ORIGEN calculations. The null hypothesis is

$$H_0: C_P \text{ or } C_O = E. \quad (14.2)$$

Including uncertainties in the hypothesis testing, regarding the significance of the bias, provided different conclusions. The bias is assumed to follow a normal distribution with mean zero, and variance obtained from uncertainties, meaning that

$$C - E \sim N(0, \sigma). \quad (14.3)$$

The hypothesis testing indicates that the observed bias is not significant for the U-235 concentration, given the calculated uncertainties. In contrast, the Pu-239 concentration bias is found to be significant. The decay heat and Cs-137 concentration biases can be significant in different sections of the data. For the decay heat, the observed biases failed to show significance only when both the calculated and the experimental uncertainties are considered. It is also shown that it is crucial to include the correlations between the benchmarks into the hypothesis testing, consequently accounting for their similarities.

Chapter 11 – Predicting the Bias of SNF Characteristics: Firstly, features were included in the ML models assuming that they are informative for the bias predictions, and this assumption is tested based on the data and conservative ML algorithms. The features were included following three approaches: (1) collecting features from literature being used in other neutronics applications, (2) applying perturbations to DO parameters, and collecting parameters that significantly affect the calculated values, and (3) based on specific assumptions. Features of the first type include the ones commonly used in validation of criticality safety analysis, such as the hydrogen-to-fissile atom ratio (H/X) and the similarity index (c_x) (Pearson correlation coefficient between calculated values). Features of the second type are such as burnup and enrichment. Features of the third type are such as the spectral index (SI) and uncertainties of both ND and DO origins.

Secondly, a novel approach is followed by applying data-driven methods to predict the bias of SNF characteristics using the validation and uncertainty analyses data. The predictive performance of the models was analyzed, comparing the original validation-based biases to the ML model-based bias predictions. The analyzed models predict the bias using highly similar or neighbors of the target benchmark, *i.e.*, neighborhood-based schemes. The models are the ensemble model random forests (RF) and the kernel-based model weighted k-nearest neighbors (KKNN).

In regard to models, the analyses show that the linear model (LM) does not provide satisfactory bias predictions in any of the analyzed characteristics. The LM-based bias predictions show low similarity to the validation-based ones, even if the LM showed statistical significance of their slopes. The promising models in terms of their bias predictive performance are the RF and the KKNN models, particularly the former, which can predict the bias with a reasonable level of ac-

curacy. The applications of these models on the decay heat and the Pu-239 concentration resulted in reduction of the variances of the original validation data and provided bias predictions having similarity to the original validation-based ones.

In regard to features, the promising models predict the bias using a few parameters, namely:

1. The SI for the decay heat bias,
2. The H/X for the Pu-239 concentration bias,
3. The c_x for both biases of the decay heat and the Pu-239 concentration.

In regard to data, bias predictions of the decay heat are analyzed using two types of data that differ in their experimental uncertainty. Bias predictions are not promising in the learning setting based on data having large experimental uncertainty. Alternatively, promising bias predictions were obtained only considering the data having low experimental uncertainty, *i.e.*, the Clab benchmarks.

Outliers were removed from the promising RF models, using SI and c_x for the decay heat and H/X and c_x for the Pu-239 concentration. Similar outliers are shared by different models using different design matrices; however, they are not identical. The outliers removal allowed further reductions of the original variance in the validation-based bias data, attaining reductions of approximately 0.5 for the decay heat, and between 0.5 and 0.63 for the Pu-239 concentration.

In contrast, the biases of the U-235 and Cs-137 concentrations could not be satisfactory predicted, and no significant reduction of the original variances of the validation data was obtained.

12.1 Applicability domain

In the present study, the prediction error is specific to the calculational tools and the validation data (*e.g.*, to Polaris and the SCALE nuclear data, and the validation benchmarks). Using a different lattice code, nuclear data, and validation benchmarks is expected to result in a different bias vector, subsequently a different prediction error. Also, the error is specific to the applied ML models and algorithms – *e.g.*, the procedures of removing outliers and also selecting the optimal model parameters. Implementing other models, *e.g.*, higher predictive models such as neural networks, or less conservative outliers criteria, *e.g.*, at $z = 2$, would therefore result in a different prediction error.

12.2 Potential applications

The mentioned SNF characteristics are typically obtained using calculations, and the calculational methods and input data are required to be validated *a priori*. The present study provides a validation of a widely used code, applied on relatively large datasets of decay heat and PIE benchmarks. The data can be used to estimate biases of realistic calculations of these SNF characteristics. Also, realistic calculations are routinely conducted on SNF, potentially having different similarities to the validation benchmarks. The analyses showed that the bias of a calculational

method and data of the SNF decay heat and Pu-239 concentration can be predicted from comparison with validation benchmark, using features such as SI , H/X , and c_x . The bias prediction techniques can be used to obtain data-informed safety margins or correction factors for SNF calculated characteristics. Applications such as subsequent safety analyses on SNF, relying on calculated inventories or decay heat, can benefit from knowledge about the bias in the upstream calculations.

12.3 Future work

The number of the analyzed benchmarks is relatively large; however, it does not cover all open-literature benchmarks, and also it does not include other proprietary benchmarks. Increasing the size of the validation data can improve the applied analyses. Also, the analyzed benchmarks cover only limited ranges of SNF properties, *e.g.*, all the decay heat benchmarks are UO₂-based fuel assemblies. Including MOX-based SNF and higher burnup assemblies can potentially improve the analyses and the bias prediction techniques. Further improvements can be achieved including data with lower uncertainties, as it was demonstrated in comparing sections of the decay heat data largely different in their experimental uncertainties.

The limitations of the LM should be analyzed in other SNF applications, as well as the applicability of the neighborhood-based models for a wider range of SNF applications. The analyzed ML models are a small fraction of the available models, and other models that differ in their assumptions can be analyzed for their predictive performance of the bias. Lastly, the applied ML algorithm is selectively conservative, placing preference on simpler models that contain few numbers of features. Indeed, the successful models of the decay heat and Pu-239 concentration contain only one feature. The latter assumption leads to conservative models, at the expense of some loss of the bias predictive performance – still acceptable. ML models that relax the latter assumption are potentially having better predictive performance and can be analyzed in the future.

Bibliography

- [1] Working Group 1 of the Joint Committee for Guides in Metrology (JCGM/WG 1), Evaluation of measurement data — Guide to the expression of uncertainty in measurement. Évaluation des données de mesure — Guide pour l'expression de l'incertitude de mesure, JCGM 100:2008, 2008. https://www.bipm.org/documents/20126/2071204/JCGM_100_2008_E.pdf/cb0ef43f-baa5-11cf-3f85-4dcd86f77bd6.
- [2] Posiva & SKB, Safety functions, performance targets and technical design requirements for a KBS-3V repository - Conclusions and recommendations from a joint SKB and Posiva working group, Posiva SKB Report 01, ISSN 2489-2742, Posiva, Finland; SKB, Sweden, 2017. <https://www.skb.se/publikation/2485568/Posiva+SKB+Report+01.pdf>.
- [3] Nagra, The Nagra Research, Development and Demonstration (RD&D) Plan for the Disposal of Radioactive Waste in Switzerland, Technical Report 16-02, Nagra, Switzerland, 2016. https://www.nagra.ch/display.cfm/id/102495/disp_type/display/filename/e_ntb16-02.pdf.
- [4] Spent Nuclear Fuel Storage and Disposal • Stimson Center, Stimson Center. (2020). <https://www.stimson.org/2020/spent-nuclear-fuel-storage-and-disposal/> (accessed August 20, 2021).
- [5] Radioactive Waste Management | Nuclear Waste Disposal - World Nuclear Association, (2021). <https://world-nuclear.org/information-library/nuclear-fuel-cycle/nuclear-wastes/radioactive-waste-management.aspx> (accessed August 20, 2021).
- [6] ENSI, Specific design principles for deep geological repositories and requirements for the safety case, Guideline ENSI-G03, Switzerland, 2009. www.ensi.ch/en/wp-content/uploads/sites/5/2011/08/g-003_e.pdf.
- [7] H. Maxeiner, M. Vespa, B. Volmert, M. Pantelias, S. Caruso, T. Müller, Development of the inventory for existing and future radioactive wastes in Switzerland: ISRAM & MIRAM, ATW-International Journal for Nuclear Power. 58 (2013) 625–634.
- [8] S. Caruso, M. Pantelias Garcés, Spent Nuclear Fuel Management in Switzerland: Perspective for Final Disposal, IAEA International Conference on the Management of Spent Fuel from Nuclear Power Reactors: An Integrated Approach to the Back End of the Fuel Cycle, IAEA Headquarters, Vienna, Austria, 2015.
- [9] gs-soft AG, Benutzerhandbuch ISRAM Version 4, gs-soft (AG), Switzerland, 2011.
- [10] BFE, Deep Geological Repositories Sectoral Plan - Sachplan geologische Tiefenlager - Dokumentation "minimales Geodatenmodell," Bundesamt für Energie, Switzerland, 2012. http://www.bfe.admin.ch/php/modules/publikationen/stream.php?extlang=de&name=de_687132619.pdf.
- [11] F. Michel-Sendis, I. Gauld, J.S. Martinez, C. Alejano, M. Bossant, D. Boulanger, O. Cabellos, V. Chrapciak, J. Conde, I. Fast, M. Gren, K. Govers, M. Gysemans, V. Hannstein, F. Havlůj, M. Hennebach, G. Hordosy, G. Ilas, R. Kilger, R. Mills, D. Mountford, P. Ortego, G. Radulescu, M. Rahimi, A. Ranta-Aho, K. Rantamäki, B. Ruprecht, N. Soppera, M. Stuke, K. Suyama, S. Tittelbach, C. Tore, S.V. Winckel, A. Vasiliev, T. Watanabe, T. Yamamoto, T. Yamamoto, SFCOMPO-2.0: An OECD NEA database of spent

- nuclear fuel isotopic assays, reactor design specifications, and operating data, *Annals of Nuclear Energy*. 110 (2017) 779–788. <https://doi.org/10.1016/j.anucene.2017.07.022>.
- [12] SKB, Measurements of decay heat in spent nuclear fuel at the Swedish interim storage facility, Clab, R-05-62, Svensk Kärnbränslehantering AB (SKB), Sweden, 2006. <https://www.skb.se/publikation/1472024/R-05-62.pdf>.
- [13] L. E. Wiles, N. J. Lornbardo, C. M. Heeh, U. P. Jenquin, T. E. Michener, C. L. Wheeler, J. M. Creer, R. A. McCann, BWR Spent Fuel Storage Cask Performance. Pre-and Post-Test Decay Heat, Heat Transfer, and Shielding Analyses, PNL-5777 Vol. II, USA, 1986.
- [14] European Joint Programme on Radioactive Waste Management | EURAD Project | H2020, CORDIS | European Commission. (2021). <https://cordis.europa.eu/project/id/847593> (accessed December 28, 2020).
- [15] SKB, Confidential communication with the SKB (Sweden), (2018).
- [16] New CRP: Spent Fuel Research and Assessment (SFERA) (T13020), (2021). <https://www.iaea.org/newscenter/news/new-crp-spent-fuel-research-and-assessment-sfera-t13020> (accessed August 20, 2021).
- [17] IAEA, Spent Fuel Performance Assessment and Research - Final Report of a Coordinated Research Project (SPAR-IV), International Atomic Energy Authority, IAEA, TECDOC Series, Vienna, Austria, 2021. <https://www-pub.iaea.org/MTCD/Publications/PDF/TE-1975web.pdf> (accessed November 12, 2021).
- [18] Working Party on Nuclear Criticality Safety (WPNCS), Nuclear Energy Agency (NEA). (2021). https://www.oecd-neo.org/jcms/pl_23012/working-party-on-nuclear-criticality-safety-wpncs (accessed August 20, 2021).
- [19] TRG SFCOMPO, TRG SFCOMPO. (2021). https://www.oecd-neo.org/jcms/pl_58104/technical-review-group-for-the-international-assay-data-of-spent-nuclear-fuel-database-trg-sfcompo.
- [20] P. Jansson et al., Blind Benchmark Exercise for Spent Nuclear Fuel Decay Heat, Submitted to Nuclear Science and Engineering. (2021).
- [21] ENSI, Swiss Federal Nuclear Safety Inspectorate (ENSI), Switzerland, 2018. <https://www.ensi.ch/en/>.
- [22] KEG, Nuclear Energy Act, NEA (KEG), Switzerland, 2003. <https://www.admin.ch/opc/de/classified-compilation/20010233/201801010000/732.1.pdf> (accessed September 1, 2018).
- [23] The Federal Council, Federal Act on the Federal Nuclear Safety Inspectorate (ENSIG), Switzerland, 2007. <https://www.admin.ch/opc/de/classified-compilation/20051479/201201010000/732.2.pdf> (accessed September 1, 2018).
- [24] U. Berner, Solubility of Radionuclides in a Bentonite Environment for Provisional Safety Analyses for SGT-E2, Nagra Technical Report NTB 14-06, Nagra, Switzerland, 2014. <https://www.nagra.ch/en/technical-report-14-06>.
- [25] W. Hummel, Chemistry of selected dose-relevant radionuclides, NTB 17-05, Nagra, Switzerland, 2017.
- [26] I.C. Gauld, B.D. Murphy, Technical Basis for a Proposed Expansion of Regulatory Guide 3.54 - Decay Heat Generation in an Independent Spent Fuel Storage Installation, NUREG/CR-6999, ORNL/TM-2007/231, ORNL (Oak Ridge National Laboratory), Oak Ridge, Tennessee, USA, 2010.
- [27] I.C. Gauld, G. Ilas, B.D. Murphy, C.F. Weber, Validation of SCALE 5 Decay Heat Predictions for LWR Spent Nuclear Fuel, NUREG/CR-6972, ORNL/TM-2008/015, ORNL (Oak Ridge National Laboratory), Oak Ridge, Tennessee, USA, 2010.

-
- [28] G. Ilas, I.C. Gauld, H. Liljenfeldt, Validation of ORIGEN for LWR used fuel decay heat analysis with SCALE, *Nuclear Engineering and Design*. 273 (2014) 58–67. <https://doi.org/10.1016/j.nuceng-des.2014.02.026>.
- [29] S. Børresen, T. Bahadir, M. Kruners, Validation of CMS/SNF Calculations Against Preliminary CLAB Decay Heat Measurements, in: *Transactions of the American Nuclear Society*, Vol. 91, 435, Washington D.C., USA, 2004.
- [30] W. Haeck, R. Ichou, F. Ecrabet, J. Dannet, Experimental Validation of Decay Heat Calculations with VESTA 2.1, in: *PHYSOR 2014 International Conference on the Physics of Reactors*, Kyoto, Japan, 2014.
- [31] A. Shama, D. Rochman, S. Caruso, A. Pautz, Validation of spent nuclear fuel decay heat calculations using Polaris, ORIGEN and CASMO5, *Annals of Nuclear Energy*. 165 (2022) 108758. <https://doi.org/10.1016/j.anucene.2021.108758>.
- [32] ANS, Validation of Neutron Transport Methods for Nuclear Criticality Safety Calculations, American Nuclear Society. ANSI/ANS-8.24, 2017.
- [33] J.-C. Sublet, JEFF-3.1, ENDF/B-VII and JENDL-3.3 Critical Assemblies Benchmarking With the Monte Carlo Code TRIPOLI, *IEEE Transactions on Nuclear Science*. 55 (2008) 604–613. <https://doi.org/10.1109/TNS.2007.911600>.
- [34] L. San Felice, R. Eschbach, R. Dewi Syarifah, S.-E. Maryam, K. Hesketh, MOx Depletion Calculation Benchmark, Organisation for Economic Co-Operation and Development (OCED), 2016. http://inis.iaea.org/Search/search.aspx?orig_q=RN:49042360 (accessed August 20, 2020).
- [35] B. Roque, R. Gregg, R. Kilger, F. Laugier, P. Marimbeau, A. Ranta-Aho, C. Riffard, K. Suyama, J.F. Thro, M. Yudkevich, K. Hesketh, E. Sartori, International comparison of a depletion calculation benchmark devoted to fuel cycle issues results from the phase 1 dedicated to PWR-UOx fuels, (2006). http://inis.iaea.org/Search/search.aspx?orig_q=RN:43130067 (accessed August 19, 2020).
- [36] OECD/NEA, Burn-up Credit Criticality Benchmark: Phase IV-A: Reactivity Prediction Calculations for Infinite Arrays of PWR MOX Fuel Pin Cells, Nuclear Science, OECD Publishing, Paris, 2003. <https://doi.org/10.1787/9789264103498-en>. (accessed August 19, 2020).
- [37] I. Gauld, U. Mertzyurek, Margins for Uncertainty in the Predicted Spent Fuel Isotopic Inventories for BWR Burnup Credit, NUREG/CR-7251. U.S. NRC, ORNL (Oak Ridge National Laboratory), Oak Ridge, Tennessee, USA, 2018.
- [38] G. Radulescu, I.C. Gauld, G. Ilas, J.C. Wagner, Approach for Validating Actinide and Fission Product Compositions for Burnup Credit Criticality Safety Analyses, *Nuclear Technology*. 188 (2014) 154–171. <https://doi.org/10.13182/NT13-154>.
- [39] J.J. Lichtenwalter, S.M. Bowman, M.D. DeHart, C.M. Hopper, Criticality Benchmark Guide for Light-Water-Reactor Fuel in Transportation and Storage Packages, NUREG/CR-6361 - ORNL/TM-13211, ORNL (Oak Ridge National Laboratory), Oak Ridge, Tennessee, USA, 1997.
- [40] J.C. Dean, R.W. Tayloe, Guide for Validation of Nuclear Criticality Safety Computational Methodology, ORNL, ORNL-6698, NUREG/CR-6698, ORNL (Oak Ridge National Laboratory), Oak Ridge, Tennessee, USA, 2001.
- [41] B.L. Broadhead, B.T. Rearden, C.M. Hopper, J.J. Wagschal, C.V. Parks, Sensitivity- and Uncertainty-Based Criticality Safety Validation Techniques, *Nuclear Science and Engineering*. 146 (2004) 340–366. <https://doi.org/10.13182/NSE03-2>.
- [42] O. W. Hermann, C. V. Parks, J. P. Renier, Technical Support for a Proposed Decay Heat Guide Using SAS2H/ORIGEN-S Data, ORNL-6698, NUREG/CR-5625, ORNL (Oak Ridge National Laboratory), Oak Ridge, Tennessee, USA, 1994.
-

-
- [43] US/NRC, Regulatory Guide 3.54, Spent Fuel Heat Generation in an Independent Spent Fuel Storage Installation Rev. 2, NRC, USA, 2018.
- [44] G. Radulescu, D.E. Mueller, J.C. Wagner, Sensitivity and Uncertainty Analysis of Commercial Reactor Criticals for Burnup Credit, *Nuclear Technology*. 167 (2009) 268–287. <https://doi.org/10.13182/NT09-A8963>.
- [45] P. Grechanuk, M.E. Rising, T.S. Palmer, Using Machine Learning Methods to Predict Bias in Nuclear Criticality Safety, *Journal of Computational and Theoretical Transport*. 47 (2018) 552–565. <https://doi.org/10.1080/23324309.2019.1585877>.
- [46] D. Neudecker, M. Grosskopf, M. Herman, W. Haeck, P. Grechanuk, S. Vander Wiel, M.E. Rising, A.C. Kahler, N. Sly, P. Talou, Enhancing nuclear data validation analysis by using machine learning, *Nuclear Data Sheets*. 167 (2020) 36–60. <https://doi.org/10.1016/j.nds.2020.07.002>.
- [47] B. Ebiwonjumi, A. Cherezov, S. Dzianisau, D. Lee, Machine Learning of LWR Spent Nuclear Fuel Assembly Decay Heat Measurements, *Nuclear Engineering and Technology*. (2021). <https://doi.org/10.1016/j.net.2021.05.037>.
- [48] V. Solans, D. Rochman, C. Brazell, A. Vasiliev, H. Ferroukhi, A. Pautz, Optimisation of used nuclear fuel canister loading using a neural network and genetic algorithm, *Neural Comput & Applic.* (2021). <https://doi.org/10.1007/s00521-021-06258-2>.
- [49] B.T. Bearden, M.A. Jessee, SCALE Code System, ORNL/TM-2005/39, Oak Ridge National Laboratory, Oak Ridge, Tennessee, USA, 2018.
- [50] V. Cloet, Selection of dose-relevant radionuclides (dRN) for reference scenario in SGT-Stage 3, AN 16-559, NAGRA, Switzerland, 2017.
- [51] SKB, Radionuclide transport report for the safety assessment SR-Site, Technical Report, TR 10-50, 2010. https://inis.iaea.org/collection/NCLCollectionStore/_Public/42/040/42040077.pdf.
- [52] Posiva, Case for the Disposal of Spent Nuclear Fuel at Olkiluoto - Models and Data for the Repository System 2012, Posiva Report 2013-01, part 2, 2013. https://inis.iaea.org/collection/NCLCollectionStore/_Public/45/087/45087751.pdf.
- [53] F. Schmittroth, ORIGEN2 Calculations of PWR Spent Fuel Decay Heat Compared with Calorimeter Data, Hanford Engineering Development Laboratory, HEDL-TME-83-32 (UC-85), USA, 1984.
- [54] M. A. McKinnon, J. W. Doman, J. E. Tanner, R. J. Guenther, J. M. Creer, C. E. King, BWR Spent Fuel Storage Cask Performance. Cask Handling Experience and Decay Heat, Heat Transfer, and Shielding Data, PNL-5777 Vol. I, USA, 1986.
- [55] I.C. Gauld, M.L. Williams, F. Michel-Sendis, J.S. Martinez, Integral nuclear data validation using experimental spent nuclear fuel compositions, *Nuclear Engineering and Technology*. 49 (2017) 1226–1233. <https://doi.org/10.1016/j.net.2017.07.002>.
- [56] Nuclear Science Committee, Working Party on Nuclear Criticality Safety (WPNCs), Expert Group on Assay Data of Spent Nuclear Fuel (EGADSNF), Evaluation Guide for the Evaluated Spent Nuclear Fuel Assay Database (SFCOMPO), NEA/NSC/R(2015)8, OCED/NEA, 2016. <https://www.oecd-neo.org/science/docs/2015/nsc-r2015-8.pdf>.
- [57] R Core Team, R: A Language and Environment for Statistical Computing, R Foundation for Statistical Computing, Vienna, Austria, 2013. <https://www.R-project.org>.
- [58] M. Kuhn, caret: Classification and Regression Training. R package version 6.0-86, 2020. <https://CRAN.R-project.org/package=caret>.
-

-
- [59] M.A. Jessee, W.A. Wieselquist, U. Mertyurek, K.S. Kim, T.M. Evans, S.P. Hamilton, C. Gentry, Lattice physics calculations using the embedded self-shielding method in Polaris, Part I: Methods and implementation, *Annals of Nuclear Energy*. 150 (2021) 107830. <https://doi.org/10.1016/j.anucene.2020.107830>.
- [60] U. Mertyurek, M.A. Jessee, B.R. Betzler, Lattice physics calculations using the embedded self-shielding method in polaris, Part II: Benchmark assessment, *Annals of Nuclear Energy*. 150 (2021) 107829. <https://doi.org/10.1016/j.anucene.2020.107829>.
- [61] M.D. DeHart, S.M. Bowman, Reactor Physics Methods and Analysis Capabilities in SCALE, *Nuclear Technology*. 174 (2011) 196–213. <https://doi.org/10.13182/NT174-196>.
- [62] I.C. Gauld, G. Radulescu, G. Ilas, B.D. Murphy, M.L. Williams, D. Wiarda, Isotopic Depletion and Decay Methods and Analysis Capabilities in SCALE, *Nuclear Technology*. 174 (2011) 169–195. <https://doi.org/10.13182/NT11-3>.
- [63] M.L. Williams, G. Ilas, M.A. Jessee, B.T. Rearden, D. Wiarda, W. Zwermann, L. Gallner, M. Klein, B. Krzykacz-Hausmann, A. Pautz, A Statistical Sampling Method for Uncertainty Analysis with SCALE and XSUSA, *Nuclear Technology*. 183 (2013) 515–526. <https://doi.org/10.13182/NT12-112>.
- [64] G. Radulescu, I.C. Gauld, G. Ilas, SCALE 5.1 Predictions of PWR Spent Nuclear Fuel Isotopic Compositions, ORNL/TM-2010/44, ORNL (Oak Ridge National Laboratory), Oak Ridge, Tennessee, USA, 2010.
- [65] D. Rochman, A. Vasiliev, H. Ferroukhi, M. Hursin, Analysis for the ARIANE GU1 sample: Nuclide inventory and decay heat, *Annals of Nuclear Energy*. 160 (2021) 108359. <https://doi.org/10.1016/j.anucene.2021.108359>.
- [66] J. R. Lamarsh, A. J. Baratta, *Introduction to Nuclear Engineering*, 4th Edition, 4th ed., Pearson, 2018. <https://www.pearson.com/content/one-dot-com/one-dot-com/us/en/higher-education/program.html> (accessed June 28, 2021).
- [67] P.J. Turinsky, Core Isotopic Depletion and Fuel Management, in: D.G. Cacuci (Ed.), *Handbook of Nuclear Engineering*, Springer US, Boston, MA, 2010: pp. 1241–1312. https://doi.org/10.1007/978-0-387-98149-9_10.
- [68] U. Mertyurek, M.W. Francis, I.C. Gauld, SCALE 5 Analysis of BWR Spent Nuclear Fuel Isotopic Compositions for Safety Studies, ORNL/TM-2010/286, Oak Ridge National Laboratory, Oak Ridge, Tennessee, USA, 2010.
- [69] H.T. Hayslett, P. Murphy, *Statistics*, Elsevier, 1981. <https://doi.org/10.1016/C2013-0-01181-4>.
- [70] R.G. Miller, Nonparametric Techniques, in: R.G. Miller (Ed.), *Simultaneous Statistical Inference*, Springer New York, New York, NY, 1981: pp. 129–188. https://doi.org/10.1007/978-1-4613-8122-8_4.
- [71] N.R. Draper, *The Cambridge Dictionary of Statistics*, Fourth Edition by B. S. Everitt, A. Skrondal, *International Statistical Review*. 79 (2011) 273–274. https://doi.org/10.1111/j.1751-5823.2011.00149_2.x.
- [72] J.D. Evans, *Straightforward statistics for the behavioral sciences*, Brooks/Cole Pub. Co., Pacific Grove, 1996.
- [73] S.A. Stouffer, E.A. Suchman, L.C. Devinney, S.A. Star, R.M. Williams Jr., *The American soldier: Adjustment during army life. (Studies in social psychology in World War II)*, Vol. 1, Princeton Univ. Press, Oxford, England, 1949.
- [74] L. Breiman, Statistical Modeling: The Two Cultures (with comments and a rejoinder by the author), *Statist. Sci.* 16 (2001) 199–231. <https://doi.org/10.1214/ss/1009213726>.
- [75] G. James, D. Witten, T. Hastie, R. Tibshirani, *An Introduction to Statistical Learning: with Applications in R*, Springer-Verlag, New York, 2013. <https://doi.org/10.1007/978-1-4614-7138-7>.
-

-
- [76] C. Rudin, J. Radin, Why Are We Using Black Box Models in AI When We Don't Need To? A Lesson From An Explainable AI Competition, *Harvard Data Science Review*. 1 (2019). <https://doi.org/10.1162/99608f92.5a8a3a3d>.
- [77] C.J. Willmott, On the Validation of Models, *Physical Geography*. 2 (1981) 184–194. <https://doi.org/10.1080/02723646.1981.10642213>.
- [78] W.W. Daniel, *Applied Nonparametric Statistics*, PWS-KENT Pub., 1990.
- [79] T.A. Jones, Fitting straight lines when both variables are subject to error, *Mathematical Geology*. 11 (1979) 1–25. <https://doi.org/10.1007/BF01043243>.
- [80] L. Breiman, J. Friedman, C.J. Stone, R.A. Olshen, *Classification And Regression Trees*, Routledge, 1984. <https://doi.org/10.1201/9781315139470>.
- [81] S. Raschka, Model Evaluation, Model Selection, and Algorithm Selection in Machine Learning, *ArXiv:1811.12808 [Cs, Stat]*. (2020). <http://arxiv.org/abs/1811.12808> (accessed March 20, 2021).
- [82] T. Hastie, R. Tibshirani, J. Friedman, *The Elements of Statistical Learning: Data Mining, Inference, and Prediction*, 2nd ed., Springer-Verlag, New York, 2009. <https://doi.org/10.1007/978-0-387-84858-7>.
- [83] B.T. Rearden, M.L. Williams, M.A. Jessee, D.E. Mueller, D.A. Wiarda, Sensitivity and Uncertainty Analysis Capabilities and Data in SCALE, *Nuclear Technology*. 174 (2011) 236–288. <https://doi.org/10.13182/NT174-236>.
- [84] Y. Lin, Y. Jeon, Random Forests and Adaptive Nearest Neighbors, *Journal of the American Statistical Association*. (2002) 101–474.
- [85] M. Kuhn, K. Johnson, *Applied Predictive Modeling*, Springer-Verlag, New York, 2013. <https://doi.org/10.1007/978-1-4614-6849-3>.
- [86] C.C. Aggarwal, *Outlier Analysis*, Second Edition, Springer, New York, NY, 2017. <https://doi.org/10.1007/978-1-4614-6396-2>.
- [87] C.M. Perfetti, B.T. Rearden, Estimating Code Biases for Criticality Safety Applications with Few Relevant Benchmarks, *Nuclear Science and Engineering*. 193 (2019) 1090–1128. <https://doi.org/10.1080/00295639.2019.1604048>.
- [88] F. Kamalov, Sensitivity Analysis for Feature Selection, in: 2018 17th IEEE International Conference on Machine Learning and Applications (ICMLA), 2018: pp. 1466–1470. <https://doi.org/10.1109/ICMLA.2018.00238>.
- [89] N. Sánchez-Marroño, A. Alonso-Betanzos, Feature Selection Based on Sensitivity Analysis, in: D. Borrajo, L. Castillo, J.M. Corchado (Eds.), *Current Topics in Artificial Intelligence*, Springer, Berlin, Heidelberg, 2007: pp. 239–248. https://doi.org/10.1007/978-3-540-75271-4_25.
- [90] T. Yamamoto, D. Iwahashi, Validation of decay heat calculation results of ORIGEN2.2 and CASMO5 for light water reactor fuel, *Journal of Nuclear Science and Technology*. 53 (2016) 2108–2118. <https://doi.org/10.1080/00223131.2016.1183528>.
- [91] H. EZURE, Calculation of Atom Ratios of $^{134}\text{Cs}/^{137}\text{Cs}$, $^{154}\text{Eu}/^{137}\text{Cs}$ and Pu/U , Burnup and Most Probable Production Amount of Plutonium in Fuel Assemblies of JPDR-1, *Journal of Nuclear Science and Technology*. 27 (1990) 562–571. <https://doi.org/10.1080/18811248.1990.9731221>.
- [92] A. Shama, D. Rochman, S. Pudollek, S. Caruso, A. Pautz, Uncertainty analyses of spent nuclear fuel decay heat calculations using SCALE modules, *Nuclear Engineering and Technology*. 53 (2021) 2816–2829. <https://doi.org/10.1016/j.net.2021.03.013>.
- [93] R. J. Guenther, D. E. Blahnik, T. K. Campbell, U. P. Jenquin, J. E. Mendel, L. E. Thomas, C. K. Thornhill, *Characterization of Spent Fuel Approved Testing Material-ATM-103*, Pacific Northwest Laboratory, Prepared for the U.S. Department of Energy, 1988.
-

-
- [94] R. J. Guenther, D. E. Blahnik, U. P. Jenquin, J. E. Mendel, L. E. Thomas, C. K. Thornhill, Characterization of Spent Fuel Approved Testing Material-ATM-104, Pacific Northwest Laboratory, Prepared for the U.S. Department of Energy, 1991.
- [95] R. J. Guenther, D. E. Blahnik, T. K. Campbell, U. P. Jenquin, J. E. Mendel, C. K. Thornhill, Characterization of Spent Fuel Approved Testing Material-ATM-106, Pacific Northwest Laboratory, Prepared for the U.S. Department of Energy, 1988.
- [96] O.W. Hermann, S.M. Bowman, C.V. Parks, M.C. Brady, Validation of the scale system for PWR spent fuel isotopic composition analyses, ORNL/TM-12667, Oak Ridge National Laboratory, Oak Ridge, Tennessee, USA, 1995. <https://doi.org/10.2172/57886>.
- [97] I.C. Gauld, G. Ilas, G. Radulescu, Uncertainties in Predicted Isotopic Compositions for High Burnup PWR Spent Nuclear Fuel, NUREG/CR-7012, ORNL/TM-2010/41, Oak Ridge National Laboratory, Oak Ridge, Tennessee, USA, 2010. <https://www.nrc.gov/reading-rm/doc-collections/nuregs/contract/cr7012/index.html> (accessed June 27, 2021).
- [98] JAERI, Dissolution studies of spent nuclear fuels, JAERI-M--91-010, Japan Atomic Energy Research Inst., 1991. http://inis.iaea.org/Search/search.aspx?orig_q=RN:22075708 (accessed June 29, 2021).
- [99] K. Suyama, H. Mochizuki, Corrections to the ^{148}Nd method of evaluation of burnup for the PIE samples from Mihama-3 and Genkai-1 reactors, *Annals of Nuclear Energy*. 33 (2006) 335–342. <https://doi.org/10.1016/j.anucene.2005.11.009>.
- [100] Y. Naito, M. Kurosawa, T. Kaneko, Data book of the isotopic composition of spent fuel in light water reactors, Japan Atomic Energy Research Inst., 1994. http://inis.iaea.org/Search/search.aspx?orig_q=RN:25047626 (accessed July 5, 2021).
- [101] M. Nichol, D. Henderson, D. Thomas, H. Benton, SAS2H Analysis of Radiochemical Assay Samples from Mihama PWR Reactor, BOOOOOOOO-01717-0200.00144 REV 00, NRC, USA, 1997. <https://www.nrc.gov/docs/ML0334/ML033450336.pdf>.
- [102] Hee S. S., Kenya S., Hiroki M., Hiroshi O., Yasushi N., Analyses of PWR spent fuel composition using SCALE and SWAT code systems to find correction factors for criticality safety applications adopting burnup credit, Japan Atomic Energy Research Inst. (JAERI). JAERI-Research 2000-066, 2001. <https://doi.org/10.11484/jaeri-research-2000-066>.
- [103] SCK-CEN, Belgonucleaire, REBUS International Programme (Reactivity Tests for a Direct Evaluation of the Burnup Credit on Selected Irradiated LWR Fuel Bundles). Fuel Irradiation History Report, BN Ref. : 0501278/221, 2005. <https://oecd-neo.org/science/wpncs/ADSNF/reports/GKN-II/RE2002-18RevB.pdf>.
- [104] SCK-CEN, Belgonucleaire, REBUS International Programme (Reactivity Tests for a Direct Evaluation of the Burnup Credit on Selected Irradiated LWR Fuel Bundles). Gamma Spectroscopy PIE on Irradiated GKN II Fuel Rods, BN Ref. : 0403182/221, 2004. <https://oecd-neo.org/science/wpncs/ADSNF/reports/GKN-II/RE2004-29.pdf>.
- [105] SCK-CEN, Belgonucleaire, REBUS International Programme (Reactivity Tests for a Direct Evaluation of the Burnup Credit on Selected Irradiated LWR Fuel Bundles). Destructive Radiochemical Spent Fuel Characterization of a PWR UO₂ Fuel Sample, BN Ref. : 0502640/221, 2006. <https://oecd-neo.org/science/wpncs/ADSNF/reports/GKN-II/RE2005-35RevA.pdf>.
- [106] U. Hesse, Verification of the OREST (HAMMER-ORIGEN) depletion program system using post-irradiation analyses of fuel assemblies 168, 170, 171 and 176 from the Obrigheim Reactor, Gesellschaft fuer Reaktorischerheit (GRS) mbH, Garching (Germany), 1984. <https://doi.org/10.2172/7777304>.
- [107] S. Guardini, G. Guzzi, Benchmark reference data on post irradiation analysis of light water reactor fuel samples, Commission of the European Communities. EUR 7879 EN, 1983. http://inis.iaea.org/Search/search.aspx?orig_q=RN:15003056 (accessed July 4, 2021).
-

- [108] K. Suyama, M. Murazaki, K. Ohkubo, Y. Nakahara, G. Uchiyama, Re-evaluation of Assay Data of Spent Nuclear Fuel obtained at Japan Atomic Energy Research Institute for validation of burnup calculation code systems, *Annals of Nuclear Energy*. 38 (2011) 930–941. <https://doi.org/10.1016/j.anucene.2011.01.025>.
- [109] S. INOUE, K. MORI, T. OKAMOTO, A. OE, Post Irradiation Examination of High Burnup PWR Fuel, *Journal of Nuclear Science and Technology*. 31 (1994) 1105–1118. <https://doi.org/10.1080/18811248.1994.9735265>.
- [110] Y. Nakahara, K. Suyama, T. Suzaki, Technical development on burn-up credit for spent LWR fuels, Japan Atomic Energy Research Inst., 2000. http://inis.iaea.org/Search/search.aspx?orig_q=RN:32011832 (accessed July 1, 2021).
- [111] Y. Nakahara, K. Suyama, J. Inagawa, R. Nagaishi, S. Kurosawa, N. Kohno, M. Onuki, H. Mochizuki, Nuclide Composition Benchmark Data Set for Verifying Burnup Codes on Spent Light Water Reactor Fuels, *Nuclear Technology*. 137 (2002) 111–126. <https://doi.org/10.13182/NT02-2>.
- [112] S.F. Wolf, D.L. Bowers, J.C. Cunnane, Analysis of high burnup spent nuclear fuel by ICP-MS, *J Radioanal Nucl Chem*. 263 (2005) 581–586. <https://doi.org/10.1007/s10967-005-0627-7>.
- [113] I.C. Gauld, J.M. Giaquinto, J.S. Delashmitt, J. Hu, G. Ilas, T.J. Haverlock, C. Romano, Re-evaluation of spent nuclear fuel assay data for the Three Mile Island unit 1 reactor and application to code validation, *Annals of Nuclear Energy*. 87 (2016) 267–281. <https://doi.org/10.1016/j.anucene.2015.08.026>.
- [114] R.D. Reager, R.B. Adamson, TRW Yucca Mountain Project. Test Report. GE Nuclear Energy, Phase 2. Ref., TRW Purchase Order No. A09112CC8A., 2000.
- [115] J.M. Scaglione, Three Mile Island Unit 1 Radiochemical Assay Comparisons to SAS2H Calculations, Yucca Mountain Project Report. CAL-UDC-NU-000011, Revision A, 2002.
- [116] A.M. Bresesti, M. Bresesti, S. Facchetti, F. Mannone, P. Barbero, C. Cerutti, F. Marell, A. Peil, R. Pietra, R. Klersy, A. Schurenkamper, A. Frigo, E. Ghezzi, J.P. Meerschman, A. Pollicini, K.H. Schrader, J. Biteau, A. Cricchio, L. Koch, Post-Irradiation Analysis of Trino Vercellese Reactor Fuel Elements. EUR 4909., (1972). <http://aei.pitt.edu/92097/> (accessed July 8, 2021).
- [117] P. Barbero, G. Bidoglio, M. Bresesti, Post irradiation examination of the fuel discharged from the Trino Vercellese reactor after the 2nd irradiation cycle, Commission of the European Communities, 1977. http://inis.iaea.org/Search/search.aspx?orig_q=RN:9360838 (accessed July 8, 2021).
- [118] S.D. Atkin, Destructive examination of 3-cycle LWR fuel rods from Turkey Point Unit 3 for the Climax-Spent Fuel Test, Hanford Engineering Development Lab., Richland, WA (USA), 1981. <https://www.osti.gov/biblio/6214864-destructive-examination-cycle-lwr-fuel-rods-from-turkey-point-unit-climax-spent-fuel-test> (accessed June 28, 2021).
- [119] R.B. Davis, V. Pasupathi, Data summary report for the destructive examination of Rods G7, G9, J8, I9, and H6 from Turkey Point Fuel Assembly B17, Hanford Engineering Development Lab., Richland, WA (USA), 1981. <https://doi.org/10.2172/6513670>.
- [120] M.D. DeHart, O.W. Hermann, An extension of the validation of SCALE (SAS2H) isotopic predictions for PWR spent fuel, ORNL/TM-13317, Oak Ridge National Laboratory, Oak Ridge, Tennessee, USA, 1996. <https://doi.org/10.2172/405743>.
- [121] H. W. Graves, Jr, R. F. Janz, C. G. Poncelet, The nuclear design of the Yankee core. R&D subcontract No.1 under USAEC-YAEC contract AT(30-3)-222, YAEC-136, 1961.
- [122] Burnup Credit – Contribution to the Analysis of the Yankee Rowe Radiochemical Assays, EPRI, 1022910, 2011. <https://www.epri.com/research/products/000000000001022910>.
- [123] J. Jedruch, R.J. Nodvik, Experimentally determined burnup and spent fuel composition of Yankee core I. Prepared for the New York Operations Office U. S. Atomic Energy Commission, Under AEC

- Contract Number AT(30-1)-3017, WCAP-6071, UC-80, Reactor Technology, TID-4500, 41st edition, 1966.
- [124] R.J. Nodvik, Evaluation of mass spectrometric and radiochemical analyses of Yankee core I spent fuel evaluation. Prepared for the New York Operations Office U. S. Atomic Energy Commission, Under AEC Contract Number AT(30-1)-3017, WCAP-6068, UC-80, Reactor Technology, 1966.
<https://doi.org/10.2172/4541710>.
- [125] R. J. Guenther, D. E. Blahnik, T. K. Campbell, U. P. Jenquin, J. E. Mendel, L. E. Thomas, C. K. Thornhill, Characterization of Spent Fuel Approved Testing Material-ATM-105, Pacific Northwest Laboratory, Prepared for the U.S. Department of Energy, 1991.
- [126] ARIANE International Programme Final Report, AR2000/15 BN Ref. 0000253/221, Revision B, Belgonucléaire, 2000.
- [127] T. YAMAMOTO, Y. KANAYAMA, Lattice Physics Analysis of Burnups and Isotope Inventories of U, Pu, and Nd of Irradiated BWR 9×9-9 UO₂ Fuel Assemblies, *Journal of Nuclear Science and Technology*. 45 (2008) 547–566. <https://doi.org/10.1080/18811248.2008.9711879>.
- [128] T. Yamamoto, Compilation of Measurement and Analysis Results of Isotopic Inventories of Spent BWR Fuels, report contributed to the OECD/NEA and included as part of the SFCOMPO spent fuel database., OCED/NEA, 2012.
- [129] M. Suzuki, T. Yamamoto, H. Fukaya, K. Suyama, G. Uchiyama, Lattice physics analysis of measured isotopic compositions of irradiated BWR 9 × 9 UO₂ fuel, *Journal of Nuclear Science and Technology*. 50 (2013) 1161–1176. <https://doi.org/10.1080/00223131.2013.837845>.
- [130] T. YAMAMOTO, M. YAMAMOTO, Nuclear Analysis of PIE Data of Irradiated BWR 8×8-2 and 8×8-4 UO₂ Fuel Assemblies, *Journal of Nuclear Science and Technology*. 45 (2008) 1193–1214.
<https://doi.org/10.1080/18811248.2008.9711908>.
- [131] A. Ariemma, L. Bramati, M. Galliani, M. Paoletti Gualandi, B. Zaffiro, A. Cricchio, L. Koch, Experimental and theoretical determination of burnup and heavy isotope content in a fuel assembly irradiated in the garigliano boiling water reactor, Commission of the European Communities, 1971.
http://inis.iaea.org/Search/search.aspx?orig_q=RN:3020670 (accessed July 4, 2021).
- [132] P. Barbero, G. Bidoglio, M. Bresesti, A. Caldiroli, F. Daniele, R. De meester, R. Dierckx, R. Ernstberger, S. Facchetti, A. Frigo, S. Guardini, E. Ghezzi, G. Guzzi, Hasib ullah, L. Lezzoli, L. Koch, W. Konrad, L. Mammarella, F. Mannone, A. Marell, A. Schurenkämper, P.r. Trincherai, H. Tsuruta, P. Barbero et al., Post-irradiation analysis of the Gundremmingen BWR spent fuel, Commission of the European Communities, 1979.
- [133] H. NATSUME, H. OKASHITA, H. UMEZAWA, S. OKAZAKI, T. SUZUKI, M. OHNUKI, T. SONOBE, Y. NAKAHARA, S. ICHIKAWA, S. USUDA, S. MATSUURA, H. TSURUTA, T. SUZAKI, T. KOMORI, S. TAMURA, K. GUNJI, K. TAMURA, Gamma-Ray Spectrometry and Chemical Analysis Data of JPDR-I Spent Fuel, *Journal of Nuclear Science and Technology*. 14 (1977) 745–761.
<https://doi.org/10.1080/18811248.1977.9730833>.
- [134] T. Shimooke, Prediction of Three-Dimensional Core Performance of JPDR (A BWR) for Burnup Cases, *Nuclear Technology*. 10 (1971) 257–272. <https://doi.org/10.13182/NT71-A30958>.
- [135] S. MATSUURA, H. TSURUTA, T. SUZAKI, H. OKASHITA, H. UMEZAWA, H. NATSUME, Non-Destructive Gamma-Ray Spectrometry on Spent Fuels of a Boiling Water Reactor, *Journal of Nuclear Science and Technology*. 12 (1975) 24–34. <https://doi.org/10.1080/18811248.1975.9733065>.
- [136] T. SUZAKI, S. OKAZAKI, H. OKASHITA, I. KOBAYASHI, T. SUZUKI, N. KOHNO, M. OHNUKI, N. SHINOHARA, T. SONOBE, A. OHNO, K. MURAKAMI, H. UMEZAWA, H. TSURUTA, S. MATSUURA, Y. ASAKURA,

S. ARAYA, T. YAMANOUCHI, Non-Destructive and Destructive Measurements on Burnup Characteristics of Japan Power Demonstration Reactor-I Full-Core Fuel Assemblies, *Journal of Nuclear Science and Technology*. 23 (1986) 53–72. <https://doi.org/10.1080/18811248.1986.9734949>.

Appendix I. Modelling the Rebuilt SFAs of Clab Benchmarks

The information about the “rebuild” SFA of the Clab benchmarks used to derive the Polaris models are the following:

1. The lattice/bundle design (or rod layouts)
2. Specifications of the number of the fuel rods, initially, and after each rebuild
3. Specifications of the replacing rods
4. The heavy mass after the rebuild

In total, 18 SFA have their rods rebuild: 14 from BWRs and 4 from PWRs. The rebuild SFAs are specified in Table 25, based on information in reference [12]. The table lists the number of rods at each lattice rebuild state (N_{rods}), and the burnup fraction after each state.

Table 25. Specifications of rebuild SFAs from the benchmarks of Clab, based on [12].

Serial	Reactor	SFA ID	No. of Rods				
			Initial N_{rods}	N_{rods} after rebuild-1	BU% after rebuild-1*	N_{rods} after rebuild-2	BU% after rebuild-2*
1	Ringhals 1	582	64	63	58%	60 58	100% 100%
2	Ringhals 1	596	64	63	56%		
3	Ringhals 1	710	64	63	55%		
4	Ringhals 1	900	64	63	58%		
5	Ringhals 1	1136	64	63	70%		
6	Ringhals 1	5829	63	62	30%		
7	Ringhals 1	6478	63	44	100%		
8	Barseback 1	2014	64	63	67%		
9	Barseback 1	2018	64	63	62%		
10	Barseback 1	2048	64	63	52%		
11	Barseback 1	2074	64	63	50%		
12	Oskarshamn 2	3054	63	56	55%		
13	Oskarshamn 2	3058	63	56	62%		
14	Oskarshamn 2	3064	63	56	72%		
15	Ringhals 2	C42	204	203	46%		
16	Ringhals 2	I24	204	202	100%		
17	Ringhals 3	3C4	264	263	100%	258	100%
18	Ringhals 3	5F2	264	261	100%		

* BU% is the burnup fraction at the rebuild. A 100% means that the rebuild occurs after the EOL.

All fuel rods were replaced with non-active rods (non-fuel rods), based on specifications of the replacing rods or specifications of the number of active rods after each rebuild state. Also, these specifications are in accordance with the lattice layout and the heavy mass of the SFA after each rebuild. The unknown information for the BWR is the materials of the replacing rod, whether it is a solid Zircaloy rod (Zr-rod) or a hollow Zr-rod.

Most of the BWRs had their rods replaced during irradiation, except for SFA 6478 of Oskarshamn, which had its rebuilt after the EOL. The case of the PWRs is different, the number of the active rods is not given after the rebuild, rather the no. of the removed rods. The relevant information for the PWRs are:

1. SFA C42: one rod is replaced with a homogenous Zr-rod during irradiation,
2. SFA I24: two rods have no replacing rods (the rods are rebuilt after EOL),
3. SFA 3C4: one rod has no replacing rod (the rods are rebuilt after EOL),
4. SFA 5F2: six rods have no replacing rods (the rods are rebuilt after EOL).

Modelling the rebuild SFAs includes two types of assumptions, related to performing the calculations and related to obtaining the decay heat from the calculations.

For the modelling related assumptions, the calculations are done in single runs, instead of terminating the calculations at a given cycle and reloading the model with the depleted material from the previous run along with the replaced rod. Two calculations on the SFA 5829 of Ringhals-1 were performed to analyze the significance of these assumptions. The SFA 5829 had 1 rod replaced earlier during irradiation compared to all of the remaining SFAs. Rod D4 was replaced at 30% of the EOL burnup. Two calculations were performed for the decay heat from all rods (excluding rod D4):

1. Rod D4 as a fuel rod
2. Rod D4 as a solid Zr-rod

The rods were the same throughout the irradiation. Between these two calculations, the obtained difference of the calculated decay heat of the non-rebuild rods is 0.2% of the calculated value. The actual difference between the two ways of modelling should be less, being exposed to a lower burnup fraction. It is assumed that this difference is an insignificant difference at the considered cooling times. Therefore, all the calculations are performed as single runs (without interruptions and re-restart) which proceeded with the initial fuel lattice.

For the decay heat calculations related assumptions, the decay heat (DH) from the rebuild SFAs was calculated as:

$$DH = \frac{DH_{all\ rod\ w/o\ rebuild}}{IHM_{all\ rods\ w/o\ rebuilt}} \times IHM_{SFA} \quad Eq\ (I.1)$$

Where IHM is the initial heavy metal mass. The code results are decay heat per ton of initial heavy metal mass. To calculate the decay heat originating from a particular set of rods, the decay heat from these rods is divided by their initial heavy mass (rather than the initial heavy mass of the SFA). The ratio is multiplied to the heavy mass after the rebuild. As an example, SFA 582 of Ringhals 1: the calculations use the initial lattice map assuming that the resulting decay heat from rods will not be significantly different if a particular rod was removed during irradiation from the lattice. Then, the decay heat per heavy metal mass from all rods is summed up except for rod D4, which was removed between the third and the fourth cycles. The resulting ratio is multiplied by the HM after the rebuild, which is 177.4 kgU.

Appendix II. Specifications of the PIE Benchmarks and Modelling Assumptions

Specifications of the modeled PIE benchmarks from the SFCOMPO database are presented in this appendix. The benchmarks are categorized by their reactor type, starting with the PWRs (section II.1.1 to II.1.11) followed by the BWRs (section II.2.1 to II.2.7). The reactors are listed in alphabetical order.

II.1 PWR cases

II.1.1 Calvert Cliffs-1 (CC-1)

Three assemblies had some of their fuel samples analyzed after their discharge, irradiated in SFAs: D101, D047, and BT03. The analyses consisted of isotopic measurements performed by the Material Characterization Center (MCC) of the Pacific Northwest Laboratory (PNL), as part of the Approved Testing Material (ATM) program. The mentioned CC-1 assemblies were part of the ATM: ATM-103, ATM-104, and ATM-106 [93–95], respectively.

The three assemblies are based on the Combustion Engineering 14X14 design, having 176 fuel rods for D101 and D047 and similar U-235 enrichment through the lattice. SFA BT03 has a similar design, except that it has 4 corner stainless-steel rods and 172 fuel rods, and also has different U-235 enrichments throughout the lattice. A specific characteristic of this fuel design is 5 large guide tubes that could be used to accommodate a control rod cluster. The lattice layouts of the three CC-1 assemblies are shown in Figure 8. The lattice design and rods enrichments are based on the values provided in the SFCOMPO [11], along with the original ATM reports [93–95]. The assemblies have quarter symmetries, and the figure shows only the south-east (S-E) quarter of the assembly. The rods in black are the rods from which the PIE samples are analyzed. Considering the quarter symmetry of the assemblies, the figure shows either the actual position of the fuel rods or their symmetrically-equivalent (*i.e.*, the mirrored) position in the S-E quarter.

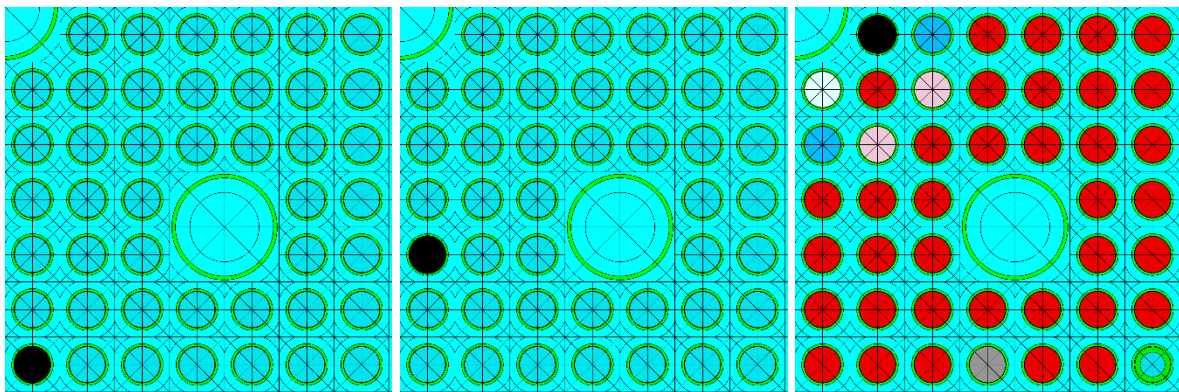


Figure 69: Polaris south-east (S-E) models of the Calvert Cliffs-1 assemblies: D101, D047, and BT03 (left to right). Rods having different enrichments are shown in different colors. The analyzed rods are shown in black color.

The CC-1 data have several samples, however, not all of them contain measurements of the analyzed isotopes in the present study. Only three samples per assembly had measurements of their Cs-137, U-235 and Pu-239 concentrations (9 PIE samples in total). Samples from a single rod are analyzed in each assembly, which are located at different axial locations. Characteristics of the considered samples are listed in Table 26.

Measurements were conducted at the PNL, using gamma-spectrometry for Cs-137 and isotope dilution inductively coupled plasma/mass spectrometry (ID-ICPMS) for both U-235 and Pu-239. The reported measurements are based on the SFCOMPO values [11], at the cooling times of 6.5, 5.1 and 6.7 years for SFA D101, D047 and BT03, respectively.

Table 26. Characteristics of the PIE samples of the Calvert Cliffs-1 reactor.

SFA	ID	U-235 wt%	Axial loc. (cm) *	BU (given) GWd/tHMi **	Mod. temp. (K)	Mod. dens. (g/cm ³)	Fuel temp. (K)
D101	JJ	2.720	11.72	18.68	557.2	0.7576	818
D101	BB	2.720	27.13	26.62	557.6	0.7570	887
D101	P	2.720	164.61	33.17	569.8	0.7305	917
D047	CC	3.038	27.39	37.12	557.6	0.7569	848
D047	LL	3.038	12.68	27.35	557.2	0.7575	794
D047	P	3.038	164.08	44.34	569.9	0.7307	878
BT03	GG	2.453	22.69	37.27	557.4	0.7572	909
BT03	MM	2.453	14.05	31.40	557.3	0.7575	823
BT03	Q	2.453	163.99	46.46	569.9	0.7308	954

* to bottom end of the active fuel rod

** Burnup (BU)

The Irradiation histories are based on the provided data in SFCOMPO [11], along with supplementary data from [64], [96] and [97]. The SFAs have been irradiated through cycles 2 to 4, 2 to 5, and 1 to 4 for D101, D047 and BT03, respectively.

Table 26 provides the burnup weighted (using cycle-wise burnup) relevant irradiation parameters, based on the evaluations provided in [64]. Missing information of the irradiation histories are not provided in the original reports, such as the boron let-down curve for the cycle 1 affecting SFA BT03. The boron let-down curve was calculated assuming the average boron in cycle 1 to be similar to its value in cycle 2 (similar to the assumptions in [64]). The samples' given burnup values are based on measurements of the Nd-148, and no burnup correction is implemented in the CC-1 samples.

II.1.2 Genkai-1 (GK-1)

A single assembly from the GK-1 reactor had two fuel samples analyzed after discharge, namely: sample 87H01 and sample 87H05 (abbreviated herein after as H1 and H5). The assembly is a 14x14 PWR design, having 179 fuel rods, 16 guide tubes to accommodate cluster control rods, and a near-central instrument tube. The fuel type is UO₂, having uniform U-235 enrichment throughout the lattice (3.4 wt%). The lattice layout of the GK-1 assembly is shown in Figure 70. The lattice design and enrichment are based on the values provided in the SFCOMPO [11]. The assembly is not symmetrical due to the position of the central instrument tube, which necessitated modelling the assembly as a whole.

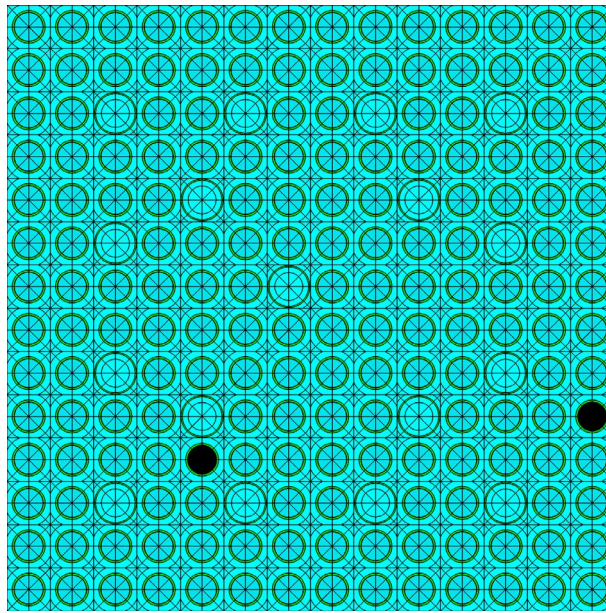


Figure 70: Polaris model of the Genkai-1 assembly JPNNG1SFA1 showing the location of the rods containing the analyzed PIE samples: rod JPNNG1PWR-1 and JPNNG1PWR-2 (in black color). The rods contain samples H01 and H05, respectively.

Characteristics of the considered PIE samples are listed in Table 27. Measurements were conducted at Japan Atomic Energy Research Institute (JAERI) [98] (in Japanese). The method of measurements could not be identified from the original reports [98]. Additionally, only sample H1 had all the three isotopes measured, whereas the reported measurements are for U-235 and Pu-239 in the H05 sample. The reported measurements are based on the SFCOMPO values [11]. The cooling times for the PIE samples are not given, however, the SFCOMPO-reported values indicate adjustments of the decay to the discharge time.

Table 27. Characteristics of the PIE samples of the Genkai-1 reactor.

SFA	ID	U-235 wt%	Axial loc. (cm)	BU (est.) GWd/tHMi	Mod. temp. (K)	Mod. dens. (g/cm ³)	Fuel temp. (K)
SFA1	H01	3.415	132	37.5	571.2	0.7303	922
SFA1	H05	3.415	92	36.9	566.2	0.7402	922

The Irradiation histories are based on the provided data in SFCOMPO [11], along with supplementary data from [99]. The GK-1 SFA has been irradiated for 5 cycles. Table 27 provides

the burnup weighted relevant irradiation parameters. The samples' given burnup values are based on the SFCOMPO listed values, which were scaled in the current calculations such that the calculated values of Nd-148 matches the measurements ($\pm 0.05\%$). The required correction factors are -3.1% and -4.7% for H01 and H05, respectively.

Missing design and irradiation data from the SFCOMPO and the reference reports necessitated implementing several assumptions, which are:

1. The reactor pressure was set equal to that of Mihama-3 reactor, considering similarity in the water inlet and outlet temperatures. Nevertheless, differences in the reactor pressure does not significantly affect the calculated water density (in the non-boiling conditions).
2. The moderator temperatures, which are provided in [99], were used along with the reactor pressure to obtain the moderator densities.
3. The samples' axial positions were inferred from the moderator temperatures, assuming that the water temperature is a cosine function in the axial position of the sample. The mentioned assumption is furtherly discussed in Chapter 4 (Validation and Uncertainty Propagation Schemes). Equation 4.1 is solved for z (the sample axial position).

A particular limitation of the samples of GK-1 is that uncertainties of the reported measurements are not available. The provided values in the original reports and therefore the SFCOMPO reported values do not include this information.

II.1.3 Mihama-3 (M-3)

Three assemblies had some of their fuel samples analyzed after discharged, irradiated in SFAs: JPNNM3SFA1, JPNNM3SFA2 and JPNNM3SFA3. The assemblies are abbreviated hereinafter as: SA1, SA2 and SA3. Eight PIE samples are analyzed, taken from five different rods. The assemblies are based on the Westinghouse 15×15 assembly design, having 204 fuel rods, 20 guide tubes and a central instrument tube. The assemblies are loaded with UO₂ fuel rods, having an enrichment of 3.21 wt% U-235. The south-east (S-E) lattice layout of the three M-3 assemblies is shown in Figure 71. The assemblies are similar to each other in their design, and only one plot is shown for the three assemblies indicating the analyzed rods in black color or their mirrored position in the S-E quarter. The assemblies have quarter symmetry, and there S-E models are implemented in Polaris. The lattice design and rods enrichments are based on the values provided in the SFCOMPO [11], and the references [100,101].

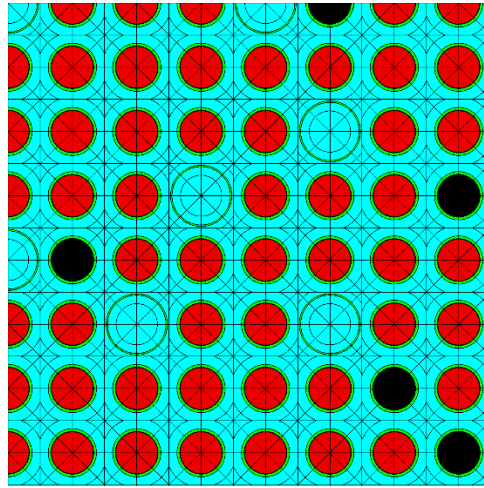


Figure 71: Polaris S-E models of the Mihama-3 assemblies SFA1, SFA2 and SFA3. The assemblies are similar to each other in their pin-layout and slightly differ in their enrichments. The S-E map show the actual position of the analyzed rods or their reflection in the S-E quarter. The analyzed rods are shown in black color.

Characteristics of the analyzed samples are listed in Table 28. The Irradiation histories are based on the provided data in SFCOMPO [11], along with supplementary data from [99,101,102]. The assemblies (SA1, SA2 and SA3) have been irradiated for 1, 3, and 4 cycles, respectively. The assemblies have not been controlled during their irradiation. Table 28 provides the burnup weighted relevant irradiation parameters. The fuel temperatures are implemented as the values provided in [102], and the moderator temperatures are implemented as the values provided in [99]. The samples' given burnup values are based on the SFCOMPO listed values, which were scaled in the current calculations by -4% to -6% such that the calculated values of Nd-148 matches the measurements ($\pm 0.05\%$).

Table 28. Characteristics of the PIE samples of the Mihama-3 reactor.

SFA	ID	U-235 wt%	Axial loc. (cm)	BU (est.) GWd/tHMi	Mod. temp. (K)	Mod. dens. (g/cm ³)	Fuel temp. (K)
SFA1	B02	3.21	37	36.40	561.2	0.7498	923
SFA1	B03	3.21	337	30.60	594.6	0.6763	863
SFA3	C03	3.21	34	23.68	561.1	0.7500	863
SFA3	C04	3.21	125	25.86	569.5	0.7339	891
SFA3	C07	3.21	51	27.01	562.0	0.7484	905
SFA3	C08	3.21	259	27.48	588.3	0.6925	913
SFA2	G03	3.21	256	30.47	587.9	0.6935	823
SFA2	G05	3.21	161	21.83	574.5	0.7237	933
SFA2	G07	3.21	254	20.98	587.7	0.6940	863

Missing design and irradiation data from the SFCOMPO and the reference reports necessitated implementing several assumptions, which are:

1. The samples' axial positions are not publicly available [99]. The samples' axial positions were inferred from the moderator temperatures, assuming that the water temperature is a cosine function in the axial position of the sample. The mentioned assumption is furtherly discussed in Chapter 4, and equation 4.1 is solved for z (the sample axial position).
2. The moderator temperatures are reported to have different values in the references [99,101,102]. Values from the most recent report [99] are implemented, which also assumes a cosine shape of the water temperature vs. the axial height.

II.1.4 Neckarwestheim-2 (N-2)

One PIE sample is listed in SFCOMPO to be irradiated in the N-2 reactor (sample M11). The sample has been irradiated and analyzed as part of the REBUS International Program (Reactivity Tests for a Direct Evaluation of the Burnup Credit on Selectected Irradiated LWR Fuel Bundles). The sample had been irradiated in an 18x18 fuel assembly at a near-central position, and in the upper third part of the fuel rod, which is expected to be exposed to a relatively uniform flux (an asymptotic part of the assembly). The sample has U-235 enrichment of 3.8 wt%, and the assembly has two types of fuel rods: 276 UO₂-based rods with U-235 enrichment of 3.8 wt%, and 12 UO₂-Gd₂O₃-based rods with U-235 enrichment of 2.6 wt% and gadolinia loading of 7 wt%. The assembly contains 24 guide tubes. The lattice layout of the N-2 assembly is shown in Figure 72. The assembly is asymmetric due to the positioning of the gadolinia-bearing rods, which necessitated modelling the assembly as a whole. The lattice design and rods' enrichments are based on the values provided in the SFCOMPO [11], and reference [103]. The reported values of the measurements are based on references [104,105], which are part of the REBUS program. The measurements were conducted by the SCK.CEN using thermal ionization mass spectrometry (TIMS) for U-235 and Pu-239, and gamma-spectrometry for Cs-137, and the reported values are after 7.1-7.3 years of cooling.

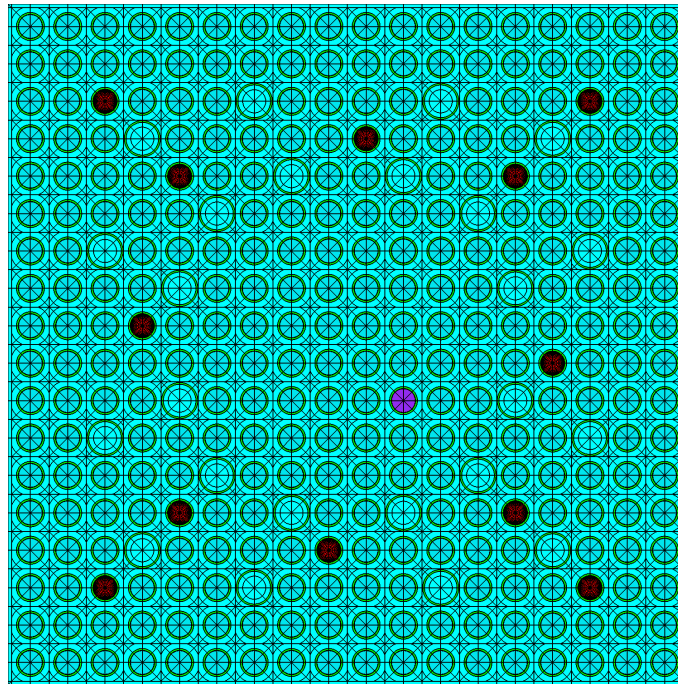


Figure 72: Polaris model of the Neckarwestheim-2 assembly 419. The analyzed rods are shown in purple color.

Table 29. Characteristics of the PIE sample of the Neckarwestheim-2 reactor.

ID	U-235 wt%	Axial loc. (cm)	BU (est.) GWd/tHMi	Mod. temp. (K)	Mod. dens. (g/cm ³)	Fuel temp. (K)	Boron (ppm)
M11	3.80	283	53.3	588.1	0.6922	895	523

Characteristics of the M11 sample are listed in Table 29. The M11 sample is one of the most well described PIE samples in SFCOMPO and the original reference [103]. Information about specific power density, fuel temperature, moderator temperature and density and the boron letdown curve are provided for the sample at high resolution of the in-core residence time. Such detailed information facilitated modelling the sample with minimal assumptions on its irradiation data. Also, the M11 sample has relatively high burnup of 53 GWd/tHMi (as implemented in Polaris), which is 0.987 of the given burnup value in SFCOMPO.

II.1.5 Obrigheim-1 (OG-1)

Several samples and assemblies have been analyzed from the OG-1 reactor for their isotopic concentrations. In this study, 14 PIE samples from assembly BE124 and 6 samples from assembly BE210 are analyzed. SFCOMPO originally contains information about 16 PIE samples from the BE124 assembly. However, two samples are excluded, namely E3_P2 and D1_P2 samples. The former sample shows large discrepancy in its burnup based on measurements of two burnup indicators, Cs-137 and Nd-148. The discrepancy is 16% which is noted also in reference [64]. The sample is excluded considering potential erroneous measurements, and potential inaccuracy in adjustment of the burnup. Sample D1_P2 does not have the concentration of Nd-148 measured, and only Cs-137 measurements are reported. The sample also does not have the concentration of U-235 and Pu-239 measured, and it was excluded from the analyses. Assembly BE210 includes 7 PIE samples. In this study, the analyses include only 6 PIE samples out of the listed 7 samples in SFCOMPO. The excluded sample is K14_P1, which also has discrepancies in its burnup based on measurements of two burnup indicators, Cs-137 and Nd-148. The noted discrepancy is 11% [64]. Potential erroneous measurements could have resulted in the observed discrepancy, leading to erroneous burnup adjustments.

RCA of 5 fuel assemblies, which were fully dissolved during their reprocessing in Karlsruhe reprocessing Plant [64,106], were performed by laboratories of the European Institute for Transuranium Elements (ITU), Institute for Radiochemistry at Karlsruhe (IRCh), Karlsruhe Reprocessing Plant (WAK), and International Atomic Energy Agency (IAEA). These PIE measurements are unique, since they correspond to the average concentrations of the isotopes in each assembly. The assemblies are: BE168, BE170, BE171, BE172 and BE176. Two individual measurements are reported for each assembly, corresponding to two halves of the assembly (axially). The current analyses compare the average of the two measurements to the average of two calculations on each section of the assembly.

The S-E lattice layouts of the OG-1 assemblies are shown in Figure 73. The assemblies are similar to each other in their design, based on a 14x14 PWR design, having 180 UO₂-based fuel rods and 16 guide tubes. The analyzed rods are indicated in black color (or their mirrored position in the S-E quarter). The assemblies have quarter symmetry, and their S-E models are implemented in Polaris. The lattice design and rods enrichments are based on the values provided in the SFCOMPO [11] and reference [64].

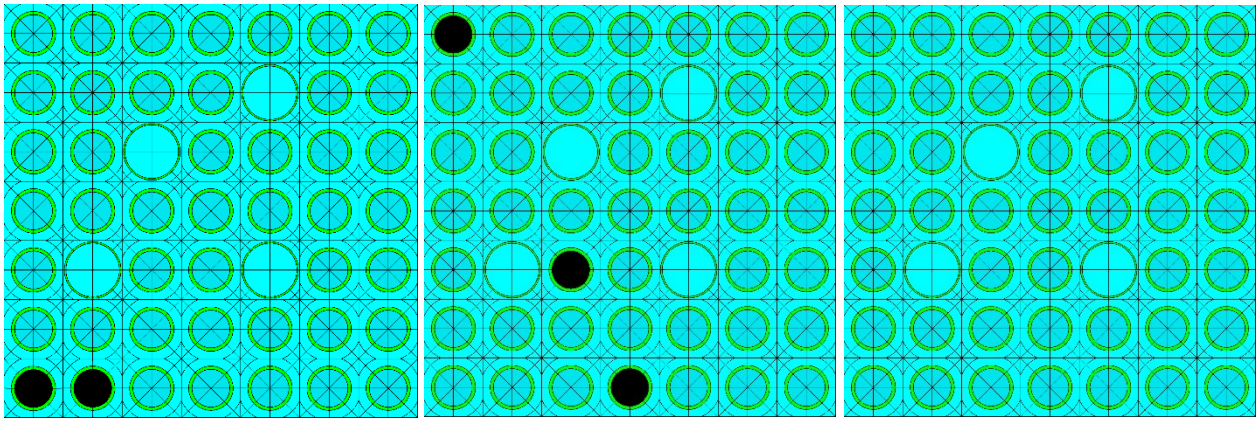


Figure 73: Polaris S-E models of the Obrigheim-1 assemblies: BE210 (left), BE124 (middle), and BE168, BE170, BE171, BE 172, and BE176 (right). The latter assemblies had all of their rods dissolved and analyzed. The analyzed rods in BE210 and BE124 are shown in black color.

Table 30. Characteristics of the PIE samples of the Obrigheim-1 reactor.

SFA	ID	U-235 wt%	Axial loc. (cm)	BU (est.) GWd/tHMi	Mod. temp. (K)	Mod. dens. (g/cm3)	Fuel temp. (K)
168	SFA	3.13	- *	29.1	571	0.730	875
170	SFA	3.13	-	26.7	571	0.730	860
171	SFA	3.13	-	28.4	571	0.730	866
172	SFA	3.13	-	28.1	571	0.730	865
176	SFA	3.13	-	28.6	571	0.730	865
124	D1_P3	3.00	144	33.4	572	0.728	998
124	E3_P1	3.00	15	20.1	556	0.759	802
124	E3_P3	3.00	144	35.9	572	0.728	1039
124	E3_P4	3.00	232	30.6	584	0.702	953
124	E3_P5	3.00	259	22.7	585	0.699	838
124	G7_P1	3.00	15	17.0	556	0.759	763
124	G7_P2	3.00	32	25.6	557	0.757	879
124	G7_P3	3.00	144	31.3	572	0.728	960
124	G7_P4	3.00	232	27.6	584	0.702	906
124	M14_P3	3.00	144	29.2	572	0.728	930
124	D1_P1	3.00	15	21.1	556	0.759	815
124	G7_P5	3.00	259	25.7	585	0.699	879
124	M14_P1	3.00	15	15.5	556	0.759	744
124	M14_P4	3.00	232	24.8	584	0.702	866
210	K14-P3	2.83	133	36.4	570	0.730	988
210	K14-P4	2.83	221	32.7	583	0.704	963
210	G14-P3	2.83	133	37.4	584	0.702	891
210	G14-P4	2.83	221	35.5	585	0.699	819
210	G14-P5-1	2.83	243	29.9	570	0.730	976
210	G14-P5-2	2.83	255	24.1	583	0.704	927

* Full length SFAs

Characteristics of the analyzed samples are listed in Table 30. The measurements had been at Ispra and Karlsruhe laboratories, of the European Commission Joint Research Center [107]. The

measurements of U-235 and Pu-239 relied on the isotope dilution mass spectrometry (IDMS) [106,107]. The measurements of Cs-137 relied on gamma-spectrometry, which are based on the values provided in [64]. Measurements of Cs-137 are not reported for all of the analyzed samples, 10 PIE samples from SFA BE_124 and 5 PIE samples from SFA_210 are reported. The reported measurements are at the time of discharge, *i.e.*, they are adjusted for the decay.

The Irradiation histories are based on the provided data in SFCOMPO [11], along with the data provided in [64]. Table 30 provides the burnup weighted relevant irradiation parameters. The moderator density and temperature and the fuel temperatures are similar to the values implemented in [64]. The samples' burnup values are based on the SFCOMPO listed values, based on Nd-148 measurements. Matching the measured Nd-148 concentrations with the Polaris calculated ones necessitated additional correction factors in the current calculations by -1.0 to 0.7% of the SFCOMPO given burnup values.

II.1.6 Ohi-1 and Ohi-2 (O1 and O2)

Two assemblies, one from O1 and the other from O2, had some of their fuel samples analyzed after discharged. The samples are irradiated in SFAs: G13 (reactor O1) and 17G (reactor O2). One PIE sample is analyzed from the O1 assembly, and 5 samples are analyzed from the O2 assembly. The assemblies are based on the Westinghouse 17×17 assembly design, having 264 fuel rods, 24 guide tubes and a central instrument tube. O1 has a uniform U-235 enrichment of 3.2 wt%, loaded with UO₂-based fuel (the PIE sample is also UO₂-based). O2 is loaded with two types of UO₂-based fuel: UO₂ with U-235 enrichment of 3.2 wt%, and UO₂-Gd₂O₃ with U-235 enrichment of 1.69 wt% and 6 wt% gadolinia loading. Layouts of the S-E quarters of the assemblies are shown in Figure 74. The assemblies have quarter symmetry, and there S-E models are implemented in Polaris. The lattice design and rods enrichments are based on the values provided in the SFCOMPO [11], and the references [108,109].

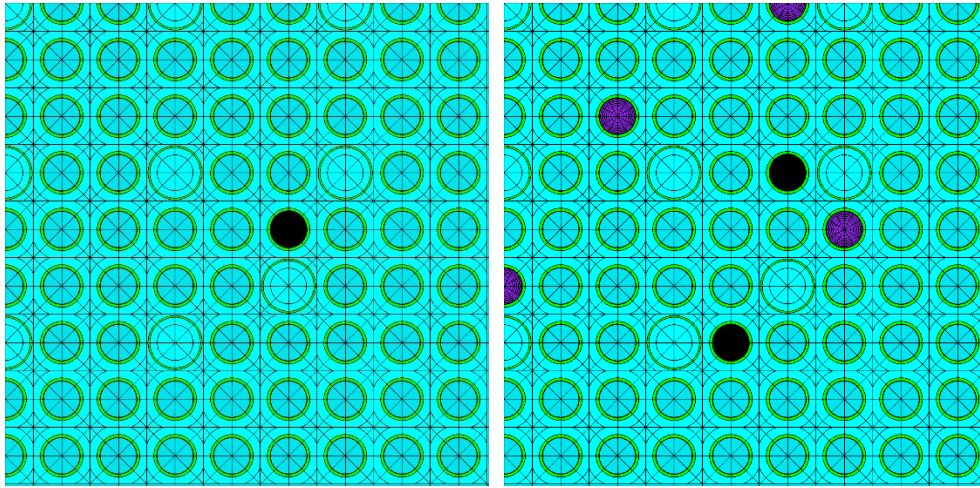


Figure 74: Polaris S-E models of the Ohi-1 and Ohi-2 assemblies (left to right). The Ohi-2 assembly shows the actual position of the analyzed rods or their reflection into the S-E quarter. The analyzed rods are shown in black color, and the gadolinia-bearing rods are shown in purple color.

Characteristics of the analyzed samples are listed in Table 31. The measurements are conducted at the JAERI [108,109]. The measurements of U-235 and Pu-239 relied on the IDMS and the measurements of Cs-137 relied on gamma-spectrometry. The measurements of U-235 and Pu-239 are reported at the discharge date (*i.e.*, adjusted for decay), and those of Cs-137 are reported at 5 years after discharge.

The Irradiation histories are based on the provided data in SFCOMPO [11], along with the data provided in [108]. O1 has been irradiated for four cycles, and the sample reached relatively high burnup (52 WGd/tU), whereas the O2 assembly is irradiated for only two cycles, reaching relatively low burnup values. The assemblies have not been in the vicinity of inserted control rods during their irradiation. Table 31 provides the burnup weighted relevant irradiation parameters. The fuel temperatures are assumed values, which are based on [108] (*i.e.*, 969 K). The boron letdown curve is also provided in SFCOMPO. Equation 4.1 is used to obtain the moderator temperatures as a function of the axial positions from the bottom of the active fuel. The latter

assumption relies also on the SFCOMPO provided reactor inlet and outlet temperatures and the gauge pressure. The samples' burnup values are based on the SFCOMPO listed values, scaled in the current calculations by -1.9% to 2.5% such that the calculated values of the Nd-148 concentrations match the measured ones (within $\pm 0.05\%$).

Table 31. Characteristics of the PIE samples of the Ohi-1 and Ohi-2 reactors.

SFA	ID	U-235 wt%	Axial loc. (cm)	BU (est.) GWd/tHMi	Mod. temp. (K)	Mod. dens. (g/cm ³)	Boron (ppm)
O1 - G13	S07	3.20	113	51.8	568.7	0.7356	667
O2 - 17G	S01	1.69	27	22.0	559.3	0.7534	552
O2 - 17G	S03	1.69	74	29.3	563.9	0.7449	552
O2 - 17G	S05	1.69	73	25.7	563.9	0.7449	556
O2 - 17G	S08	3.20	27	29.6	559.3	0.7534	588
O2 - 17G	S10	3.20	74	37.8	563.9	0.7447	588

II.1.7 Takahama-3 (T3)

The two assemblies of the T3 reactor in the SFCOMPO data are analyzed. The assemblies are: NT3G23 and NT3G24 (abbreviated hereinafter as G23 and G24). For G23, two fuel rods had some of their fuel samples analyzed after their irradiation. Two rods are analyzed in G23, which are SF95 and SF96. The former is UO_2 -based, with U-235 enrichment of 4.1 wt%, and the latter is $\text{UO}_2\text{-Gd}_2\text{O}_3$ -based with U-235 enrichment of 2.6 wt% and gadolinia loading of 6 wt%. A single rod is analyzed in G24, which is rod SF97. The PIE samples are taken from different axial positions in each rod, as shown in Figure 75.

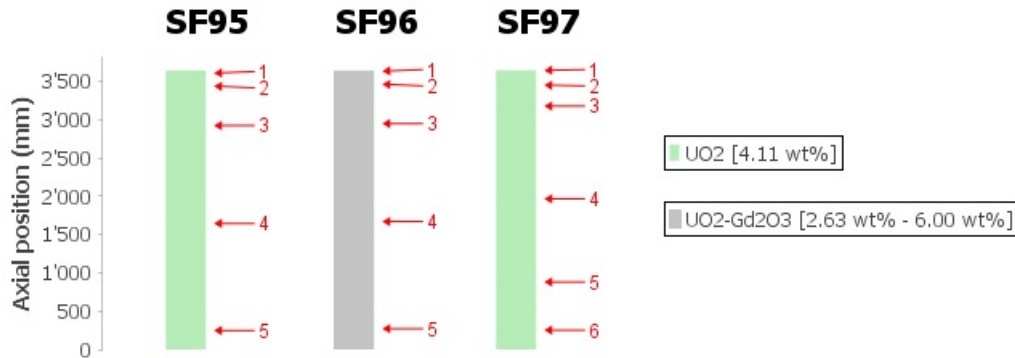


Figure 75: Axial locations of the analyzed PIE samples of T3 reactor.

The assemblies are based on the PWR 17×17 assembly design, having 264 fuel rods and 25 guide tubes. 14 of the fuel rods are $\text{UO}_2\text{-Gd}_2\text{O}_3$ -based. The S-E lattice layouts of the 3 assemblies are shown in Figure 76. The assemblies are similar to each other in their design, and the three analyzed rods are shown in the same plot in black color (or their mirrored position in the S-E quarter). The assemblies have quarter symmetry, and S-E models are implemented in Polaris. The lattice design and rods enrichments are based on the values provided in the SFCOMPO [11], and the references [110,111].

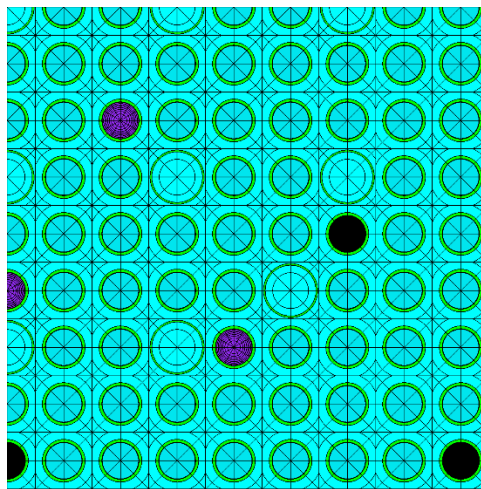


Figure 76: Polaris S-E model of the Takahama-3 assemblies G23 and G24. The S-E map shows the actual positions of the analyzed rods (or their reflection in the S-E quarter). The analyzed rods are shown in black color, and the gadolinia-bearing rods are shown in purple color.

Characteristics of the analyzed samples are listed in Table 32. The measurements are conducted at the JAERI [110,111]. The measurements of U-235 and Pu-239 relied on the IDMS and the measurements of Cs-137 relied on gamma-spectrometry. The reported values for the measurements are at the discharge date, *i.e.*, corrected for the decay at the time of measurements.

Table 32. Characteristics of the PIE samples of the Takahama-3 reactor.

SFA	ID	U-235 wt%	Axial loc. (cm)	BU (est.) GWd/tHMi	Mod. temp. (K)	Mod. dens. (g/cm ³)	Boron (ppm)
SF95	1	4.11	361	14.1	593.0	0.6819	677
SF95	2	4.11	345	24.3	592.8	0.6826	677
SF95	3	4.11	293	35.3	589.4	0.6912	677
SF95	4	4.11	165	36.6	570.4	0.7330	677
SF95	5	4.11	25	30.2	554.2	0.7632	677
SF96	1	2.63	363	8.6	593.1	0.6819	633
SF96	2	2.63	347	17.3	592.8	0.6825	633
SF96	3	2.63	295	29.4	589.6	0.6906	633
SF96	4	2.63	167	30.0	570.8	0.7330	633
SF96	5	2.63	27	25.2	554.3	0.7600	633
SF97	1	4.11	364	17.3	593.1	0.6819	655
SF97	2	4.11	346	30.3	592.8	0.6826	655
SF97	3	4.11	318	41.7	591.5	0.6859	655
SF97	4	4.11	197	46.5	575.8	0.7219	655
SF97	5	4.11	88	46.7	559.1	0.7544	655
SF97	6	4.11	25	40.2	554.2	0.7632	655

The irradiation histories are based on the provided data in SFCOMPO [11], along with supplementary data from the references [110,111]. G23 has been irradiated for 2 cycles, reaching relatively low burnup values, and G24 has been irradiated for three cycles reaching higher burnup values up to 47 GWd/tHMi for sample 5 of SF97. Since the samples are distributed axially in their host fuel rods, samples with very low burnup values are analyzed, such as samples with identifier 1 (which are located at the top of the fuel rods). The assemblies have not been controlled during their irradiation. Table 32 provides the burnup weighted relevant irradiation parameters. The fuel temperatures are assumed, which are similar to the assumptions in [110]. The moderator temperatures are also implemented as the values provided in [110]. The latter values are based on the interpolation of the moderator temperature based on the axial height of the sample and assuming that the temperature rise in the moderator follows a cosine shape function. The samples' given burnup values are based on the SFCOMPO listed values, scaled in the current calculations such that the calculated values of Nd-148 concentrations matches the measured ones ($\pm 0.05\%$). The UO₂-based samples did not require significant corrections in their burnup values (-0.2% to -2.0%), whereas the UO₂-Gd₂O₃ -based samples required larger corrections. Finally, the boron letdown curve is also provided for the samples in SFCOMPO and in [111].

II.1.8 Three Mile Island-1 (TMI-1)

The two assemblies of the TMI-1 reactor listed in SFCOMPO are analyzed. Fuel samples are analyzed after their discharge, irradiated in SFAs: NJ05YU and NJ070G. The former SFA initially had 11 PIE samples measured by Argonne National Laboratory (ANL) [112]. However, for the purpose of independent cross-checking and resolving anomalies in Plutonium measurements, recent measurements of 5 PIE samples were conducted by Oak Ridge National Laboratory (ORNL) [113]. The considered samples within this study are the 5 PIE that are recently measured by ORNL, considering the higher precision of the ORNL-based measurements, and that the older measurements by ANL are likely to be biased and to contain anomalies [113]. The considered PIE samples of SFA NJ05YU belong to two rods: D5 and H6. The SFA NJ070G had 8 PIE samples measured by the General Electric Vallecitos Nuclear Center (GEVNC) [114]. The considered PIE samples of the latter SFA belongs to three rods: O1, O12 and O13.

The two assemblies are based on the Babcock & Wilcox Company (B&W) Mark B8 15×15 assembly design. The NJ05YU SFA has 208 UO₂ fuel rods, a central instrument tube, and 16 guide tubes that provide place for discrete absorbers. The NJ070G SFA is similar to the NJ05YU SFA, except that it has 4 of its fuel rods being gadolinia-bearing rods (4.19 wt% gadolinia). The lattice layouts of the two TMI-1 assemblies are shown in Figure 77. The assemblies were controlled during their irradiation, and Figure 77 shows the inserted absorber rods. The lattice design and rods enrichments are based on the values provided in the SFCOMPO [11], and reference [113] for the NJ05YU SFA, and references [64,115] for the NJ070G SFA. The assemblies have quarter symmetries, and the figure shows only the S-E quarter of the assembly. The rods in black are the rods from which the PIE samples are taken, and which reflect their actual position or their mirrored position in the S-E quarter.

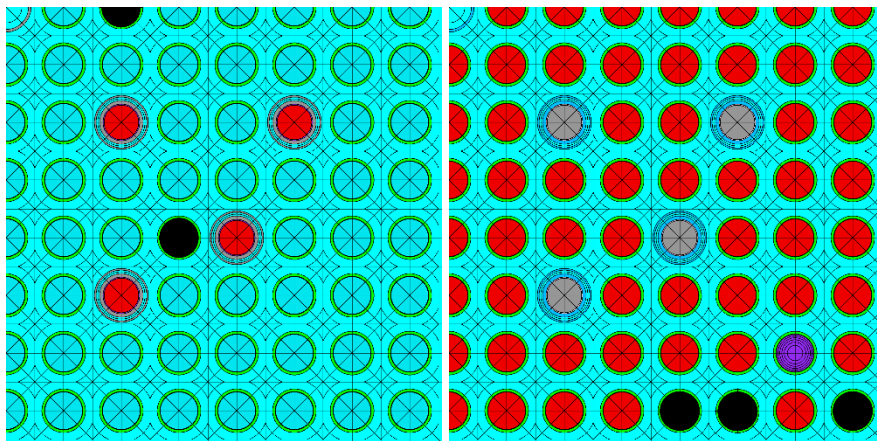


Figure 77: Polaris S-E models of the Three Mile Island-1 assemblies: NJ05YU and NJ070G (left to right). Rods having different enrichments are shown in different colors. Four discrete absorber rods are shown inserted in their guide tubes. The analyzed rods are shown in black color (2 in NJ05YU and 3 in NJ070G).

5 PIE samples are analyzed from the NJ05YU SFA, and 8 samples are analyzed from the NJ070G SFA. Characteristics of the considered samples are listed in Table 33. The measurements are conducted by ORNL for the NJ05YU samples, which relied on the ID-ICPMS for the three analyzed

isotopes. The measurements conducted at GE for the NJ070G samples relied on the TIMS for the three analyzed isotopes. The reported measurements are based on the SFCOMPO values [11], which are cross-checked with values reported in [113,115]. The cooling times of the PIE samples of the NJ05YU SFA ranged from 17.4 to 18.2 years. The cooling times of the PIE samples of the NJ070G SFA reported in Reference [115] are 3.6 years (samples: S1, S3, S4, and S6) and 4.2 years (samples: S2, S5, S7, and S8). These values are inconsistent with the reported ones in the SFCOMPO database (3.3 years for all samples). In the present work, the SFCOMPO value is used (3.3 years). The calculated concentrations at the different cooling times, the values in Reference [115] and the value in SFCOMPO, show that the U-235 and Pu-239 concentration differences are not significant ($<0.01\%$), whereas Cs-137 concentrations have $<0.6\%$ and $<2.1\%$ differences. Nevertheless, resolving the discrepancy is not performed in the present work, and the SFCOMPO value is used (3.3 years).

Table 33. Characteristics of the PIE samples of the Three Mile Island-1 reactor.

SFA	ID	U-235 wt%	Axial loc. (cm)	BU (given) GWd/tHMi	Mod. temp. (K)	Mod. dens. (g/cm ³)	Fuel temp. (K)
NJ05	A1	4.013	3421.0	45.9	591.7	0.6832	871
NJ05	B1	4.013	2670.0	55.0	585.8	0.6979	902
NJ05	B2	4.013	2820.0	52.4	587.4	0.6942	904
NJ05	C2D1	4.013	1972.0	53.5	581.1	0.7090	922
NJ05	C2D2	4.013	2332.0	52.7	584.4	0.7013	925
NJ07	S1	4.657	393.7	25.8	567.7	0.7371	940
NJ07	S2	4.657	1971.0	29.9	583.0	0.7046	992
NJ07	S3	4.657	2781.3	26.7	590.2	0.6873	993
NJ07	S4	4.657	393.7	23.7	567.2	0.7382	937
NJ07	S5	4.657	1971.0	26.5	583.0	0.7046	992
NJ07	S6	4.657	2781.3	24.0	590.2	0.6873	992
NJ07	S7	4.657	393.7	22.8	567.2	0.7382	937
NJ07	S8	4.657	1971.0	26.3	583.0	0.7046	992

The Irradiation histories are based on the provided data in SFCOMPO [11], along with supplementary data from [113,115]. The NJ05YU SFA has been irradiated for cycles 9 and 10, whereas in cycle 9, it was fully exposed to the discrete absorber rods. The NJ070G SFA was irradiated in cycle 10 only, therefore reaching significantly lower burnup values, also the absorber rods were fully inserted throughout the cycle. Table 33 provides the burnup weighted relevant irradiation parameters, based on [11,113,115]. The samples' given burnup values are based on the SFCOMPO listed values (which are obtained based on the assembly operational data). The burnup values were scaled in the current calculations such that the calculated values of Nd-148 concentrations match the measured ones ($\pm 0.05\%$). The required correction factors were within 2% of the given burnup values for both SFAs.

II.1.9 Trino Vercellese-1 (TV1)

Four assemblies are analyzed from the TV1 reactor, which had some of their fuel samples removed for RCA. The four assemblies are: 509-032, 509-049, 509-104 and 509-069, abbreviated hereinafter as: A32, A49, A104 and A69. The first three assemblies have been irradiated for one cycle only, whereas the A069 assembly has been irradiated for two cycles (including the same first cycle as for the other assemblies). The first cycle is subdivided into three sub-cycles with two downtimes: 1A, 1B and 1C, having effective full power days between 7.5 and 9.7 months.

The lattice design, dimensions, and rods enrichments are based on the values provided in the original report describing the design of the TV-1 assemblies [116]. The four assemblies are based on UO₂ fuel rods, having homogenous U-235 enrichment, and a central instrument tube. The TV-1 assemblies are modelled as a whole in Polaris, as shown in Figure 78. The design of the TV-1 assemblies is unique with respect to PWR common designs [107]. The assemblies are based on a 15x15 Westinghouse assembly design, with a central guide tube. However, 16 fuel rods are removed from the assembly, 15 from a corner and 1 from the opposite corner, as shown in Figure 78. The removed rods provide space for cruciform assemblies to be located between the square assemblies. The fuel in the cruciform assemblies have 2.72 wt% U-235 enrichment. 24 cruciform assemblies were always positioned in the core [64], and another 28 were designed for control purposes with a fuel follower section. 18 of the cruciform control assemblies were fully withdrawn from the core acting as shutdown rods, and 10 were actively moving for control purposes during operation [64]. The cruciform control rod assemblies were used for shutdown and reactivity control instead of the typical cluster-like control rods. These assemblies are composed of an upper section of control rods, made of Ag-In-Cd alloy, and a lower section of 32 fuel rods (control rod followers). The assembly configuration in TV-1 reactor has some similarity to the Yankee-1 assembly designs (section II.1.11). Both designs have removed peripheral rods from the assemblies. In the TV-1 reactor, the peripheral space accommodates cruciform control assembly with a fuel-follower section, and the space in Yankee-1 assemblies accommodates cruciform control blades.

Table 34 lists characteristics of the analyzed samples, which are 31 PIE samples. The sample's identifier starts with the rod number followed by a number, indicating the axial position of the sample in its host rod. Numbering starts from 1 to 9, from top to bottom of the fuel rod. The TV-1 had more samples than those analyzed in this study. Samples taken from rods located at the corner or edge of the assembly are excluded from the present study. Irradiation of these samples is affected by the enrichment and burnup of the neighboring assemblies, and such information are not available for the current TV-1 data. Also, additional approximations on the gap between the assemblies were implemented in the current models, also affecting these corner and edge samples. Only samples located in near-central positions are included in the current analyses, considering them being distant from the neighboring assemblies and the CR or its follower section.

Two assumptions are implemented in the TV-1 assembly models:

1. The control rods were modelled with the follower section in-place (*i.e.*, the fuel bearing section). A control rod insertion of 30% were located adjacent to assembly A32 and A69 during the first part of cycle 1, the affected samples at these locations are E11-1 in A032 and E11-1 and E11-2 in A069. These samples were modelled with the control rod inserted during the first part of cycle-1.
2. The assemblies are encased in a stainless-steel 304 channel having 0.6 mm thickness. The material of the casing is homogenized with the peripheral cooling water in-between the assemblies using their mass ratios.

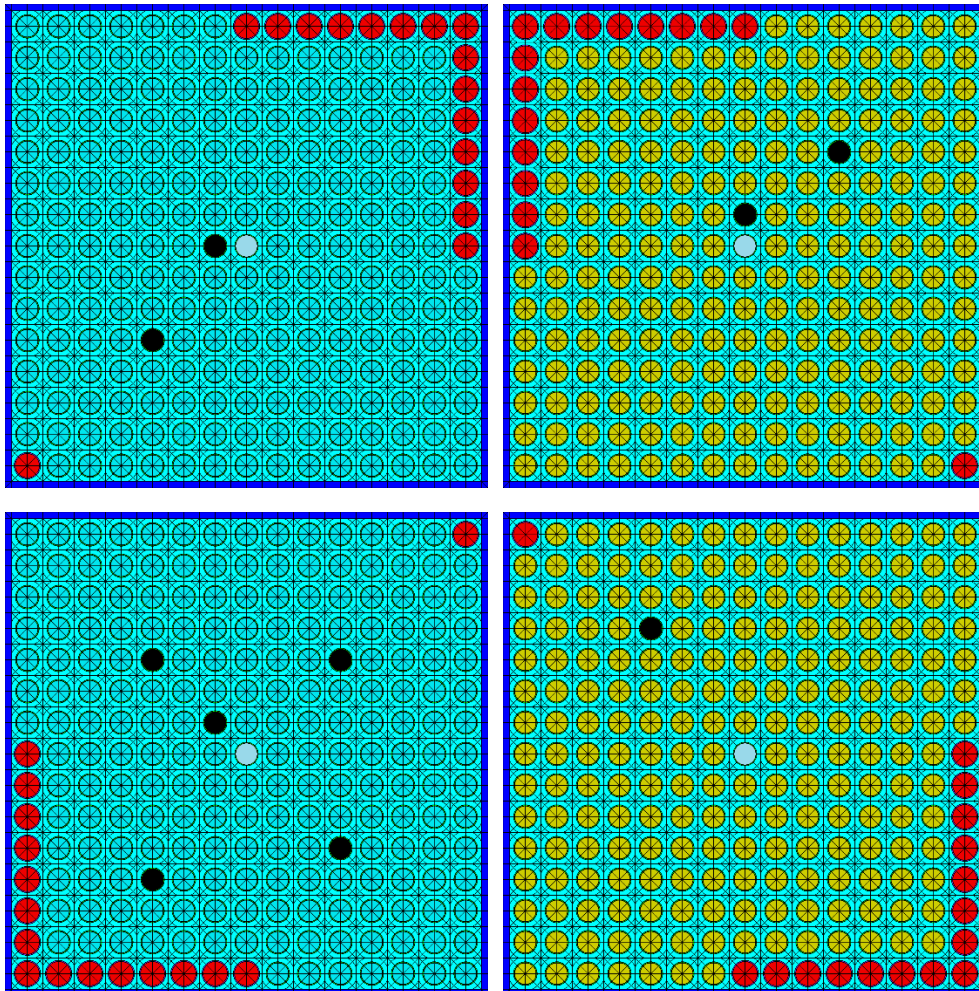


Figure 78: Polaris models of the Trino Vercellese-1 assemblies: A32 and A49 (top row, left to right), and A69 and A104 (bottom row, left to right). The analyzed rods are shown in black color. The peripheral rods (in red color) are rods that belong to the control rod follower part, which are fuel rods of 2.72 wt% U-235 enrichment.

The irradiation histories are compiled from the provided data in SFCOMPO [11], along with data from other references [64,107,116]. Table 34 provides the burnup weighted relevant irradiation parameters. The samples' axial positions were implemented similar to [64], which are based on gamma-activity plots provided in [107]. The inferred samples' axial positions are used in equation 4.1, along with the water inlet and outlet temperatures, to estimate the coolant

temperatures. The assembly specific power was scaled in each sample irradiation history to achieve the given burnup of the sample, *i.e.*, the sample power density is assumed to have the same ratio to the assembly power density throughout the irradiation.

Reference [116] provides different values for the burnup of the considered PIE samples, based on measurements of the concentrations of Nd-148, Cs-137, and also the residual heavy elements in the samples. The burnup values listed in Table 34, are based on Nd-148 measurements, except for four samples that do not have measurements of their Nd-148 concentrations. These samples are marked with (*), and their reported burnup values are based on their Cs-137 measurements. The implemented burnup values of these samples are the provided values in reference [116], without adjustment. The burnup of the other samples, that have measurements of Nd-148 concentrations, were scaled such that the Polaris calculated values of Nd-148 concentrations match the measured ones ($\pm 0.05\%$). The required correction factors are within 4% of the provided burnup values. The samples located at lower sections of the fuel rods required more corrections to their burnup values than upper samples.

The measured concentrations of the analyzed isotopes were obtained from the SFCOMPO database [11], based on reference [116,117]. Cs-137 measurements relied on gamma-spectrometry, and U-235 and Pu-239 measurements relied on the IDMS. The reported values of the measurements are adjusted to the discharge time of the samples. The RCA of the 31 PIE samples were performed at either Ispra or Karlsruhe laboratories, of the European Commission Joint Research Center. Eight PIE samples had their samples measured at both laboratories, for cross-checking. The isotopic concentrations of the samples that have duplicate measurements were obtained by averaging the measured values in both laboratories.

Table 34. Characteristics of the PIE samples of the Trino Vercellese-1 reactor.

SFA	ID	Axial loc. (cm)	BU (est.) GWd/tHMi	Mod. temp. (K)	Mod. dens. (g/cm ³)	Fuel temp. (K)	Boron (ppm)
A032	E11-1	246.7	7.2	563.2	0.7437	740	693
A032	E11-4	165.6	15.4	553.5	0.7616	859	693
A032	E11-7	81.4	15.9	537.8	0.7878	867	693
A032	E11-9	28.8	11.5	531.6	0.7975	803	693
A032	H9-4	165.6	16.6	553.5	0.7616	876	693
A032	H9-7	81.4	17.5	537.8	0.7878	890	693
A032	H9-9	28.8	12.4	531.6	0.7975	815	693
A049	J8-1	246.7	8.7	563.2	0.7437	762	693
A049	J8-4	165.6	14.8	553.5	0.7616	851	693
A049	J8-7	81.4	15.2	537.8	0.7878	857	693
A049	J8-9	28.8	11.1	531.6	0.7975	797	693
A049	L5-1	246.7	7.8*	563.2	0.7437	749	693
A049	L5-4	165.6	14.3	553.5	0.7616	844	693
A049	L5-9	28.8	10.2	531.6	0.7975	784	693
A069	E11-1	246.7	12.9	562.7	0.7447	756	660
A069	E11-2	221.1	20.6	560.9	0.7481	828	660
A069	E11-4	165.6	23.7	552.9	0.7627	858	660
A069	E11-5	137.1	24.5	547.5	0.7721	865	660
A069	E11-7	81.4	24.3	537.1	0.7888	863	660
A069	E11-8	55.4	23.4	533.4	0.7948	854	660
A069	E11-9	28.8	19.3	530.9	0.7985	815	660
A069	E5-4	165.6	23.9	552.9	0.7627	859	660
A069	E5-7	81.4	24.5	537.1	0.7888	865	660
A069	E5-9	28.8	19.2	530.9	0.7985	815	660
A069	J9-4	165.6	24.8*	552.9	0.7627	868	660
A069	J9-7	81.4	25.3	537.1	0.7888	872	660
A069	L11-4	165.6	23.9	552.9	0.7627	860	660
A069	L11-7	81.4	24.4	537.1	0.7888	864	660
A069	L5-4	165.6	24.3	552.9	0.7627	863	660
A069	L5-7	81.4	24.3*	537.1	0.7888	863	660
A104	M11-7	81.4	12.0	537.8	0.7878	811	693

* The burnup is based on Cs-137 measurements.

II.1.10 Turkey Point-3 (TP-3)

Three assemblies from the TP-3 reactor are available in SFCOMPO, which had some of their fuel samples analyzed after their discharge. The samples are irradiated in SFAs: D01, D04 and B17. SFA D01 and D04 had 5 of their full length fuel rods dissolved for examination by Battelle Columbus Laboratories [118], *i.e.*, they had the average isotopic concentrations being measured. The considered full-rods are G9, G10 and H9 for SFA D01 and G9 and G10 for SFA D04. SFA B17 had 8 PIE samples measured also by Battelle Columbus Laboratories [119], however, these are typical short rod-sections PIE samples. The considered PIE samples belong to rods: G7, G9, H6, I9 and J8 (which are all close to the SFA center).

The three assemblies are based on the West OFA/LOPAR 15×15 assembly design. The assemblies have similar designs: 204 UO₂ fuel rods, 20 guide tubes for accommodations of cluster-type control rods, and a central instrument tube. Also, the three SFAs have the same U-235 enrichment for all rods (2.56 wt% U-235). The lattice layouts of the TP-3 SFAs are shown in Figure 79. The lattice design and rods enrichments are based on the values provided in the SFCOMPO [11]. The assemblies have quarter symmetries, and the figure shows only the S-E quarter of the assembly. The rods in black are the rods from which the PIE samples are taken, reflecting their mirrored position into the S-E quarter.

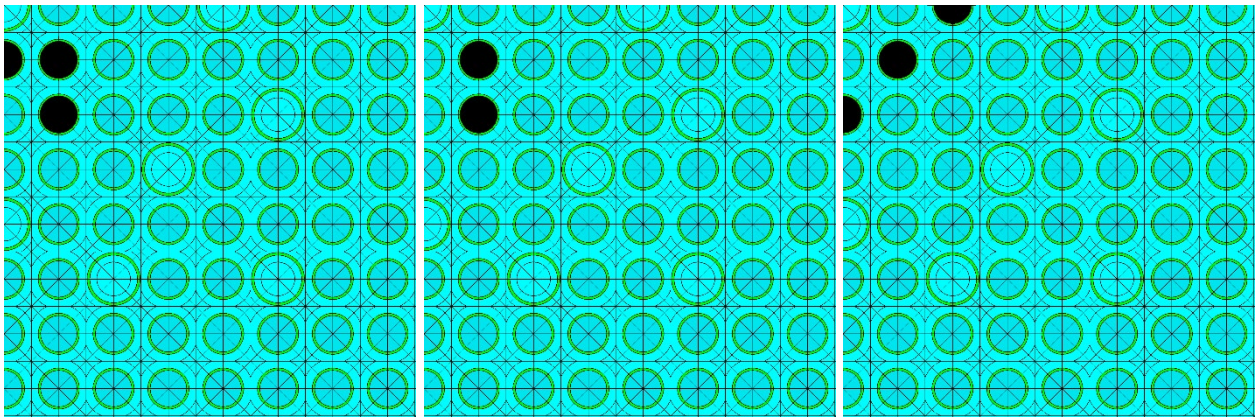


Figure 79: Polaris S-E models of the Turkey Point-3 assemblies: D01 and D04 and B17 SFA (left to right). The shown rods (in black color) reflect the symmetric reflection of the rods' actual positions into the S-E quarter.

Characteristics of the analyzed samples are listed in Table 35. All measurements are conducted at Battelle Columbus Laboratories [118,119], which were compiled in this study from the SFCOMPO values [11]. Cs-137 is not measured in any of the considered rods or samples, and only U-235 and Pu-239 had their concentrations measured using Mass-Spectrometry (MS). The full-rods isotopic concentration measurements are conducted 2.5 years after discharge, whereas the PIE samples of B17 SFA were measured 4.6 years after discharge.

Table 35. Characteristics of the PIE samples of the Turkey Point-3 reactor.

SFA	ID	U-235 wt%	Axial loc. (cm)	BU (est.) GWd/tHMi	Mod. temp. (K)	Mod. dens. (g/cm ³)	Fuel temp. (K)
B17	G7_6	2.556	41	24.6	556.8	0.7566	922
B17	G7_15	2.556	177	26.5	581.8	0.7059	922
B17	G7_30	2.556	295	26.2	606.1	0.6379	922
B17	G7_35	2.556	341	19.2	610.4	0.6222	922
B17	G9_13	2.556	177	25.9	581.8	0.7059	922
B17	H6_13	2.556	177	26.6	581.8	0.7059	922
B17	I9_13	2.556	177	25.6	581.8	0.7059	922
B17	J8_13	2.556	177	26.6	581.8	0.7059	922
D01	G10_4	2.556	*	30.5	581.0	0.7075	922
D01	H9_7	2.556	*	30.7	581.0	0.7075	922
D01	G9_15	2.556	*	31.6	581.1	0.7072	922
D04	G10_7	2.556	*	31.3	581.0	0.7075	922
D04	G9_9	2.556	*	31.3	581.1	0.7072	922

* Full length fuel rod

The irradiation histories are based on the provided data in SFCOMPO [11], along with supplementary assumptions. The SFA B17 was irradiated for two consecutive cycles, whereas D01 and D04 were irradiated for three consecutive cycles. Information about the usage of control rods is not available for the analyzed SFAs, and based on assumptions similar to those in [64]. Therefore, the Polaris models do not include any usage of the control rod cluster.

Table 35 provides the burnup weighted relevant irradiation parameters, compiled from the SFCOMPO database [11]. For B17, the samples' given burnup values are based on the SFCOMPO listed values, obtained based on the assembly operational data. The given burnup values were scaled in the current calculations such that the calculated values of the Nd-148 concentrations match the measured ones ($\pm 0.05\%$). The applied correction factors were between -2.1 and -3.8% of the given burnup values. For the D01 and D04 SFAs, the given burnup values are already based on the measured Nd-148 concentration, and no burnup correction was applied for the 5 rods in these SFAs.

A missing information of the TP-3 reactor data is the cycle-wise cumulative burnup values, or cycle-wise assembly power densities. The currently analyzed SFA are modelled assuming a constant power for all of the active cycles. The assumption is similar to the assumption in [64], relying on that other assemblies in the core have small differences in their power densities in different cycles. Also, the guide tube dimensions are taken from [64] for the D01 and D04 SFAs, and from [119] for the B17 SFA. The latter reference also provided the rod dimensions of the SFA B17. Fuel effective temperatures are assumed values, they are based on values provided in literature studies that analyzed the sample samples of the TP-3 reactor. The fuel effective temperatures are obtained from references [64,120].

II.1.11 *Yankee-1 (Y-1)*

Four assemblies are analyzed from the Y-1 reactor, which had some of their fuel samples removed for RCA. The design of the Y-1 assemblies is unique with respect to PWR common designs [121]. Control blades were used for shutdown and reactivity control instead of the typical cluster-like control rods. Also, the control rod blades (or control rod followers) occupy the location of peripheral rods of the outer row of the assembly. The layouts of the analyzed assemblies are shown in Figure 80. These assemblies have rods and rod-pitch dimensions of a typical Westinghouse 15x15 [122]. However, the layout is 18x18 along with removal of particular peripheral rods to provide a place for the control blades.

Selected PIE samples located in these assemblies have been analyzed in this study. Y-1 had significant large number of their fuel samples examined by RCA, totaling 78 samples. However, due to limited information and modelling complexity, only 22 of them are analyzed in this study. The major modelling approximation is the homogenization of the Zircalloy control blade with the surrounding water. Such approximation was necessary since the Y-1 assembly design is not a typical PWR design that could be implemented in the current version of Polaris. The selection criteria for the selected 22 PIE samples are:

- 1- Nd-148 concentration is measured in their RCA.
- 2- They are located in near-central positions in the assembly, such that they are distant from the peripheral regions affected by the control blades followers. The Y-1 fuel assembly design is radially divided into nine subassemblies [122], and only samples located in the central subassembly C are analyzed (with are the 3x3 central rods).
- 3- Several samples were located at the same axial position in the same host rod. These samples were combined into a single benchmark, and the measured concentrations were assigned the average values of the measurements in all samples.

The lattice design, dimensions, and rods enrichments are based on the values provided in the original report describing the design of the Yankee core and assemblies [121]. The four assemblies are based on UO₂ fuel rods, all having the same U-235 enrichment of 3.4 wt%. With respect to their design, the assemblies have diagonal symmetry; however, they are modelled as a whole in Polaris. The Polaris models of the analyzed assemblies are shown in Figure 81.

The space accommodating the control blades and their follower part is created by removing some (almost half) of the fuel rods located in the periphery of the assembly. Two geometrical designs result from this modification, such that they fit together in their core position, as shown in [121]. The two designs result from removing rods from adjacent edges on the assembly. The first design had rods adjacent to each other in their edges removed, such as the design of E5 and F4 assemblies (top row in Figure 81) (the two wings of the CR are in the same assembly). The other design had rods distant from each other in their edges removed, as the design of E6 and F5 assemblies (bottom row in Figure 81) (two control rod wings from two control rods have their place in the assembly). The control rod follower is made of a Zirconium alloy (Zircaloy-2). In the Polaris models, the follower material (*e.g.*, the friction strip) was homogenized with the

surrounding water, and a homogenous mixture were used to fill the position of the removed fuel rods and their surrounding water, as shown in blue color in Figure 81. Other geometrical approximations are applied, including treatment of the fuel assembly spacers (*i.e.*, ferrules) and the rubbing straps for CR alignment (*i.e.*, sheath). They were modelled by adding their material as extra thickness to the cladding (applied on all rods). These materials add 4% to the total volume of the cladding (the ratio of their volume to the cladding volume is 0.40/10.89).

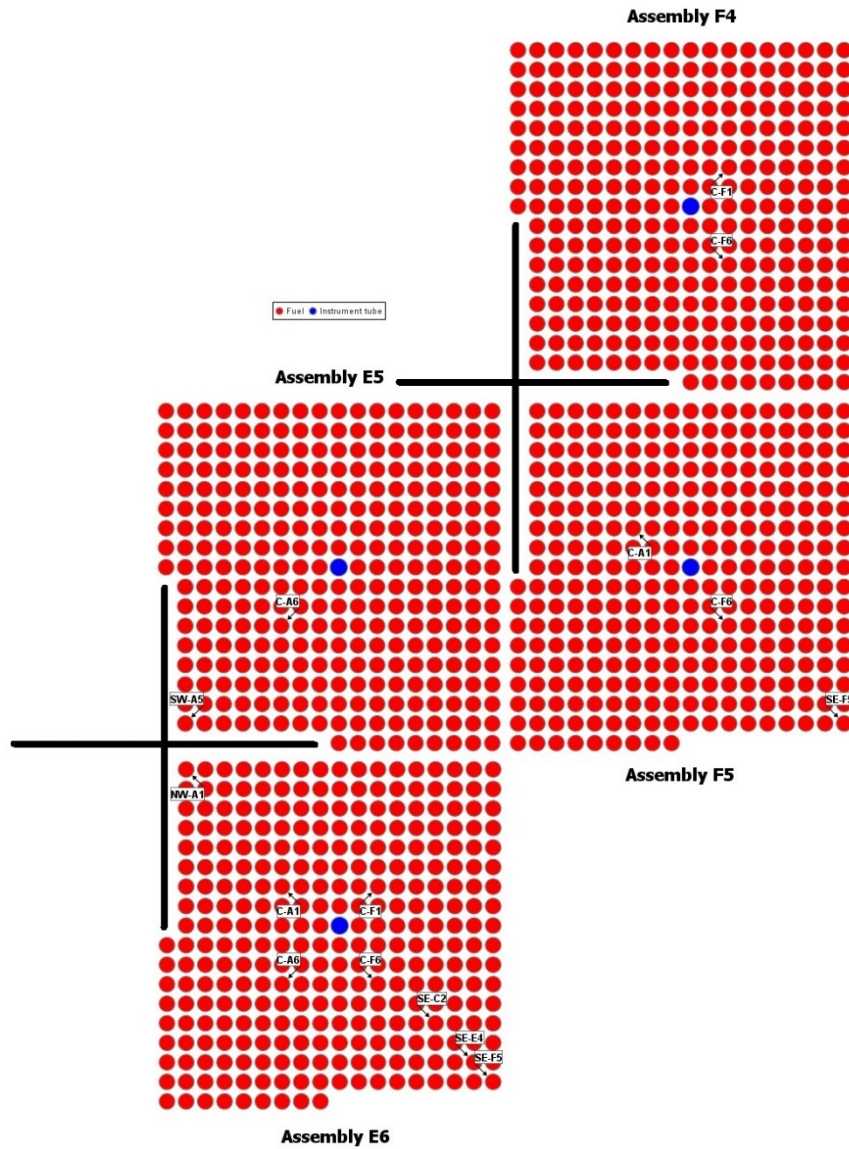


Figure 80: Layouts of the analyzed assemblies of Yankee-1 reactor: E5, E6, F4 and F5 with respect to each other and the control rods, based on SFCOMPO [11]. The implemented dimensions and span of the control rod wings are based on the original reference [121].

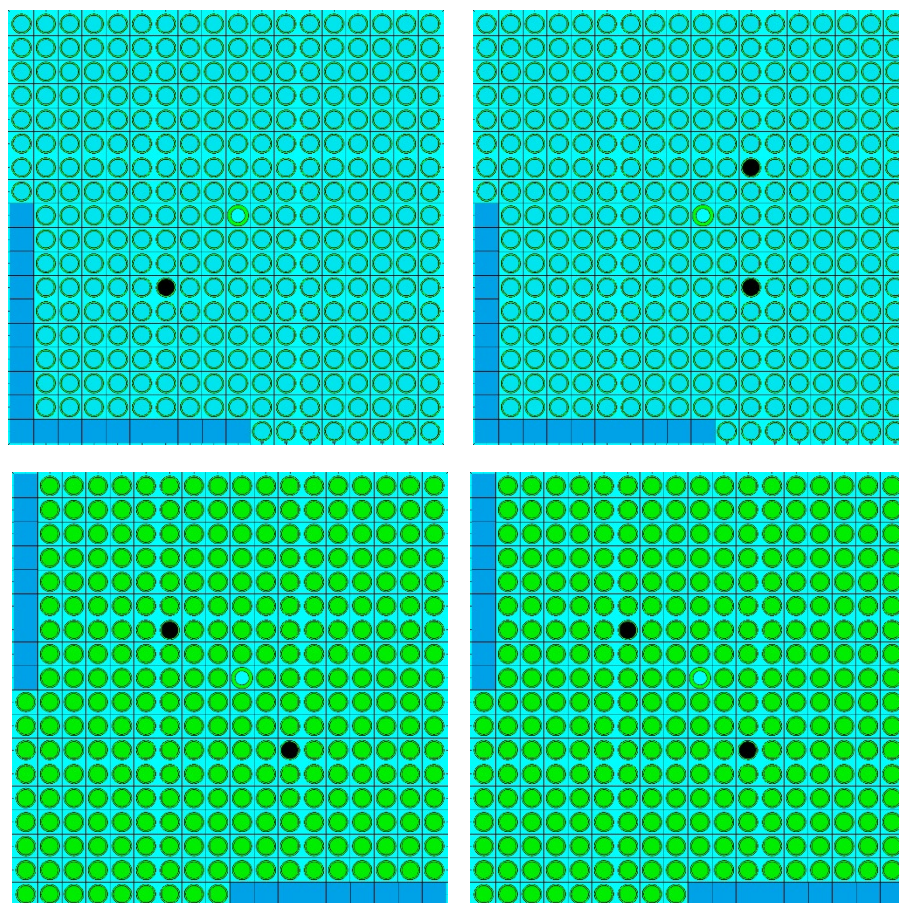


Figure 81: Polaris models of the Yankee-1 assemblies: E5 and F4 (top row) and E6 and F5 (bottom row). The rods in black color are the rods from which RCA samples are analyzed in this study. The peripheral location of the CR follower is shown in different color.

The RCA were performed at the Vallecitos Nuclear Center (GE-Hitachi Nuclear Energy). These RCA data correspond to the selected 22 PIE samples in this study, which had the concentration of the Nd-148 measured. Other measurements were conducted by the New Brunswick Laboratory (NBL) (Argonne National Laboratory (ANL)) and Tracerlab, which did not have the concentration of the Nd-148 measured. The latter measurements of NBL and Tracerlab are excluded from the current analyses. Characteristics of the considered samples are listed in Table 36. All PIE samples had their measurements conducted at GE Vallecitos Nuclear Center, compiled in this study from the SFCOMPO values [11], along with their reported measurements in the original reports [123,124]. Cs-137 is measured in 20 of the analyzed PIE samples, relying on gamma-spectrometry. The U-235 and Pu-239 measurements relied on the IDMS (for the 22 PIE samples).

Table 36 provides the burnup weighted relevant irradiation parameters. The irradiation histories are compiled from the provided data in SFCOMPO [11]. Assemblies E5 and F4 are irradiated for a single cycle, F5 is irradiated for two cycles, and E6 is irradiated for three cycles. The latter assembly, E6, had being controlled by soluble boron during its last irradiation cycle. Information about the average boron content in the cooling water were available at three irradiation intervals of the last cycle. Burnup weighting were used to derive the boron values in

Table 36. The control rods were not inserted near the analyzed assemblies during their irradiation, and the materials of the follower and the friction strips were only considered in the periphery of the assembly.

Table 36. Characteristics of the PIE samples of the Yankee-1 reactor.

SFA	ID	Axial loc. (cm)	BU (est.) GWd/tHMi	Mod. temp. (K)	Mod. dens. (g/cm ³)	Fuel temp. (K)	Boron (ppm)
E5	G-101	139	12.78	540.9	0.7820	894	0
E5	G-102	58	12.38	530.9	0.7979	885	0
E5	G-103	17	8.64	527.0	0.8042	788	0
F5	G-104	220	9.26	548.6	0.7697	755	0
F5	G-105	139	22.90	540.9	0.7820	903	0
F5	G-106	220	9.08	548.6	0.7697	755	0
E6	G-107*	179.6	27.18	527.9	0.7697	927	92
E6	G-108*	138.9	28.77	513.7	0.7822	1132	92
E6	G-109*	57.7	29.94	497.7	0.7968	1112	92
F4	G-113	220	5.96	548.2	0.7705	755	0
F4	G-114	98	13.15	535.9	0.7900	890	0
F4	G-115	58	13.01	530.9	0.7979	885	0
F4	G-116	139	12.85	540.9	0.7820	894	0
F4	G-117	98	11.53	535.9	0.7900	890	0
F5	G-118	180	20.73	548.6	0.7697	755	0
F5	G-119	98	23.93	536.8	0.7886	843	0
F5	G-120	58	22.57	530.9	0.7979	887	0
F5	G-121	17	14.72	526.8	0.8045	791	0
E6	G-125*	180	26.40	527.9	0.7697	927	92
E6	G-126*	139	27.65	513.7	0.7822	1132	92
F5	T-211	139	23.32	540.9	0.7820	903	0

* measurements are averaged between multiple samples at the same axial location

Power densities were obtained assuming that the relative value of the sample power to the assembly power is constant. The sample power densities are then scaled to obtain the target burnup given in the SFCOMPO database for each particular sample [11]. Samples' burnups were scaled in the current calculations such that the calculated values of the Nd-148 concentrations match the measurements ($\pm 0.05\%$). The required correction factors were between -6% and +5% of the given burnup values, except for sample G-103 which required 15% correction of its burnup to match the measured value of the Nd-148 concentration.

The PIE samples from the Yankee-1 reactor (listed in SFCOMPO) are originally more than those listed in Table 36. However, certain samples appear to be extracted from the same location of the fuel rods, *i.e.*, the same axial height in the fuel rod. The PIE samples sharing the same locations are:

1. G-107 and G-169
2. G-108, T-319, N-19 and T212
3. G-109 and G-172

4. G-125 and G-176
5. G-126, N-26 and T-177

Duplicate samples are combined into a single PIE benchmark, marked with an asterisk in Table 36. The assigned measured values in the samples are averages from the multiple measurements. The uncertainty of the measurement is the quadrature sum of the uncertainties in the multiple measurements. The irradiation parameters in both samples are the same, except for their burnup normalized to the measured Nd-148 concentration. Typically, the measured Nd-148 concentration in multiple samples located at the same position is not identical. Therefore, burnup is considered as an average value between both samples, as it is based on normalizing the calculated value to the measured one, whereas the latter is the average measured value in the analyzed samples.

II.2 BWR cases

II.2.1 *Cooper-1 (C-1)*

Assembly CZ346 of the C-1 reactor had two of its rods (ADD2966 and ADD2974) being examined after discharge. The rods are abbreviated hereinafter as rod 66 and rod 74, which are in B3 and C3 positions in the assembly, respectively. The assembly has been irradiated for 5 cycles, and 18 PIE samples are analyzed (9 from each rod), which are listed in the SFCOMPO database [11]. Only 6 PIE samples are considered in this study, which had the concentrations of Cs-137, U-235 and Pu-239 measured. The other 12 PIE samples had their C-14 or I-129 concentrations measured, which is outside the scope of the present study. The analyses consisted of RCA of the fuel samples, performed by the Material Characterization Center (MCC) of the Pacific Northwest Laboratory (PNL), as part of the Approved Testing Material (ATM) program, the ATM-105 program [125].

The assembly is a General Electric GE 7x7 (GE-3B), having a diagonal symmetry and two wide and two narrow water gaps. The assembly contains 49 fuel rods and no water rods. The design layout of the assembly is shown in Figure 82. The figure is also showing the location of the host rods of the PIE samples (in black color). The enrichments of the considered PIE samples are listed in Table 37, along with other relevant irradiation parameters. All samples have a U-235 enrichment of 2.94 wt%. However, the assembly is quite heterogenous, having seven types of fuel rods. Four rods are UO₂-based, which have U-235 enrichment values of 1.33, 1.69, 1.94 and 2.93 wt%. Three rods are UO₂-Gd₂O₃-based (integral absorbers). The gadolinia-loaded rods have the following enrichments, and gadolinia fractions, respectively:

1. 1.94%, 4%
2. 2.93%, 4%
3. 2.93%, 3%

The lattice design and enrichments are based on the values provided in SFCOMPO [11], along with the original ATM report (ATM-105) [125]. The box geometry and the dimensions of the water gaps were set similar to values implemented in reference [68]. The assemblies were modelled as a whole (no symmetries are applicable to BWR models in the current version of Polaris). Nevertheless, the assemblies show symmetries around their diagonal, two wide gaps to the west and north sides, and two narrow water gaps to the east and south sides (based on the orientation of the assembly in Figure 82). The wide water gaps can accommodate a cross-type control rods (a cruciform CR). However, the considered PIE samples were not reported to be exposed to control rods during their irradiation, and the CR modelling is excluded from the implemented models. Also, the CR position is always facing the low enriched rods (the rods in purple color in Figure 82), which is separated from the analyzed rods by at least one row of fuel rods (their effect, if present, is assumed negligible).

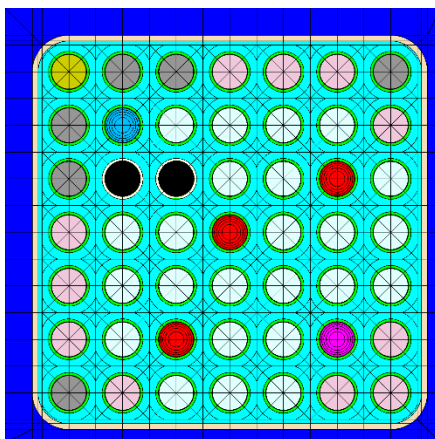


Figure 82: Polaris model of the Cooper-1 assembly CZ346. The rods containing the analyzed samples are shown in black color (rod B3 and C3).

The RCA of the 6 PIE samples were conducted at the PNL [125]. All the PIE samples had the concentrations of the Cs-137, U-235 and Pu-239 measured. The measurements of U-235 and Pu-239 relied on MS in both laboratories. Gamma spectrometry is used in both laboratories for Cs-137 measurements. The reported measurements are compiled from the SFCOMPO values [11], which are cross-checked with values reported in [125]. The measured values were reported at 5.2 years for the measurements of the samples of rod 66, and 5.1 years for the measurements of the samples of rod 74.

Table 37. Characteristics of the PIE samples of the Cooper-1 reactor.

SFA	ID	U-235 wt%	Axial loc. (cm)	BU (given) GWd/tHMi	Cool. temp. (K)	Cool. dens. (g/cm ³)	Fuel temp. (K)
CZ346	66-B	2.94	316	18.96	558	0.320	833
CZ346	66-K	2.94	152	33.07	558	0.509	833
CZ346	66-T	2.94	96	33.94	558	0.652	833
CZ346	74-B	2.94	315	17.84	558	0.320	833
CZ346	74-U	2.94	79	31.04	558	0.320	833
CZ346	74-J	2.94	255	29.23	558	0.349	833

The irradiation histories are based on the provided data in SFCOMPO [11]. The fuel temperatures are based on the values provided in [68]. The given power density is per assembly. The power density in the fuel rod hosting the analyzed sample is assumed to have the same relative variations during irradiation as for the whole assembly. The power density in each fuel rod is then scaled to achieve the reported burnup of the sample under analyses. Missing information in the original reports of the PIE, such as the void fraction, and therefore the moderator density, were set equal to values reported and analyzed in reference [68]. Table 37 provides the burnup weighted relevant irradiation parameters. The samples' given burnup values are based on the SFCOMPO listed values (obtained based on the assembly operational data). No measurements of Nd-148 are reported for the analyzed samples, and the implemented burnups are the given values.

II.2.2 Dodewaard-1 (D-1)

Five PIE samples located in three assemblies of the D-1 reactor are available in the SFCOMPO. The samples were irradiated in SFAs: Y012, Y013 and Y014. The Y012 and Y014 are MOX-based assemblies, and the Y013 is a UO₂-based assembly. Y012 has been irradiated for four cycles, and from which two PIE samples are analyzed: DM2 and DM3 (where D stands for Dodewaard, and M stands for MOX). Y013 and Y014 have been irradiated for five cycles. One PIE sample is analyzed from the Y013 assembly (DU1, where U stands for UO₂). Two PIE samples are analyzed from Y014 assembly (DM1 and DM4). In total, 4 PIE samples are MOX-based, and 1 PIE is UO₂-based. The considered MOX samples are taken from the E4 rod of the Y012 SFA and the D5 rod of Y014 SFA, with symmetric reflections of each other around the SFA diagonal (the assemblies have diagonal symmetry). The UO₂ sample of Y013 is taken from rod B2.

The assemblies are based on the General Electric 6x6 assembly design. The assemblies contain 35 active fuel rods and a single water rod. The design layouts of the three assemblies are shown in Figure 83 at axial locations of selected PIE samples. The layouts are at the axial locations of DM1, DM2 and DU1 from assemblies Y014, Y012 and Y013 (following the order shown in the figure). The enrichments and the plutonium fractions of the MOX rods are listed in Table 38, along with other relevant irradiation parameters. The assemblies are heterogeneous in terms of U-235 enrichments, having both radial and axial zoning as given in the original ARIANE report [126]. The assemblies were modelled without control rod usage. Only DM2 had a relatively short exposure to a control rod (5% of the total irradiation), which is deemed to be a relatively short time, and also the rod is located in a central position of the lattice being less affected by the CR usage. The lattice design and enrichments are based on the values provided in reference [126]. The assemblies were modelled as a whole (no symmetries are applicable to BWR models in the current version of Polaris). Nevertheless, the assemblies show symmetries around their diagonal; two narrow gaps to the east and south sides, and two wide water gaps to the west and north sides. The wide gaps are used to accommodate cross-type control rods. However, usage of the control rods is not implemented as discussed previously.

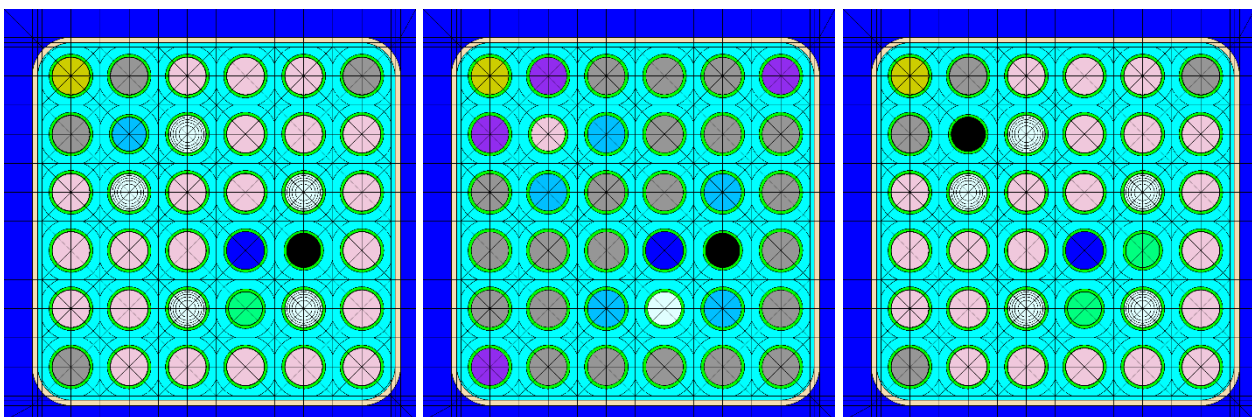


Figure 83: Polaris models of the Dodewaard-1 assemblies: Y014, Y012 and Y013 (left to right). The Y014 and Y012 SFAs have MOX-based fuel, and the Y013 has UO₂ fuel. Two PIE samples are analyzed from each rod of the MOX based SFAs (4 MOX PIE samples) and only one samples is analyzed from the rod of the UO₂ based SFA.

Measurements of the 5 PIE samples from D-1 are performed in SCK.CEN [126], and two PIE samples from adjacent locations to the original ones are also measured in Paul Scherrer Institute (PSI). The PIE samples that had multiple measurements are DM1 and DU1. All PIE samples had their Cs-137, U-235 and Pu-239 contents measured. Also, the PSI measurements include these three isotopes. The measurements conducted at the SCK.CEN uses TIMS for U-235 and Pu-239, and gamma-spectrometry for Cs-137. PSI measurements are based on high-performance liquid chromatography coupled to inductively coupled plasma - mass spectrometry (HPLC-ICPMS) for all of the three isotopes. The reported measurements are compiled from the SFCOMPO values [11], which are cross-checked with values reported in [126]. The measurements at the SCK.CEN are considered, and the ones at the PSI are excluded. The SCK.CEN measurements are considered since all the samples have been measured in this laboratory, and only two are measured in PSI. The time of measurements is not consistent between the samples and also the isotopes, ranging from 3.3 to 6.0 years after discharge.

Table 38. Characteristics of the PIE samples of the Dodewaard-1 reactor.

SFA	ID	U-235 wt%	MOX wt%	Axial loc. (cm)	BU (est.) GWd/tHMi	Cool. temp. (K)	Cool. dens. (g/cm ³)	Fuel temp. (K)
Y013	DU1	4.941	0	111	56.3	566.15	0.3855	1094
Y014	DM1	0.239	6.431	111	64.9	566.15	0.3857	1116
Y012	DM2	0.239	6.431	15	40.6	566.15	0.7088	1040
Y012	DM3	0.239	6.431	113	53.6	566.15	0.3612	1152
Y014	DM4	0.239	6.431	164	39.6	566.15	0.3083	991

The irradiation histories are based on the provided data in SFCOMPO [11], along with supplementary data from [126]. Contradicting information, such as 2 days discrepancy in the length of cycle 2, is resolved by implementing the values provided in the original ARIANE report [126]. Table 38 provides the burnup weighted relevant irradiation parameters. The given reactor pressure is interpreted as the gauge pressure. At this pressure, and at water saturation, water density 0.7283 g/cm³ and steam density is 0.0404 g/cm³. The samples' given burnup values are based on the SFCOMPO listed values (obtained based on the assembly operational data). The burnup values were scaled in the current calculations such that the calculated values of the Nd-148 concentrations match the measured ones ($\pm 0.05\%$). The required correction factors are significant, and the given burnup values are corrected by the following percentages to match the measured Nd-148 concentrations:

1. DU1: 1.5%
2. DM1: 10.2%
3. DM2: 12.0%
4. DM3: 9.0%
5. DM4: 3.0%

Another assumption of the implemented models of samples DM2 and DM4, is that their axial position is approximately in between two lattice layouts. In one layout, fuel rods of type 1,

adjacent to the considered rods, have lower U-235 enrichment of 1.8 wt%. In the other layout, the adjacent rods have higher U-235 enrichments of 3.2 wt%. The models of DM2 and DM4 implement an average enrichment value (2.5 wt%) for rods of type-1. Nevertheless, the calculated values of the considered isotopes are not significantly affected by the value of U-235 enrichment in these other rods in the lattice. The implemented approximation was considered acceptable, also given limitations of lattice codes of 2D nature.

II.2.3 Fukushima Daini-1 (FD1)

The FD1 data in the SFCOMPO database are 9 PIE samples [11]. The samples belong to two assemblies 2F1ZN2 and 2F1ZN3. “2F1” in the beginning of each assembly name stands for Fukushima Daini-2, unit 1, which will be dropped hereinafter from the naming of the assemblies. The assemblies are based on a 9x9 design loaded with quarter symmetric enrichment layout. The assemblies are heterogenous with respect to their radial zoning. They are loaded with six different rod types, which differ in their enrichment or gadolinia loading. The assemblies are characterized by a large central water-hole of size 3x3, replacing 9 central rods – the assembly design is commonly referred to as 9x9-9. The design layouts of the two assemblies are shown in Figure 84, showing the locations of the rods hosting the PIE samples (in black color). The assemblies were not close to control rods during their irradiation [127]. The lattice design and enrichments are based on the values provided in SFCOMPO [11], along with the references [127–129].

The enrichments of the considered PIE samples are listed in Table 39, along with other relevant irradiation parameters. The sample ID starts with the rod position: A9 or C2 or C3, followed by U or Gd for UO_2 or $\text{UO}_2\text{-Gd}_2\text{O}_3$ fuel, followed by B or M or T for samples located in the bottom or middle or top positions of the fuel rod (Figure 85). From ZN2 SFA, 4 samples are analyzed from the top and bottom positions of two rods: C2 and C3. From ZN3 SFA, 9 samples are analyzed from the three axial positions of the three rods: A9, C2 and C3. The rod C2 is $\text{UO}_2\text{-Gd}_2\text{O}_3$ -based, and the other rods are UO_2 -based. Rod A9 is a peripheral rod located at the corner of the assembly, and C2 and C3 are near-central rods.

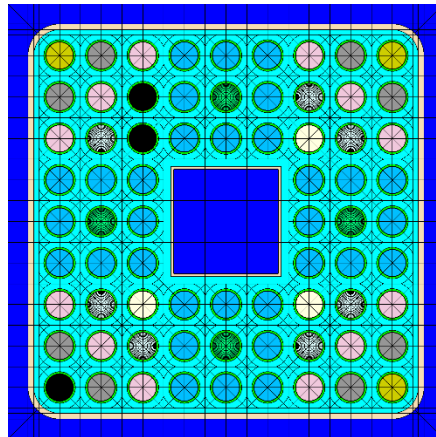


Figure 84: Polaris model of the Fukushima Daini-1 9x9-9 assembly design (ZN2 and ZN3 assemblies). The rods positions A9, C2 and C3 are shown in black color.

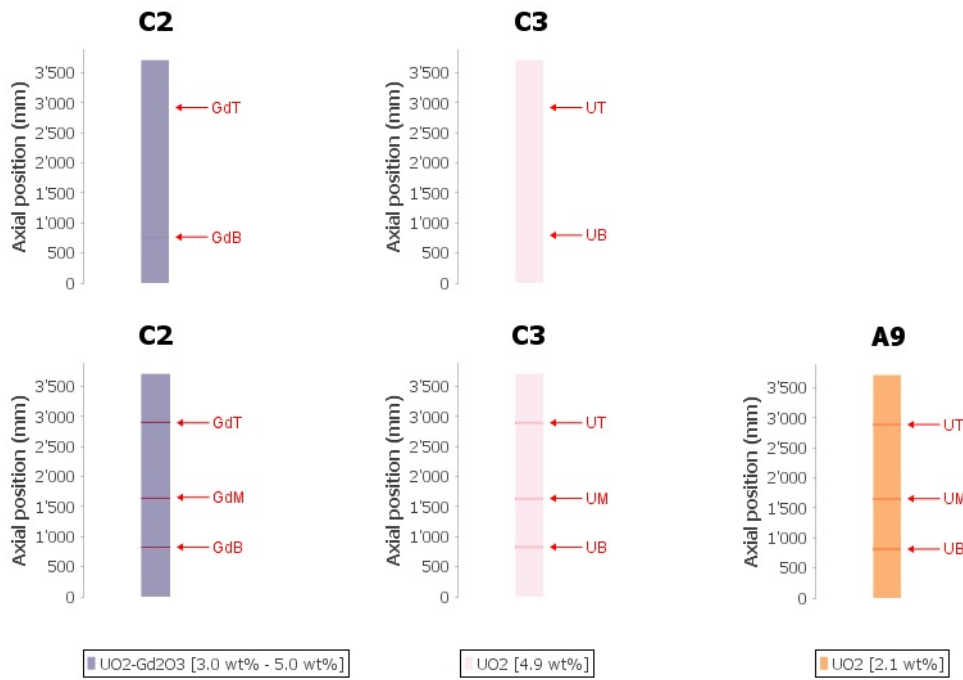


Figure 85: Axial locations of the PIE samples of the SFAs: ZN2 (top row) and ZN3 (bottom row).

Table 39. Characteristics of the PIE samples of the Fukushima Daini-1 reactor.

SFA	ID	U-235 wt%	Gd wt%	BU (est.) GWd/tHMi	Mod. temp. (K)	Mod. dens. (g/cm ³)	Fuel temp. (K)
N3	A9-UB	2.10	0.00	60.44	559	0.630	900
N3	A9-UM	2.10	0.00	63.73	559	0.413	900
N3	A9-UT	2.10	0.00	55.75	559	0.259	900
N3	C3-UB	4.90	0.00	67.06	559	0.630	900
N3	C3-UM	4.90	0.00	67.55	559	0.413	900
N3	C3-UT	4.90	0.00	58.13	559	0.259	900
N3	C2-GdB	3.00	5.00	54.65	559	0.630	900
N3	C2-GdM	3.00	5.00	54.76	559	0.413	900
N3	C2-GdT	3.00	5.00	46.62	559	0.259	900
N2	C2-GdB	3.00	5.00	35.61	559	0.606	900
N2	C2-GdT	3.00	5.00	28.20	559	0.223	900
N2	C3-UB	4.90	0.00	46.39	559	0.606	900
N2	C3-UT	4.90	0.00	37.37	559	0.223	900

The measurements were conducted at facilities of the Japan Atomic Energy Agency (JAEA) [128], using IDMS for U-235 and Pu-239 and gamma-spectrometry for Cs-137. U-235 and Pu-239 were measured in all samples, and Cs-137 were measured in the “T” samples of ZN2 and the “M” samples of ZN3 – total 9 Cs-137 measurements. The U-235 and Pu-239 measurements were done at different cooling times, between 2.4 and 12.2 years. Cs-137 were measured at cooling times between 7.0 and 9.7 years.

The irradiation histories are based on the provided data in SFCOMPO [11], and reference [128]. The void fractions at the samples’ axial locations were interpolated from the nodal values provided in [128]. The samples’ given burnup values are based on the values provided in [129].

The burnup values were scaled in the current calculations such that the calculated values of Nd-148 concentrations match the measured ones ($\pm 0.05\%$). The estimated burnup values are between -2.3% and +1.1% from the given ones.

II.2.4 Fukushima Daini-2 (FD2)

Five assemblies of the FD2 reactor are included in the SFCOMPO database [11]. The assemblies are 2F2D1, 2F2D2, 2F2D3, 2F2D8 and 2F2DN23, which are UO_2 -based. “2F2” in the beginning of each assembly name stands for Fukushima Daini-2, unit 2, dropped hereinafter from the naming of the assemblies. In total, 44 PIE samples are analyzed from the mentioned assemblies, which are listed in the SFCOMPO database [11]. The considered PIE samples are listed in Table 40. For clarity, the sample ID from the DN23 assembly is specified as the rod number, followed by a number identifying the sample in the SFCOMPO database.

Several samples are analyzed from two rods of the DN23 assembly (rod 98 and 99), located at the B2 and C2 positions, as shown in Figure 86. The samples of the DN23 assembly are peculiar since they are taken from different axial positions of the same rods (98 is UO_2 and 99 is $\text{UO}_2\text{-Gd}_2\text{O}_3$) as shown in Figure 87. The other assemblies, D1, D2, D3 and D8 also had their samples taken from different axial positions as shown in Figure 88. The rods hosting the PIE samples in the latter assemblies are 3 types, with respect to their enrichments and radial locations within the assemblies:

- 1- F6 (UO_2 -based rod with two axial U-235 enrichments of 2.9 and 3.9 wt%),
- 2- B3 ($\text{UO}_2\text{-Gd}_2\text{O}_3$ -based rod with U-235 enrichment of 3.4 wt%, and 4.5 wt% gadolinia),
- 3- A4, H4 and H5 (UO_2 -based rod with uniform axial U-235 enrichment of 4.5 wt%). These rods are identical considering the quarter symmetry of the lattice, with respect to their enrichments and dimensions.

The design layouts of the assemblies are shown in Figure 86, also showing the locations of the rods hosting the PIE samples (in black color). The assemblies are based on an 8x8 assembly design, having a diagonal symmetry in the DN23 assembly, and a quarter symmetry in the D1, D2, D3 and D8 assemblies. The DN23 assembly has two central water rods (based on the 8x8-2 assembly design). The D1, D2, D3, and D8 assemblies have a large central water channel occupying the position of 4 fuel rods (based on the 8x8-4 assembly design). The assemblies are heterogenous, with respect to their radial and axial zoning. The PIE samples are taking from different axial positions, which coincide in some samples with different axial zoning (different fuel lattices). Sample 1 of rod 98 and samples 1, 9, and 10 of rod 99 are peripheral with respect to their axial positions. They are located in the axial low-enriched blanket (A fuel zone of natural uranium). All the PIE samples are UO_2 -based (with/without integral absorber based on gadolinia). The enrichments of the considered PIE samples are listed in Table 40, along with other relevant irradiation parameters.

The lattice design and enrichments are based on the values provided in SFCOMPO [11], along with reference [110] for the DN23 assembly, and reference [128] for the D1, D2, D3 and D8 assemblies. No information is available about the size of the water gaps, and it is assumed that they are equal in the implemented models. The assemblies were not close to control rods during

their irradiation [130], and were modelled as a whole (no symmetries are applicable to BWR models in the current version of Polaris).

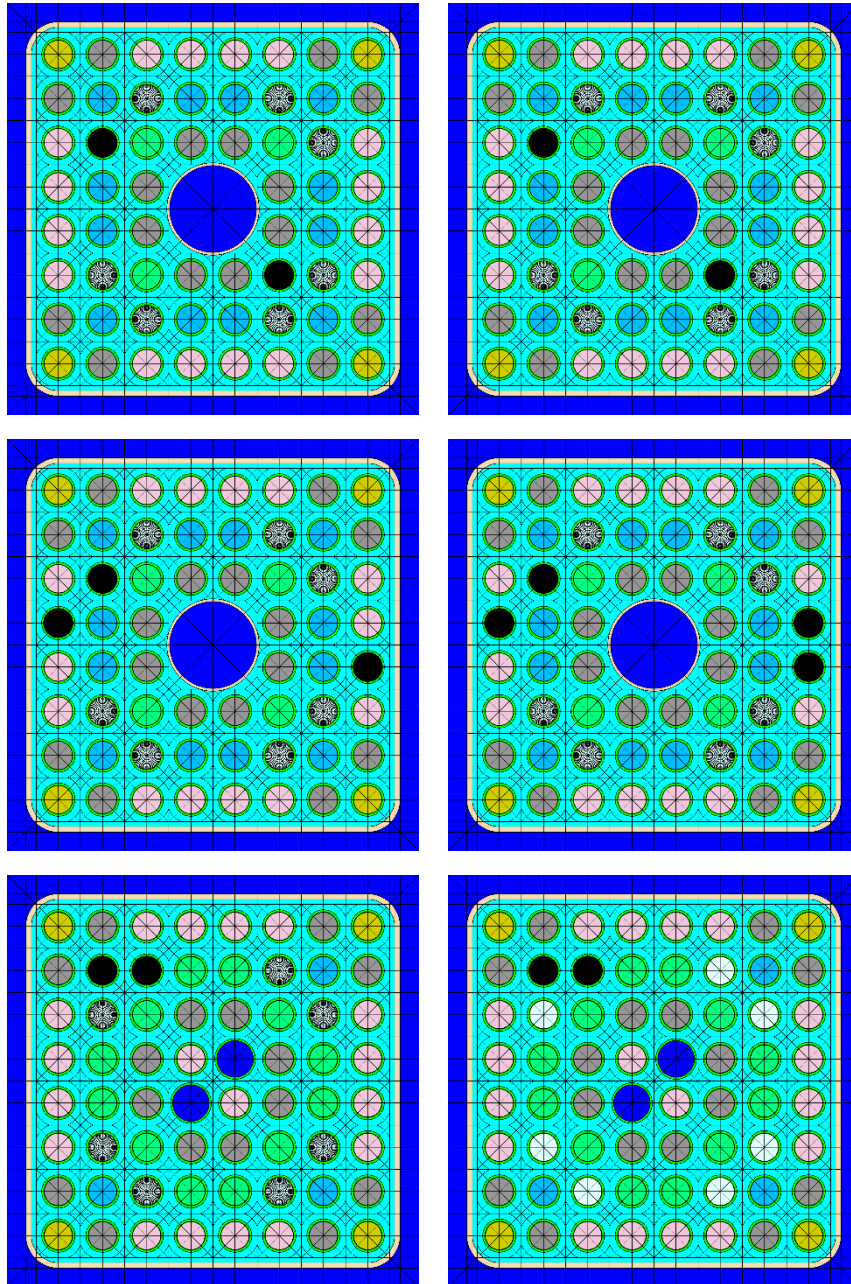


Figure 86: Polaris models of the Fukushima Daini-2 assemblies. The top row contains the D1 and D2 assemblies. The middle row contains the D3 and D8 assemblies (left to right). The bottom row contains fuel designs of the DN23 assembly. Assembly DN23 had most of its samples based on the middle design (left), and samples 89-1, 99-1 and 99-10 are based on the top and bottom designs (right). The rods hosting the analyzed samples are shown in black color.

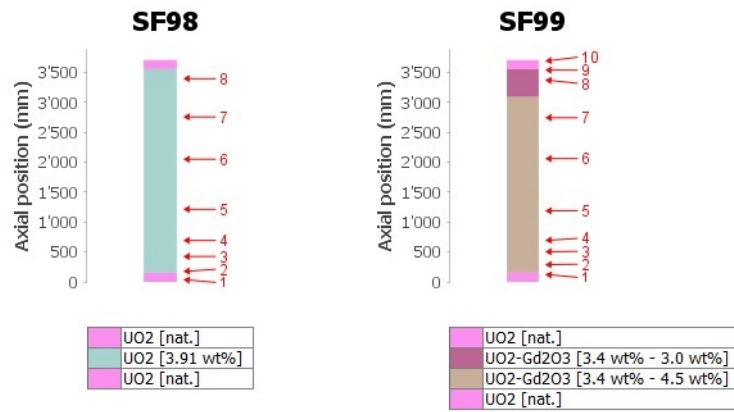


Figure 87: Axial positions of the PIE samples of the rods 98 and 99 of the DN23 assembly. Different colors indicate differences in enrichment or gadolinia content in the rods.

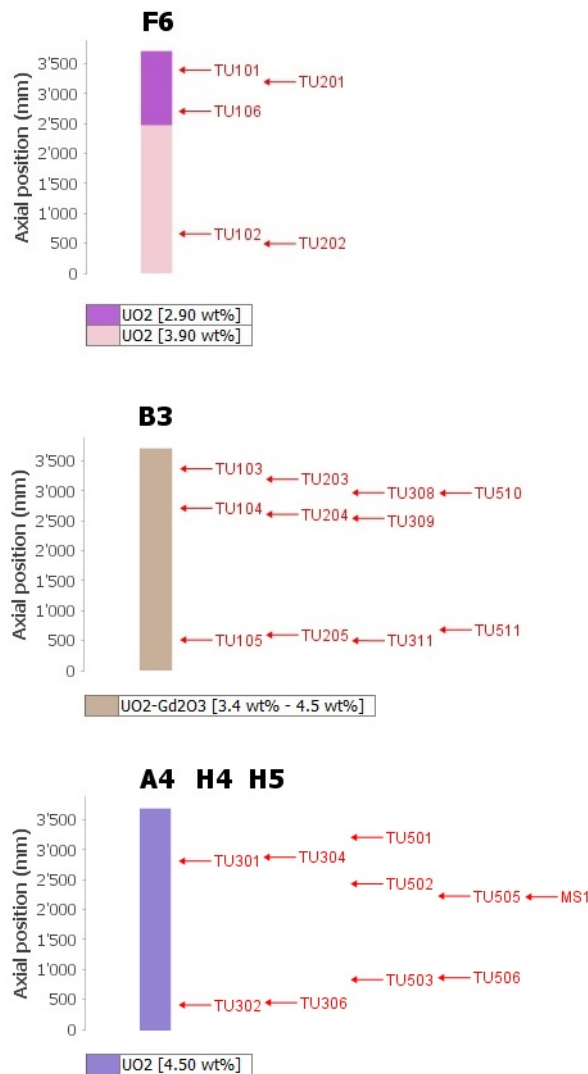


Figure 88: Axial positions of the PIE samples from the D1, D2, D3, and D8 assemblies. The third letter in the sample ID is a number indicating the assembly of origin; 1, 2, 3, and 5 for D1, D2, D3 and D8, respectively. Different colors indicate differences in enrichment or gadolinia content in the rods.

Table 40. Characteristics of the PIE samples of the Fukushima Daini-2 reactor.

SFA	ID	U-235 wt%	Gd wt%	Axial loc. (cm)	BU (est.) GWd/tHMi	Cool. temp. (K)	Cool. dens. (g/cm ³)
DN23	98_1	0.71	0	4	4.11	551.6	0.7401
DN23	98_2	3.91	0	17	25.78	553.1	0.7401
DN23	98_3	3.91	0	42	35.97	556.0	0.7192
DN23	98_4	3.91	0	69	41.32	559.2	0.6627
DN23	98_5	3.91	0	121	43.04	559.2	0.5151
DN23	98_6	3.91	0	205	39.19	559.2	0.3567
DN23	98_7	3.91	0	276	38.80	559.2	0.2617
DN23	98_8	3.91	0	340	26.68	559.2	0.2265
DN23	99_1	0.71	0	13	7.47	552.7	0.7401
DN23	99_2	3.40	4.5	29	22.68	555.0	0.7304
DN23	99_3	3.40	4.5	50	32.34	556.9	0.6995
DN23	99_4	3.40	4.5	69	35.31	559.2	0.6641
DN23	99_5	3.40	4.5	119	37.37	559.2	0.5452
DN23	99_6	3.40	4.5	206	32.51	559.2	0.3553
DN23	99_7	3.40	4.5	274	32.38	559.2	0.2722
DN23	99_8	3.40	3.0	339	21.89	559.2	0.2357
DN23	99_9	3.40	3.0	354	16.74	559.2	0.2272
DN23	99_10	0.71	0	368	7.18	559.2	0.2173
D1	TU101	4.50	0	338	14.01	559.3	0.2898
D1	TU102	4.50	0	64	18.20	559.3	0.6486
D1	TU103	3.40	4.5	334	16.10	559.3	0.2898
D1	TU104	3.40	4.5	274	10.01	559.3	0.3179
D1	TU105	3.40	4.5	74	9.41	559.3	0.6203
D1	TU106	4.50	0	269	12.32	559.3	0.3179
D2	TU201	4.50	0	318	29.14	559.3	0.2968
D2	TU202	4.50	0	48	32.92	559.3	0.6910
D2	TU203	3.40	4.5	318	24.55	559.3	0.2968
D2	TU204	3.40	4.5	259	23.55	559.3	0.3250
D2	TU205	3.40	4.5	58	23.50	559.3	0.6698
D3	TU301	3.40	0	279	34.67	559.3	0.3109
D3	TU302	3.40	0	42	31.40	559.3	0.7051
D3	TU304	3.40	0	286	37.86	559.3	0.3109
D3	TU306	3.40	0	45	32.30	559.3	0.6981
D3	TU308	3.40	4.5	324	30.23	559.3	0.2968
D3	TU309	3.40	4.5	278	34.94	559.3	0.3179
D3	TU311	3.40	4.5	54	33.52	559.3	0.6769
D8	TU501	3.4	0	320	53.13	559.3	0.2968
D8	TU502	3.4	0	245	58.87	559.3	0.3320
D8	TU503	3.4	0	80	55.60	559.3	0.5922
D8	TU505	3.4	0	223	59.16	559.3	0.3532
D8	TU506	3.4	0	85	57.63	559.3	0.5782
D8	TU510	3.4	4.5	295	53.10	559.3	0.3038
D8	TU511	3.4	4.5	67	48.15	559.3	0.6415
D8	MS1	3.4	0	222	57.46	559.3	0.3532

The measurements were conducted by the JAERI, within a research project titled: “Technical Development on Criticality Safety Management of Spent LWR Fuels” [110,111]. The concentrations of the Cs-137, U-235, and Pu-239 were measured in the PIE samples of the DN23 assembly. Only U-235 and Pu-239 were measured in the PIE samples of the D1, D2, D3 and D8 assemblies. Also, the measurements on the DN23 assembly were adjusted for the decay, and the reported values correspond to the time of discharge of the assembly. The measurements on the D1, D2, D3, and D8 assemblies are conducted between 2.4 and 6.9 years of decay after discharge. Mass-spectrometry is used for the U-235 measurements in the PIE samples of the DN23 assembly. The IDMS technique is used for the U-235 measurements in the PIE samples of the D1, D2, D3, and D8 assemblies. The MS is used for the measurements of Pu-239 in all assemblies. Gamma-spectrometry is used for the measurements of Cs-137 (measured only in DN23). The reported measurements are compiled from the SFCOMPO values [11], cross-checked with the reference values reported in [110,128].

The irradiation histories are based on the provided data in SFCOMPO [11], cross-checked with their values reported in the original references [110,128]. Contradicting information between the values in SFCOMPO and the original references are resolved by implementing the values in the references. SFCOMPO and the references provide the void fractions for the considered samples, which were used to obtain moderator densities at the given reactor pressure (gauge pressure). The samples’ given burnup values are based on the SFCOMPO listed values, scaled in the current calculations such that the calculated values of the Nd-148 concentration match the measured ones ($\pm 0.05\%$). The estimated burnup values are between $\pm 3\%$ from the given ones.

II.2.5 Garigliano-1 (G1)

Two assemblies from the G1 reactor are listed in the SFCOMPO database [11]. The assemblies are A-106 and SA-13. Assembly A-106 had 18 PIE samples analyzed from 18 different rods at the same axial position as shown in Figure 89. The total active length of the A-106 assembly is 268 cm, and all the PIE samples of the A-106 assembly are taken from an axial height of 162 cm from the bottom of the fuel stack. The PIE samples were chosen at this level since the void fraction at this level is representative of the average void fraction of the core. Assembly SA-13 had 8 PIE samples analyzed from the same rod (E6), being a near-central rod, at different axial positions as shown in Figure 89. The PIE samples of the G1 reactor combine unique characteristics of different samples analyzed from different rods at the same axial positions, and different samples from the same rod at different axial heights. The considered PIE samples from the G1 reactor are listed in Table 41 along with relevant design and irradiation parameters.

The assemblies are based on a General Electric 8x8 assembly design. The two assemblies are UO₂-based, homogeneous with respect to modern BWR designs, having only two values of U-235 enrichments (1.6 and 2.1 wt%). The design layouts of the two assemblies are shown in Figure 89, also indicating the locations of the rods hosting the PIE samples (in black color). The assemblies have quarter symmetry, including two wide and two narrow water gaps. The wide gaps are in the north and south sides, and the narrow gaps are in the east and west sides, resulting in larger assembly pitch in the wide-wide side than the narrow-narrow side.

The lattice design and enrichments are based on the values provided in SFCOMPO [11], along with the original references [107,131]. The SA-13 assembly has been irradiated for a single cycle, achieving burnup values between 4 and 9 GWd/tHMi (in the analyzed samples). The A-106 assembly has been irradiated for 5 cycles: 1a, 1b, 1c, 1e, and 1f. The downtimes are short, 1 to 2 days between the cycles, except for the downtime between cycles 1c and 1e which is 219 days. The A-106 assembly was controlled during its irradiation. The control rods were active during cycles 1a and 1e. The control rods were used during a fraction of the burnup (with respect to the discharge burnup). These burnup fractions are listed in Table 41 (rightmost column). A Duralife 230L type control rod has been used, based on an active absorber part of 20 B₄C-type rods. The configuration of the cruciform-type control rod is shown in Figure 89.

Another particular aspect of the assembly A-106 is that the sheath is not the same material throughout its irradiation history [131]. During cycle A1 the assembly has been encased by a stainless-steel 304 sheath, replaced from cycle 1B by a Zircaloy-2 sheath. The implemented material in the current models is a sheath made of a mixture of SS304 and Zirc-2. The mixing ratio of the two materials corresponds to their exposure (the burnup fraction of their residence time in the assembly).

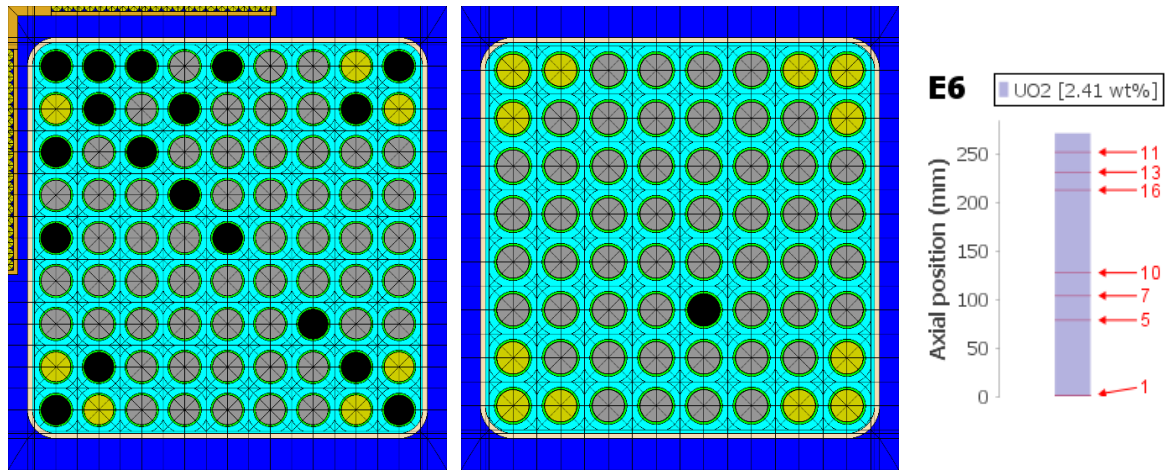


Figure 89: Polaris models of the Garigliano-1 assemblies: A-106 (left) and SA-13 (middle). The rods hosting the analyzed samples are shown in black color. The elevation of the samples from the SA-13 assembly are shown in the right plot.

The measurements of the 18 PIE samples of the A-106 assembly were conducted at the Karlsruhe laboratories of the Joint Research Centre. The measurements of the 8 PIE samples of the SA-13 assembly were conducted at the Ispra laboratories of the Joint Research Centre [107,131]. Cs-137 measurements at both laboratories relied on gamma-spectrometry, and also MS (two measurements are reported using both methods). Measurements of U-235 and Pu-239 relied on MS methods. The measured values were corrected for the decay, and the reported values correspond to the time of discharge of the assemblies.

The irradiation histories are based on the provided data in SFCOMPO [11], along with supplementary data from [107,131]. Table 41 provides the burnup weighted relevant irradiation parameters. The samples' given burnup values are based on the SFCOMPO listed values, which are based on isotopic measurements of Nd-148 concentrations. The implemented burnup values were scaled such that the Polaris calculated values of the Nd-148 concentration match the measured ones ($\pm 0.05\%$). The implemented burnup corrections are not significant. The corrected burnup values are listed in Table 41, within 0.7% of the given values (for the A-106 assembly), and within 1.6% of the given values (for the SA-13 assembly).

Table 41. Characteristics of the PIE samples of the Garigliano-1 reactor.

SFA	ID	U-235 wt%	BU (est.) GWd/tHMi	Mod. temp. (K)	Mod. dens. (g/cm3)	Fuel temp. (K)	Control fraction
A-106	A1	1.60	10.62	558	0.4572	900	0.39
A-106	A3	2.10	10.52	558	0.4572	900	0.39
A-106	A5	2.10	10.57	558	0.4572	900	0.39
A-106	A9	1.60	14.08	558	0.4572	900	0.39
A-106	B1	1.60	9.80	558	0.4572	900	0.39
A-106	B2	2.10	10.24	558	0.4572	900	0.39
A-106	B8	2.10	12.10	558	0.4572	900	0.39
A-106	C1	2.10	10.63	558	0.4572	900	0.39
A-106	C3	2.10	9.11	558	0.4572	900	0.39
A-106	D2	2.10	9.44	558	0.4572	900	0.39
A-106	D4	2.10	8.78	558	0.4572	900	0.39
A-106	E1	2.10	10.79	558	0.4572	900	0.39
A-106	E5	2.10	8.89	558	0.4572	900	0.39
A-106	G7	2.10	10.49	558	0.4572	900	0.39
A-106	H2	2.10	11.89	558	0.4572	900	0.39
A-106	H8	2.10	12.68	558	0.4572	900	0.39
A-106	J1	1.60	12.86	558	0.4572	900	0.39
A-106	J9	1.60	14.56	558	0.4572	900	0.39
SA-13	1	2.41	5.98	542	0.7375	900	0
SA-13	3	2.41	8.22	542	0.7378	900	0
SA-13	5	2.41	8.59	558	0.5679	900	0
SA-13	7	2.41	8.28	558	0.4815	900	0
SA-13	10	2.41	8.09	558	0.4099	900	0
SA-13	11	2.41	4.16	558	0.2583	900	0
SA-13	13	2.41	5.52	558	0.2417	900	0
SA-13	16	2.41	6.59	558	0.2278	900	0

II.2.6 Gundremmingen-1 (GN1)

Two assemblies from the GN1 reactor are listed in the SFCOMPO database [11]. The assemblies are B23 and C16, which are UO_2 -based. The B23 has been irradiated for four cycles and the C16 has been irradiated for three cycles. 15 PIE samples are analyzed from the two assemblies, which are listed in the SFCOMPO database [11]. The considered PIE samples are listed in Table 42. For clarity, the sample ID is specified as the rod number, followed by the first two letters identifying the sample in the SFCOMPO. For instance, sample I2680 of rod A1 is listed as sample A1-I2. The sample identifier starts with either I or K, standing for Ispra and Karlsruhe. Laboratories in Ispra and Karlsruhe, of the European Commission Joint Research Center laboratories, have conducted the RCA measurements. All samples stand at two axial positions: 268 and 44 cm from the bottom end of the fuel rods (abbreviate as 2 and 4 in the sample ID). For the B23 assembly, the samples are analyzed from the rods: A1, B3, B4, C5, E3 and E5 (one sample from each rod). For the C16 assembly, the samples are analyzed from the rods: A1, B3, C5 and E5. Most of the rods are in near-central positions, having at least one row of fuel rods separating them from the water gaps, except from rod A1 which is a corner rod.

The assemblies are based on an early 6x6 assembly design, containing 36 fuel rods and no water rods. The assemblies have diagonal symmetry and include two wide water gaps and two narrow ones. The design layouts of the two assemblies are shown in Figure 90, also showing the locations of the rods hosting the PIE samples (in black color). The enrichments of the considered PIE samples are listed in Table 42, along with other relevant irradiation parameters. All samples have 2.53 wt% U-235 enrichment. The assemblies are homogeneous, with respect to modern BWR designs, having only two types of fuel rods (1.87 and 2.53 wt% U-235 enrichments).

The lattice design and enrichments are based on the values provided in SFCOMPO [11]. The box geometry and the dimensions of the water gaps were compiled from figure 16 of reference [68]. The mentioned figure indicates that the wide gaps could accommodate a cruciform control rod, facing the low enriched fuel rods. Such orientation would position the wide and narrow gaps as shown in Figure 90. The position of the control rod is in accordance with figure 3 of reference [132]. The assemblies were modelled as a whole (no symmetries are applicable to BWR models in the current version of Polaris). Nevertheless, the assemblies show symmetries around their diagonal, having two wide water gaps to the east and south sides, and two narrow water gaps to the west and north sides. The wide water gaps can accommodate a cross-type control rods (a cruciform CR). However, the considered PIE samples were not reported to be exposed to control rods during their irradiation. Also, the CR position is always facing the low enriched rods (the rods in purple color in Figure 90), which is separated from the analyzed rods by at least one row of fuel rods. It is assumed that their effect, if present, would be negligible.

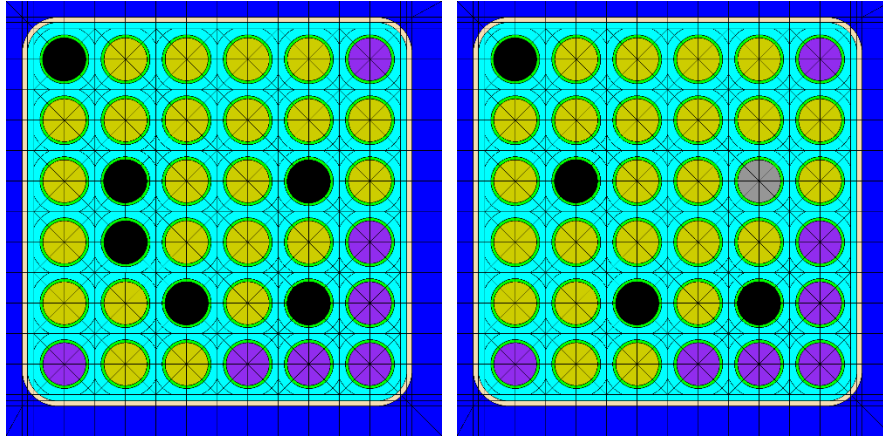


Figure 90: Polaris models of the Gundremmingen-1 assemblies B23 and C16 (left to right). The rods containing the analyzed samples are shown in black color.

Measurements of 9 PIE samples were conducted at the Ispra, and 6 PIE samples were measured at the Karlsruhe establishments of the Joint Research Centre [132]. All PIE samples had the concentrations of the Cs-137, U-235 and Pu-239 measured. Mass spectrometry is used in both laboratories for the measurements of U-235 and Pu-239 concentrations. Gamma spectrometry is used in both laboratories for the measurements of Cs-137 concentrations. The reported measurements are compiled from the SFCOMPO [11], which are cross-checked with values in [132]. The reported measurements were corrected for decay, *i.e.*, they correspond to the time of discharge of the assemblies.

Table 42. Characteristics of the PIE samples of the Gundremmingen-1 reactor.

SFA	ID	U-235 wt%	Axial loc. (cm)	BU (est.) GWd/tHMi	Cool. temp. (K)	Cool. dens. (g/cm ³)	Fuel temp. (K)
B23	A1-I2	2.5	268	27.69	559	0.388	923
B23	A1-I4	2.5	44	25.90	559	0.740	923
B23	B3-I2	2.5	268	21.69	559	0.388	923
B23	B3-K2	2.5	269	21.39	559	0.388	923
B23	B4-I2	2.5	268	22.41	559	0.388	923
B23	C5-K2	2.5	268	23.12	559	0.388	923
B23	E3-I2	2.5	268	24.28	559	0.388	923
B23	E5-I2	2.5	268	25.38	559	0.388	923
B23	E5-K2	2.5	269	26.05	559	0.388	923
C16	A1-I2	2.5	268	19.80	559	0.388	923
C16	A1-I4	2.5	44	20.19	559	0.740	923
C16	B3-I2	2.5	268	15.22	559	0.388	923
C16	B3-K2	2.5	269	14.52	559	0.388	923
C16	C5-K2	2.5	268	15.73	559	0.388	923
C16	E5-K2	2.5	269	17.68	559	0.388	923

The irradiation histories are based on the provided data in SFCOMPO [11], along with supplementary data from [132]. Table 42 provides the burnup weighted relevant irradiation parameters. The implemented moderator densities are similar to the values implemented in reference [68]. They correspond to a 50% void fraction for the samples at the 268 cm elevation,

and a 0% void fraction for the samples at the 44 cm elevation. The implemented fuel temperatures are the values provided in [132]. The samples' given burnup values are based on the SFCOMPO listed values (obtained based on the assembly operational data). The burnup values were adjusted in the current calculations such that the calculated values of the Nd-148 concentration match the measured ones ($\pm 0.05\%$). The corrected burnup values are listed in Table 42. The required correction factors are significant, as large as +16% and -18% for the A1-I2 sample in the B23 assembly and the A1-I2 sample in the C16 assembly, respectively.

II.2.7 Japan Power Demonstrations Reactor-1 (JPDR-1)

Japan Power Demonstration Reactor-1 was an experimental reactor of BWR type in Japan. The reactor relied on natural circulation and a core having a uniform U-235 enrichment of 2.6 wt%. A unique characteristic of the samples analyzed from the JPDR-1 is their low burnup values. The highest burnup value (after implementing a burnup correction) is 9.1 GWd/tHMi. Such values are important to extend the burnup validation range of the analyzed PIE data, and also to cover an interesting burnup range of low burnup SFA, which could be discharged from the last operational cycles of the core.

The core and the assemblies have two active axial zones, based on UO_2 fuel. Each zone has approximately 72 cm height, and they are separated by a 2.7 cm active zone of integral absorber ($\text{UO}_2\text{-Dy}_2\text{O}_3$). All samples are located in the UO_2 zones, having U-235 enrichment of 2.6 wt%. Three assemblies hosted 30 samples were examined after the end-of-life (EOL). The assemblies are A14, A18 and A20 are shown in their core positions in Figure 91. The samples of the A14 and A18 assemblies (3 samples from each assembly) are from rod C13, and they are designated by their elevation with respect to the midplane of the core (as listed in Table 43). The samples of the A20 assembly belong to 8 different rods, whereas those taken from rod C3 are also designated by their elevation with respect to the midplane of the core. The other samples of the A20 assembly are 2 per rod, designated by their rod number, followed by “KA” for samples from the upper level of the core, or “KC” for samples from the lower level of the core.

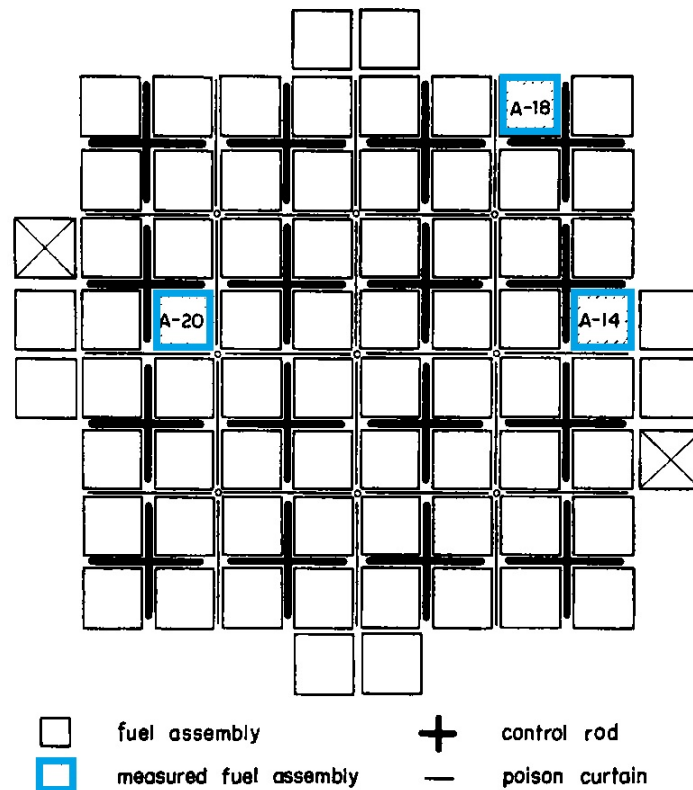


Figure 91: Layout of the Japan Power Demonstration Reactor-1 core showing the three analyzed assemblies based on [133].

The assemblies are based on a 6x6 design, having 36 fuel rods without water rods. The assemblies have diagonal symmetry. Two sides of the water gaps are wide to accommodate cross control blades, and two sides are narrow which accommodate a poison curtain (*i.e.*, sheath plates). The positions of the analyzed assemblies are shown in Figure 91. The A20 assembly is exposed to a control blade from the wide gap sides, and a poison curtain from the narrow gap sides. The A14 and A18 assemblies are also exposed to control blades from the wide gap sides, however, only one of the narrow sides contain a poison curtain. Such design details necessitated implementing the following approximations:

1. The control rod blades are modelled as described in the original reports [133,134]. They were not active in the neighborhood of the analyzed assemblies, and the follower part of the control rod blades is used in the Polaris models. The follower section is a cross blade of Zircaloy-4 material.
2. The poison curtain is a stationary thin sheet of 304 stainless-steel material, and it could not be implemented in the current version of Polaris. The poison curtain material is homogenized with the surrounding moderating water to obtain an equivalent homogenous mixture applied to the narrow sides of the assemblies. A20 had this mixture in both of the narrow sides, whereas A14 and A18 had it only in one of the narrow sides.

The design layouts of the assemblies are shown in Figure 92, also indicating the locations of the rods hosting the PIE samples (in black color). The lattice design and dimensions are based on SFCOMPO [11], and references [133,134]. The assemblies were modelled as a whole, implementing the wide and narrow gaps, the control rod follower, and the homogenized poison curtain and moderator part.

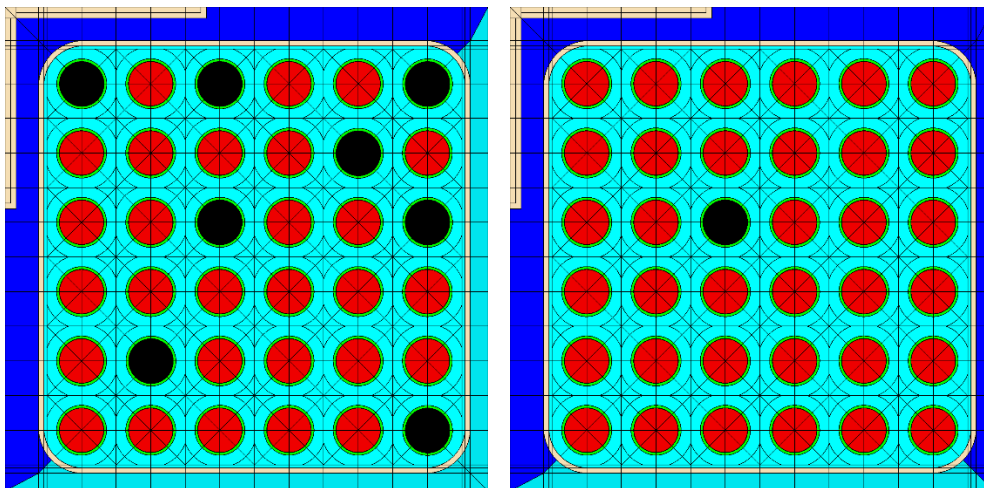


Figure 92: Polaris models of the Japan Power Demonstrations Reactor-1 assemblies: A20 (left) and both A14 and A18 (right). The rods hosting the analyzed samples are shown in black color. The water gaps are either non-boiling moderator (heavy blue) or a mixture of the moderator and the poison curtain (light blue).

The RCA of the PIE samples of the JPDR-1 reactor were performed at laboratories of JAERI [133,135,136]. All PIE samples had the concentrations of Cs-137, U-235 and Pu-239 measured.

IDMS was used for the measurements of both U-235 and Pu-239, and the reported values are at 5.6 years of decay for U-235 and between 0.5 and 1.4 years of decay for Pu-239 [11]. Gamma spectrometry was used for the measurements of the Cs-137 concentrations, and the reported values are at the discharge time [11]. The measured values were compiled from SFCOMPO [11], which are cross-checked with values reported in [133,135,136].

Table 43. Characteristics of the PIE samples of the Japan Power Demonstrations Reactor-1.

SFA	ID	U-235 wt%	Axial loc. (cm)	BU (est.) GWd/tHMi	Cool. temp. (K)	Cool. dens. (g/cm ³)	Fuel temp. (K)
A14	+049	2.60	77	4.15	550.2	0.5171	900
A14	-293	2.60	43	2.81	550.2	0.6254	900
A14	+538	2.60	126	2.28	550.2	0.4295	900
A18	+049	2.60	77	2.56	550.2	0.5171	900
A18	-293	2.60	43	1.42	550.2	0.6254	900
A18	+538	2.60	126	1.54	550.2	0.4295	900
A20	A1_KA	2.60	114	8.23	550.2	0.4464	900
A20	A1_KC	2.60	31	9.10	550.2	0.6755	900
A20	A3_KA	2.60	114	6.66	550.2	0.4464	900
A20	A3_KC	2.60	31	7.66	550.2	0.6755	900
A20	A6_KA	2.60	114	8.10	550.2	0.4464	900
A20	A6_KC	2.60	43	7.32	550.2	0.6254	900
A20	B5_KA	2.60	114	5.31	550.2	0.4464	900
A20	B5_KC	2.60	31	5.54	550.2	0.6755	900
A20	C3_+171	2.60	89	5.26	550.2	0.4907	900
A20	C3_+293	2.60	101	5.09	550.2	0.4672	900
A20	C3_+415	2.60	114	4.33	550.2	0.4464	900
A20	C3_+538	2.60	126	3.45	550.2	0.4295	900
A20	C3_+660	2.60	138	2.21	550.2	0.4172	900
A20	C3_-171	2.60	55	5.66	550.2	0.5850	900
A20	C3_-293	2.60	43	5.69	550.2	0.6254	900
A20	C3_-415	2.60	31	5.19	550.2	0.6755	900
A20	C3_-538	2.60	18	3.84	550.2	0.7301	900
A20	C3_-660	2.60	6	1.91	550.2	0.7555	900
A20	C6_KA	2.60	114	5.74	550.2	0.4464	900
A20	C6_KC	2.60	31	4.92	550.2	0.6755	900
A20	E2_KA	2.60	114	5.25	550.2	0.4464	900
A20	E2_KC	2.60	31	5.86	550.2	0.6755	900
A20	F6_KA	2.60	114	7.10	550.2	0.4464	900
A20	F6_KC	2.60	31	5.74	550.2	0.6755	900

The irradiation histories are based on the provided data in SFCOMPO [11]. The reactor was operated for experimental purposes, and the irradiation history is quite intermittent. The assemblies have been irradiated for 38 cycles over 2153 days, during which they were active for 577 days. The in-between cycles down times ranged also from very short down times (less than a day) up to 441 days. Table 43 provides the burnup weighted relevant irradiation parameters. The void fractions at the samples' axial positions were used along with the water and steam

densities at the given reactor pressure to obtain the cycle wise coolant densities. The samples' given burnup values are based on SFCOMPO, adjusted in the current calculations such that the calculated values of the Nd-148 concentration match the measured ones ($\pm 0.05\%$). Significant corrections for the burnups were implemented, which ranged between -51% to +34% of the given burnup values.

Appendix III. Polaris Input Files

In this section, two Polaris inputs are provided for two PIE samples. The samples are DM3 and GG samples, of Dodewaard-1 and Calvert Cliffs-1 reactors, respectively. Figure 93 shows Polaris models of the two samples. The BWR model is the full assembly (2D section) and the PWR model is the south-east (SE) corner of the assembly. The rods in black color contain the analyzed samples. The BWR sample is in its exact position, while the PWR sample is at rod location G6, and the shown position is its symmetric position in the modelled SE quarter – the assembly is quarter symmetric.

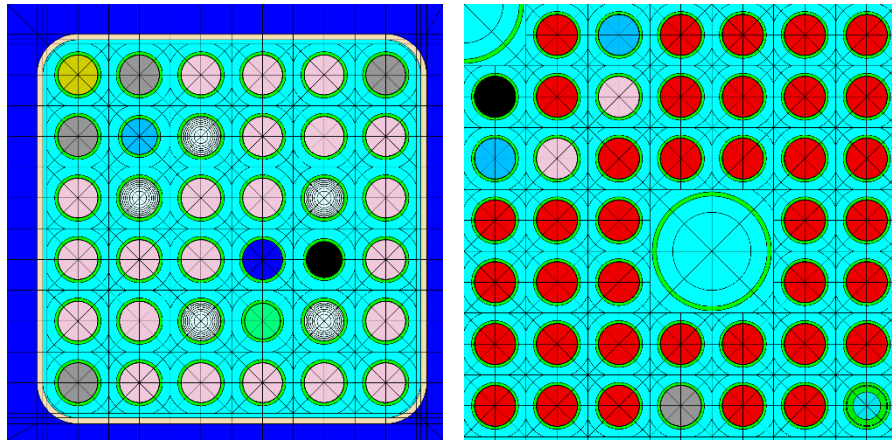


Figure 93. Polaris models of two SFAs: a BWR (left) and a PWR (right). Within each model, the fuel rods are shown in different colors to reflect differences in their densities, enrichments, and gadolinium percentage. The rod containing the analyzed sample is colored in black.

IV.1. Polaris input for PIE sample DM3, SFA Y012, reactor Dodewaard-1

```
=polaris_6.3

title "DM3"
opt DEPL
opt KEFF      RaySpacing=0.02
opt CRITSPEC  mode="NONE"
lib  "broad_n"
sys  BWR

geom DM3 : ASSM sym=FULL npins=6 ppitch=1.793

hgap    0.476  0.872  0.872  0.476
        : MOD.1  MOD.1  MOD.1  MOD.1

box    thick=0.17 rad=1.0225 hspan=5.505 Mbox=CAN.1

mat UO2.1 : UO2_1    dens=10.412  temp=933.46
mat UO2.2 : UO2_2    dens=10.412  temp=933.46
mat UO2.3 : UO2_3    dens=10.412  temp=933.46
mat UO2.G : UO2_G    dens=10.412  temp=933.46
mat UO2.U : UO2_U    dens=10.460  temp=933.46
mat UO2.M : UO2_M    dens=10.340  temp=933.46

comp UO2_1 : UOX 1.8
comp UO2_2 : UOX 2.6
comp UO2_3 : UOX 3.2
comp UO2_G : WT
              6_uox=97.3  gd2o3=2.7
comp 6_uox : UOX 3.2
comp gd2o3 : FORM Gd=2 O=3
mesh UO2.G : nr=8 ns=8

comp UO2_U : WT
              Fuel_U=99.9999126  Imp_U=0.0000874
comp Fuel_U : UOX 4.941
comp Imp_U  : FORM B=1
comp UO2_M : FORM Mix_M=1 O=2
comp Mix_M  : WT Fuel_M=99.9998843  Imp_M=0.0001157
comp Fuel_M : WT M_U92=93.569  M_M94=6.431
comp M_U92  : WT U234=0.003 U235=0.239 U236=0.001 U238=99.757
comp M_M94  : WT Am241= 1.1330 Pu238= 1.3891 Pu239=61.1423
              Pu240=23.1151 Pu241= 8.7260 Pu242= 4.4945
comp Imp_M  : FORM B=1

pin 1 : 0.574  0.5855 0.6745
      : UO2.1  GAP.1  CLAD.1  COOL.1
pin 2 : 0.574  0.5855 0.6745
      : UO2.2  GAP.1  CLAD.1  COOL.1
pin 3 : 0.574  0.5855 0.6745
      : UO2.3  GAP.1  CLAD.1  COOL.1
```

```

pin G   : 0.574    0.5855 0.6745
          : UO2.G   GAP.1  CLAD.1  COOL.1
pin U   : 0.5176   0.5275 0.6135
          : UO2.U   GAP.1  CLAD.1  COOL.1
pin M   : 0.51785  0.5275 0.6135
          : UO2.M   GAP.1  CLAD.1  COOL.1
pin W   : 0.5855   0.6745
          : MOD.1   CLAD.1  COOL.1

mat COOL.1 : H2O      dens=0.7262  temp=566.15
mat MOD.1  : H2O      dens=0.7262  temp=566.15
          comp H2O    : FORM      H=2 O=1
mat GAP.1  : He       dens=0.001   temp=600
mat CLAD.1 : ZIRC2    dens=6.57    temp=566.15
mat CAN.1  : ZIRC4    dens=6.57    temp=566.15

pinmap
1 2 3 3 3 2
2 U G 3 3 3
3 G 3 3 G 3
3 3 3 W M 3
3 3 G M G 3
2 3 3 3 3 3

deplete ALL=False UO2.1=True UO2.2=True UO2.3=True UO2.U=True
UO2.M=True UO2.G=True
basis   All=no     UO2.M=yes
shield  ALL=N UO2.1=P UO2.2=P UO2.3=P UO2.U=P UO2.M=P UO2.G=R

read history
pow
31.831721 32.518266 33.488147 34.152897 34.185590 33.379172
34.643287 35.874709 36.027275 35.961889 35.885607 37.280492
38.947816 39.732439 41.279890 42.413234 42.870931 42.870931
41.944640 40.004877 37.781779 36.125352
0

34.763160 37.738189 39.460000 37.781779 37.291389 37.008053
37.709075 40.523686 41.711054 40.575394 35.368370
0

40.142470 46.766641 46.432186 44.413050 42.610518 39.300428
39.155673 41.955924 45.189474 44.305262 38.896533
0

37.071294 46.494812 48.241876 46.838565 42.692247 47.631957
45.181156 42.360340 37.883858 35.960876 32.840594
0 0 0 0 0 0 0 0 0 0 0 0 0

state
UO2 :
temp=

```

```

961.65 990.15 999.15 1025.2 1008.7 1013.2 1047.2 1051.2
1054.7 1055.2 1057.7 1097.2 1108.2 1124.2 1151.2 1159.2
1167.2 1162.2 1147.2 1116.2 1090.7 1074.7
600

```

```

1058.2 1146.2 1112.7 1108.2 1106.7 1107.7 1134.2 1190.3
1187.4 1139.8 1073.7
600

```

```

1164.1 1171.7 1136.2 1115.4 1104.5 1060.0 1087.5 1130.5
1257.5 1191.2 1149.0
600

```

```

1206.0 1252.1 1273.8 1268.1 1221.8 1273.2 1275.8 1232.0
1163.2 1126.0 1109.0
600 600 600 600 600 600 600 600 600 600 600 600 600 600

```

```
Cool.1 :
```

```
dens=
```

```

0.3541 0.3575 0.3596 0.3603
0.3554 0.3554 0.3575 0.3554
0.3541 0.3513 0.3479 0.3527
0.3486 0.3465 0.3486 0.3492
0.3479 0.3479 0.3444 0.3486
0.3541 0.3582
0.74

```

```

0.4105 0.3589 0.3492 0.3520
0.3506 0.3513 0.3541 0.3557
0.3616 0.3663 0.3649
0.74

```

```

0.4099 0.3176 0.3193 0.3238
0.3322 0.3407 0.3555 0.3702
0.3704 0.3653 0.3537
0.74

```

```

0.3808 0.3415 0.3751 0.4083
0.4320 0.4010 0.3900 0.3887
0.3852 0.3825 0.3794
0.74 0.74 0.74 0.74 0.74 0.74 0.74 0.74 0.74 0.74 0.74 0.74 0.74

```

```
dt
```

```

6.300 12.03 21.54 20.87 7.300 15.67 11.48 7.290
13.55 14.09 9.900 17.89 17.71 20.90 23.47 22.07
20.03 20.74 10.60 16.89 6.750 11.04
77.89

```

```

4.200 13.14 13.92 28.73 21.13 26.09 65.34 19.28
26.91 41.36 24.03
50

```

```
7.140 26.96 27.86 33.64 42.12 41.98 31.98 44.88  
17.46 16.80 25.16  
54.02
```

```
20.43 34.08 50.92 41.65 36.07 26.70 42.09 20.58  
13.29 13.88 18.25  
200 700 1235 19 3 10 7 42 2 6 171 510 108
```

```
end history  
end
```

IV.2. Polaris input for PIE sample GG, SFA BT03, reactor Calvert Cliffs-1

```
=polaris_6.3

title "CC-BT03-GG"
opt DEPL
opt KEFF      RaySpacing=0.02
opt CRITSPEC  mode="NONE"
lib  "broad_n"
sys  PWR

geom CC-BT03-GG : ASSM sym=SE npins=14 ppitch=1.4732

hgap  0.0776  0.0776  0.0776  0.0776
      :COOL.1  COOL.1  COOL.1  COOL.1

mat UO2.1 : UO2_11  dens=10.193  temp=938
mat UO2.4 : UO2_14  dens=10.412  temp=938
mat UO2.5 : UO2_15  dens=10.412  temp=938
mat UO2.6 : UO2_16  dens=10.412  temp=938
mat UO2.8 : UO2_18  dens=10.193  temp=938

pin 1  : 0.48195  0.49276  0.5588
      : UO2.1    GAP.1    CLAD.1    COOL.1
pin 4  : 0.48195  0.49276  0.5588
      : UO2.4    GAP.1    CLAD.1    COOL.1
pin 5  : 0.48195  0.49276  0.5588
      : UO2.5    GAP.1    CLAD.1    COOL.1
pin 6  : 0.48195  0.49276  0.5588
      : UO2.6    GAP.1    CLAD.1    COOL.1
pin 8  : 0.48195  0.49276  0.5588
      : UO2.8    GAP.1    CLAD.1    COOL.1

pin X size=2 : 1.314    1.416
      : COOL.1    CLAD.1  COOL.1

comp UO2_11 : WT scale=PCT
Impur= 0.0264
Metal_1=99.9736

comp UO2_14 : WT scale=PCT
Impur= 0.0264
Metal_4=99.9736

comp UO2_15 : WT scale=PCT
Impur= 0.0264
Metal_5=99.9736

comp UO2_16 : WT scale=PCT
Impur= 0.0264
Metal_6=99.9736
```

```
comp UO2_18 : WT scale=PCT
Impur= 0.0264
Metal_8=99.9736

comp Impur : WT scale=PCT
C= 7.197 N= 16.667 F= 1.894 Cl= 3.788
Fe=17.045 Ag= 0.379 Al=43.560 Ni= 9.470

comp Metal_1 : WT scale=PCT
Metal-O=11.86
Metal-U1=88.14

comp Metal_4 : WT scale=PCT
Metal-O=11.86
Metal-U4=88.14

comp Metal_5 : WT scale=PCT
Metal-O=11.86
Metal-U5=88.14

comp Metal_6 : WT scale=PCT
Metal-O=11.86
Metal-U6=88.14

comp Metal_8 : WT scale=PCT
Metal-O=11.86
Metal-U8=88.14

comp Metal-O : FORM o=1

comp Metal-U1 : WT scale=PCT
92235=2.453 92234=0.022
92236=0.011 92238=97.514

comp Metal-U8 : WT scale=PCT
92235=2.453 92234=0.022
92236=0.011 92238=97.514

comp Metal-U4 : WT scale=PCT
92235= 2.33 92234= 0.02
92236= 0.01 92238=97.64

comp Metal-U5 : WT scale=PCT
92235= 2.82 92234= 0.02
92236= 0.01 92238=97.15

comp Metal-U6 : WT scale=PCT
92235=2.453 92234=0.022
92236=0.011 92238=97.514

mat COOL.1 : WATER dens=0.7572 temp=557.4
comp WATER : LW 694
```

```
mat  GAP.1   : He      dens=0.001  temp=620
mat  CLAD.1   : ZIRC4   dens=6.56   temp=620
mat  Stain.1   : Stain   dens=7.76   temp=557.4
mat  GAP.2     : He      dens=0.001  temp=557.4

comp Stain : WT
C=  0.04 Cr=18.3 Fe=70.068 Mn= 1.29
Mo= 0.132 Ni=10.035 Si= 0.135

pin S   : 0.330  0.4725  0.49276  0.5588
        : GAP.2  Stain.1 GAP.2     CLAD.1   COOL.1

pinmap
X 1 6 1 1 1 1
8 1 4 1 1 1 1
6 4 1 1 1 1 1
1 1 1 X X 1 1
1 1 1 X X 1 1
1 1 1 1 1 1 1
1 1 1 5 1 1 S

state
UO2   : temp=940
COOL  : boron=694

deplete ALL=false  UO2.1=True  UO2.4=True  UO2.5=True  UO2.6=True
UO2.8=True
basis   All=no      UO2.8=yes
shield  ALL=N       UO2.1=P  UO2.4=P  UO2.5=P  UO2.6=P  UO2.8=P

read history

pow
22.29582  27.98590  27.98590  27.75365  27.52141  27.40528  27.28916
27.40528
27.40528  27.28916  27.05691  26.82466  26.59241  26.24404  0.000000
26.01179
25.77955  25.54730  24.50218  17.30249  14.28326
0 0
15.44450  19.85722  22.06358  21.94745  21.94745  21.94745  21.94745
21.94745
21.83133  22.41195  22.52807  22.99257  22.76032  22.99257  21.36683
21.25071
0
14.63163  14.39939  7.780310  16.25737  16.48962  17.65086  16.60574
16.95412
16.95412  16.95412  17.18636  0.000000  17.30249  18.69598
0
16.02512  16.02512  16.14125  16.37350  7.780310  7.315820  8.128690
14.39939
17.30249  17.65086  17.53474  18.11536  17.99923  18.23148
```

0 0 0 0 0

state

UO2 :

temp=

938 938 938 938 938 938 938 938
938 938 938 938 938 938 938 938
938 938 938 938 938
938 938
938 938 938 938 938 938 938 938
938 938 938 938 938 938 938 938
938
926 926 926 926 926 926 926 926
926 926 926 926 926 926
926
793 793 793 793 793 793 793 793
793 793 793 793 793 793
793 793 793 793 793

COOL :

boron=

694 672 644 605 567 529 491 454
416 378 341 303 265 227 192 157
119 91 71 47 16
10 10
697 653 598 566 539 497 444 392
356 311 236 178 137 100 45 2
10
1057 1022 967 914 874 830 755 658
571 483 378 282 163 39
10
1144 1055 995 934 861 763 643 567
540 468 372 299 178 47
10 10 10 10 10

dt

24.20 19.60 39.70 39.60 39.40 39.30 39.10 38.90
39.00 39.10 39.10 39.40 39.30 39.30 33.00 39.20
39.20 19.60 20.40 30.80 32.80
47 120
7.20 31.00 16.40 11.40 12.60 23.20 22.70 23.00
8.20 31.00 33.80 16.50 19.10 12.80 35.20 1.90
71
10.90 14.10 25.30 12.20 16.30 15.10 38.10 30.90
31.40 31.50 43.20 25.00 60.00 28.00
81
45.00 24.10 22.40 25.20 31.00 44.80 48.10 10.90
10.60 45.30 28.70 27.90 65.90 36.10
70 200 600 1500 61

end history

end

Appendix IV. Permutation Tests on the Decay Heat Data

This section provides results of the permutation tests conducted on the decay heat bias data, for testing the significance of the observed average biases. The null distributions generated using permutations of the biases data are shown in Figure 94. The red lines mark the observed average biases on each validation category. By counting observations that are equal to, or more extreme than, the observed average bias with respect to all permutations, a p -value is obtained for each observed average bias. The p -value for all the PWR sections of the data are near zero, and they are greater than the set threshold of 0.05 for all the BWR sections of the data. Again, the null hypothesis is rejected, and the alternative is accepted that the calculations of these characteristics on the PWR sections of the data are systematically or significantly different from the measurements. The observed average biases of these characteristics are statistically significantly, *i.e.*, they are extreme of significant with respect to the null distributions. Similar to the bootstrap tests, the tests failed also to reject the null hypothesis using the permutation tests on all BWR sections of the data. There is no evidence from the data that the calculations on the BWR characteristics are significantly different from the measurements, and the observed differences between the calculations and measurements are likely to be due to chance or could result from randomness in the data. The conclusions drawn from the permutation tests conducted on the different sections of the data are similar to those obtained through bootstrap tests, however, at slightly different significance levels.

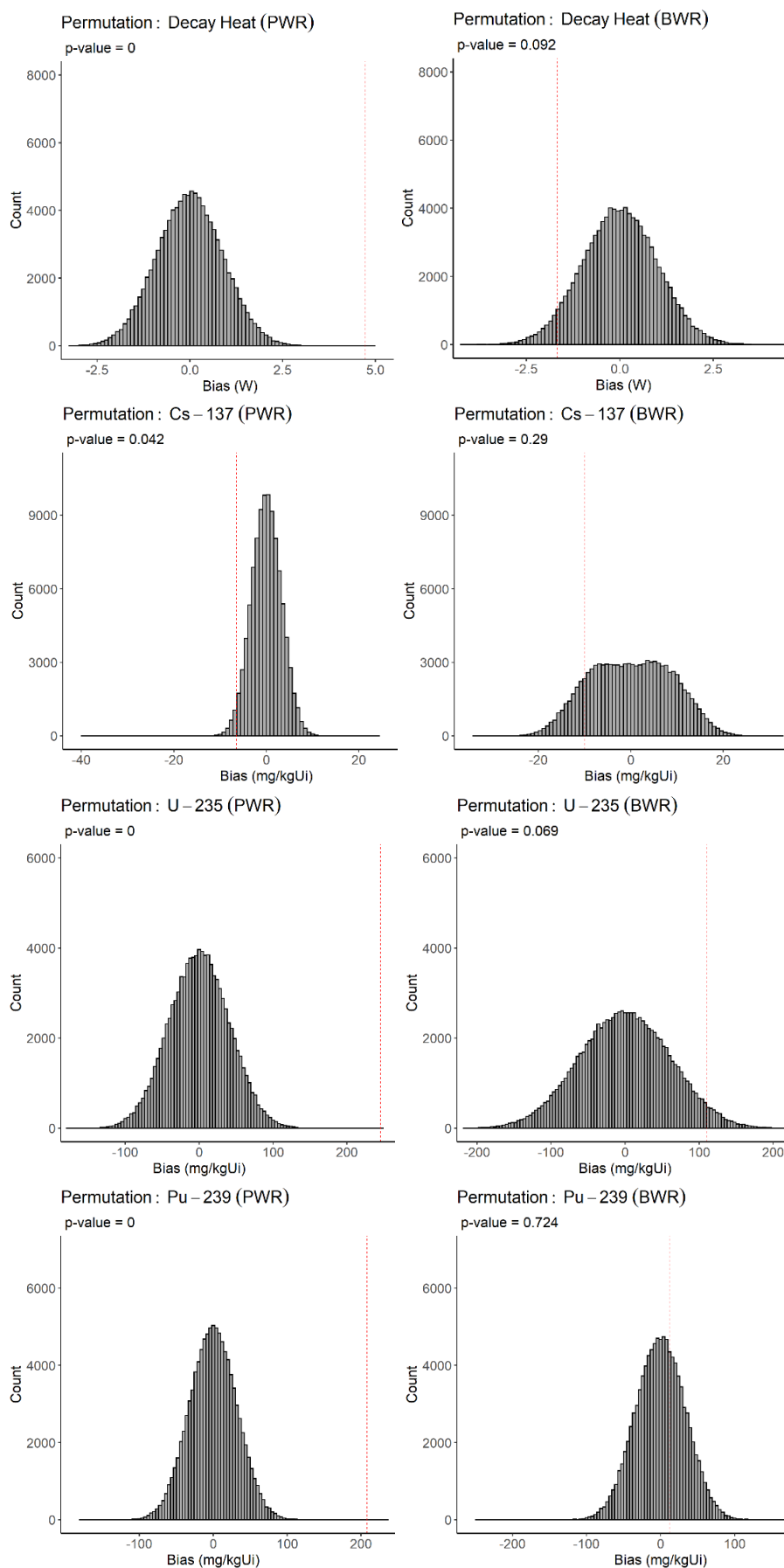


Figure 94. Permutation distributions of the average biases (the red lines are the observed values).

Appendix V. ORIGEN Calculations of the Decay Heat

Decay heat calculations of the decay heat benchmarks were also performed using ORIGEN code of the SCALE code system (version 6.2.3) [49] – in addition to the reference calculations performed using Polaris. The approach has been selected considering its lower computational requirements and widespread usage. The used nuclear data are the SCALE cross-sections, fission yields, and decay data based primarily on the ENDF/B-VII.1 nuclear data [49].

The ORIGEN calculations rely on several steps unlike the approach in Polaris. Firstly, TRITON is used, which is a generalized-geometry multi-purpose control module with discrete ordinates lattice-physics capabilities. The module has been used to perform neutron transport and depletion calculations for all assembly designs and subcategories (32 categories). Similar to Polaris, the TRITON models are also 2D models of the assemblies along with reflective boundary conditions. The outputs of the TRITON models include lattice-specific, enrichment-dependent, burnup-dependent, weighted 1-group cross-sections for each individual SFA design and subcategory.

The ARP module interpolates between pre-computed, problem-dependent transition matrices that are generated using standalone depletion calculations [49]. The ARP module has been used to import the specific TRITON-generated cross-sections and perform interpolation between them, based on enrichments, water densities, and burnups of the benchmark to generate specific cross-sections for the benchmark under consideration. The interpolated cross-sections are then used by ORIGEN for the depletion and decay calculations up to the specified cooling time.

The following are major modelling assumptions – whenever they diverge from the former approach of Polaris:

1. Rebuilt SFAs were not considered in TRITON, *i.e.*, the lattice-wise cross-sections of the rebuilt SFAs correspond to the design subcategory. ORIGEN performed depletion and decay for a ton of the initial heavy mass, and the decay heat of the SFA is calculated by scaling the decay heat per ton to the heavy mass of the SFA after the rebuild.
2. Activation and the source term from the cladding and the spacers were accounted for in ORIGEN models, they were added to the models as extra material in addition to the material of the fuel matrix.

Curriculum Vitae

Personal Details

Nationality: Egyptian

Address: Stadtbachstrasse 63, 5400 Baden, Switzerland

e-mail: ahmed.shama@outlook.com

Tel. /Mob. : +41-561371332 / +41-786621101

Affiliation

Doctoral Assistant - EPFL (École Polytechnique Fédérale de Lausanne)

Engineer (part-time) - NAGRA (Nationale Genossenschaft für die Lagerung radioaktiver Abfälle)

Education

1. Doctoral Studies

EPFL, Laboratory for Reactor Physics and Systems Behaviour (LRS), Switzerland

Thesis: Data-Driven Predictive Models: Computational Bias in Characterization of Spent Nuclear Fuel

Started: Oct. 2017 - Expected end-date: Nov. 2021

2. M.Sc. in Nuclear Engineering

Swiss Federal Institute of Technology Zürich (ETHZ) and EPF Lausanne (EPFL), Switzerland

Thesis: Study of Microfluidic Mixing and Droplet Generation for 3D Printing of Nuclear Fuels

Project: Fluid Structure Interaction (FSI) in SFR Fuel Assemblies

Completed: Sep 2015 – Sep 2017

3. M.Sc. in Engineering Physics

Faculty of Engineering, Cairo University, Egypt

Thesis: Validation and Benchmarking of the Deterministic Diffusion Method for the Neutronic Calculations of Thermal Research Reactors

Completed: Sep 2008 – Apr 2012

Education (continues)

4. B.Eng. in Metallurgical and Materials Engineering

Faculty of Petroleum and Mining Engineering, Suez University, Egypt

Project: Production of Mg-Base Tertiary Alloys AZ91-E/D

Completed: Sep 2000 – Aug 2005

Thesis

M.Sc. Nuclear Engineering: Study of Microfluidic Mixing and Droplet Generation for 3D Printing of Nuclear Fuels. <https://infoscience.epfl.ch/record/254925?ln=en>

M.Sc. Engineering Physics: Validation and Benchmarking of the Deterministic Diffusion Method for the Neutronic Calculations of Thermal Research Reactors. [https://DOI: 10.13140/RG.2.2.35261.97760](https://doi.org/10.13140/RG.2.2.35261.97760)

Publications

- A. Shama, S. Caruso, V. Bykov, A. Noël, G. Anton, A. Bashe, A. Pautz, T. Simeonov. Verification of SCALE Modules against CMS5/SNF sequence for Depletion and Decay Calculations of BWR Fuel Assemblies. In proceedings of the 19th International Symposium on the Packaging and Transportation of Radioactive Materials (PATRAM). Aug. 4-9, 2019, New Orleans, LA, USA.
- A. Shama, S. Caruso, A. Pautz. Quantification of the Computational Biases in Fuel Depletion for the Swiss Disposal Concept. International High-Level Radioactive Waste Management 2019 (IHLRWM 2019). Knoxville, TN, April 14-18, 2019.
- A. Shama, M. Pouchon, I. Clifford. Simulation of the microfluidic mixing and the droplet generation for 3D printing of nuclear fuels. Additive Manufacturing. Vol. 26 (2019) 1-14. [https://doi: 10.1016/j.addma.2018.12.011](https://doi.org/10.1016/j.addma.2018.12.011)
- E. Amin, A. Shama, H. Hussein, Benchmarking of the WIMSD/CITATION deterministic code system for the neutronic calculations of TRIGA Mark-III research reactors. Annals of Nuclear Energy. Vol. 66 (2014) 113–123. [https://doi:10.1016/j.anucene.2013.12.005](https://doi.org/10.1016/j.anucene.2013.12.005)
- A. Shama, D. Rochman, S. Pudollek, S. Caruso, A. Pautz. Uncertainty analyses of spent nuclear fuel decay heat calculations using SCALE modules. Nuclear Engineering and Technology. Vol. 53, Issue 9 (September 2021), 2816-2829. <https://doi.org/10.1016/j.net.2021.03.013>
- A. Shama, D. Rochman, S. Caruso, A. Pautz. Validation of Spent Nuclear Fuel Decay Heat Calculations Using Polaris, ORIGEN and CASMO5. Annals of Nuclear Energy. Vol. 165 (January 2022), <https://doi.org/10.1016/j.anucene.2021.108758>

Skills

Python and **R**: applications on data analysis and machine learning

FORTRAN and **MATLAB**: generic applications

SALOME and **Trelis**: Meshing software

OpenFOAM: Computational fluid dynamics

WIMSD and **CITATION**: lattice physics and core behavior codes

SCALE: Polaris, TRITON, KENO, MAVRIC, ORIGEN: Lattice physics, criticality, shielding and depletion calculations

Basic Knowledge: CASTEM (FSI), FLUENT (CFD), and NJOY21 and AMPX (cross-section processing)

Work Experiences

Nov 2017 to now: Doctoral Assistant

University: EPFL

Country: Switzerland

Jun – Sep 2016 + June 2020-Nov 2020 + June 2021 to now: Internship/Engineer

Company: NAGRA

Country: Switzerland

Project: Burnup credit, and activation calculations of cladding and structural materials of SNF

2012 – 2015: Inspection Engineer

Company: Det Norske Veritas/Germanischer Lloyd (DNV-GL)

Country: Oman

Project: Umm Lulu & Nasr Phase-1 – Construction of Oil/Gas Offshore platforms and installations

Activity: Materials, pressure vessels, and Static Mechanical Inspection

American Petroleum Institute: Piping Inspector ID#46799 (expired)

American Petroleum Institute: Corrosion and Materials Professional ID#52608 (expired)

2006 – 2012: Quality Control Engineer

Company: OPCO

Country: Egypt (2006-2009 full-time, 2009-2012 par-time)

Several projects

Activity: Oil/Gas – Material and Static Mechanical Inspection of Pipings / Oil Storage Tanks / Gas Pressure Vessels / Pipelines (onshore and offshore) / Offshore installations (Structural Material of Offshore Platforms)